Huchon, P., Taylor, B., and Klaus, A. (Eds.)
Proceedings of the Ocean Drilling Program, Scientific Results Volume 180

25. Presentation and Structural Analysis of FMS Electrical Images in the Northern Margin of the Woodlark Basin[1]

Bernard Célérier,[2] Véronique Louvel,[3] Bernard Le Gall,[4] Véronique Gardien,[5] and Philippe Huchon[6]

ABSTRACT

More than 2 km of Formation MicroScanner (FMS) electrical images were acquired during Ocean Drilling Program Leg 180 at Sites 1109, 1115, and 1118 along a north-south–trending transect across the northern margin of the western Woodlark Basin. These data are analyzed to complement the shipboard core structural observations with oriented measurements.

Unambiguous fractures are identified only in the dolerite at the bottom of Hole 1109D. Strike is mainly east-west, and dip ranges from 5° to 30°.

Only few fractures are identified in the sediments of Sites 1118, 1109, and 1115, even though they were frequently observed in cores.

Bedding orientation deviates from subhorizontal only in a few intervals. These deviations are often associated with fracturing and are compatible with horizontal axis folding. This geometry suggests two possible interpretations: gravity-driven slumping and growth faulting or tectonic-driven extension associated with folding. These two processes may result in similar structural axis orientation along the east-west strike of the Moresby detachment.

Full borehole dynamic and static FMS image coverage is also provided and is related to the lithologies described in cores. Typical dynamic image facies of sandy, calcareous, and clayey formations are shown in a catalog of larger-scale images. The static image, which is di-

[1]Célérier, B., Louvel, V., Le Gall, B., Gardien, V., and Huchon, P., 2002. Presentation and structural analysis of FMS electrical images in the northern margin of the Woodlark Basin. *In* Huchon, P., Taylor, B., and Klaus, A. (Eds.), *Proc. ODP, Sci. Results,* 180, 1–159 [Online]. Available from World Wide Web: <http://www-odp.tamu.edu/publications/180_SR/VOLUME/CHAPTERS/177.PDF>. [Cited YYYY-MM-DD]
[2]ISTEEM, CNRS-Université de Montpellier II, cc MSE, 34095 Montpellier Cedex 5, France. **Bernard.Celerier@dstu.univ-montp2.fr**
[3]Laboratoire de Mesures en Forage, ODP-NEB, 13545 Aix-en-Provence Cedex 4, France. Present address: 12, Impasse Jean Giono, 13830 Roquefort-La Bedoule, France.
[4]Institut Universitaire Européen de la Mer, CNRS UMR 6538, 29280 Plouzané, France.
[5]Université Lyon I, UMR 5570, 69622 Villeurbanne Cedex, France.
[6]Géosciences Azur, Observatoire de Villefranche, BP 48, 06235 Villefranche sur mer, France.

Initial receipt: 19 March 2001
Acceptance: 16 May 2002
Web publication: 28 August 2002
Ms 180SR-177

rectly related to resistivity, seems to be mainly controlled by carbonate content, as also suggested by conventional logs.

INTRODUCTION

The Moresby detachment (Figs. F1, F2) at the western tip of the Woodlark rift basin is one of the few known examples of seismically active low-angle normal faults (Abers, 1991; Wernicke, 1995; Abers et al., 1997). It therefore provides the opportunity to study the poorly understood mechanics and evolution of such faults. Ocean Drilling Program (ODP) Leg 180 was designed to address three different aspects of this problem by drilling three types of sites along a north-south transect across the Moresby detachment (Taylor, 1999; Shipboard Scientific Party, 1999b).

Site 1108 objectives were to drill the fault zone at depth to study its in situ physical properties and state of stress. Difficult drilling conditions and hydrocarbon safety concerns required the abandonment of this goal. The fault zone was drilled instead at Site 1117 on the northern slope of the Moresby Seamount, where it is exposed. This confirmed that it is a major shear zone (Shipboard Scientific Party, 1999b).

Southern Sites 1116 and 1114 were drilled to study the nature and deformation of the footwall and basement of the detachment (Shipboard Scientific Party, 1999b).

Sites 1118, 1109, and 1115 recovered 1.7 km of core in the synrift, and, in the case of Hole 1115C, prerift sediments of the northern margin of the basin. These three sites document the subsidence history of the hanging wall of the detachment and the interaction of sedimentation with extensional tectonics through numerous instances of soft sediment deformation associated with normal to oblique normal faulting (Shipboard Scientific Party, 1999b). These sites are also integrated with seismic reflection data, which allows extension of the borehole observations to a regional scale (Goodliffe et al., 1999; **Goodliffe et al.,** this volume).

Four boreholes (Holes 1114A, 1118A, 1109D, and 1115C) were logged with the Formation MicroScanner (FMS), providing 2.3 km of continuous oriented high-resolution images of the sediment infill of the Woodlark rift basin. A preliminary analysis of these FMS data done on board is reported in Shipboard Scientific Party (1999b, 1999c, 1999d, 1999e)

FMS and core data are complementary for structural studies in many respects. Important detailed structures such as slickensides are only observed in core, but FMS images are oriented in space, whereas cores are not oriented in the horizontal plane (for vertical wells).

Core recovery is often incomplete and biased with respect to lithology or fracturation, whereas FMS data are continuous but do not cover the upper 100 m of boreholes, where the bottom-hole assembly is located during logging operations. The resulting coverage for the four sites is summarized in Table T1. In the footwall Site 1114, where recovery is low, the FMS images cover an interval that is 4.3 times larger than the recovered core length. In the northern margin Sites 1118, 1109, and 1115, where core recovery is high, FMS data cover an interval that is 1.1 to 1.6 times longer than the recovered core length.

A comprehensive structural analysis conducted postcruise is presented in this paper for the northern margin Sites 1118, 1109, and 1115

F1. Leg 180 drill sites, p. 25.

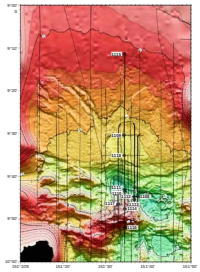

F2. Cross section of Leg 180 sites, p. 26.

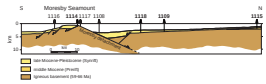

T1. Core and log data coverage, p. 111.

and in a companion paper for the footwall Site 1114 (**Louvel et al.**, this volume).

The main goal of the FMS structural analysis is to provide the bedding and fracture dip direction that is missing from core observations, to study the organization of these structures, and to relate them both to regional tectonics and to the results of core analysis.

This, however, requires the identification of lithology because it affects the expression of strain. A few typical FMS image facies related to specific lithologies were indeed identified. The exceptional amount of FMS data this identification is based on and its integration within seismic profiles suggested a secondary goal, to present a catalog of detailed images of these typical facies and full borehole coverage images that relate them to the lithologic and logging units defined by the Shipboard Scientific Party. The full borehole coverage can be used to locate other studies of the Woodlark drill holes, and the catalog of larger-scale FMS facies provides a comparison basis for facies encountered in other sedimentary basins. This goal became possible because the new electronic format of the Ocean Drilling Program (ODP) *Scientific Results* does not place severe limitations on color figures.

The method and the resulting documents will be presented first. The data from each of the three sites and their interpretation will be discussed next. The discussion will proceed from south to north, that is, from the depocenter to the northern border of the basin. Finally, the results concerning fracturation, bed deformation, and the role of lithology will be discussed.

METHODS

Schlumberger introduced the FMS in 1986 to measure the electrical resistivity of boreholes with an array of sensors sufficiently dense to produce high-resolution resistivity images of the borehole wall (Ekstrom et al., 1987). A slim version of this tool was designed to pass through the drill pipe and was introduced during Leg 126 (Shipboard Scientific Party, 1990; Pezard et al., 1990). The image resolution is on the order of a few millimeters. However, because of the slim design, the four pads produce an image that covers only about 25% of the usual 25-cm-diameter ODP boreholes and good pad contact with the formation is ensured only in holes with a diameter <37 cm.

The FMS data are processed separately from the conventional logs. In particular, the depth computation includes a sticking detection procedure that uses the tool accelerometer data to correct the winch cable depth data when the tool gets stuck and the two measurements conflict. This correction is applied from the bottom of the hole, which is set to be consistent with that of the other logs, and can accumulate significant depth differences upward in some instances. It is therefore necessary to correlate FMS and classical logs. This is possible because the FMS tool string records natural gamma ray and caliper data that are processed in two different manners: a first processing is identical to that of classical logs and produces ASCII data given in the *Initial Reports* volume; a second processing that is made together with the electrical images, and therefore includes the same depth correction as these images, is included in the input DLIS file used in the Schlumberger Geoframe interpretation software. Correlation can then be made between these two different outputs for the same measurements. For Leg 180, caliper data provide a good reference for correlation and are therefore system-

atically displayed alongside the FMS images in this paper. The "Appendix," p. 24, lists a few offsets at selected tie points for each hole. In the case of Holes 1118A and 1115C, this offset from the conventional logs can reach a few meters.

Two types of images are constructed: a dynamic image, where the color equalization is done in a 2-m sliding window, and a static image, where the color equalization is done for the whole borehole. The static FMS image is a qualitative measure of resistivity, whereas the dynamic image, by enhancing local contrast, reveals detailed sedimentary or tectonic features.

These FMS electrical images are then analyzed with the Schlumberger Geoframe software. A key feature of this software lies in its ability to interactively renormalize the color scale within any depth interval to help identify features of various sizes. The image variations were noted to build a catalog of typical facies that are naturally related to the core-defined lithologic units and to the logging units defined by the Shipboard Scientific Party (1999c, 1999d, 1999e).

The sedimentary fill of the northern margin is mainly composed of alternating clay, silt, carbonates, and sands mixed in various proportions, as summarized in the lithologic units (numbered I–XII; Table T2). Holes 1118A and 1109D bottom in a prerift dolerite overlain by a conglomerate, whereas Hole 1115C bottoms in prerift forearc sediments.

T2. Lithologic unit intervals and summary description, p. 112.

The logging units (numbered L1–L12) were defined after a quick-look analysis of mainly neutron porosity (APLC), lithodensity (RHOM), photoelectric effect (PEFL), and gamma ray (NGR) (Shipboard Scientific Party, 1999a). The photoelectric effect is a direct indication of carbonate content. Clay content is usually estimated from gamma ray, but the presence of radioactive sands made this impractical in the Woodlark Basin. The difference between neutron and lithodensity porosity was therefore used instead as an indicator of clay content. The density porosity (DPHI) is computed from the density measurement (RHOM) by

$$DPHI = (dm - RHOM)/(dm - dw), \quad (1)$$

where,

dm = grain density (2.71 g/cm^3) and
dw = seawater density (1.03 g/cm^3).

The porosity difference (DPORO) is then computed by

$$DPORO = APLC - DPHI. \quad (2)$$

DPORO ranges from –1.8 in pure sand to 0 in pure limestone to 0.4 in clay or dolomite. The analysis uses the separation of the APLC and DPHI curves, which represents DPORO. Further details can be found in Shipboard Scientific Party (1999a). It is useful to remember that the terminology clay, silt, and sand used in core descriptions is based on grain size, whereas that used in log interpretation, clay, carbonate, and sand, is related to mineralogy and porosity. As a consequence, an interval with low clay and carbonate content may be described as sandy from logs while being described as silty from core.

The structural analysis determines planar structure orientations by fitting sinusoids of observed features on 1/10 to 1/20 vertical scale dynamic images. Most of these structures are either sedimentary bedding

or fractures and were labeled as bedding 1 and 2 or fracture 1 and 2 according to a decreasing degree of confidence. Bedding confidence is limited by the lack of resistivity contrast within some formation and/or by sediment reworking (synsedimentary deformation or bioturbation), which attenuates that contrast. Fractures are identified indirectly by bed truncation or abnormal contacts. These abnormal contacts have to be traced from pad to pad, which is made difficult by the low coverage of slim FMS data. Ambiguous planar features that could not be properly identified were also recorded and labeled as unknown. Erosional surfaces or unconformities were also attributed to this category to separate sedimentary structures such as channels from deformational structures. These measurements are discussed and related to the core-derived structural domains (numbered I–III) below.

The intervals where bedding orientation varies are then isolated to determine whether these orientations can be accounted for by simple folds, and, in the cases where they can, whether folding is related to nearby faulting. This is done by using the stereographic projection where the poles of cylindrical or conical structures fall within a great or small circle, respectively.

FMS images and structural interpretation are presented at three different scales:

First, a synthetic view is provided by whole borehole static images at the scale ~1/1000, integrated with core recovery, lithologic, log, and structural units boundaries. Only the static image is shown because the 2-m equalization window makes the dynamic images uniform at this scale.

Second, full borehole coverage static and dynamic images and interpretation are given in the **"Appendix,"** p. 24, at ~1/200 vertical scale, which was found to be sufficiently small for each full borehole image to be limited to a few pages yet sufficiently large to appraise the structural interpretation and the lithologic variations.

Finally, close ups of selected typical facies intervals are presented at ~1/60 to ~1/20 scales, which are close to the ~1/20 to ~1/10 interpretation scale.

HOLE 1118A

A synthetic view of the results for Hole 1118A is given in Figure **F3,** where core recovery, static FMS image, FMS structural interpretation tadpoles, shipboard lithologic units (Table **T2**), logging units, and structural domains are shown together. Further details on shipboards units can be found in figures F1 (lithologic units), F42 (structural domains), F71 (logs and logging units), and F76 (synthesis) of Shipboard Scientific Party (1999e).

The structural measurement orientation is shown on stereographic projection and on strike and dip histograms for bedding (Fig. **F4**), fracture (Fig. **F5**), and unknown structures (Fig. **F6**).

Only 24 fractures are identified, and all of them belong to the fracture 2 set (Table **T3**), which means that the determination always had some ambiguity. The fracture distribution is scattered but shows steep 35°–80° dips (Fig. **F5**).

The FMS bedding dip distribution, based on 589 measurements (Table **T3**), shows that most dips are <10° (Fig. **F4**) and are compatible

F3. Composite log of Hole 1118A, p. 27.

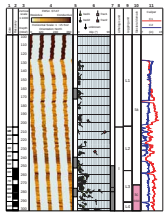

F4. Hole 1118A global bed orientations, p. 31.

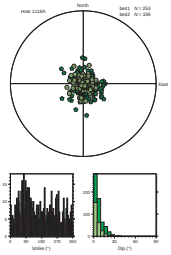

F5. Hole 1118A global fracture orientations, p. 32.

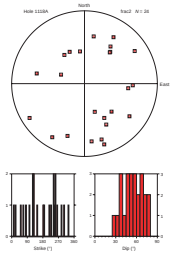

F6. Hole 1118A global unknown planar structure orientations, p. 33.

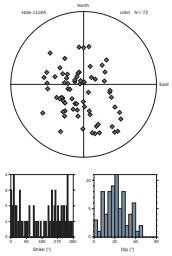

T3. Number of planar structure measurements, p. 113.

with those obtained from 301 measurements in cores (fig. F43 in Shipboard Scientific Party, 1999e). The dip direction is scattered, with a slight trend toward the south (strike peak = ~90°). The less well defined bed 2 distribution is more dispersed than the bed 1 distribution, as expected, but displays similar mean orientations. The depth dependence of these structures is illustrated in the tadpole plots of Figure F3. Five intervals contain most of the beddings that deviate from the horizontal: 250–340, 390–410, 565–596, 630–651, and 840–890 meters below seafloor (mbsf) (Fig. F3; column 7).

Four of these intervals (250–340, 390–410, 565–596, and 840–890 mbsf) correspond to locations where soft sediment deformation or faulting was observed in core (shown in pink in the structure column of Fig. F3), and three among these (250–340, 565–596, and 840–890 mbsf) strikingly correspond to locations where faults are identified on FMS images. This association of folding with faulting was also noted in the shipboard structural analysis of cores.

Further analysis requires focus on specific depth intervals. Intervals where either larger-scale images or where detailed stereograms and histograms of structure will be introduced in this discussion are marked in columns 5 and 7 of Figure F3, respectively. The discussion will proceed from uppermost to lowermost. The ~1/200 vertical scale full coverage of the hole with a dynamic image given in the "Appendix," p. 24 (Fig. AF1) can be used to bridge the gap between Figure F3 and the larger-scale figures presented below.

Depth shifts of FMS with respect to conventional log data can reach 9 m near the top but become negligible at the bottom of the hole (see "Appendix," p. 24). As a consequence, the discussion below will first describe FMS images and their depth and then correlate them to core and log units with their own depth. In the lower part of the hole, this distinction will vanish.

130–196 mbsf

Bedding is poorly defined (Fig. F7), and few structural measurements are therefore available (Fig. F3) in this interval, which was not cored and is therefore known only from logs. Logging Unit L1 (100–204 mbsf) is characterized by large divergence between neutron and lithodensity porosity, which indicates a high clay content.

196–247 mbsf

The borehole diameter is often reduced below the bit size of 25 cm (9.875 in) in this interval (Fig. F3). The FMS static image is more conductive than in the previous interval and is even more so where the borehole diameter is reduced (Fig. F3). This suggests that clay swelling may have caused these restrictions. Bedding remains poorly defined on the dynamic FMS image (Fig. F8).

This interval corresponds to logging Unit L2 (204–255 mbsf), defined by a higher bulk density than Units L1 above and L3–L7 below and the major seismic reflector (Light Green 1), discussed in Goodliffe et al. (this volume). It also corresponds to the upper part of lithologic Unit I, which begins at 205 mbsf with the first recovered core.

F7. FMS image, Hole 1118A, 160–172.5 mbsf, p. 34.

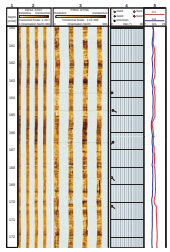

F8. FMS image, Hole 1118A, 240–252.5 mbsf, p. 35.

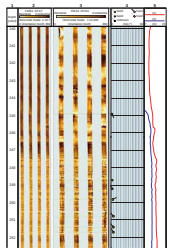

247–372 mbsf

This interval, also within lithologic Unit I (205–378 mbsf), corresponds to logging Units L3 (255–292 mbsf), L4 (292–347 mbsf), and the upper part of L5 (347–402 mbsf).

Within the 247- to 286-mbsf interval, the static FMS image is more resistive than above (Fig. F3) and the dynamic image shows clearly defined thin resistive beds (Fig. F8). These beds are often deformed; dipping and sometimes nonplanar structures are observed, such as those around 281 mbsf (Fig. F9). The corresponding logging Unit L3 was defined by a separation of the two porosity logs, with no detectable clean beds and a slightly elevated PEFL, indicating high clay and carbonate content. The thin resistive beds seen on the FMS may then be due to higher carbonate content. Alternatively, if they are related to lower clay content, their deformation may partly explain why they are not identified on the lower-resolution density and neutron logs.

The static image shows a downward-decreasing resistivity in the 286- to 341-mbsf interval (Fig. F3). Evidence of deformation can be observed but not correlated from pad to pad because of poorly defined bedding (Fig. F10). This corresponds to logging Unit L4, where the two porosity logs are separated but by less than in Unit L3, converging often, indicating slightly lower clay content and thin clean beds. PEFL is lower than in Unit L3, indicating lower carbonate content. The likely cause of lower resistivity is then lower carbonate content because indications point to a clay content decrease.

Soft sediment deformation was observed in core from this interval, with centimeter-sized folds in structural domain Ic (272–320 and 335–396 mbsf) and decimeter-sized folds in domain Ib (320–335 mbsf) (fig. F4 in Shipboard Scientific Party, 1999e).

The numerous dipping beds and the few fractures on the FMS tadpole plot within the 250- to 340-mbsf interval underscore this zone of deformation (Fig. F3). The small scale of the structures observed in core suggests reduction of the analysis interval. Nearly flat beds at 271–277 mbsf allow the definition of two subintervals: an upper interval at 250–280 mbsf, mainly associated with folding, and a lower 275- to 340-mbsf interval associated with both folding and faulting.

A stereographic projection of the poles to bedding in the 250- to 280-mbsf interval suggests a poorly defined horizontal folding axis trending N67°E (Fig. F11).

The same projection of the poles to bedding within the 275- to 340-mbsf interval shows a large scatter with a slight trend along a great circle with a horizontal axis trending N52°E (Fig. F12). That circle almost contains a south-dipping fracture (#3 on Fig. F12) that is located at 309 mbsf (Fig. F3). This suggests a genetic link between folding and fracturing. The fact that most beds dip to the north while the fracture dips to the south suggests reverse drag (i.e., roll over) along the probably normal fault. If we follow this hypothesis, then the northeast fold axis trend with a south-dipping fault would suggest a significant strike component of slip. However, the scatter of the data, the fact that the bed 2 category dominates the bedding measurements, and the fact all the fractures belong to the fracture 2 category, make this highly hypothetical.

The more conductive static FMS image observed in the 341- to 372-mbsf interval (Fig. F3) is consistent with the increased clay content inferred from the higher neutron and lithodensity porosity separation, which defines logging Unit L5 at the bottom of lithologic Unit I.

F9. FMS image, Hole 1118A, 276–286 mbsf, p. 36.

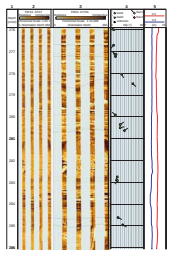

F10. FMS image, Hole 1118A, 325–335 mbsf, p. 37.

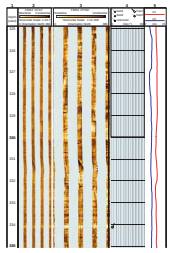

F11. Structure orientations, Hole 1118A, 250–280 mbsf, p. 38.

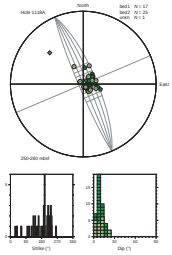

F12. Structure orientations, Hole 1118A, 275–340 mbsf, p. 39.

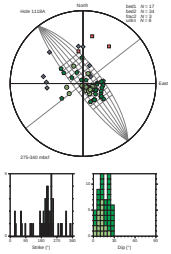

372–485 mbsf

This interval corresponds to lithologic Unit II (378–492 mbsf) once the depth offset is taken into account. Unit II is described as more sandy in cores. Further subdivision, defined by logs and core structural observations, can be recognized on the FMS images.

The upper interval (372–395 mbsf) corresponds to the bottom part of logging Unit L5. The FMS static image shows a sharp increase in resistivity in the 383- to 392-mbsf interval (Fig. F3), which correlates with the 390- to 399-mbsf interval of Unit L5, where the neutron and density porosity curves get closer and the photoelectric effect increases, suggesting the presence of calcareous sands.

In the next 395- to 401-mbsf interval, the image becomes conductive again (Figs. F3, F13). This corresponds to the uppermost 402- to 408-mbsf interval of logging Unit L6 (402–438 mbsf), which is characterized by high gamma ray, low PEFL, and neutron and density porosity convergence, suggesting a radioactive, relatively clean, and therefore sandy or silty, formation.

The resistive 401- to 431-mbsf interval on the static FMS image (Figs. F3, F13) corresponds to the bottom 30 m of logging Unit L6 (408–438 mbsf), which combines high PEFL and neutron density porosity divergence, indicating significant carbonate and clay content. A change is also seen in the dynamic FMS image, which shows flat-lying thinly laminated sediments below 404 mbsf (Fig. F13).

In this instance, the silty upper interval (395–401 mbsf) is conductive because of porosity, whereas the lower interval (401–431 mbsf) is resistive because of its carbonate content and despite its clay content.

A spectacular decimetric slump structure can be observed on the FMS image at ~401 mbsf (Figs. F13, F14). This interval corresponds to high recovery, and many similar structures are observed on the corresponding core Section 180-1118A-21R-4. However, only that seen at 125–148 cm and shown on figure F9 of Shipboard Scientific Party (1999e) matches the size of that observed on the FMS image. It is therefore very likely that figure F9 of Shipboard Scientific Party (1999e) and Figure F14 represent the same object. This would locate it at the bottom of the radioactive silt discussed above.

Dipping beds in the 390- to 410-mbsf interval (Fig. F3) outline a deformed zone that was also observed in core with centimeter-sized folds (domain Ic; 335–397 and 406–474 mbsf) and decimeter-sized folds (domain Ib; 397–406 mbsf) (fig. F9 in Shipboard Scientific Party, 1999e). No fault is identified on FMS images within this interval, but one fault is identified below it at ~415 mbsf (Fig. F3). The stereographic projection of the poles to bedding shows a cluster along a north-south vertical plane that suggests an east-west horizontal fold axis (Fig. F15) that remains poorly constrained because of the small number of data points. The steepest dip (#5 on Fig. F15) corresponds to a limb of the slump at 401 mbsf, as can be seen on the tadpole plot of Figure F14.

The bottom interval (431–485 mbsf), clearly marked by a more conductive static image, corresponds to the upper part of logging Unit L7 (438–682 mbsf), which is characterized by lower PEFL, and thus carbonate content.

485–679 mbsf

This interval is clearly defined by a resistive static image (Fig. F3) and corresponds closely to lithologic Unit III (492–679 mbsf). This higher

F13. FMS image, Hole 1118A, 398–410.5 mbsf, p. 40.

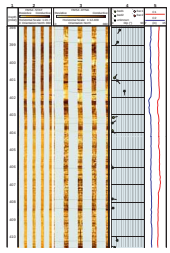

F14. FMS image, Hole 1118A, 400–402.5 mbsf, p. 41.

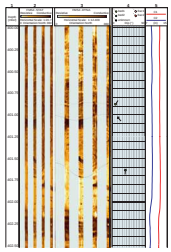

F15. Structure orientations, Hole 1118A, 390–410 mbsf, p. 42.

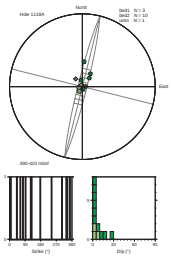

resistivity is correlated with higher sand content and a downward increase in carbonate content documented in the core and in logging Unit L7. Larger-scale images show the intercalation of conductive layers in a generally resistive formation (Fig. F16).

Curved boundaries observed at 527–528 mbsf (Fig. F17) suggest small-scale slumping.

Dipping structures at 570–610 mbsf (Figs. F3, F18, F19) correspond closely to a zone of sediment folding (domain Ic; 560–584 mbsf) and faulting (domain IIa, fault zone 1; 584–608 mbsf) observed in core (figs. F16 and F46 in Shipboard Scientific Party, 1999e). The interval is reduced to 570–596 mbsf after eliminating unknown measurements. It presents one of the clearest association of dipping beds and fractures on the FMS images (Figs. F3, F18, F19). The six fractures identified on FMS in this interval represent a quarter of all fractures identified in Hole 1118A (Table T3).

The orientation plots (Fig. F20) show a cluster of bedding poles along a great circle with a horizontal axis trending N97°E. This circle contains the pole to the fracture at 578.1 mbsf and is close to that at 586.8 mbsf. This again suggests the folding may be related to drag along the faults. The north-northeast bedding dip with a north-northeast dipping fault suggests a normal drag fold, and the east-west horizontal fold axis suggests a mainly dip-slip movement.

The bottom of lithologic Unit III shows very conductive thin beds (Fig. F21) with a different facies than that observed higher uphole (Fig. F16).

A few dipping beds are measured in the 630- to 651-mbsf interval where no deformation is observed in core (domain Ia; 608–714 mbsf). The orientation plot shows a slight (at most 15°) dip toward the southeast (Fig. F22).

679–811 mbsf

The transition at ~679 mbsf is marked by lower resistivity on the static FMS image (Fig. F3).

This interval corresponds to lithologic Unit IV (679–811 mbsf) and logging Unit L8 (682–857 mbsf), with lower carbonate content.

The poorly recovered low-resistivity 692- to 732-mbsf interval (Fig. F3) corresponds to the 690-to 730-mbsf interval on logs where neutron and density logs converge, indicating a sandy formation (fig. F71 in Shipboard Scientific Party, 1999e). The typical FMS facies of this sandy formation is displayed in Figure 23, where bedding contrast disappears below 727 mbsf. A fracture at 717 mbsf falls into the core-defined fracture zone 2 (domain IIb; 714–716 mbsf).

Around 775 mbsf, dipping structures are observed (Fig. F3), but the poorly defined bedding makes it difficult to assess their nature (Fig. F24). This interval had low recovery and is located just above fault zone 3 (domain IIb; 784–813 mbsf) described in core.

811–890 mbsf

A progressive downward resistivity increase (Fig. F3) in the 811- to 856-mbsf interval corresponds to lithologic Unit V (811–857 mbsf) and to increasing PEFL in logging Unit L8.

The resistive interval at 856–858 mbsf (Fig. F25) correlates with the limestone of lithologic Unit VI (857–859 mbsf) and with a high PEFL and density at the top of logging Unit L9 (857–873 mbsf).

F16. FMS image, Hole 1118A, 499.5–512 mbsf, p. 43.

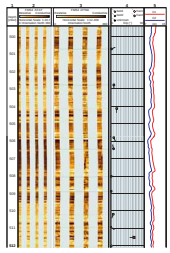

F17. FMS image, Hole 1118A, 523–533 mbsf, p. 44.

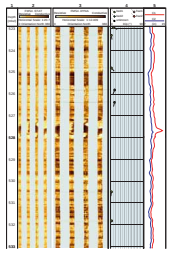

F18. FMS image, Hole 1118A, 572–584.5 mbsf, p. 45.

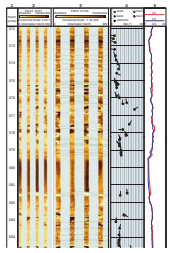

F19. FMS image, Hole 1118A, 584–596.5 mbsf, p. 46.

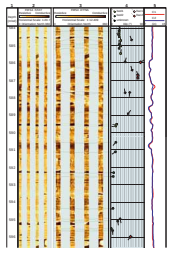

F20. Structure orientations, Hole 1118A, 570–596 mbsf, p. 47.

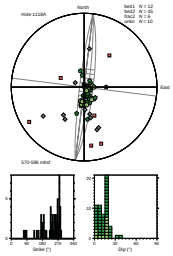

The 859- to 861-mbsf more conductive image (Fig. F25) can be correlated with a lower PEFL and density and high gamma ray levels within logging Unit L9, suggesting a radioactive sand. The dynamic image facies (Fig. F25) is indeed similar to that of a sand, such as that at 780 mbsf (Fig. F24).

The 861- to 873-mbsf resistive interval corresponds to the paraconglomerate of lithologic Unit VII (859–873 mbsf) and to the lower part of logging Unit L9, where a high PEFL indicates high carbonate content. The dynamic image shows various facies, from laminated at the top (Fig. F25) to sandy at the base, where bedding disappears (Fig. F26).

Below 873 mbsf, the dolerite conglomerate of lithologic Unit VIII (873–930 mbsf) and logging Unit L10 (873–890 mbsf) is clearly identified on the FMS dynamic images where individual cobbles can be seen (Fig. F26).

Dipping structures are identified on the FMS images in the 840- to 890-mbsf interval (Fig. F3). Bedding can be identified in the sediments down to 860 mbsf (Fig. F25). Below that depth, pseudoplanar structures were identified in the paraconglomerate and conglomerate (Fig. F26) in an attempt to define the layering, but their significance as bedding is unsure and they are labeled as unknown. Core analysis showed undeformed sediments (domain Ia) above alternating brecciated (domain IIIB) and unbrecciated (domain IIIa) conglomerate. However, the conglomerate was poorly recovered.

The poles to bedding and to a few of the unknown structures seem to cluster around a north-northwest–striking plane steeply dipping to the west (Fig. F27). This plane contains the pole of the fracture located at 853 mbsf. This is poorly constrained but is consistent with folding around a horizontal axis trending N77°E, which suggests a mainly dip-slip movement along the south-southeast–dipping fault. The dominant north-northwest bedding dip suggests reverse drag (i.e., roll-over folding).

HOLE 1109D

A synthetic view of FMS interpretation and core- and log-defined units for Hole 1109D is given in Figure F28. Hole 1109D was not cored above 355 mbsf, and therefore the upper lithologic and structural units are defined in Hole 1109C. Further details on shipboard units can be found in figures F1 (lithostratigraphy), F50 and F52 (structures), F88 (logging), and F92 (synthesis) of Shipboard Scientific Party (1999c).

An obstruction at 351 mbsf, due to clay swelling, required two FMS runs to log Hole 1109D: an upper run, covering 351–115 mbsf, and a lower run with the drill pipe lowered below the obstruction, covering 781–380 mbsf (see the "Operations" and "Downhole Measurements" sections in Shipboard Scientific Party, 1999c). The data from both runs are shown, together with the data gap in the 351- to 380-mbsf interval (Fig. F28).

The structural measurement orientation is shown on stereographic projection and on strike and dip histograms for bedding (Fig. F29), fracture (Fig. F30), and unknown structures (Fig. F31).

The 471 bedding measurements show that most dips are <10° (Fig. F29). This agrees with the 120 core measurements (figs. F51 and F53 in Shipboard Scientific Party, 1999c). The south-southwest dip direction (Fig. F29) confirms that obtained on fewer shipboard FMS measurements (fig. F103 in Shipboard Scientific Party, 1999c). The density

F21. FMS image, Hole 1118A, 600–612.5 mbsf, p. 48.

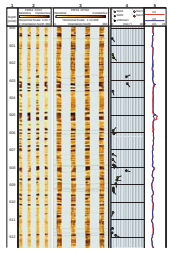

F22. Structure orientations, Hole 1118A, 630–651 mbsf, p. 49.

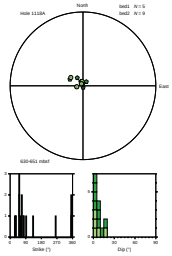

F23. FMS image, Hole 1118A, 720–732.5 mbsf, p. 50.

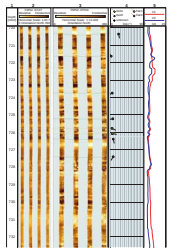

F24. FMS image, Hole 1118A, 772–784.5 mbsf, p. 51.

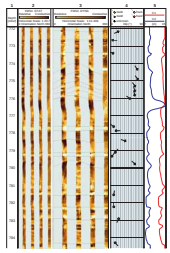

F25. FMS image, Hole 1118A, 852–864.5 mbsf, p. 52.

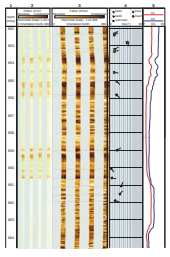

of bedding measurement varies as a function of depth according to how clearly bedding is defined (Fig. F28). Six depth intervals where bedding deviates from subhorizontal were identified: 190–202, 218–223, 240–252, 255–266, 310–320, and 670–680 mbsf (Fig. F28, column 7). These intervals are further analyzed below. They are all located below structural domain II (26–83 mbsf; Hole 1109C), where soft sediment deformation was observed in core.

The 44 fractures seen on the FMS images are located within the bottom dolerite except for one located at 220 mbsf (Figs. F28, F30). Core observations did not find evidence of brittle deformation in Hole 1109C (i.e., above 370 mbsf) and located three fracture zones in Hole 1109D. The uppermost zone (domain IVb; 359–370 mbsf) is present within the FMS data gap, the middle one (domain Vb; 676–684 mbsf) where no fractures are detected on FMS images, and the lower one (domain VII; 766–802 mbsf) corresponds to the massive dolerite. The last two fracture zones are further discussed below.

The depth shown on the FMS images is consistent with that of the conventional logs (see "Appendix," p. 24).

115–170 mbsf

The FMS images show little structure and dull bedding boundaries (Fig. F32), and therefore only a few structural measurements are available in the 115- to 170-mbsf interval that corresponds to lithologic Unit II (83–170 mbsf). This interval corresponds to the upper part of logging Unit L1 (82–219 mbsf), where neutron and density porosity separation indicate a high clay content with a few sandy or carbonate cleaner beds.

170–219 mbsf

Thicker resistive beds appear as lithologic Unit III (170–247 mbsf) is entered, but initially their boundary remains dull and the structural measurements sparse (Fig. F33). Below 190 mbsf, the thickness and occurrence rate of resistive beds increases and their boundary and resistivity contrast becomes sharper, yielding denser structural measurements. Log analysis described the 192- to 197- and 197- to 200-mbsf intervals as sands and sandy carbonates, respectively (fig. F94 in Shipboard Scientific Party, 1999c); the respective FMS images show numerous resistive beds in the first interval (Fig. F34) and a uniform facies in the second one (Fig. F35).

Dipping structures are identified in the 190- to 202-mbsf interval on the FMS images (Fig. F28), both in the sandy upper part of the interval (Fig. F34) and at the very bottom of the lower carbonate part (Fig. F35). The fact that these dipping surfaces are found between horizontal bedding and seem related to varying bedding thickness suggests depositional structures. Gravity flow and drilling-induced fracturing were observed in core from this low-recovery interval. The orientation plot is consistent with a cylindrical structure with a horizontal axis trending N60°E (Fig. F36) that may be related to the depositional slope.

219–234 mbsf

This interval is the second most resistive interval of the borehole as seen on the static FMS image (Fig. F28). It corresponds to logging Unit L2 (219–234 mbsf), defined by a characteristic log signature: neutron and density porosity convergence and high density, resistivity, and seis-

F26. FMS image, Hole 1118A, 868–880.5 mbsf, p. 53.

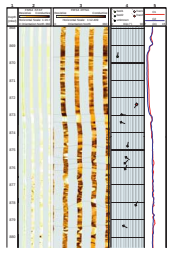

F27. Structure orientations, Hole 1118A, 840–890 mbsf, p. 54.

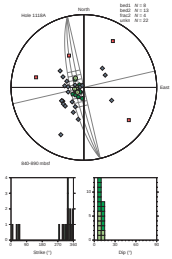

F28. Composite log of Hole 1109D, p. 55.

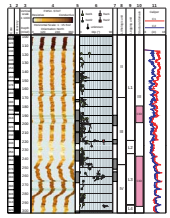

F29. Hole 1109D global bed orientations, p. 58.

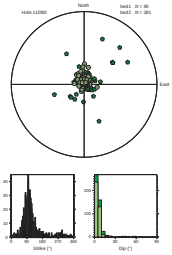

F30. Hole 1109D global fracture orientations, p. 59.

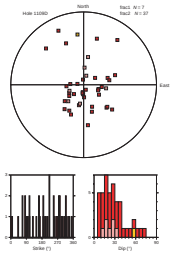

mic velocity, which suggests calcareous sands (see fig. F94 in Shipboard Scientific Party, 1999c). This formation, which was barely recovered and therefore defined on the basis of logs only, also corresponds the major seismic reflector, Light Green 1, that can be traced to the similar logging Unit L2 in Hole 1118A (**Goodliffe et al.,** this volume). Very resistive layers at 219.5 (Fig. **F37**) and 233–234 (Fig. **F38**) mbsf correlate with PEFL peaks on the logs, which indicates increased carbonate content.

The dynamic image shows a massive 223- to 234-mbsf lower section with rare bedding (Fig. **F38**) and a facies similar to that of the carbonate at 197–200 mbsf (Fig. **F35**) but for higher overall resistivity.

On the contrary, dipping structures are identified within the 218- to 223-mbsf upper section (Fig. **F37**). The resistive layer at 219.5 mbsf is cut by a steeply dipping discontinuity that suggests the only fault identified in the sediments on the FMS image from this hole. The orientation plot shows bedding and unknown planes compatible with a cylindrical structure with a horizontal axis trending N8°E (Fig. **F39**).

234–293 mbsf

This interval corresponds to logging Unit L3 (234–293 mbsf), where neutron and density porosity divergence indicates an increased clay content (Figs. **F28, F38**). Core recovery is nearly complete in this interval but is affected by drilling-induced fractures.

The conductivity increases progressively downward in the 234- to 247-mbsf interval (Fig. **F3**), which corresponds to the bottom of lithologic Unit III, is similar to the bottom of logging Unit L1 (Fig. **F32**), except for thinner resistive beds, and yields numerous bedding orientations.

The 247- to 293-mbsf interval, which corresponds to the upper part of lithologic Unit IV (247–362 mbsf), is characterized by a conductive static image (Fig. **F3**) and by a lower contrast of the dynamic image where the clear thin resistive beds observed above are replaced by thicker beds with dull boundaries (Fig. **F40**).

Two intervals with dipping structures are observed on the FMS images.

In the upper 240- to 252-mbsf interval, dip is <25° and the orientation plot suggests a weakly constrained cylindrical structure with a horizontal axis trending N152°E (Fig. **F41**).

The lower low bedding contrast 255- to 266-mbsf interval shows steeply dipping (up to 60°) structures (Fig. **F40**). Most of these structures define intervals of consistent orientation and are interpreted as bedding, whereas a few discordant boundaries are classified as unknown. Steeply dipping fractures were observed in cores from this interval (Cores 180-1109C-28X and 29X), but no clear criterion allows to relate them to either type of dipping structures on the FMS image. The orientation plot shows a main southwest dip direction but no simple organization (Fig. **F42**).

293–330 mbsf

The static FMS images show higher resistivity (Fig. **F28**) in the 293- to 330-mbsf interval, which corresponds to logging Unit L4 (293–330 mbsf), where intervals of neutron and density porosity convergence indicate the presence of clean beds. This correlates with a better contrast

F31. Hole 1109D global unknown planar structure orientations, p. 60.

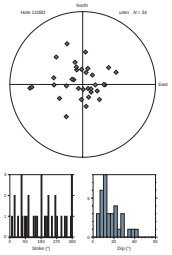

F32. FMS image, Hole 1109D, 140–152.5 mbsf, p. 61.

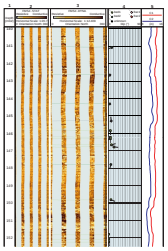

F33. FMS image, Hole 1109D, 172–174.5 mbsf, p. 62.

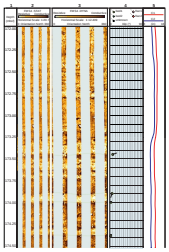

F34. FMS image, Hole 1109D, 184–196.5 mbsf, p. 63.

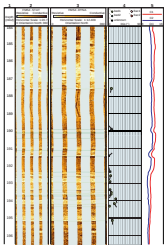

F35. FMS image, Hole 1109D, 196.5–209 mbsf, p. 64.

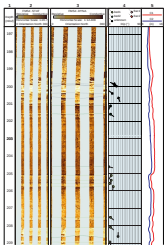

in the dynamic image that better constrains structural measurements (Fig. F43).

Moderately dipping beds are found in the 310- to 320-mbsf interval. Again, the dipping beds seem to be present between flat-lying beds, as seen at ~311 mbsf (Fig. F43), suggesting depositional structures. The orientation plot shows a poorly constrained cylindrical structure with a horizontal axis striking N75°E (Fig. F44).

430–570 mbsf

The static FMS image is relatively conductive within the 430- to 570-mbsf interval (Fig. F28), which corresponds to lithologic Unit VI (388–570 mbsf) and most of logging Unit L6 (390–599 mbsf). However, detailed dynamic images show highly contrasted decimetric resistive beds with sharp boundaries (Fig. F45). This is consistent with the observation of well layered sandstones in cores from Unit VI and with the frequent neutron density porosity convergence in Unit L6, which indicates clean intervals. The increasing photoelectric effect below 540 mbsf, indicative of an increasing carbonate content, is correlated with an increasing resistivity in the static FMS image (Fig. F28).

570–672 mbsf

This interval corresponds to lithologic Unit VII (570–672 mbsf), mainly composed of sandstones and carbonates. However, contrary to the mixing or alternating beds seen in most other units, three thick units with distinct lithologies are distinguished on the basis of logs and can therefore be correlated with FMS facies.

In the lower part of logging Unit L6, neutron density porosity separation and high PEFL indicate high clay and carbonate content, with the intercalation of a radioactive sand marked by high gamma ray and lower PEFL in the 593- to 598-mbsf interval. The dynamic FMS reflects this transition: above 592 mbsf (Fig. F46) it is similar to that of the carbonates at 197–200 and 233–234 mbsf (Figs. F35, F38); below that depth, grainy, more conductive layers are intercalated in the previous facies.

Logging Unit L7 (599–643 mbsf) is marked by lower PEFL, neutron density porosity convergence, and high gamma ray, which indicates a massive sand that was poorly recovered in core. The static FMS image is slightly more conductive than in Unit L6 above (Fig. F28) and the dynamic image displays a distinct grainy facies with less distinct bedding below 599 mbsf (Fig. F46).

Logging Unit L8 (643–673 mbsf), with high PEFL, neutron density–porosity convergence, and low gamma ray, corresponds to a massive carbonate that was also poorly recovered in core. The FMS static image is very resistive (Fig. F28). The dynamic image at the transition from logging Unit L7 to L8 (Fig. F47) shows alternating sandy (644–648 mbsf) and carbonate (642–643 mbsf) facies. The latter becomes dominant below 648 mbsf, where bedding disappears completely.

672–714 mbsf

Lithologic Unit VIII (672–705 mbsf) and logging Unit L9 (673–714 mbsf) correspond to a lagoonal alternating organic-rich claystone and siltstone deposit with abundant shell and wood fragments. On the FMS images, a facies change from the carbonates of Unit L8 is seen at 675

F36. Structure orientations, Hole 1109D, 190–202 mbsf, p. 65.

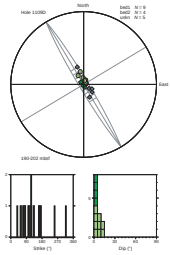

F37. FMS image, Hole 1109D, 210–222.5 mbsf, p. 66.

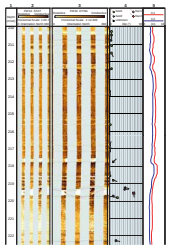

F38. FMS image, Hole 1109D, 230–242.5 mbsf, p. 67.

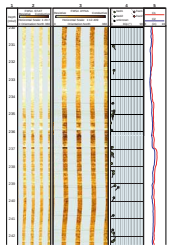

F39. Structure orientations, Hole 1109D, 218–223 mbsf, p. 68.

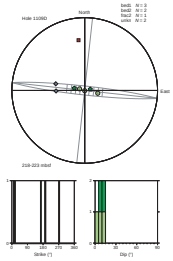

F40. FMS image, Hole 1109D, 255–267.5 mbsf, p. 69.

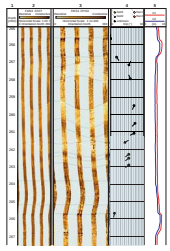

mbsf (Fig. F48). The static image becomes slightly more conductive, and the dynamic image shows thin (5 cm thick), dipping conductive layers in the 675- to 678-mbsf interval.

Despite good core recovery, the FMS and core observations remain difficult to match; the dipping beds seen on the FMS did not stand out in the core and the steeply dipping fractures observed in core, defining fracture zone 2 (domain Vb; 676–686 mbsf), are not seen on the FMS (Fig. F48). Even though the 25% borehole wall coverage by the FMS pads lowers the odds of detecting steep structures, the complete absence of discontinuity within the massive resistive facies of this interval suggests that the fractures observed in core do not generate a resistivity contrast and therefore are not open. The orientation plot of the structure within the 674- to 680-mbsf interval does not define a clear structure (Fig. F49).

Below 681 mbsf, the facies changes again to a generally more conductive formation with resistive pieces and many intervals are washed out. This could be correlated with the increased clay content observed in core below 685 mbsf. FMS images from non–washed out intervals show alternating conductive and resistive layers consistent with the alternating sandstone and claystone described in core (Figs. F50, F51). In most instances a weak layering can be inferred, but a few intervals with nonplanar contacts suggest either possible conglomerate clasts or complex depositional structures (689–691 mbsf) (Fig. F50).

714–776.5 mbsf

This interval corresponds to the poorly recovered dolerite conglomerate of lithologic Units IX (705–737 mbsf) and X (737–773 mbsf) and logging Units L10 (714–762 mbsf) and L11 (762–781 mbsf). Hole conditions are degraded by washouts in the upper interbedded conglomerate but become good in the more massive lower conglomerate, where high-resistivity pebbles can be seen on the images (Fig. F52).

776.5–781 mbsf

The massive dolerite of lithologic Unit XI (773–802 mbsf) and logging Unit L11 is sharply defined by the highest resistivity on the static image for this hole (Fig. F28). Only the upper 5 m of the 50 m of cored dolerite (Units L11 and XI) could be reached and logged with the FMS. It is densely fractured (Fig. F53). The static image allows definition of the relative aperture of the fractures. A few of the widest fractures can be unambiguously traced on all four pads and are labeled as fracture 1. The orientation plot for the fractures is that of Figure F30, except for the single fracture outside this interval (labeled #37). The dip direction is scattered, with a weak north-northeast trend that is compatible with the main Moresby fault trend. The 126 core measurements showed a complex dip distribution with three peaks: 0°–5°, 20°–30°, and 60° (fig. F58A in Shipboard Scientific Party, 1999c). The 43 FMS measurements are compatible with the first two peaks but underestimate those of the steeply dipping structures around 60° (Fig. F30). This can be due in part to small borehole wall coverage but also to the fact that the logged interval represents only the upper part and a tenth of the length of the recovered dolerite cores.

F41. Structure orientations, Hole 1109D, 240–252 mbsf, p. 70.

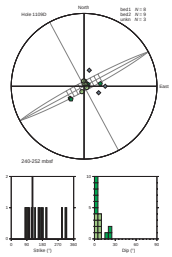

F42. Structure orientations, Hole 1109D, 255–266 mbsf, p. 71.

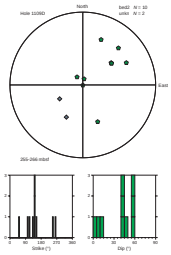

F43. FMS image, Hole 1109D, 300–312.5 mbsf, p. 72.

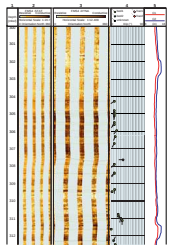

F44. Structure orientations, Hole 1109D, 310–320 mbsf, p. 73.

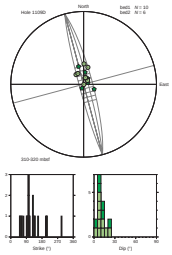

F45. FMS image, Hole 1109D, 460–472.5 mbsf, p. 74.

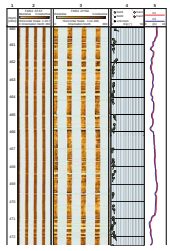

HOLE 1115C

A synthetic view of FMS interpretation and core- and log-defined units for Hole 1115C is given in Figure F54. Hole 1115C was not cored above 283 mbsf, and therefore the upper lithologic and structural units are defined in Hole 1115B. Further details on shipboards units can be found in figures F1 (lithostratigraphy), F30 (structures), F59 (logging), and F62 (synthesis) in Shipboard Scientific Party (1999d).

The structural measurement orientation is shown on stereographic projection and on strike and dip histograms for bedding (Fig. F55), fracture (Fig. F56), and unknown structures (Fig. F57).

The global distribution of bedding orientation is more dispersed for bed 2 than for bed 1 but otherwise has similar trends: the orientation is subhorizontal with most dips within [0°,15°] and with a west-northwest preferential dip direction (Fig. F55). This distribution, based on 416 data points (Table T3), is compatible with the dip distribution based on 220 core measurements (fig. F31A in Shipboard Scientific Party, 1999d).

Core analysis yielded 127 fracture measurements concentrated in three fracture zones, fracture zone 1 (domain IIa; 552–566 mbsf), fracture zone 2 (domain IIb; 604–696 mbsf), and fracture zone 3 (domain IIc; 725–802 mbsf), with a dip distribution with a 45°–50° and a 70°–75° peak (figs. 30B and F31B in Shipboard Scientific Party, 1999d). The FMS analysis clearly underestimates the fracture population because only ten fractures are identified (Fig. F56). Nine of them are located within the three fracture zones defined in cores (Fig. F54). These fractures are steeply dipping, eight of them dipping between 65° and 80°, with a dip direction to the south. The underestimation does not seem solely due to the incomplete borehole wall coverage, which lessens the chance of detecting steeply dipping fractures, because both the moderately and the steeply dipping fractures are underrepresented.

From the top of the logged section down to 475 mbsf, most beds dip <10° with only rare exceptions (Fig. F54). Most dipping beds and unknown structures and all fractures are found below 475 mbsf, either in the 500- to 570-mbsf interval of early synrift sediments, where the borehole is enlarged, or in the prerift units. Eight intervals with dipping beds are identified and further discussed in the next section: 245–265, 480–505, 506–527, 527–532, 552–572, 615–620, 622–634, and 690–785 mbsf.

Fractures identified on the FMS images strikingly correspond to intervals where bedding or unknown structures are dipping >10° (Fig. F54). However, bedding dips remain moderate (<35°), which is consistent with core observation (figs. F32A and F33 in Shipboard Scientific Party, 1999d), whereas unknown structure dips are in the 10°–60° range (Fig. F57). The low recovery within fracture zones 1 and 2 makes it possible for some of these structures to correspond to unrecovered steep beddings.

Further analysis from top to bottom of the hole is presented below. The maximum depth differences between the conventional logs and the processed FMS data is ~1.2 m and occurs around middepth in the hole (see "Appendix," p. 24).

Prerift vs. Synrift

The lower section of this hole (573.5–802 mbsf) is within forearc prerift sediments that were reached in this hole only during Leg 180. Pre-

F46. FMS image, Hole 1109D, 591–603.5 mbsf, p. 75.

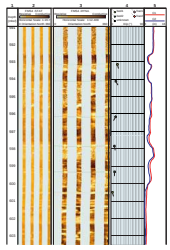

F47. FMS image, Hole 1109D, 640–652.5 mbsf, p. 76.

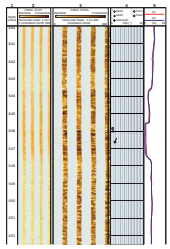

F48. FMS image, Hole 1109D, 671–683.5 mbsf, p. 77.

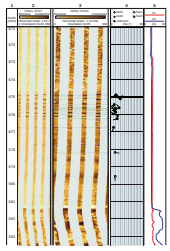

F49. Structure orientations, Hole 1109D, 670–680 mbsf, p. 78.

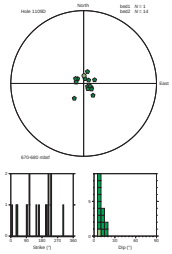

F50. FMS image, Hole 1109D, 685–695 mbsf, p. 79.

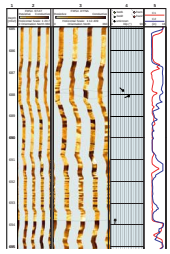

rift and synrift bedding orientations differ only slightly; the prerift beddings dip mostly <15° toward the northwest (Fig. F58), whereas the synrift beddings dip <10° toward the west (Fig. F59). The unconformity between prerift and synrift sediments is therefore not associated with a significant angular change in bedding orientation. This confirms the conclusion reached on the basis of core bedding dip measurements (fig. F34 in Shipboard Scientific Party, 1999d). The number of prerift and synrift measurements are 128 and 288 for the FMS and 151 and 69 for the cores.

119–150 mbsf

The conductive formation seen on the FMS static image in the 119- to 150-mbsf interval corresponds to lithologic Unit II (36–150 mbsf) and logging unit L1 (79–153 mbsf), which are dominated by clay, as indicated by neutron and density porosity log separation. The dynamic image shows low bedding contrast (Fig. F60), and therefore very few structural measurements are available in this interval.

150–413 mbsf

This interval corresponds to logging Unit L2 (153–413 mbsf). This unit is differentiated from Unit L1 by a neutron and density porosity log with less general separation and frequent punctual convergence, which suggests lower clay content and thin clean beds. A slightly increasing resistivity of the static image, especially at 192 mbsf (Fig. F54), is well correlated with a downward-increasing photoelectric effect, which indicates an increasing carbonate content (fig. F59 in Shipboard Scientific Party, 1999d).

Most of this interval is within lithologic Unit III (150–389 mbsf), which is distinguished from the unit above by the apparition of silty calcareous beds in cores and of thin resistive beds on the FMS dynamic image below 149 mbsf (Fig. F60). The general pattern of thin resistive beds against a conductive background is sometimes reversed with thin very conductive beds (Fig. F61). The very resistive beds at 247.3, 248.9, and 256.7 mbsf (Fig. F61) were identified as carbonates on conventional logs. A third very resistive bed at 292.2 mbsf (Figs. F3, AF3) corresponds to dolomite and is located at the depth where coring had to switch from extended core barrel to rotary core barrel.

The 245- to 265-mbsf interval provides the only nonisolated beds dipping >10° in the upper section of the hole (Fig. F54). It contains the resistive carbonate beds just mentioned and the depths where cores were noted to become indurated (256 mbsf) and lithified (264 mbsf). No significant deformation was noted in core. The dipping beds are overlaying and being overlain by more horizontal beds, suggesting synsedimentary structures (Fig. F61). The orientations are not sufficiently diverse to provide good constraint on a possible cylindrical axis trending N138°E (Fig. F62).

In the bottom (389–413 mbsf) of logging Unit L2, increasing lithification and grain size change was observed in core-defined lithologic Unit IV (389–417 mbsf). The FMS images, like the conventional logs, do not register a significant change (Figs. F54, F63).

F51. FMS image, Hole 1109D, 700–710 mbsf, p. 80.

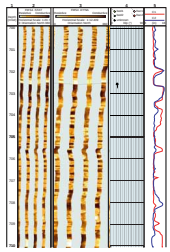

F52. FMS image, Hole 1109D, 767–777 mbsf, p. 81.

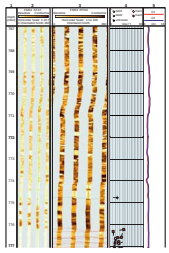

F53. FMS image, Hole 1109D, 776–781 mbsf, p. 82.

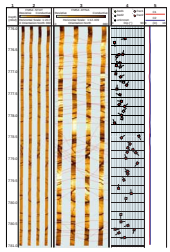

F54. Composite log of Hole 1115C, p. 83.

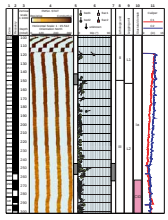

F55. Hole 1115C global bed orientations, p. 86.

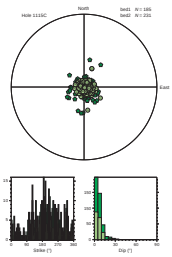

413–474 mbsf

Resistivity increases on the static image (Fig. F54), and bedding becomes more diffuse on the dynamic image (Fig. F63) in the 413- to 474-mbsf interval corresponding to logging Units L3 (413–474 mbsf) and lithologic Unit V (417–475 mbsf). Elevated PEFL and neutron and density porosity log moderate separation with intervals of convergence within Unit L3 indicate an increase in carbonate content but a still significant clay content with thin clean beds. In core, lithologic Unit V is marked by a grain size increase. The lower resistivity below 440 mbsf, which correlates with higher gamma ray and slightly lower PEFL logs, may correlate with an increased sand content.

474–506 mbsf

Higher resistivity and a more homogeneous static image (Fig. F54) characterizes the 474- to 506-mbsf interval corresponding to logging Unit L4 (474–506 mbsf) and most of lithologic Unit VI (475–513 mbsf). Higher sand content in a coastal depositional environment were deduced from core observation, whereas high PEFL and gamma ray as well as neutron and density porosity convergence indicate low clay content and mixed sands and carbonates. The dynamic image oscillates indeed between the laminated carbonate and grainy sandstone facies (Fig. F64).

Within the 480- to 505-mbsf interval, bedding dips reach up to 30° toward the southwest but do not define a clear structure (Fig. F65). However, bedding is not sharply defined, so that the determinations are in the bed 2 category, and no significant deformation was noted in cores from this interval.

506–535 mbsf

The 506- to 535-mbsf interval, which corresponds to logging Unit L5 (506–535) and lithologic Unit VII (513–552 mbsf), is marked by borehole enlargements that degrade the log data (Fig. F54). The FMS tracks along the shorter diameter of the enlargements, where the pad is in contact with the formation, show conductive layers that are not visible on the orthogonal tracks that are along the larger diameter (Fig. F66). The dynamic image grainy facies at 517–519 mbsf (Fig. F66) is consistent with the presence of sandy intervals suggested by conventional logs and the siltstone recovered in core.

In the short intervals where the hole is not enlarged, a few dipping beds are identified. In the enlarged intervals, where only two FMS pads are clearly in contact with the formation, the nature and geometry of structures is poorly constrained and those that are tentatively interpreted are attributed to the unknown category. The dipping structures are separated into two intervals.

In the 506- to 527-mbsf interval, the orientation plot shows scattered data with no clear organization (Fig. F67). A few of the unknown planes have an orientation close to that of bedding, but the nature of those more remote from bedding remains uncertain. The fracture is the only fracture identified on FMS in this hole that does not belong to a fracture zone defined from core. However, it belongs to the lower confidence frac 2 category, and core structural observations were hampered by the poor recovery.

F56. Hole 1115C global fracture orientations, p. 87.

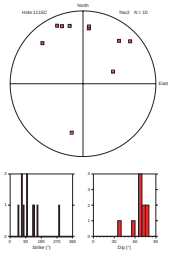

F57. Hole 1115C unknown planar structures orientations, p. 88.

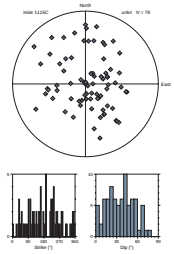

F58. Prerift bed orientations, Hole 1115C, 573.5–790 mbsf, p. 89.

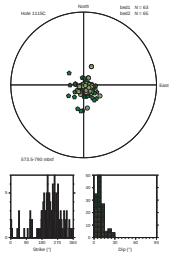

F59. Synrift bed orientations, Hole 1115C, 119–573.5 mbsf, p. 90.

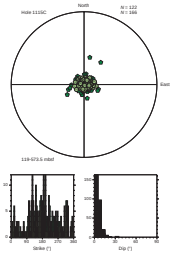

F60. FMS image, Hole 1115C, 142–154.5 mbsf, p. 91.

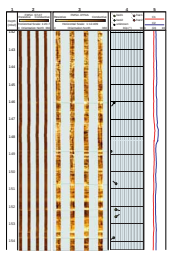

In the 527- to 532-mbsf interval the orientations appear organized within a cylindrical structure with a north-south horizontal axis (Fig. F68). However, too few data points are available and the nature of too many of them is undetermined to further interpret this geometry.

535–573.5 mbsf

In the 535- to 565-mbsf interval, which corresponds to logging Unit L6 (535–565 mbsf), the borehole enlargements are more developed than in the above interval and severely affect FMS images (Fig. F54) and the scalar logs that suggest clay and sand layers. This interval also corresponds to the lower part of lithologic Unit VII and the organic-rich claystone and bioclastic limestone of lithologic Unit VIII (552–566 mbsf).

The 565- to 573.5-mbsf interval, which corresponds to logging Unit L7 (565–573.5 mbsf) and lithologic Unit IX (566–572 mbsf), is radically different (Fig. F69).

In the upper 2 m (565.5–567.5 mbsf), the hole diameter is restricted below bit size (9.875 in or 25 cm). High PEFL logs indicate significant carbonate content, whereas high porosity logs as well as the hole restriction suggests significant clay content. The FMS dynamic image facies is compatible with the carbonate, sand, and clay mixture seen in other intervals. This unit appears separated from that just below by a steep south-dipping fault.

In the next 567.5- to 573.5-mbsf interval, the FMS dynamic image shows a conglomerate (Fig. F69) with one of the most resistive static images of the borehole (Fig. F54). The northwest-dipping structure at the bottom of this conglomerate at 573.5 mbsf is interpreted as the rift onset unconformity separating the synrift (Units I–IX) from the prerift forearc (Units X–XII) sediments.

The poles distribution of the structural measurements within the 552- to 572.5-mbsf interval does not show an interpretable organization (Fig. F70). Core analysis identified fracture zone 1 (domain IIa; 552–566 mbsf) and synsedimentary deformation in this interval, despite poor recovery.

573.5–629 mbsf

This interval corresponds to logging Unit L8 (573.5–628 mbsf), where PEFL, neutron density porosity, and gamma ray indicate succession of two similar sequences of sands overlaying carbonates.

The upper sequence can be recognized on the FMS images (Fig. F71); the upper sand corresponding to lithologic Unit X (572–604 mbsf) is more conductive than the very resistive basal carbonate at 604–618 mbsf.

In the lower sequence, the upper sand interval at 618–625 mbsf corresponds to a borehole elongation where only two FMS pads are in contact with the formation and the basal carbonates at 625–629 mbsf are not as resistive as those of the above sequence (Fig. F72). Lithologic Unit XI (604–658 mbsf) includes the lower sequence and the carbonate base of the upper sequence.

Many dipping structures are observed on the FMS image within the core-defined fracture zone 2 (domain IIb; 604–697 mbsf) (Fig. F54). Those that are identified as bed or fractures can be grouped into two subintervals separated by the borehole elongation (615–620 and 622–634 mbsf). The orientation plots show north-dipping beds (Figs. F73,

F61. FMS image, Hole 1115C, 245–257.5 mbsf, p. 92.

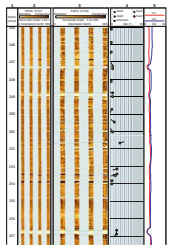

F62. Structure orientation, Hole 1115C, 245–265 mbsf, p. 93.

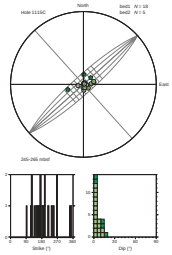

F63. FMS image, Hole 1115C, 407–419.5 mbsf, p. 94.

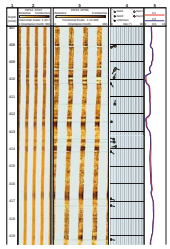

F64. FMS image, Hole 1115C, 469–4815 mbsf, p. 95.

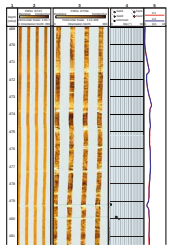

F65. Structure orientation, Hole 1115C, 480–505 mbsf, p. 96.

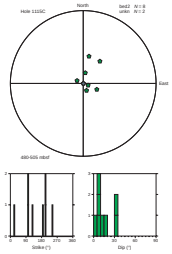

F74). In the lower interval, four south-dipping fractures are identified and bedding seems organized in a cylindrical structure with a horizontal axis trending N88°E that almost contains the fractures (Fig. F74). This suggests a fault-related folding with a mainly dip-slip movement that is consistent with core observations. The north-dipping beds with the south-dipping fractures suggests a reverse drag (i.e., roll over) fold.

629–785 mbsf

The last interval corresponds to logging Unit L9 (628–784 mbsf), which was defined by a higher clay content than the above unit but with still significant carbonate content. It also corresponds to the lower part of lithologic Units XI and XII (658–802 mbsf). The resistivity on the static image is lower than above but remains high (Fig. F54). The dynamic image (Fig. F75) shows rare poorly defined bedding in a facies that is different from that of the above carbonates of Figure F71. Many dipping unknown structures are present within the bottom part of the core-defined fracture zone 2 (domain IIb; 604–697 mbsf), within which slumping was also observed at ~690 mbsf.

A change is noted below 695 mbsf; resistive, probably calcareous, thin beds are clearly identified on the FMS image (Fig. F76) and are consistently tilted 10°–15° toward the northwest (Fig. F54), as confirmed by the orientation plot (Fig. F77). The bedding of the overlaying forearc sequence dips toward a more northerly direction (Fig. F78). This suggests that a slight angular unconformity may separate these two forearc sequences.

Three faults are identified on FMS within fracture zone 3 (domain IIc; 725–802 mbsf) and dip toward the south (Figs. F54, F77). The orientation of the unknown planar data spans a large space that includes that of bedding but also gets close to that of fractures, suggesting that this set contains both types of structures.

DISCUSSION

Fractures

The only observed unambiguous fractures (frac 1) are all located in the dolerite at the bottom of Hole 1109D (Table T3; Fig. F28). They dip 10°–35°, mainly to the north, but with a few, probably conjugates, to the south (Fig. F30). The lesser quality frac 2 distribution is more dispersed, as expected, but with a similar mean orientation. This orientation is subparallel to that of the Moresby detachment fault. Whether these faults are related to the regional north-south extensional stress field raises the question of their unfavorable low dip, as in the case of the detachment, but for much smaller structures with no large gouge. Steeper fractures, dipping ~60°, observed in core indicate that the FMS data undersamples the steep fractures.

Very few fractures are observed in the sediments, despite numerous observations in core, and all of them belong to the lower confidence frac 2 category. This disappointing result may be due to three causes: (1) the incomplete coverage of the borehole wall by the slim FMS used in ODP operations; (2) low resistivity contrast between the fractures and the formation, which would suggest that these fractures are closed; and (3) typical geometrical undersampling of steep structures by a vertical borehole. However, the few identified fractures are encouragingly often

F66. FMS image, Hole 1115C, 506.5–519 mbsf, p. 97.

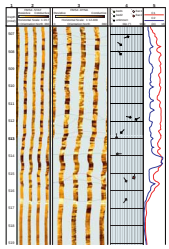

F67. Structure orientation, Hole 1115C, 506–527 mbsf, p. 98.

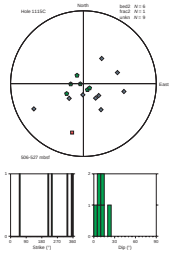

F68. Structure orientation, Hole 1115C, 527–532 mbsf, p. 99.

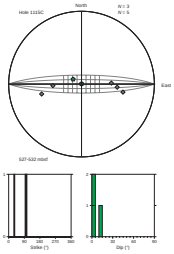

F69. FMS image, Hole 1115C, 565–577.5 mbsf, p. 100.

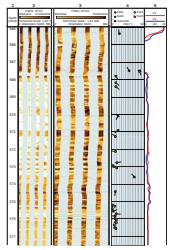

F70. Structure orientation, Hole 1115C, 552–572 mbsf, p. 101.

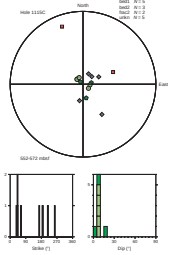

located within core-defined fracture zones (Holes 1118A and 1115C). They are concentrated within the prerift and earliest synrift sediments in Hole 1115C.

Bedding

The number of bedding structural measurements (Table T3) on the FMS images is comparable to those in core. For each hole, the lower confidence bed 2 distribution is more dispersed than the bed 1 distribution, as expected, but displays similar mean orientations (Figs. F4, F29, F55).

Bedding is mostly subhorizontal (<15° dip), except in a few intervals (Figs. F3, F28, F54). Most of those intervals correspond to zones where soft-sediment deformation or fractures were observed in core. Many also include a few of the fractures that were identified on the FMS images. Slumping is observed on the FMS images and, in one instance, is correlated with the corresponding core feature (Fig. F14; Section 180-1118A-21R-4).

The orientation analysis determines a few fold axes that are always subhorizontal (within 5° of horizontal) and are summarized in Table T4. These fold axes can be interpreted either as being orthogonal to the depositional slope for gravity sliding or as striking along a fault that caused the bed rotation by its movement. However, in the case of synsedimentary extensional tectonics, such as that of the Woodlark Basin, the sedimentary slope may be controlled by large normal faults, and therefore gravity sliding along this slope and tectonic bed rotations due to fault movements may produce structures with similar axes. This is compatible with the core observation of soft-sediment deformation and slumping associated with extensional faulting.

The 250- to 280- and 275- to 340-mbsf intervals of Hole 1118A and the 190- to 202-mbsf interval of Hole 1109D yield similar northeast-east folding axis (Table T4). Because soft-sediment gravity deformation is the most likely cause of these folds, the axis direction may be orthogonal to the depositional slope.

The 570- to 596- and 840- to 890-mbsf intervals of Hole 1118A and the 622- to 634-mbsf interval of Hole 1115C, which correspond to core-defined fracture zones, yield consistent east-west fold axes and north- or south-dipping associated fractures (Table T4). Even if these fractures are not necessarily those responsible for the folding, it is reasonable to infer that both the folding and the faulting are the expression of the regional north-south extension.

At Site 1115 the angular unconformity between prerift and synrift sediments is very small. The FMS analysis suggests a possible slight angular unconformity within the prerift sediments at ~695 mbsf, that is, below fracture zone 2. Intervals of dipping beds are mostly located below 480 mbsf, that is within the prerift or early synrift sediments.

Lithology and Deformation

Sandy or silty intervals often correspond to borehole enlargement and poor recovery. FMS analysis shows that they are frequently the locus of dipping beds and/or fractures, and core observations show them frequently associated with fracture zone and/or soft sediment deformation. All this suggests that they are mechanically weak and concentrate deformation. The fact that these intervals are poorly recovered suggests that core analysis missed a large amount of hanging wall deformation.

F71. FMS image, Hole 1115C, 602–614.5 mbsf, p. 102.

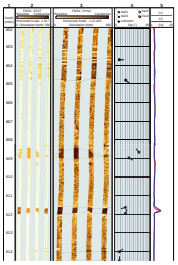

F72. FMS image, Hole 1115C, 615–630 mbsf, p. 103.

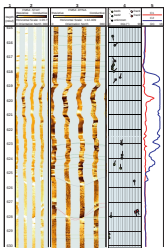

F73. Structure orientation, Hole 1115C, 615–620 mbsf, p. 104.

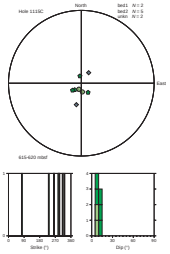

F74. Structure orientation, Hole 1115C, 622–634 mbsf, p. 105.

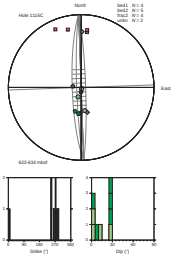

F75. FMS image, Hole 1115C, 655–667.5 mbsf, p. 106.

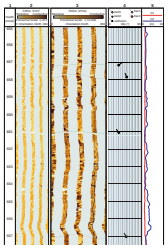

FMS data do not compensate for this because they reveal too small a proportion of the fracturation in the sediments.

Fracture zone 2 in Hole 1109D and fracture zone 3 in Hole 1115C occur in the similar lithologic Unit VIII organic-rich claystone that also seems to concentrate deformation.

Lithology and FMS Facies

Most outstanding sediment lithologies are related to an increase in sand or carbonate content against a background clay content. The analysis of the FMS dynamic image identified typical facies related to these increased sand or carbonate contents that are summarized in Table T5.

The static FMS image is very resistive in carbonates but is relatively conductive in sands and seems more sensitive to carbonate than to clay content. This can be verified with conventional logs. The shallow spherically focused electrical measurement (SFLU) is the closest to FMS measurement in terms of resolution and depth of investigation, the photoelectric effect (PEFL) is a direct indication of carbonate content, and clay content can be estimated by the difference (DPORO; Eq. 2) between neutron (APLC) and lithodensity (DPHI) porosity (Shipboard Scientific Party, 1999a). SFLU is represented as a function of PEFL and DPORO for each borehole in Figure F79; a strong correlation of resistivity (SFLU) with carbonate content (PEFL) is clear at Sites 1115 and 1109 and is still visible at Site 1118. No simple correlation appears between clay content (DPORO) and resistivity (SFLU).

CONCLUSIONS

The FMS images provide a good description of the fracturation in the basal dolerite of Hole 1109D but underestimate steep dips. The east-west strike of these fractures is compatible with the Woodlark Basin north-south extension, but their low dip is not.

The fracture zones observed in the northern margin sediment cores are not clearly visible on the FMS images, probably due to the lack of coverage of the tool pads. However the analysis of bedding orientations documents the association of bed deformation and faulting. The bed deformation can be caused by the fault movement or by gravity sliding along the depositional slope with small-scale growth faulting, roll-over folding, and slumping. These two processes are likely to produce similar structural axis orientations because the depositional slope is also controlled by the major normal faults.

Deformation seems to localize in a few lithologies. In particular, sands, which are poorly recovered, are often associated with deformation. Faulting in the sediments may therefore be more important than what was observed in core and on FMS. Tectonic studies of sedimentary sites may therefore require an electrical imaging tool with better borehole wall coverage, such as the Fullbore Formation MicroImager (FMI).

ACKNOWLEDGMENTS

We wish to acknowledge the cooperative spirit of the shipboard scientific party, technical staff, and crew of Leg 180, which made working on this cruise a special experience. Help from the Lamont-Doherty Earth Observatory Borehole Research Group in general, and Florence

F76. FMS image, Hole 1115C, 713–725.5 mbsf, p. 107.

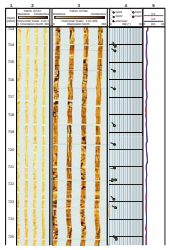

F77. Structure orientation, Hole 1115C, 695–785 mbsf, p. 108.

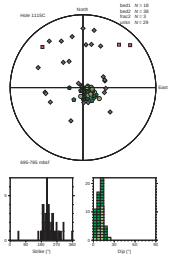

F78. Bedding orientation, Hole 1115C, 573.5–695 mbsf, p. 109.

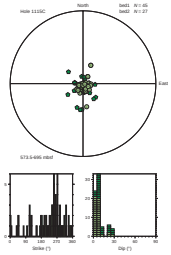

T4. Bedding folding axis, p. 114.

T5. Sand and carbonate FMS image facies, p. 115.

F79. SFLU vs. PEFL and DPORO, p. 110.

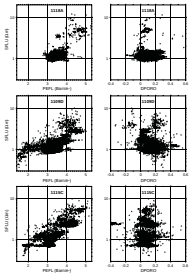

Einaudi in particular, was determinant in overcoming some of the FMS analysis software perversity. Philippe Gaillot gracefully helped with the integration of core recovery with his odp-plot program. Reviews by Heike Delius and Trevor Williams improved the paper.

This research used samples and/or data provided by the Ocean Drilling Program (ODP). ODP is sponsored by the U.S. National Science Foundation (NSF) and participating countries under management of Joint Oceanographic Institutions (JOI), Inc. Funding for this research was partially provided by the CNRS-INSU Geoscience Marine program.

REFERENCES

Abers, G.A., 1991. Possible seismogenic shallow-dipping normal faults in the Woodlark-D'Entrecasteaux extensional province, Papua New Guinea. *Geology,* 19:1205–1208.

Abers, G.A., Mutter, C.Z., and Fang, J., 1997. Shallow dips of normal faults during rapid extension: earthquakes in the Woodlark-D'Entrecasteaux rift system, Papua New Guinea. *J. Geophys. Res.,* 102:15301–15317.

Ekstrom, M.P., Dahan, C., Chen, M.-Y., Lloyd, P., and Rossi, D.J., 1987. Formation imaging with microelectrical scanning arrays. *Log Analyst,* 28:294–306.

Goodliffe, A.M., Taylor, B., and Martinez, F., 1999. Data report: Marine geophysical surveys of the Woodlark Basin region. *In* Taylor, B., Huchon, P., Klaus, A., et al., *Proc. ODP Init. Repts.,* 180, 1–20 [CD-ROM]. Available from: Ocean Drilling Program, Texas A&M University, College Station, TX 77845-9547, U.S.A.

Pezard, P., Lovell, M., and ODP Leg 126 Shipboard Scientific Party, 1990. Downhole images: electrical scanning reveals the nature of subsurface oceanic crust. *Eos,* 71:709, 718.

Shipboard Scientific Party, 1990. Explanatory notes. *In* Taylor, B., Fujioka, K., et al., *Proc. ODP, Init. Repts.,* 126: College Station, TX (Ocean Drilling Program), 13–42.

————, 1999a. Explanatory notes. *In* Taylor, B., Huchon, P., Klaus, A., et al., *Proc. ODP, Init. Repts.,* 180, 1–75 [CD-ROM]. Available from: Ocean Drilling Program, Texas A&M University, College Station, TX 77845-9547, U.S.A.

————, 1999b. Leg 180 summary: active continental extension in the western Woodlark Basin, Papua New Guinea. *In* Taylor, B., Huchon, P., Klaus, A., et al., *Proc. ODP, Init. Repts.,* 180: College Station, TX (Ocean Drilling Program), 1–77.

————, 1999c. Site 1109. *In* Taylor, B., Huchon, P., Klaus, A., et al., *Proc. ODP Init. Repts.,* 180, 1–298 [CD-ROM]. Available from: Ocean Drilling Program, Texas A&M University, College Station, TX 77845-9547, U.S.A.

————, 1999d. Site 1115. *In* Taylor, B., Huchon, P., Klaus, A., et al., *Proc. ODP Init. Repts.,* 180, 1–226 [CD-ROM]. Available from: Ocean Drilling Program, Texas A&M University, College Station, TX 77845-9547, U.S.A.

————, 1999e. Site 1118. *In* Taylor, B., Huchon, P., Klaus, A., et al., *Proc. ODP Init. Repts.,* 180, 1–213 [CD-ROM]. Available from: Ocean Drilling Program, Texas A&M University, College Station, TX 77845-9547, U.S.A.

Taylor, B., 1999. Background and regional setting. *In* Taylor, B., Huchon, P., Klaus, A., et al., *Proc. ODP, Init. Repts.,* 180, 1-20 [CD-ROM]. Available from: Ocean Drilling Program, Texas A&M University, College Station, TX 77845-9547, U.S.A.

Wernicke, B., 1995. Low-angle normal faults and seismicity: a review. *J. Geophys. Res.,* 100:20159–20174.

APPENDIX

Full borehole coverage with images at the ~1/200 scale are provided here to bridge the gap between the selection of large-scale images presented in the paper and the synthetic ~1/1000 vertical-scale images. This scale is sufficiently large for the dynamic image to start displaying some character; the color equalization window of 2 m is represented by 1 cm. Lithologic boundaries and structural measurements can also be located within a few decimeters.

The correlation between FMS images and other logs can be done with the caliper data attached to the images. A few tie points are given below.

Depth Correlation

Hole 1118A

Significant depth shifts with respect to the conventional log data occur in this hole. The restriction seen here at 175 mbsf and the elongations seen at 528 and at 703 mbsf (Fig. AF1) can be found on the conventional log data (fig. F71 in Shipboard Scientific Party, 1999e) at 184, 532, and 705 mbsf, respectively. The depth shift between these two data sets, which is negligible at the bottom of the hole, grows on the way up.

Hole 1109D

The depth shown on the FMS images is consistent with that of the conventional logs. The FMS caliper elongations at 246.5, 311.5, and 598 mbsf as well as the restrictions at 735.5 and 743.5 mbsf (Fig. AF2) are found within 20 cm on the triple combination tool string (fig. F88A in Shipboard Scientific Party, 1999c).

Hole 1115C

Depth differences between the conventional logs and the processed FMS data reach up to a meter at middepth of the hole. The sharp borehole diameter variations seen on the conventional log caliper (fig. F59 in Shipboard Scientific Party, 1999d) at 611.7, 567.0, 521.5, and 120 mbsf can be found within 25 cm on the FMS calipers (Fig. AF3). However, those seen at 464, 291, and 247 mbsf are located 1.2, 1.0, and 0.4 m below these depths on the FMS data.

AF1. FMS image, Hole 1118A, p. 116.

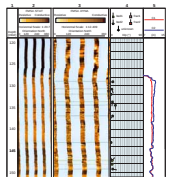

AF2. FMS image, Hole 1109D, p. 132.

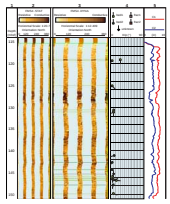

AF3. FMS image, Hole 1115C, p. 146.

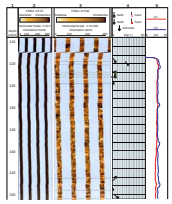

Figure F1. Location map of Leg 180 drill sites (from Goodliffe et al., 1999).

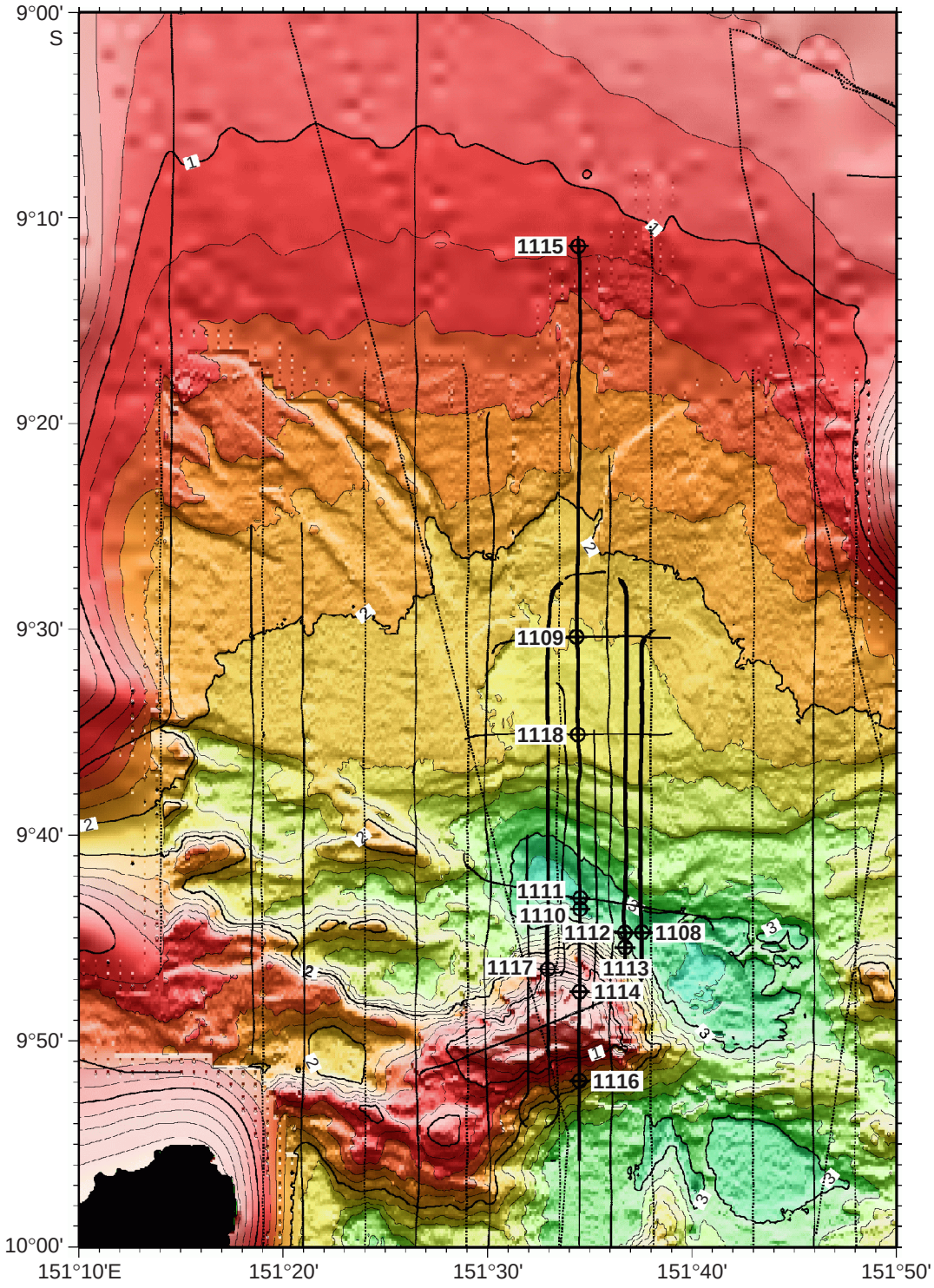

Figure F2. Schematic cross section of Leg 180 sites. Sites logged with FMS are highlighted in bold. Only Site 1115 reaches prerift sediments (modified from Shipboard Scientific Party, 1999b; **Taylor and Huchon,** this volume).

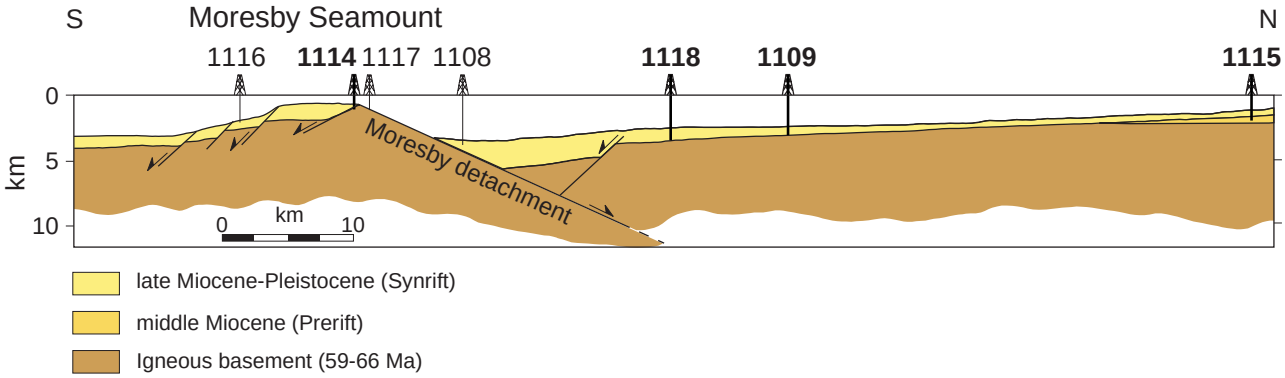

Figure F3. Composite log of Hole 1118A. From left: (1) core number, (2) core recovery, (3) depth, (4) static FMS image, (5) location of detailed FMS figures, (6) structural interpretation tadpoles, (7) depth intervals of detailed orientation plots, (8) lithologic units (summarized in Table T2, p. 112), (9) logging units, (10) structural domains, and (11) caliper measurements. The thin vertical green line on the FMS images indicates the orientation of pad 1 that corresponds to the C1 caliper reading. The tadpole position on the horizontal axis indicates the dip magnitude, and its tail points toward the dip direction. In the structure column (10), deformed zones are highlighted in pink. SSD = soft-sediment deformation, SL = slump, FZ = fracture zone, BRC = breccia. The global image is cut in consecutive page-sized pieces. (Continued on next three pages.)

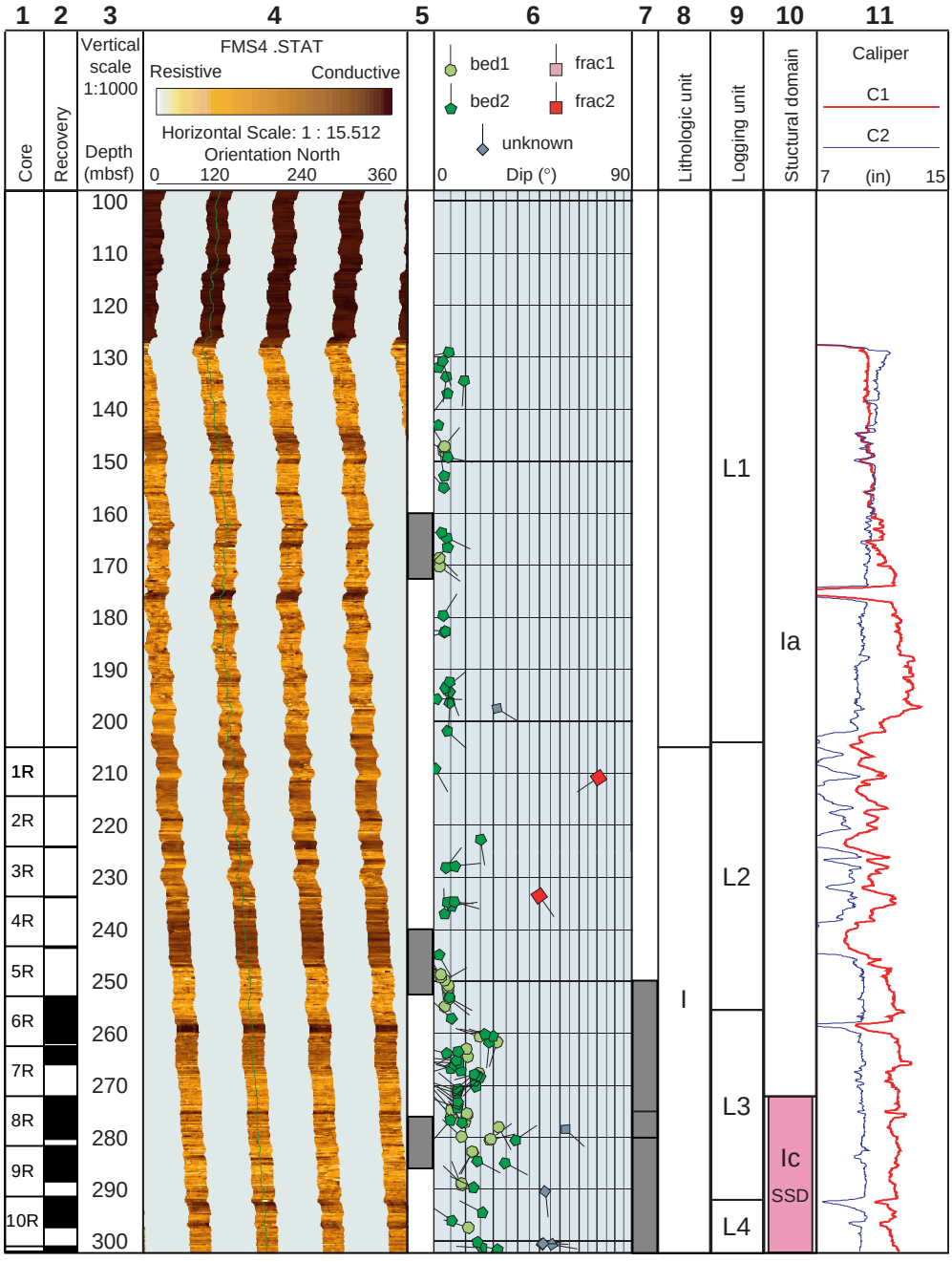

Figure F3 (continued).

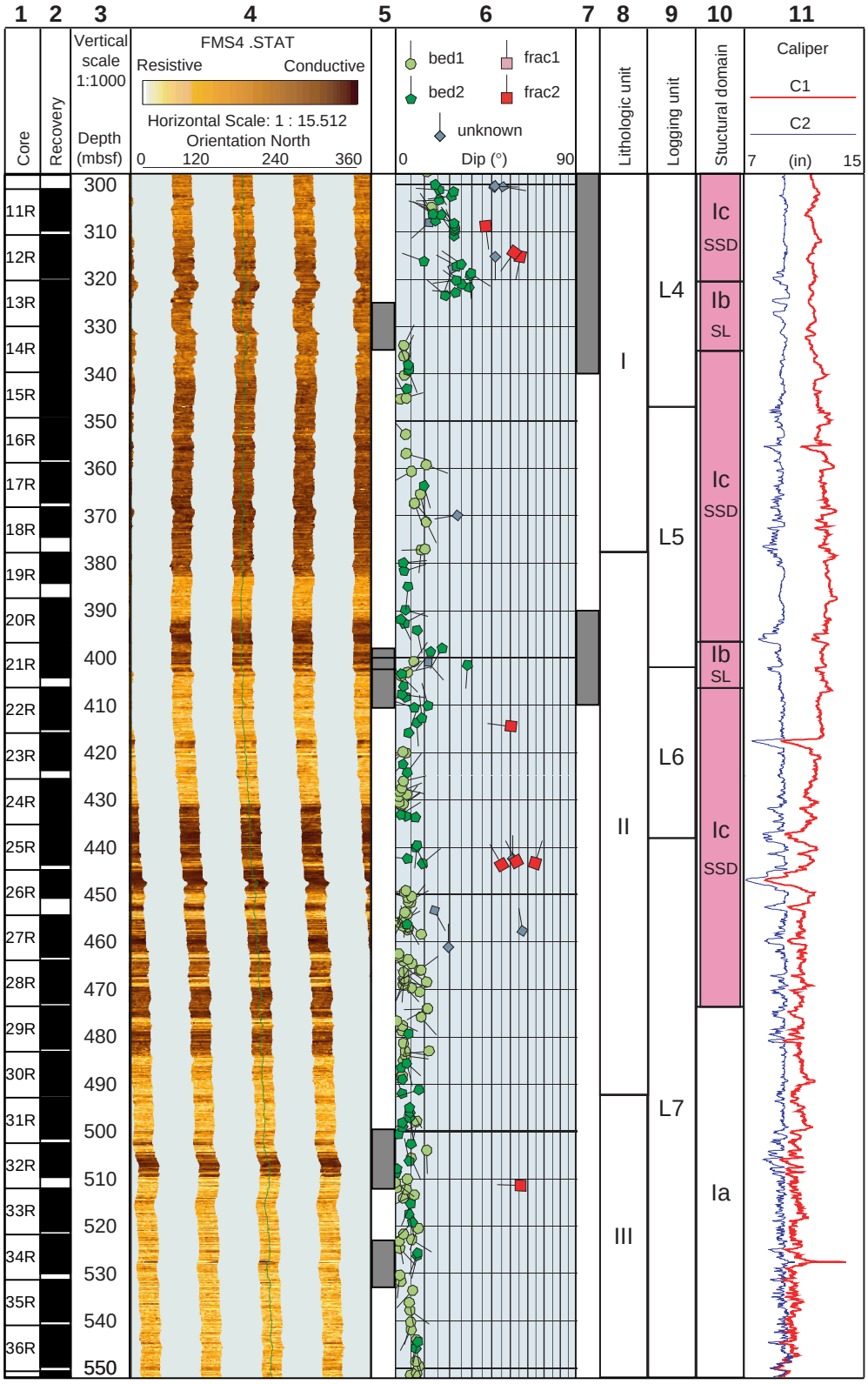

Figure F3 (continued).

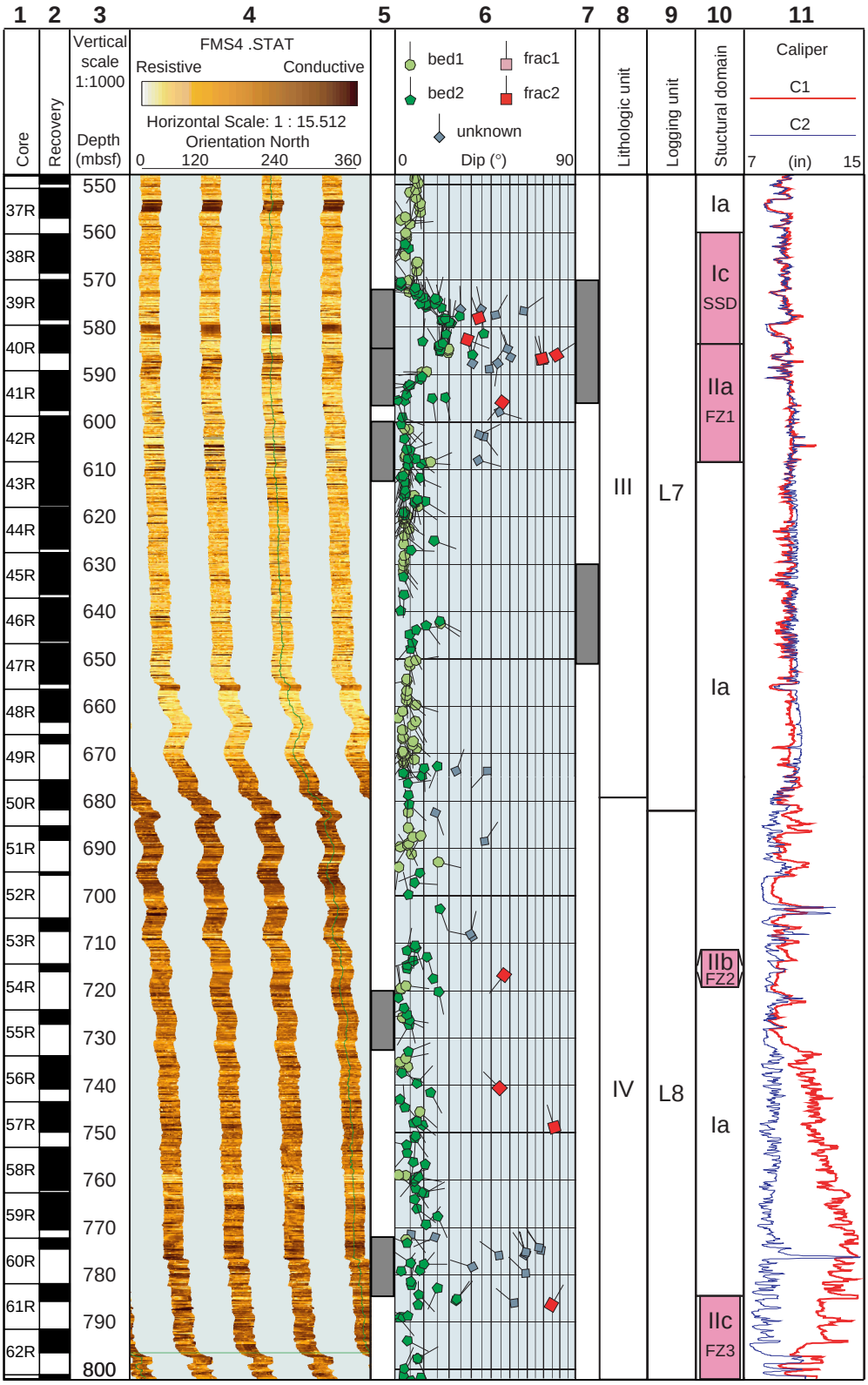

Figure F3 (continued).

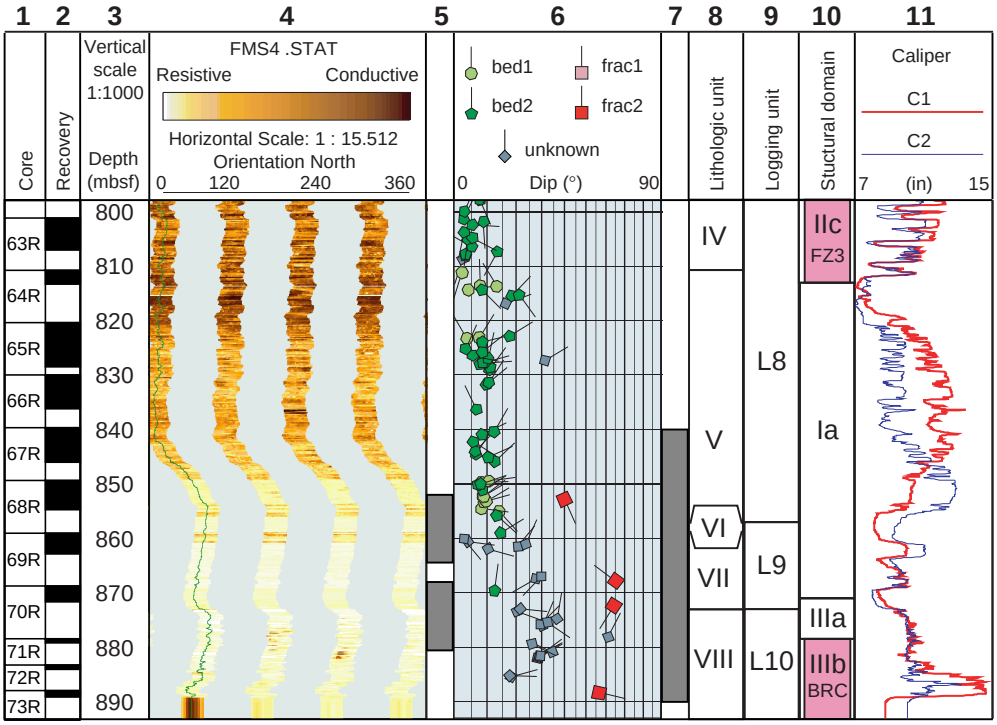

Figure F4. Hole 1118A global bed orientations. Equal area stereographic projection, lower hemisphere. Poles to bed 1 and bed 2 are shown as light green circles and darker green pentagons, respectively. Strike and dip histograms use 5° bins. Strike is normalized so that the dip direction is 90° clockwise from strike. Bed 1 and bed 2 histograms are stacked with same color code as stereonet poles.

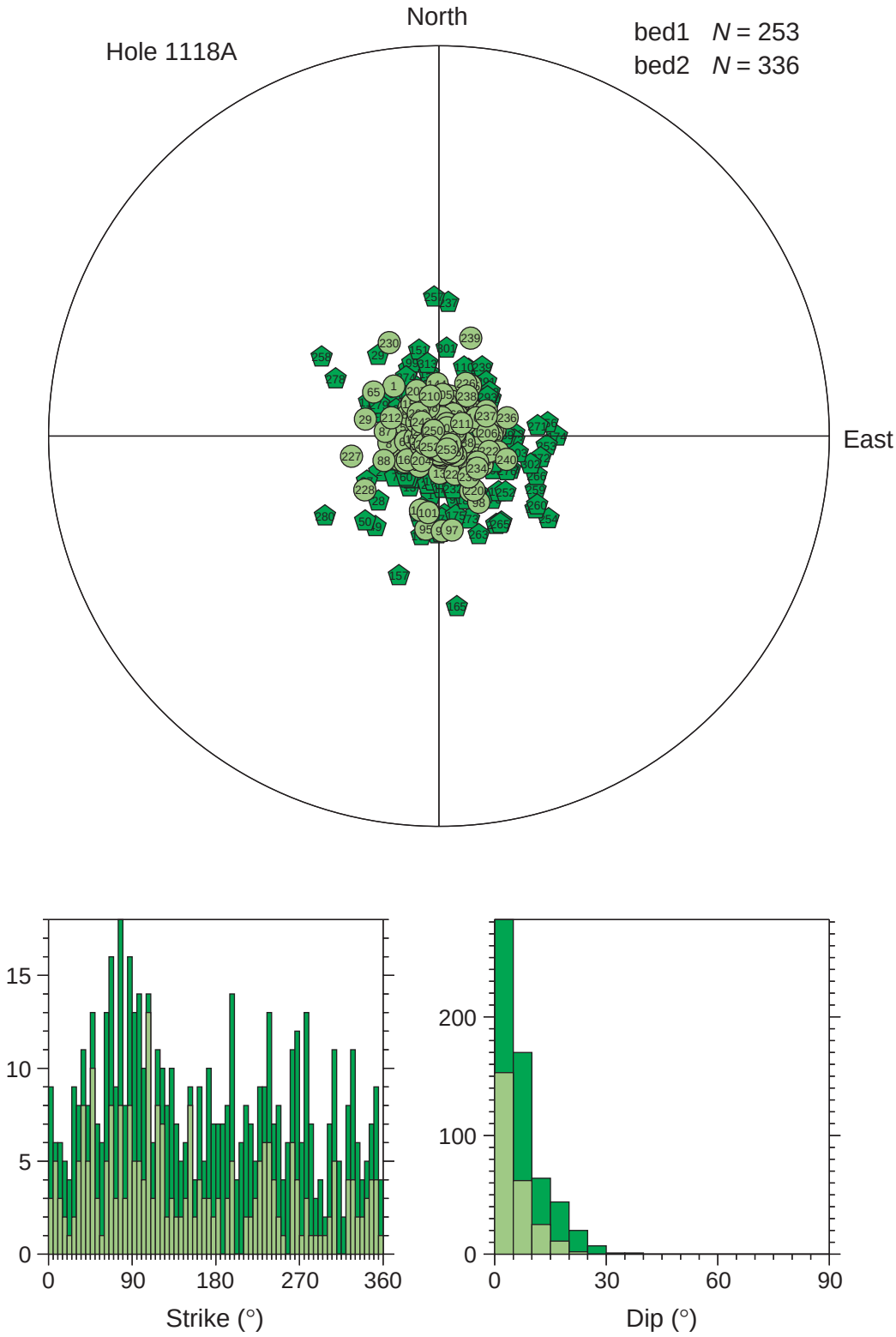

Figure F5. Hole 1118A global fracture orientations. Equal area stereographic projection, lower hemisphere. Poles to frac 1 (none here) and frac 2 are shown as pink and red squares, respectively. Strike and dip histograms use 5° bins. Strike is normalized so that the dip direction is 90° clockwise from strike. Frac 1 and frac 2 histograms are stacked with same color code as stereonet poles.

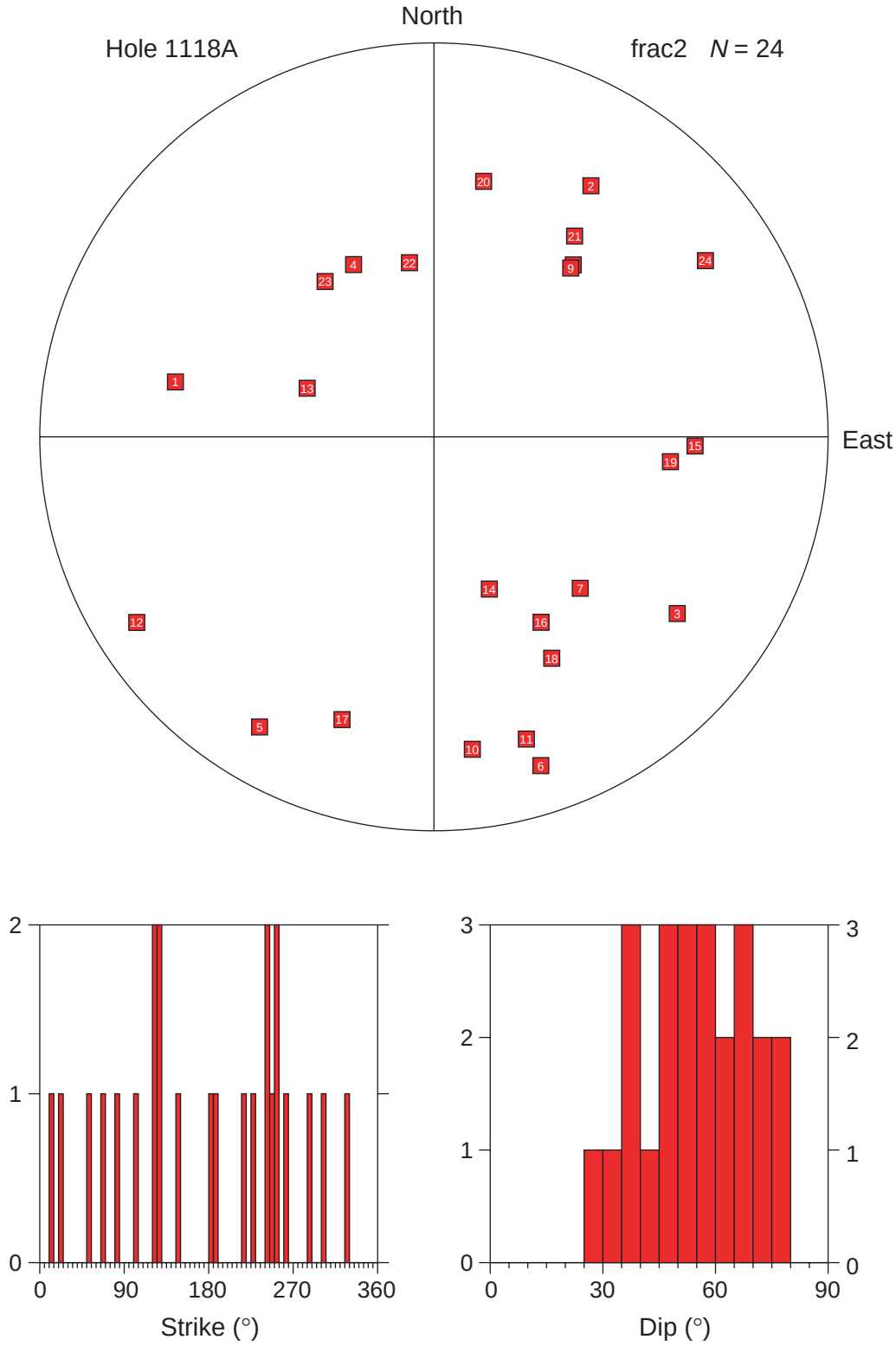

Figure F6. Hole 1118A global unknown planar structure orientations. Equal area stereographic projection, lower hemisphere. Poles are shown as gray diamonds. Strike and dip histograms use 5° bins. Strike is normalized so that the dip direction is 90° clockwise from strike.

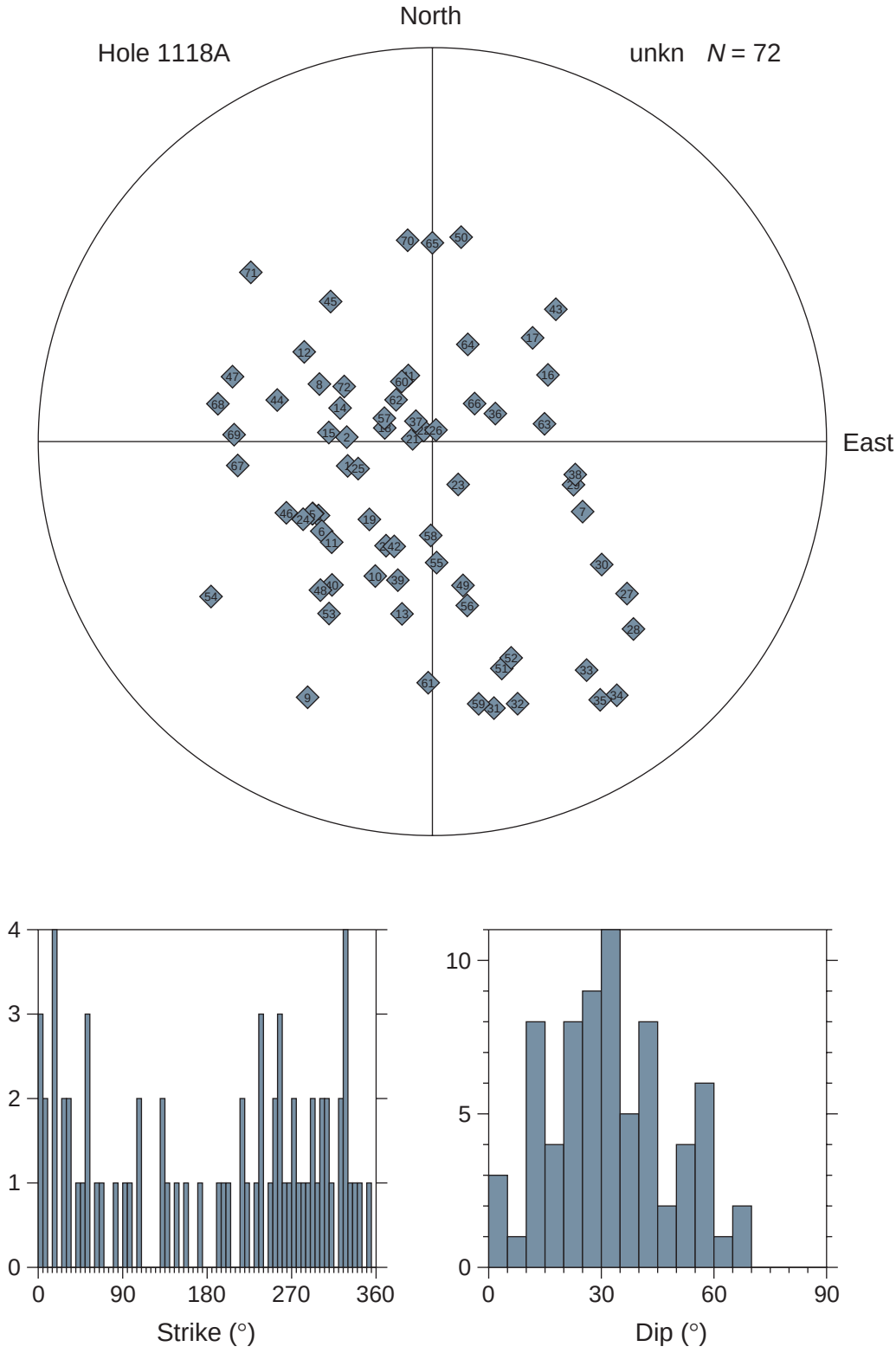

Figure F7. FMS image and analysis, Hole 1118A, 160–172.5 mbsf, reduced to ~70%. From left: (1) depth, (2) static FMS image, (3) dynamic FMS image with a 2-m color equalization sliding window; sinusoids correspond to the structural measurements, (4) structural measurement tadpoles, and (5) caliper measurements. The thin vertical green line on the FMS images indicates the orientation of pad 1, which corresponds to the C1 caliper reading. The tadpole position on the horizontal axis indicates the dip magnitude, and its tail points toward the dip direction.

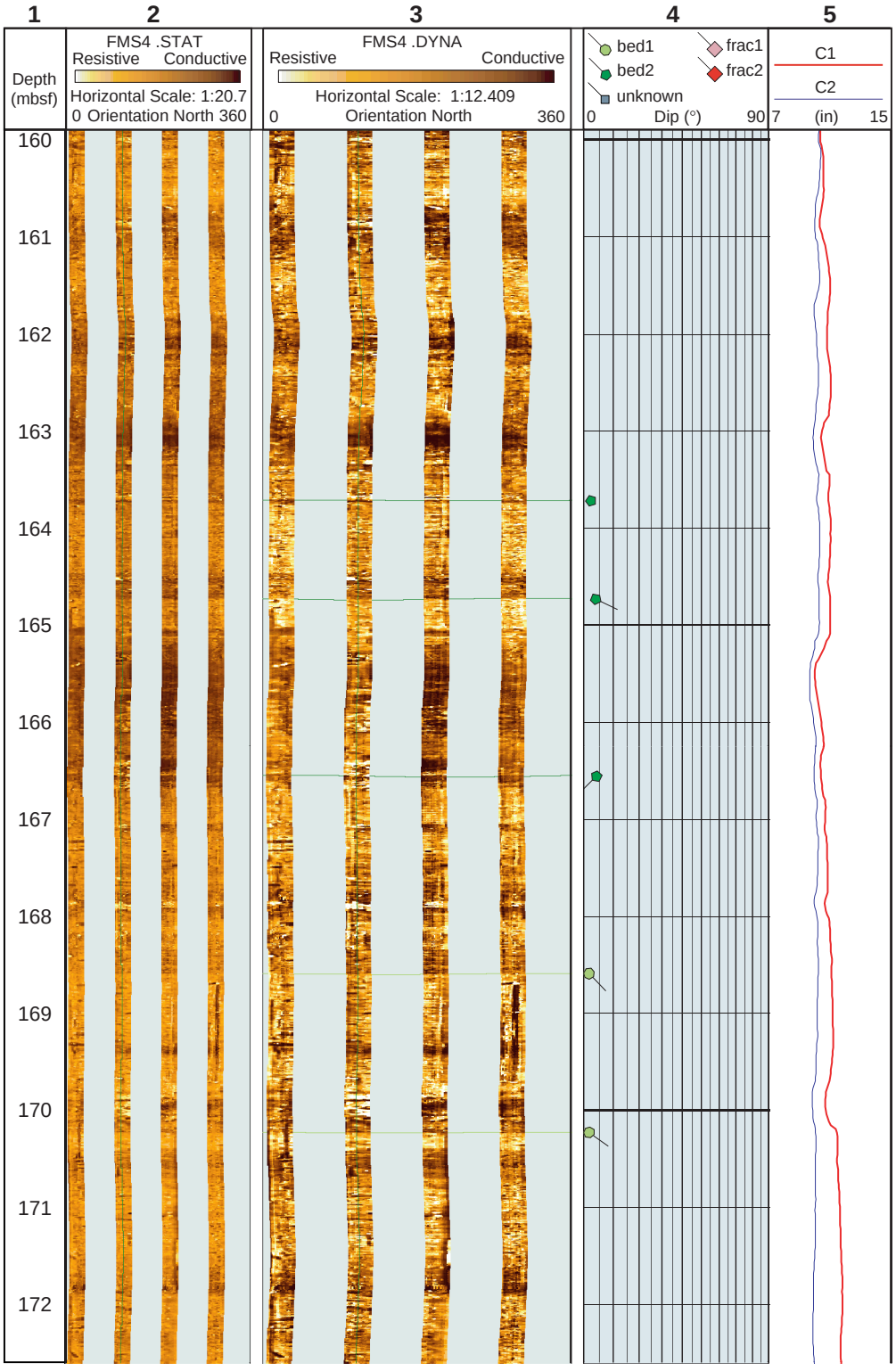

Figure F8. FMS image and analysis, Hole 1118A, 240–252.5 mbsf, reduced to ~70%. From left: (1) depth, (2) static FMS image, (3) dynamic FMS image with a 2-m color equalization sliding window; sinusoids correspond to the structural measurements, (4) structural measurement tadpoles, and (5) caliper measurements. The thin vertical green line on the FMS images indicates the orientation of pad 1, which corresponds to the C1 caliper reading. The tadpole position on the horizontal axis indicates the dip magnitude, and its tail points toward the dip direction.

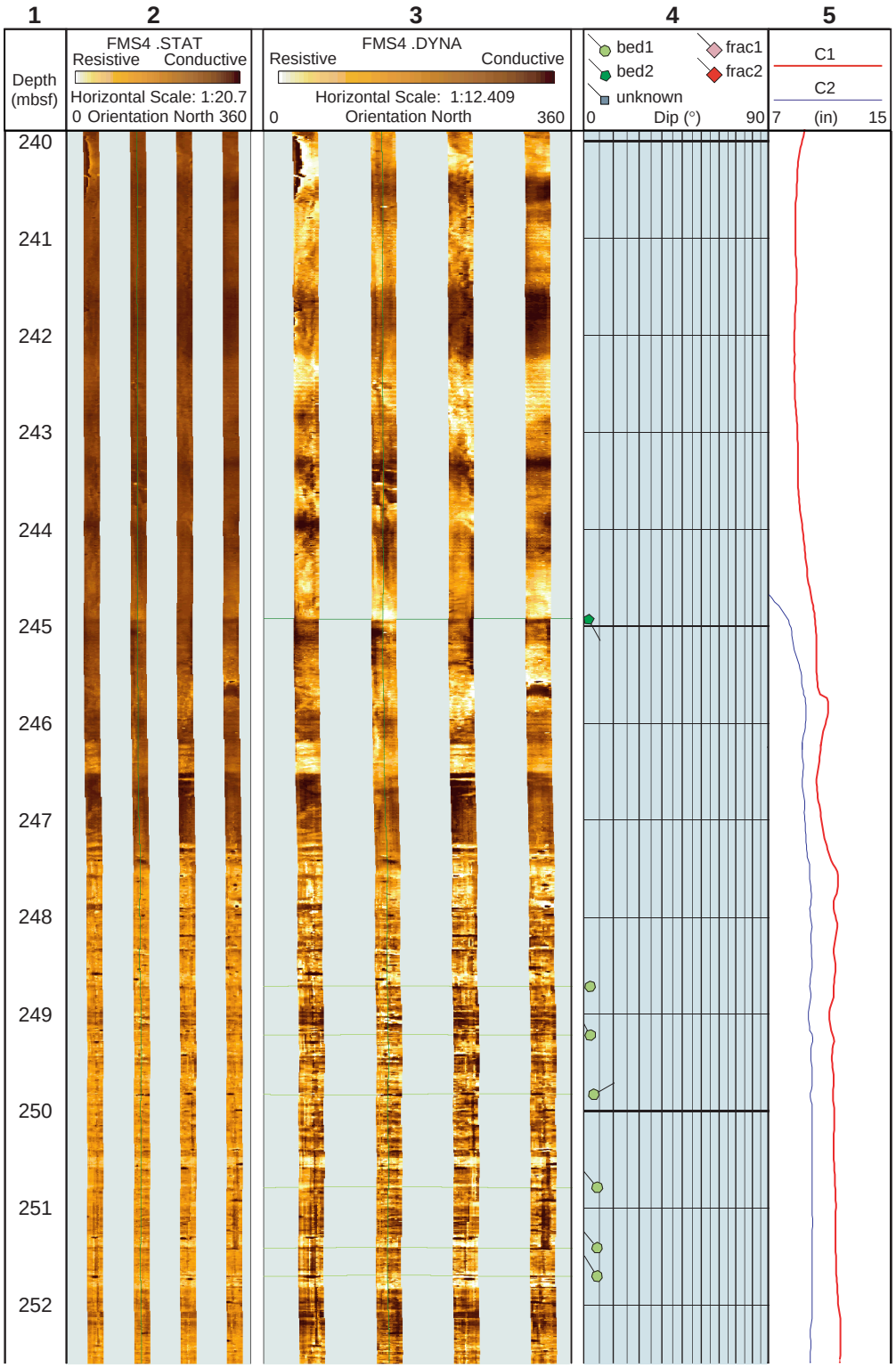

Figure F9. FMS image and analysis, Hole 1118A, 276–286 mbsf, reduced to ~70%. From left: (1) depth, (2) static FMS image, (3) dynamic FMS image with a 2-m color equalization sliding window; sinusoids correspond to the structural measurements, (4) structural measurement tadpoles, and (5) caliper measurements. The thin vertical green line on the FMS images indicates the orientation of pad 1, which corresponds to the C1 caliper reading. The tadpole position on the horizontal axis indicates the dip magnitude, and its tail points toward the dip direction.

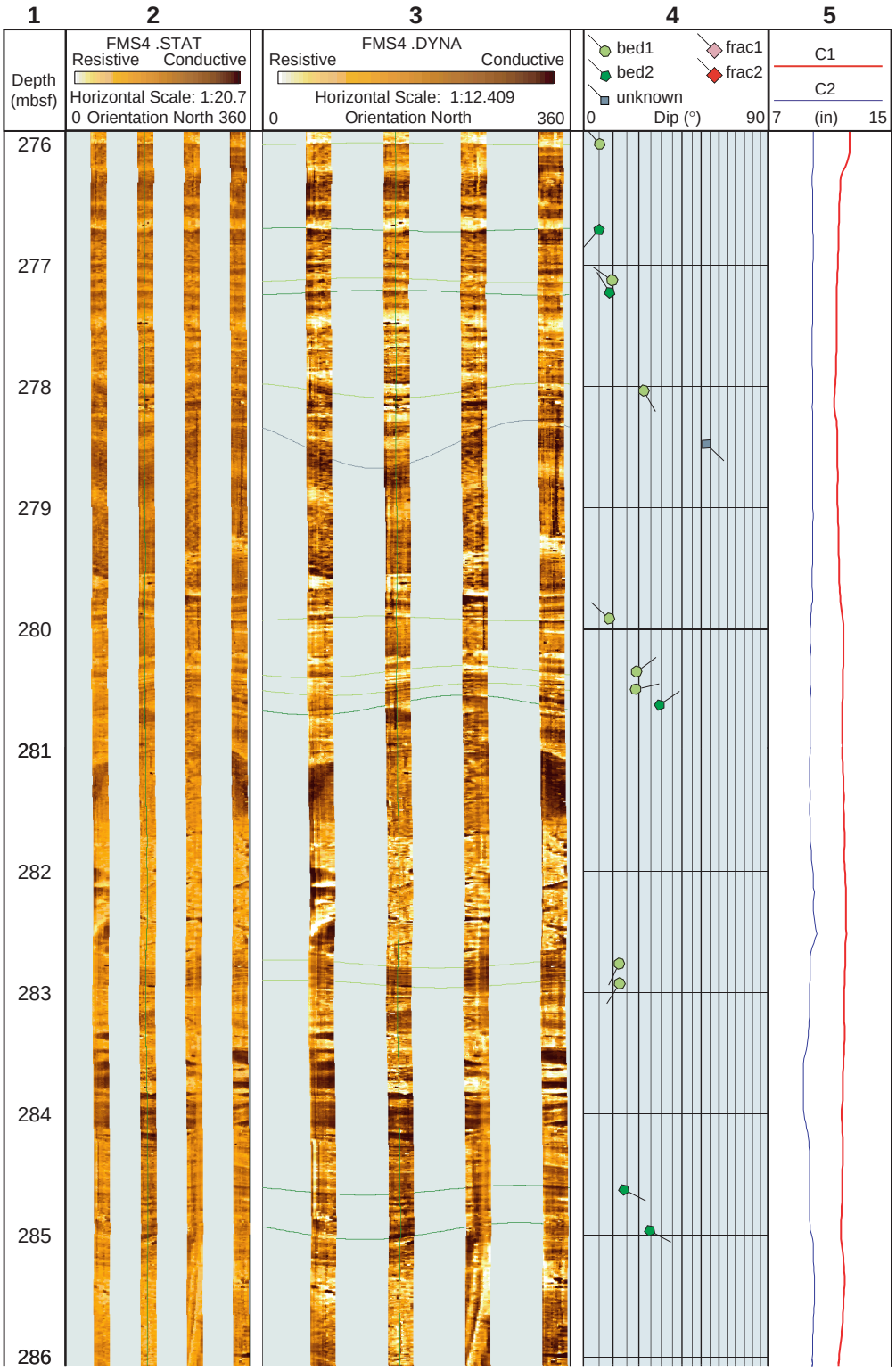

Figure F10. FMS image and analysis, Hole 1118A, 325–335 mbsf, reduced to ~70%. From left: (1) depth, (2) static FMS image, (3) dynamic FMS image with a 2-m color equalization sliding window; sinusoids correspond to the structural measurements, (4) structural measurement tadpoles, and (5) caliper measurements. The thin vertical green line on the FMS images indicates the orientation of pad 1, which corresponds to the C1 caliper reading. The tadpole position on the horizontal axis indicates the dip magnitude, and its tail points toward the dip direction.

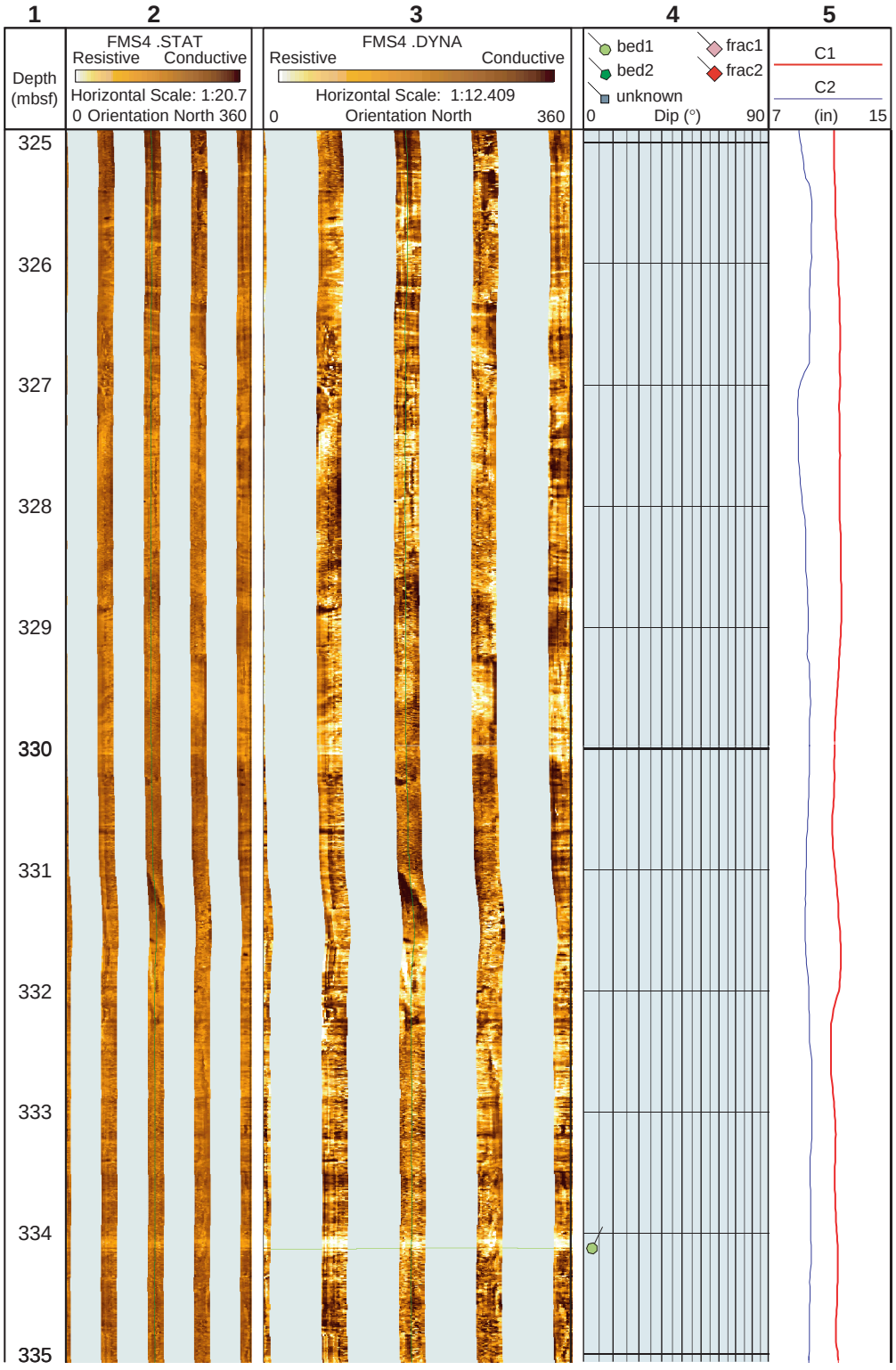

Figure F11. Structure orientations, Hole 1118A, 250–280 mbsf. Stereographic projection of poles to bed 1, bed 2, frac 2 (none in this interval), and unknown structures (light green circles, darker green pentagons, red squares, and gray diamonds, respectively). Equal area stereographic projection, lower hemisphere. Strike and dip histograms of bedding only, where bed 1 and bed 2 are stacked with same color code as stereonet poles. Histograms use 5° bins. Strike is normalized so that the dip direction is 90° clockwise from strike. A partial 5° stereonet is shown in the background to highlight a cylindrical structure.

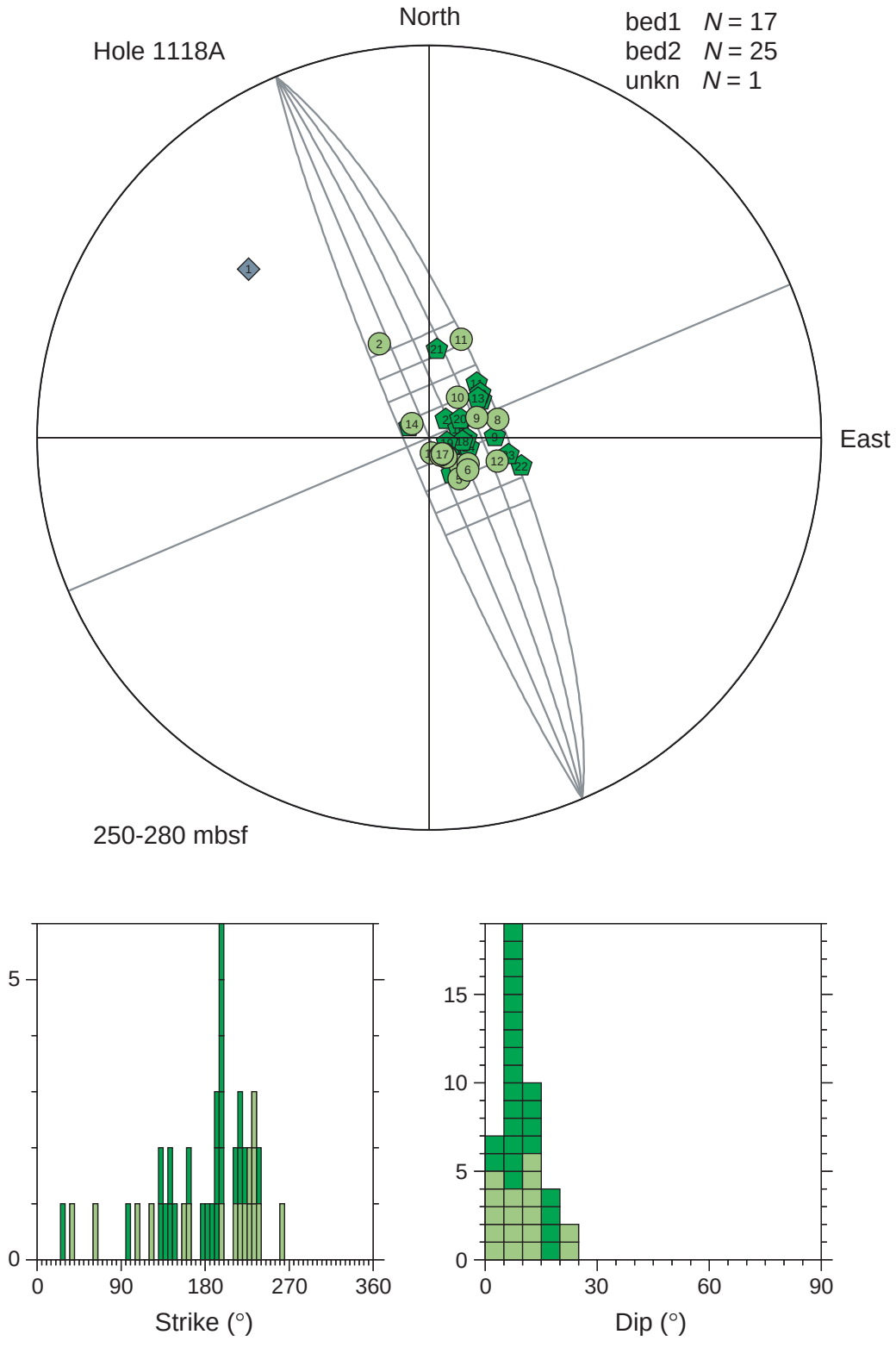

Figure F12. Structure orientations, Hole 1118A, 275–340 mbsf. Stereographic projection of poles to bed 1, bed 2, frac 2 (none in this interval), and unknown structures (light green circles, darker green pentagons, red squares, and gray diamonds, respectively). Equal area stereographic projection, lower hemisphere. Strike and dip histograms of bedding only, where bed 1 and bed 2 are stacked with same color code as stereonet poles. Histograms use 5° bins. Strike is normalized so that the dip direction is 90° clockwise from strike. A partial 5° stereonet is shown in the background to highlight a cylindrical structure.

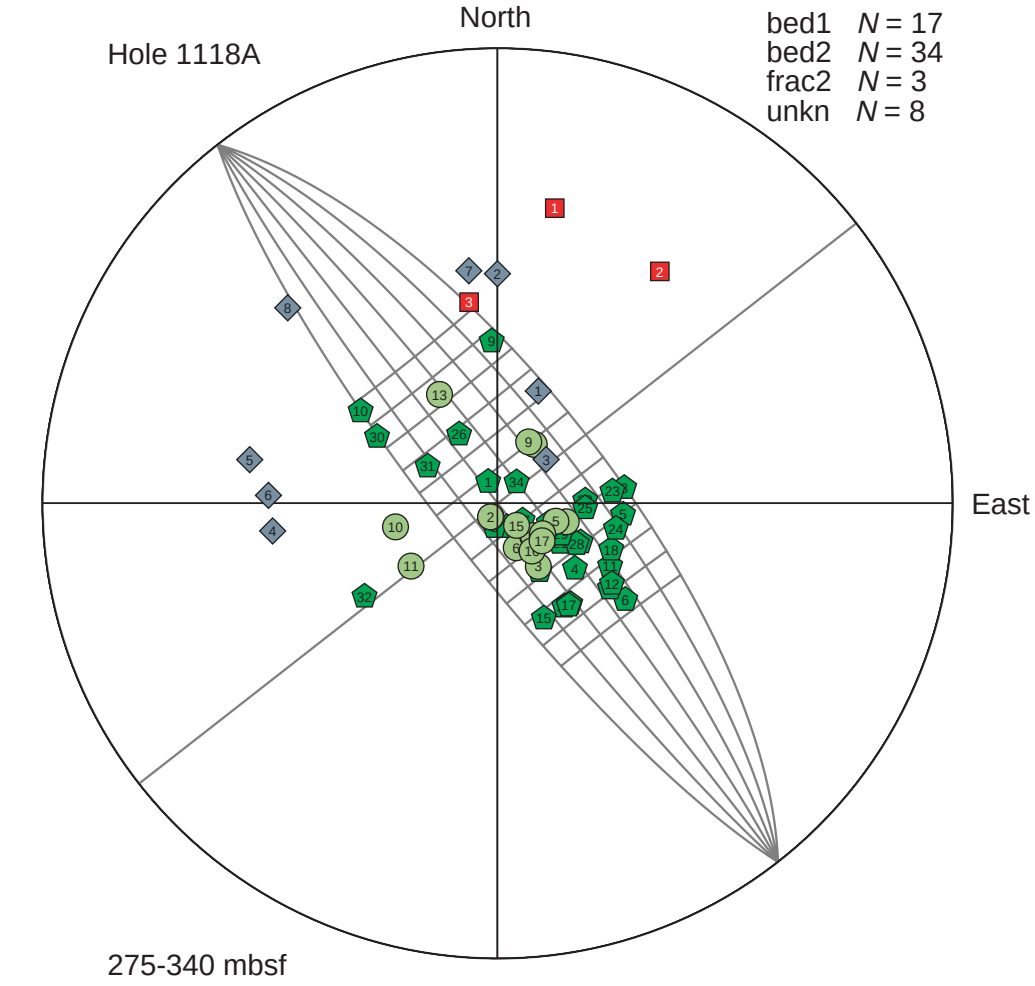

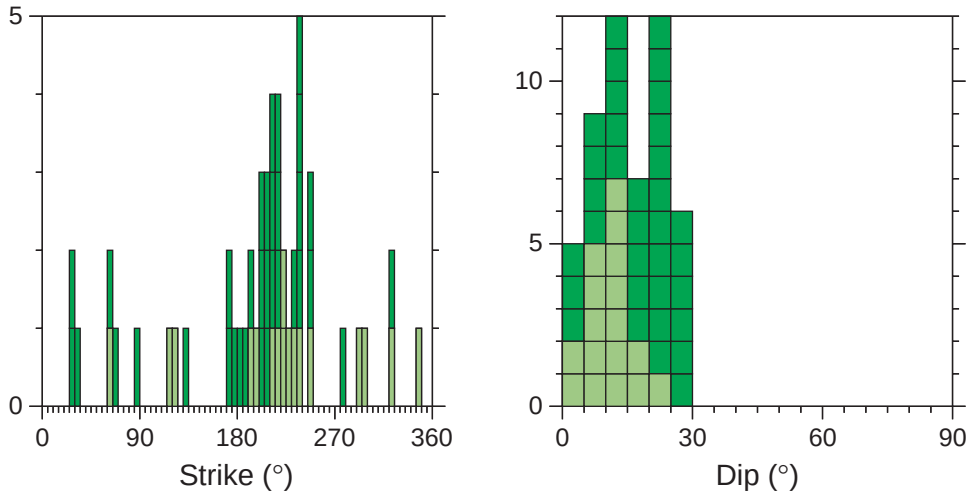

Figure F13. FMS image and analysis, Hole 1118A, 398–410.5 mbsf, reduced to ~70%. From left: (1) depth, (2) static FMS image, (3) dynamic FMS image with a 2-m color equalization sliding window; sinusoids correspond to the structural measurements, (4) structural measurement tadpoles, and (5) caliper measurements. The thin vertical green line on the FMS images indicates the orientation of pad 1, which corresponds to the C1 caliper reading. The tadpole position on the horizontal axis indicates the dip magnitude, and its tail points toward the dip direction.

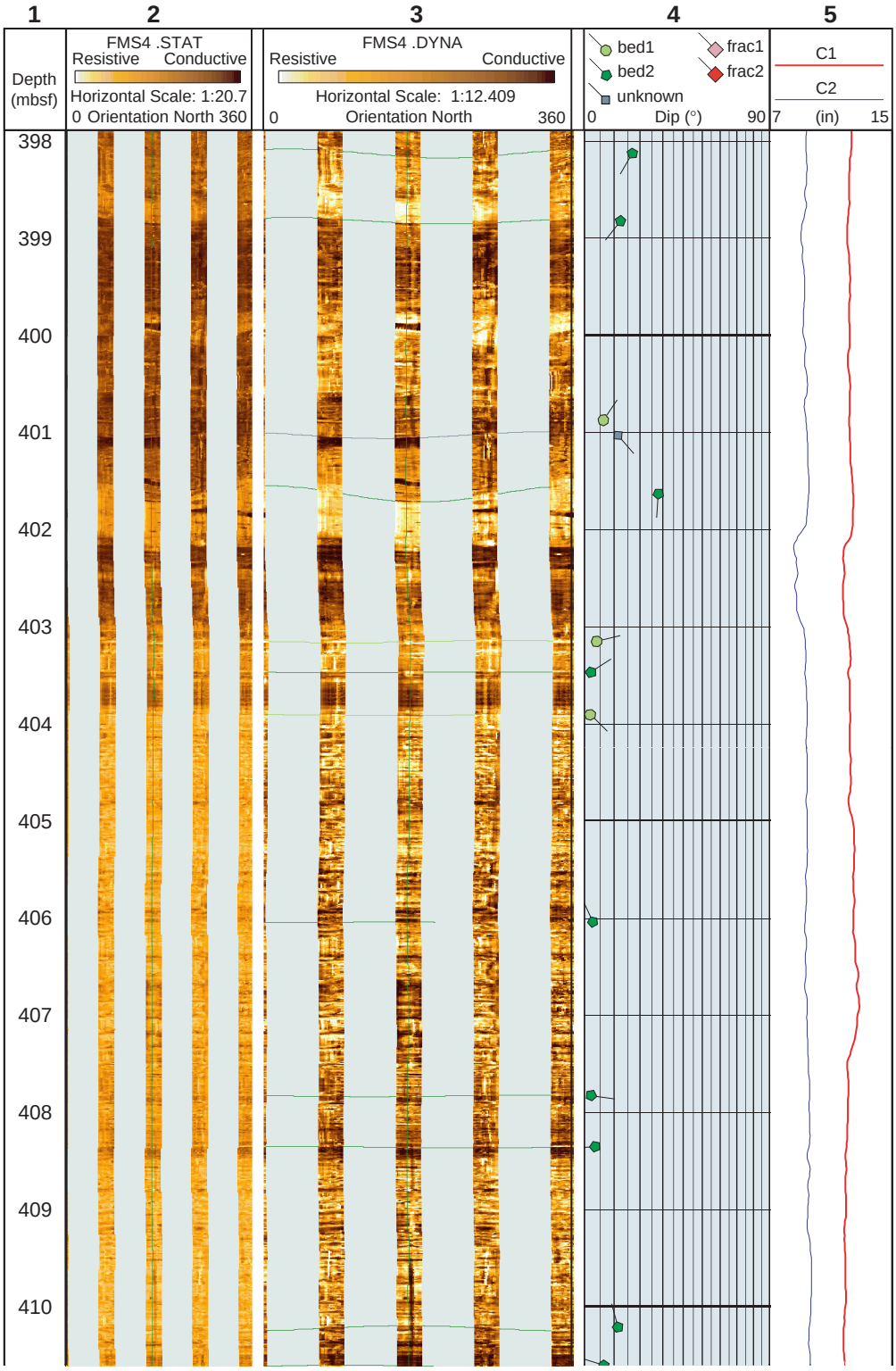

Figure F14. FMS image and analysis, Hole 1118A, 400–402.5 mbsf, reduced to ~70%. From left: (1) depth, (2) static FMS image, (3) dynamic FMS image with a 2-m color equalization sliding window; sinusoids correspond to the structural measurements, (4) structural measurement tadpoles, and (5) caliper measurements. The thin vertical green line on the FMS images indicates the orientation of pad 1, which corresponds to the C1 caliper reading. The tadpole position on the horizontal axis indicates the dip magnitude, and its tail points toward the dip direction.

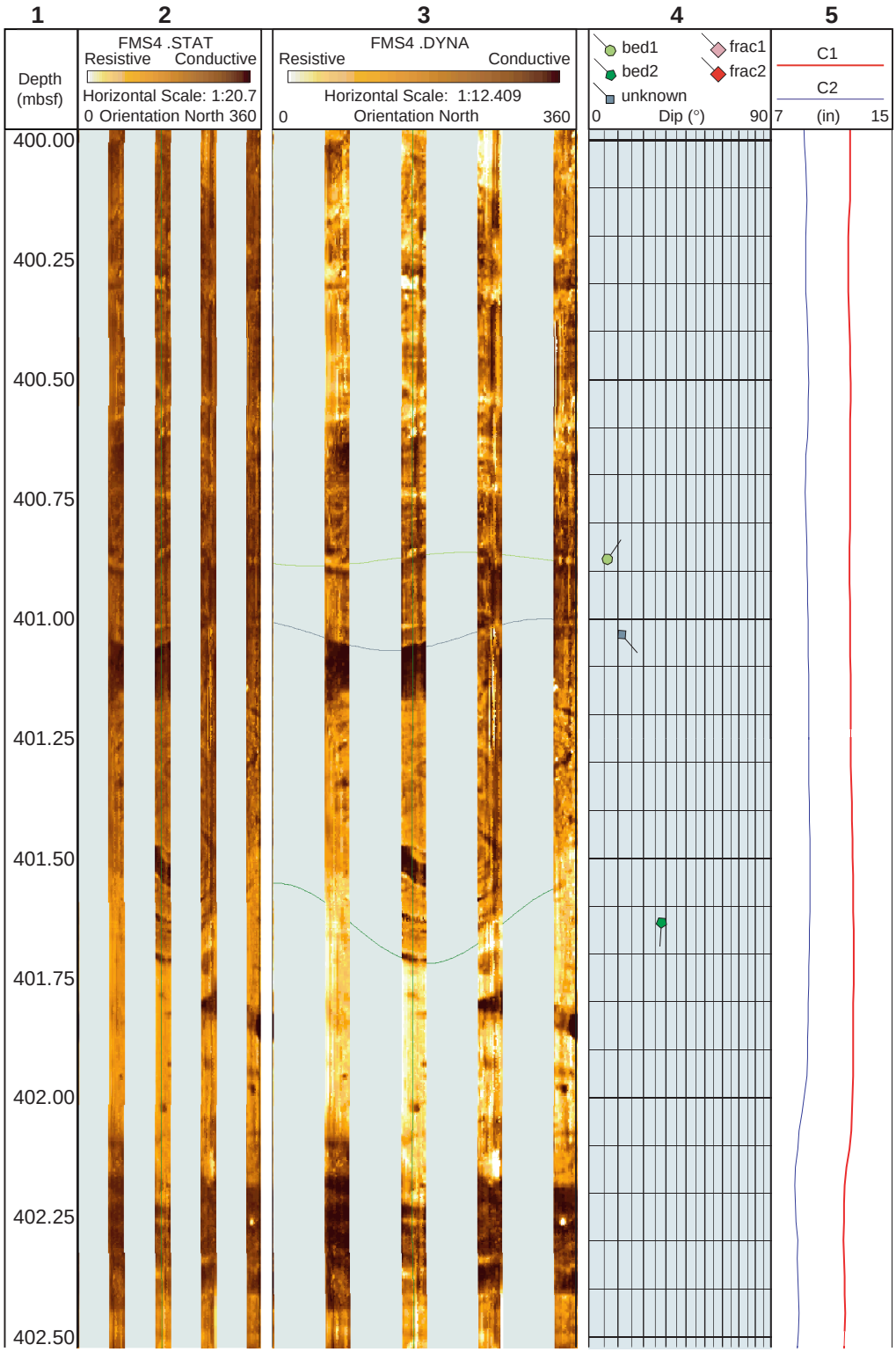

Figure F15. Structure orientations, Hole 1118A, 390–410 mbsf. Stereographic projection of poles to bed 1, bed 2, frac 2, and unknown structures (light green circles, darker green pentagons, red squares, and gray diamonds, respectively). Equal area stereographic projection, lower hemisphere. Strike and dip histograms of bedding only, where bed 1 and bed 2 are stacked with same color code as stereonet poles. Histograms use 5° bins. Strike is normalized so that the dip direction is 90° clockwise from strike. A partial 5° stereonet is shown in the background to highlight a cylindrical structure.

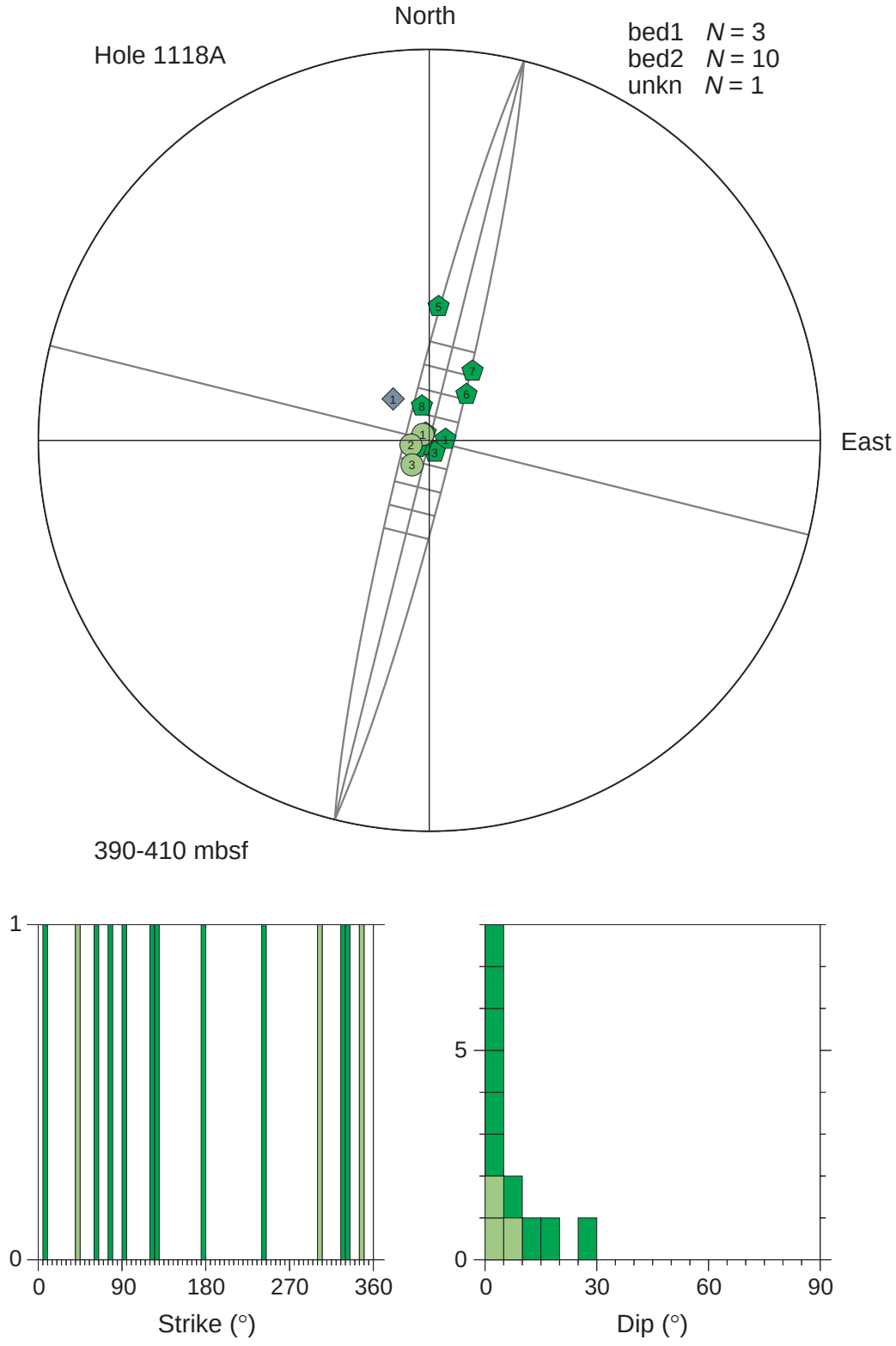

Figure F16. FMS image and analysis, Hole 1118A, 499.5–512 mbsf, reduced to ~70%. From left: (1) depth, (2) static FMS image, (3) dynamic FMS image with a 2-m color equalization sliding window; sinusoids correspond to the structural measurements, (4) structural measurement tadpoles, and (5) caliper measurements. The thin vertical green line on the FMS images indicates the orientation of pad 1, which corresponds to the C1 caliper reading. The tadpole position on the horizontal axis indicates the dip magnitude, and its tail points toward the dip direction.

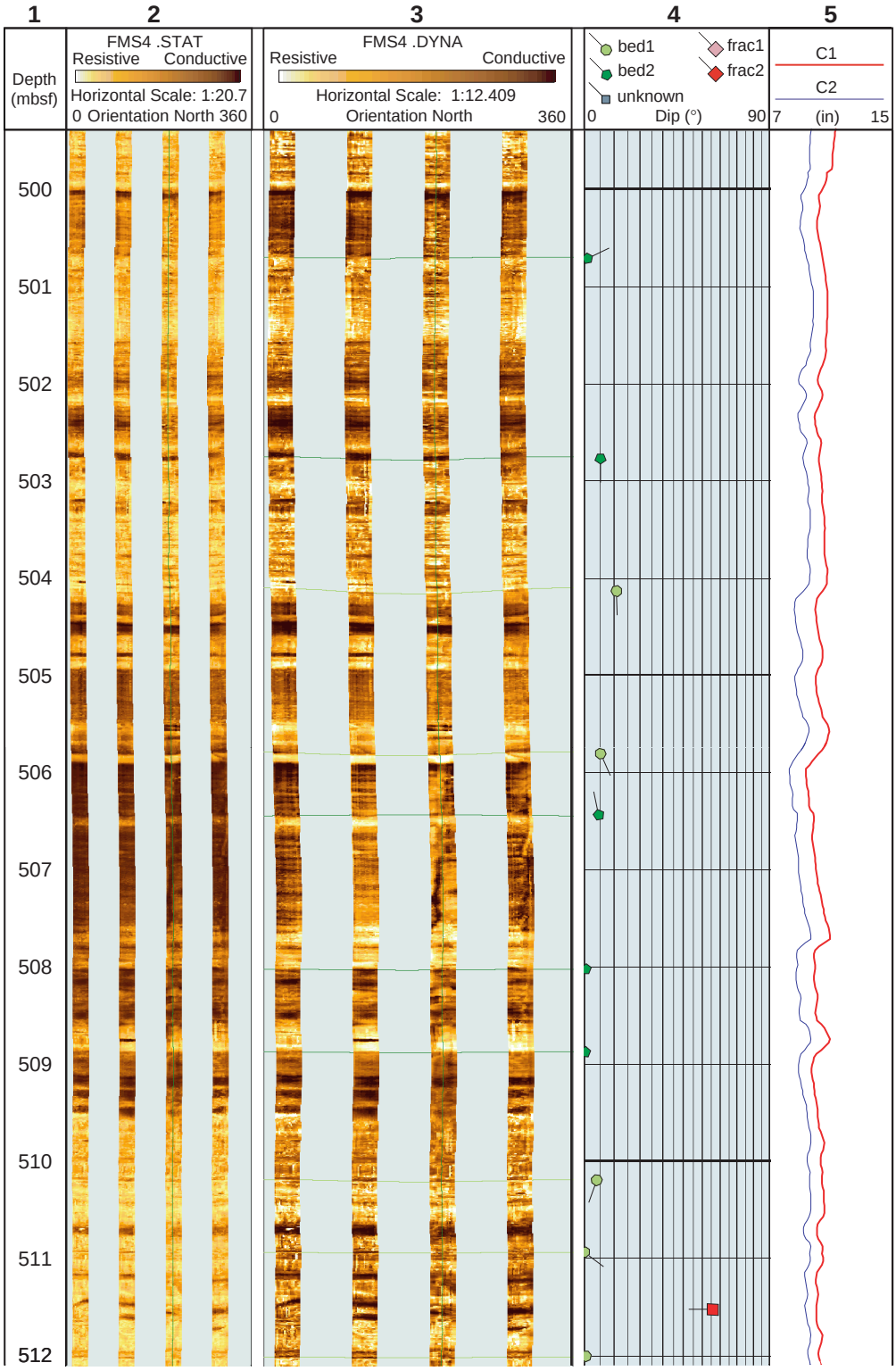

Figure F17. FMS image and analysis, Hole 1118A, 523–533 mbsf, reduced to ~70%. From left: (1) depth, (2) static FMS image, (3) dynamic FMS image with a 2-m color equalization sliding window; sinusoids correspond to the structural measurements, (4) structural measurement tadpoles, and (5) caliper measurements. The thin vertical green line on the FMS images indicates the orientation of pad 1, which corresponds to the C1 caliper reading. The tadpole position on the horizontal axis indicates the dip magnitude, and its tail points toward the dip direction.

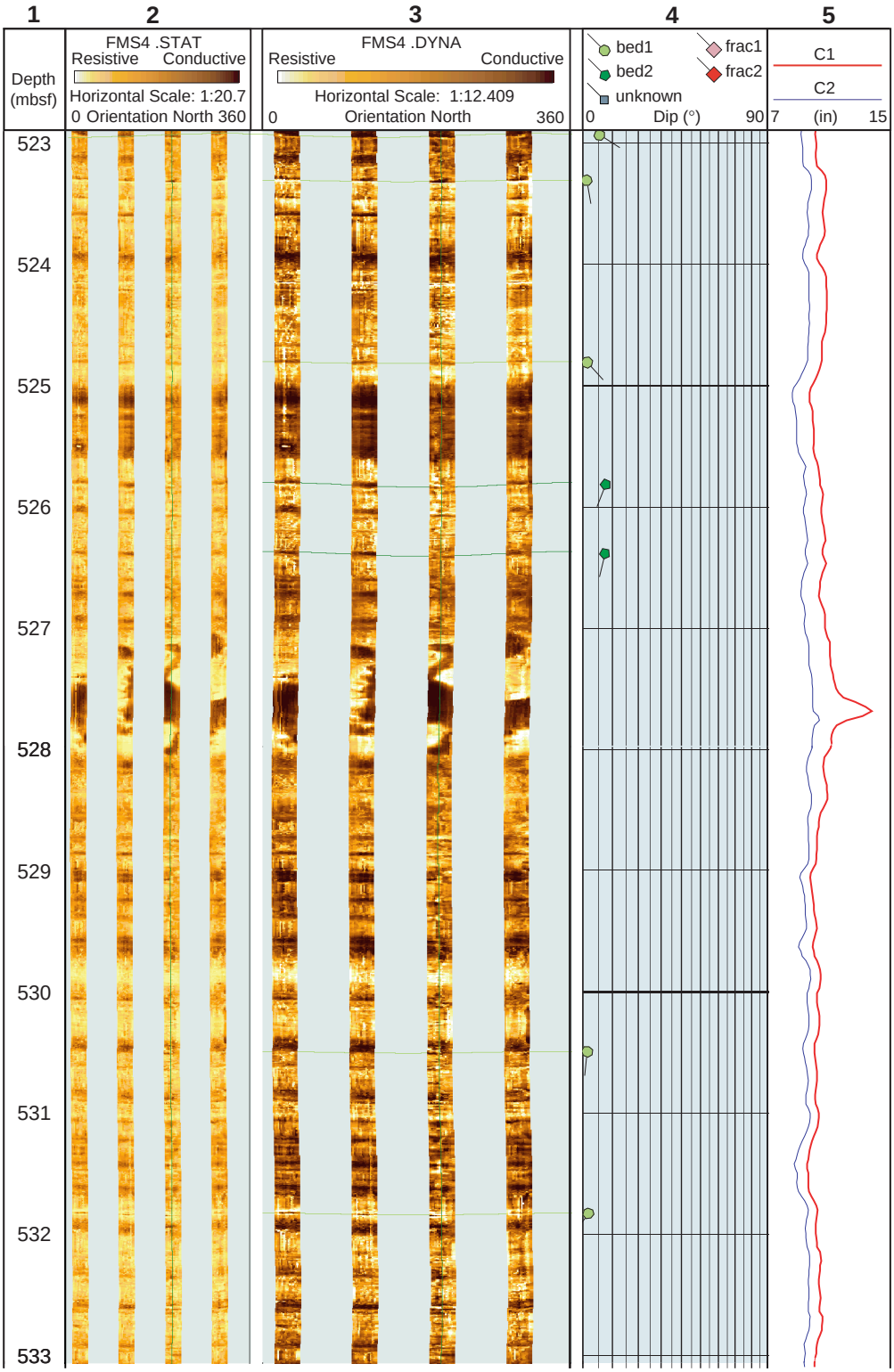

Figure F18. FMS image and analysis, Hole 1118A, 572–584.5 mbsf, reduced to ~70%. From left: (1) depth, (2) static FMS image, (3) dynamic FMS image with a 2-m color equalization sliding window; sinusoids correspond to the structural measurements, (4) structural measurement tadpoles, and (5) caliper measurements. The thin vertical green line on the FMS images indicates the orientation of pad 1, which corresponds to the C1 caliper reading. The tadpole position on the horizontal axis indicates the dip magnitude, and its tail points toward the dip direction.

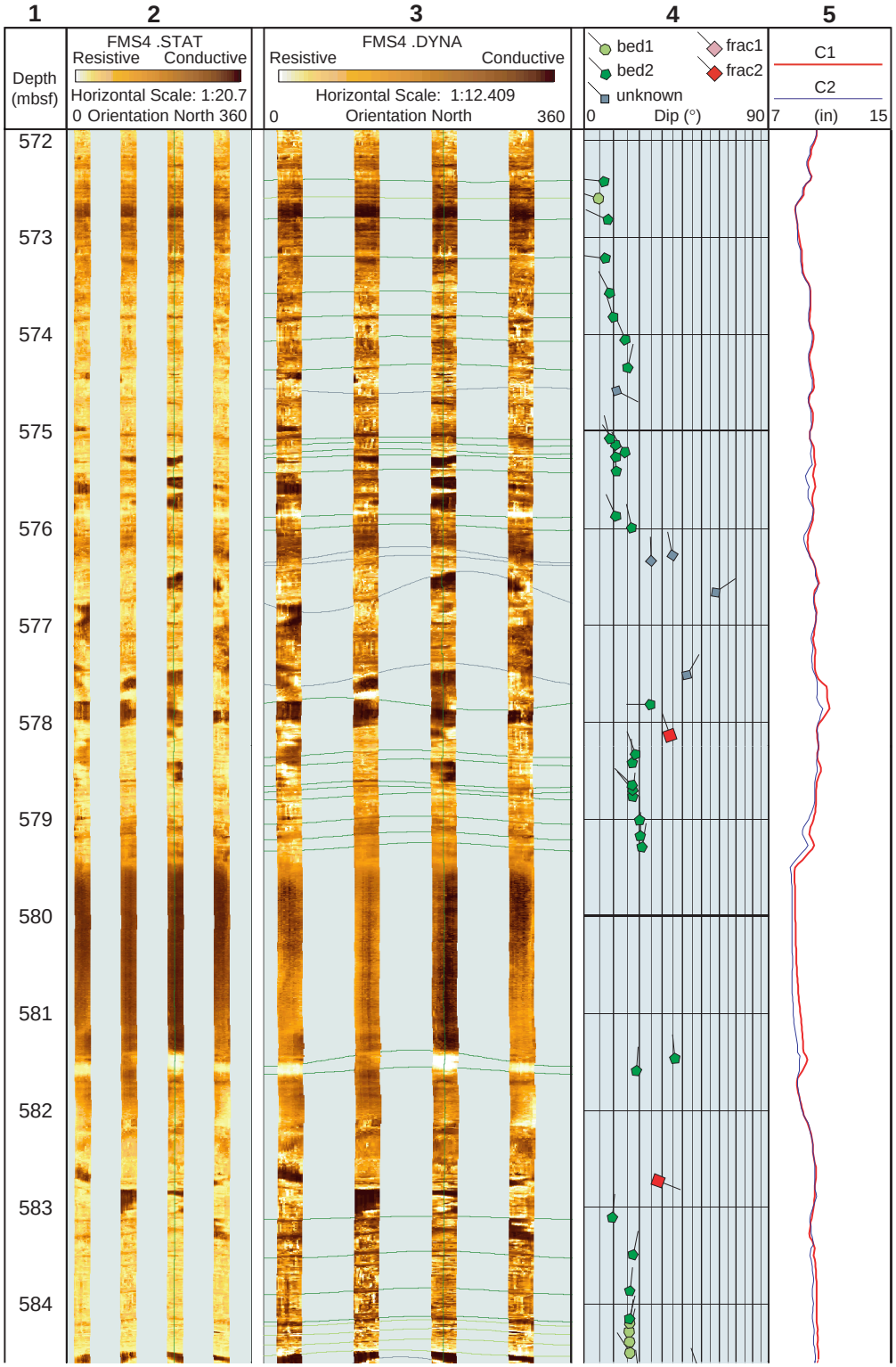

Figure F19. FMS image and analysis, Hole 1118A, 584–596.5 mbsf, reduced to ~70%. From left: (1) depth, (2) static FMS image, (3) dynamic FMS image with a 2-m color equalization sliding window; sinusoids correspond to the structural measurements, (4) structural measurement tadpoles, and (5) caliper measurements. The thin vertical green line on the FMS images indicates the orientation of pad 1, which corresponds to the C1 caliper reading. The tadpole position on the horizontal axis indicates the dip magnitude, and its tail points toward the dip direction.

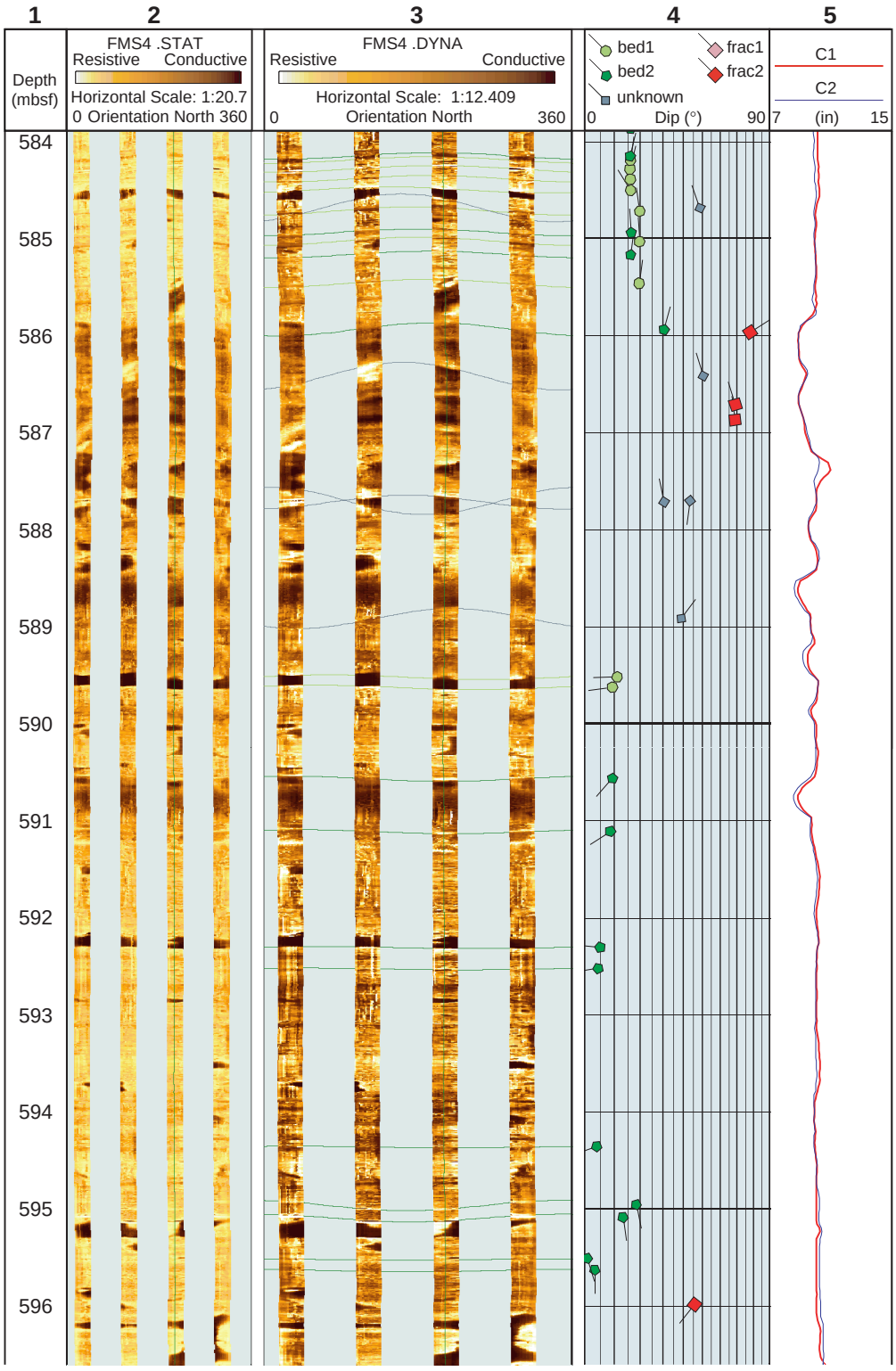

Figure F20. Structure orientations, Hole 1118A, 570–596 mbsf. Stereographic projection of poles to bed 1, bed 2, frac 2, and unknown structures (light green circles, darker green pentagons, red squares, and gray diamonds, respectively). Equal area stereographic projection, lower hemisphere. Strike and dip histograms of bedding only, where bed 1 and bed 2 are stacked with same color code as stereonet poles. Histograms use 5° bins. Strike is normalized so that the dip direction is 90° clockwise from strike. A partial 5° stereonet is shown in the background to highlight a cylindrical structure. Fractures 2 and 6 are located at 586.8 and 578.1 mbsf, respectively.

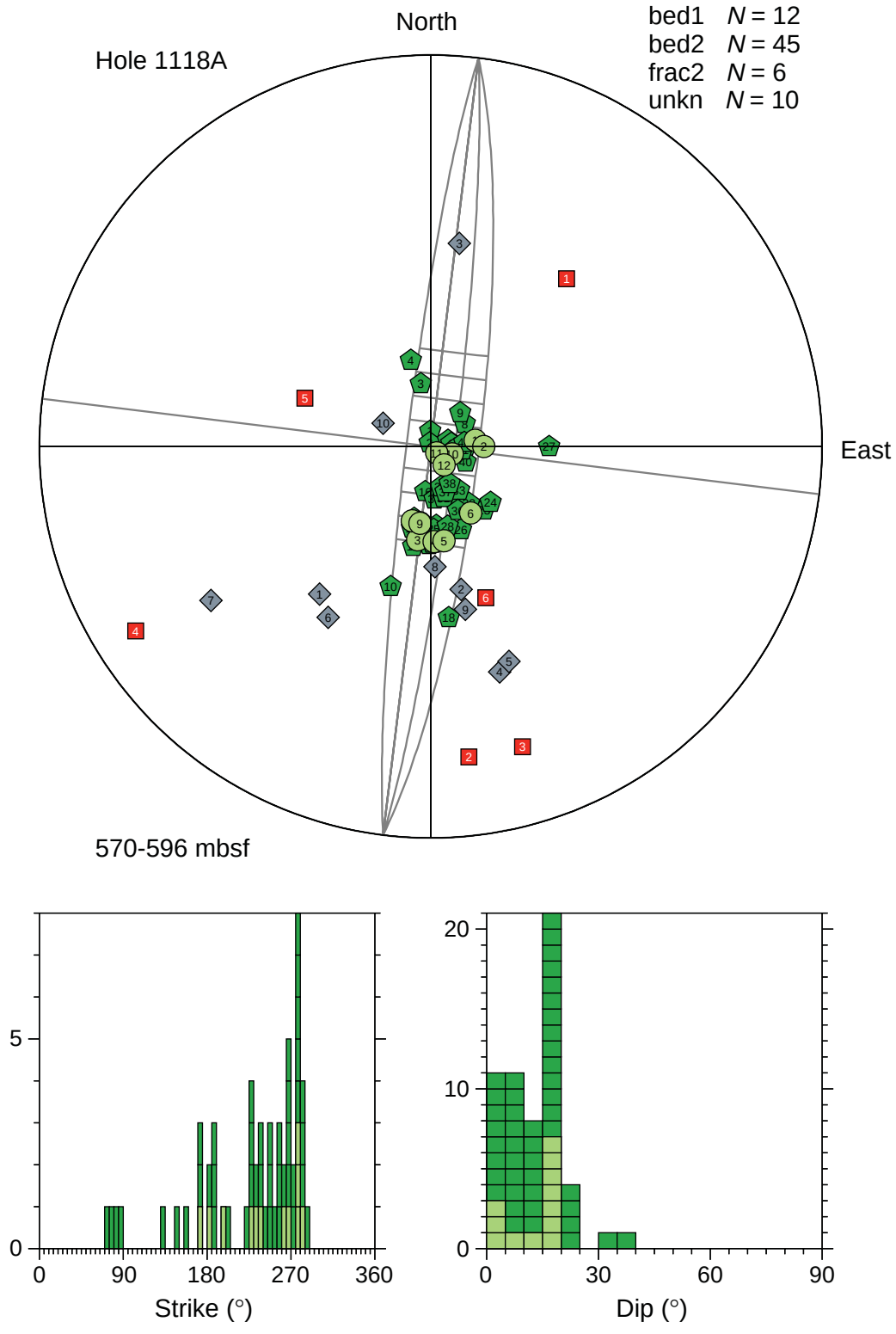

Figure F21. FMS image and analysis, Hole 1118A, 600–612.5 mbsf, reduced to ~70%. From left: (1) depth, (2) static FMS image, (3) dynamic FMS image with a 2-m color equalization sliding window; sinusoids correspond to the structural measurements, (4) structural measurement tadpoles, and (5) caliper measurements. The thin vertical green line on the FMS images indicates the orientation of pad 1, which corresponds to the C1 caliper reading. The tadpole position on the horizontal axis indicates the dip magnitude, and its tail points toward the dip direction.

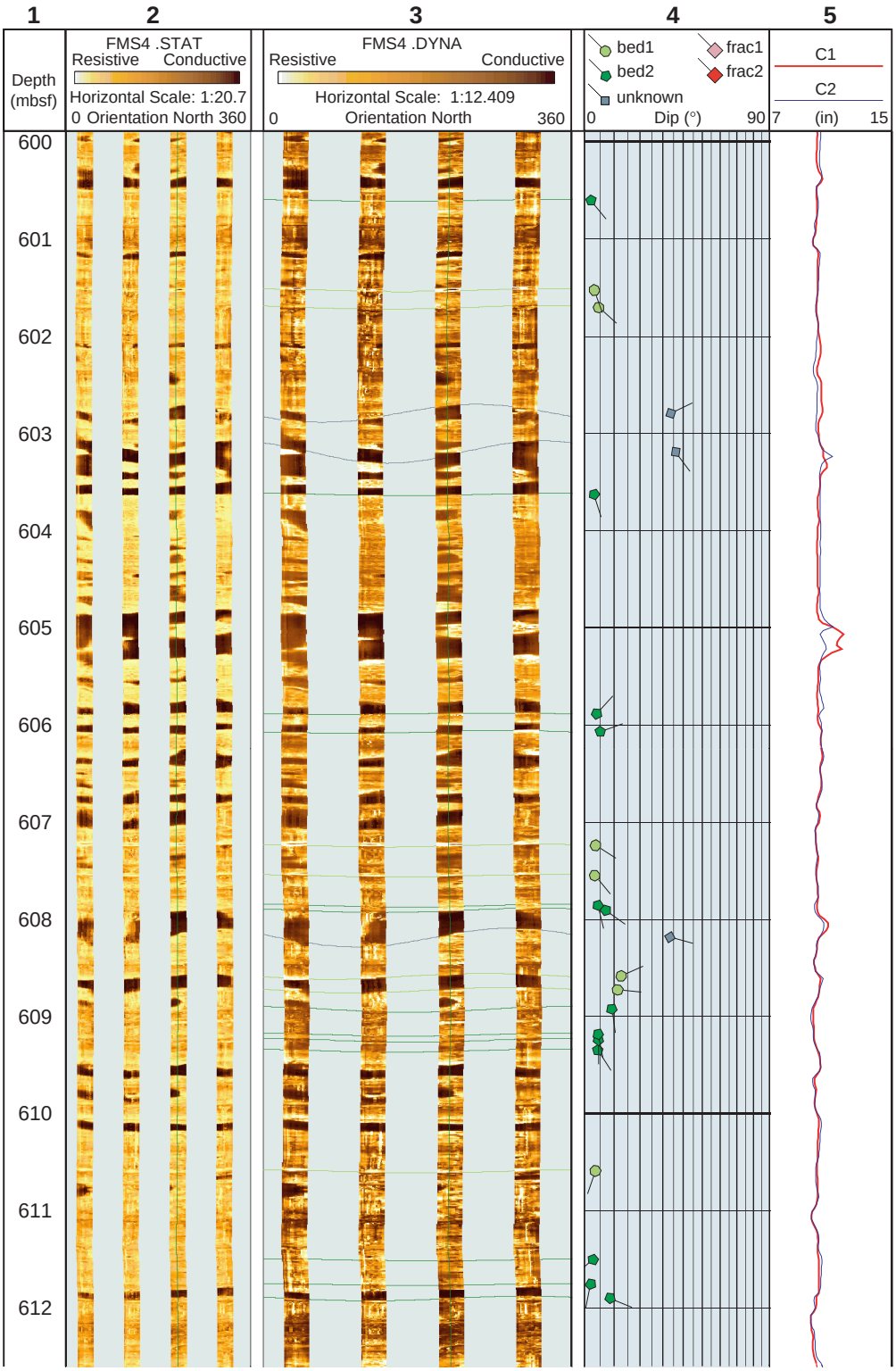

Figure F22. Structure orientations, Hole 1118A, 630–651 mbsf. Stereographic projection of poles to bed 1, bed 2, frac 2, and unknown structures (light green circles, darker green pentagons, red squares, and gray diamonds, respectively). Equal area stereographic projection, lower hemisphere. Strike and dip histograms of bedding only, where bed 1 and bed 2 are stacked with same color code as stereonet poles. Histograms use 5° bins. Strike is normalized so that the dip direction is 90° clockwise from strike. Neither fault nor unknown structure in this interval.

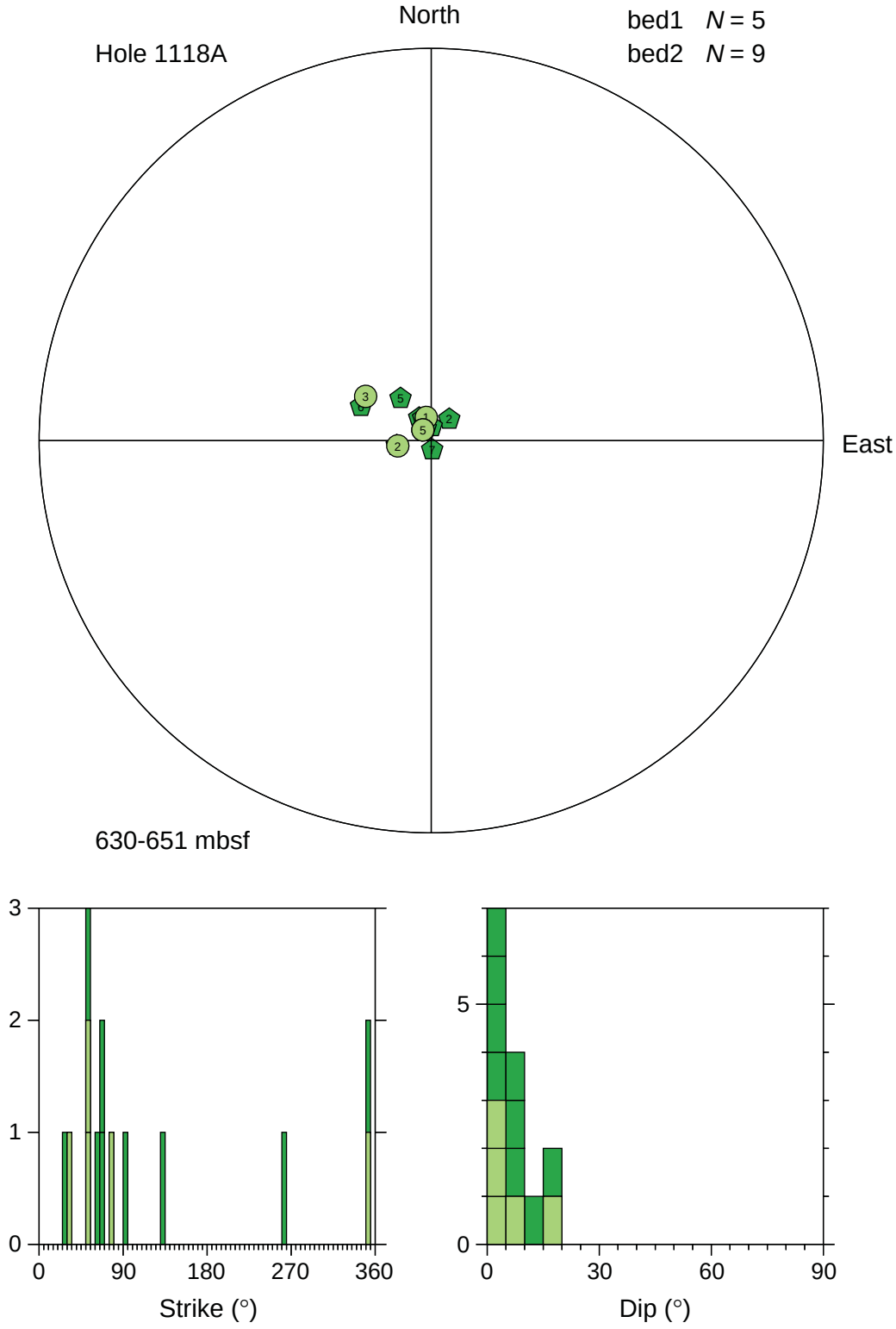

Figure F23. FMS image and analysis, Hole 1118A, 720–732.5 mbsf, reduced to ~70%. From left: (1) depth, (2) static FMS image, (3) dynamic FMS image with a 2-m color equalization sliding window; sinusoids correspond to the structural measurements, (4) structural measurement tadpoles, and (5) caliper measurements. The thin vertical green line on the FMS images indicates the orientation of pad 1, which corresponds to the C1 caliper reading. The tadpole position on the horizontal axis indicates the dip magnitude, and its tail points toward the dip direction.

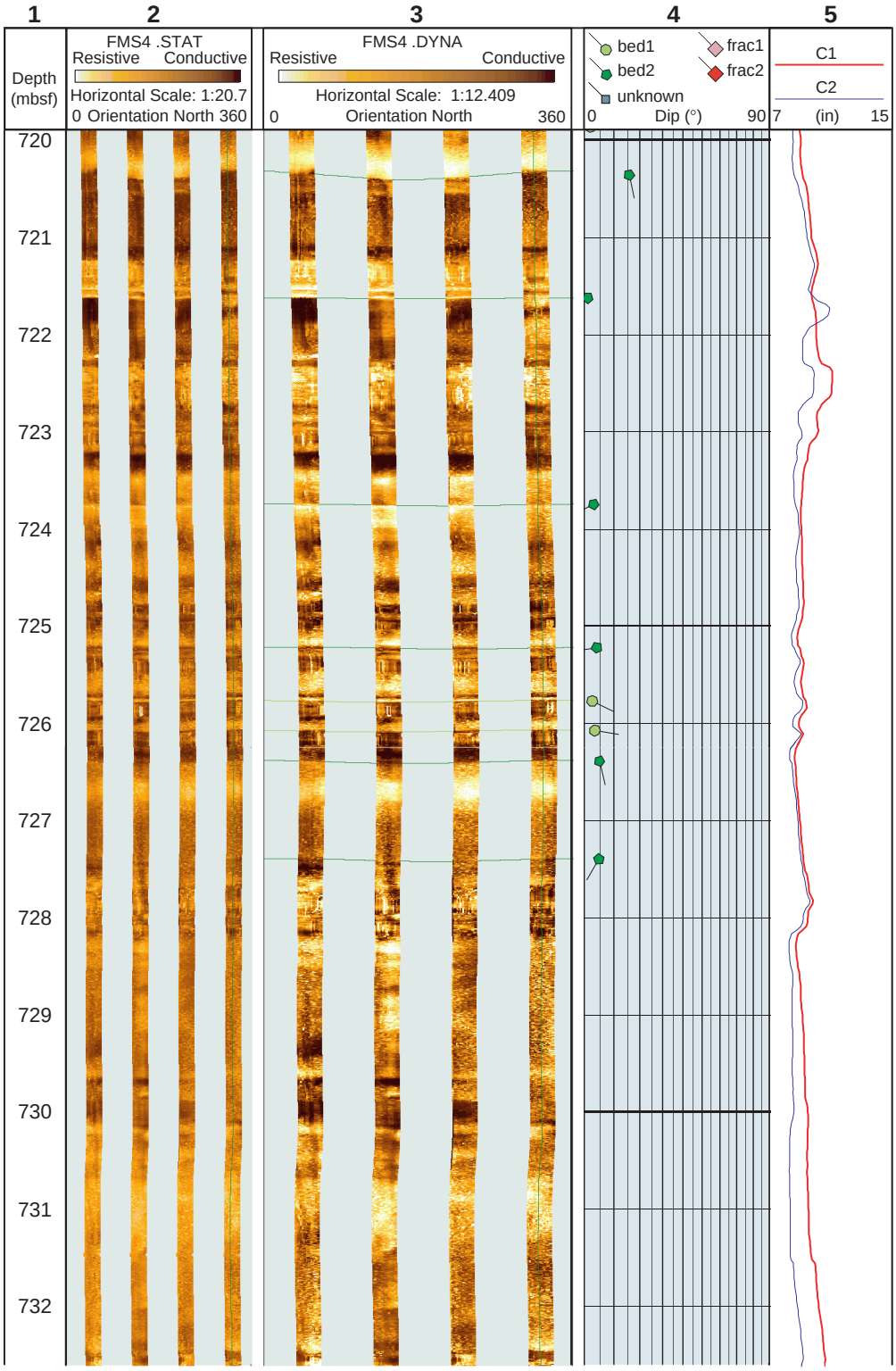

Figure F24. FMS image and analysis, Hole 1118A, 772–784.5 mbsf, reduced to ~70%. From left: (1) depth, (2) static FMS image, (3) dynamic FMS image with a 2-m color equalization sliding window; sinusoids correspond to the structural measurements, (4) structural measurement tadpoles, and (5) caliper measurements. The thin vertical green line on the FMS images indicates the orientation of pad 1, which corresponds to the C1 caliper reading. The tadpole position on the horizontal axis indicates the dip magnitude, and its tail points toward the dip direction.

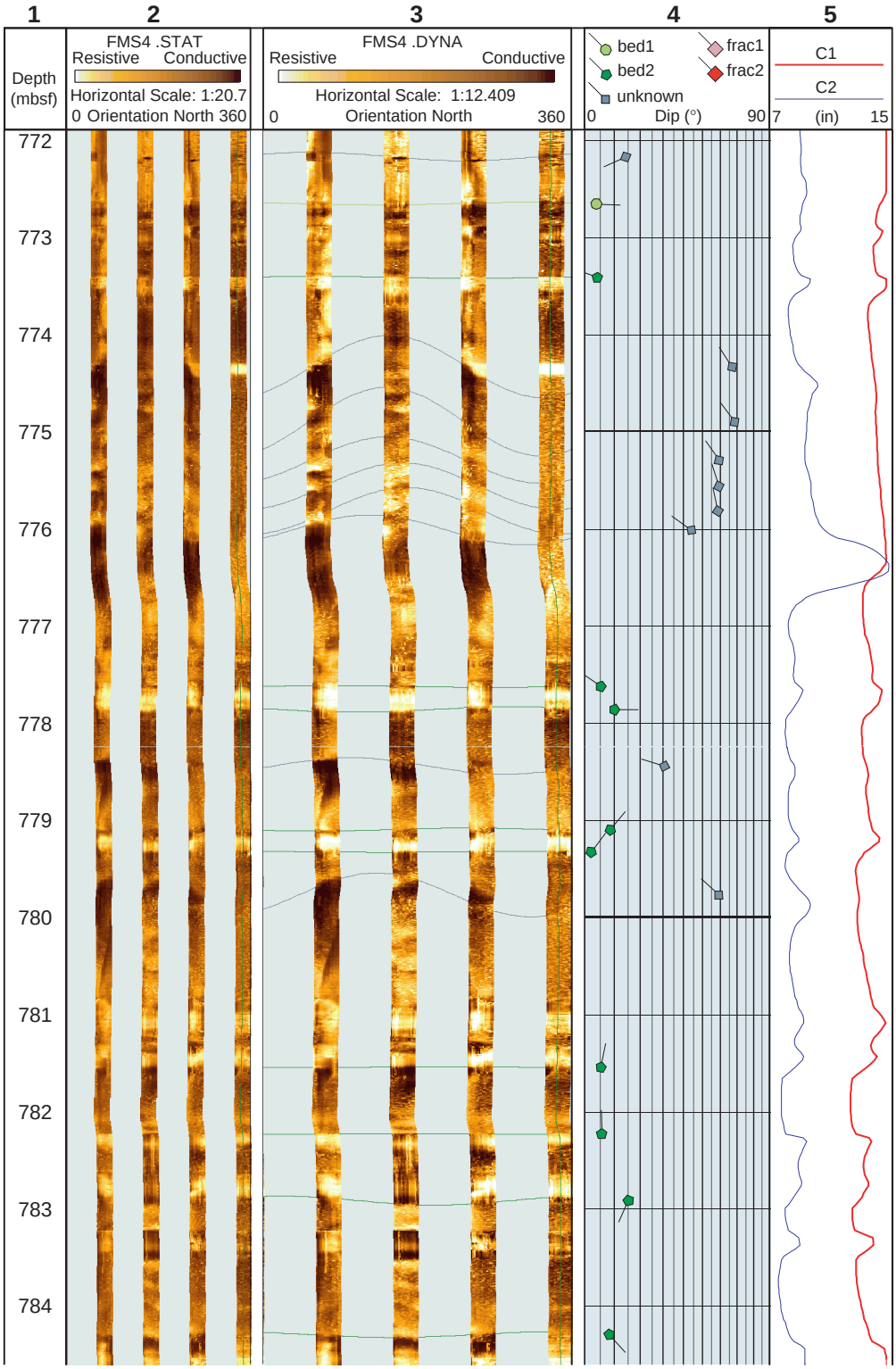

Figure F25. FMS image and analysis, Hole 1118A, 852–864.5 mbsf, reduced to ~70%. From left: (1) depth, (2) static FMS image, (3) dynamic FMS image with a 2-m color equalization sliding window; sinusoids correspond to the structural measurements, (4) structural measurement tadpoles, and (5) caliper measurements. The thin vertical green line on the FMS images indicates the orientation of pad 1, which corresponds to the C1 caliper reading. The tadpole position on the horizontal axis indicates the dip magnitude, and its tail points toward the dip direction.

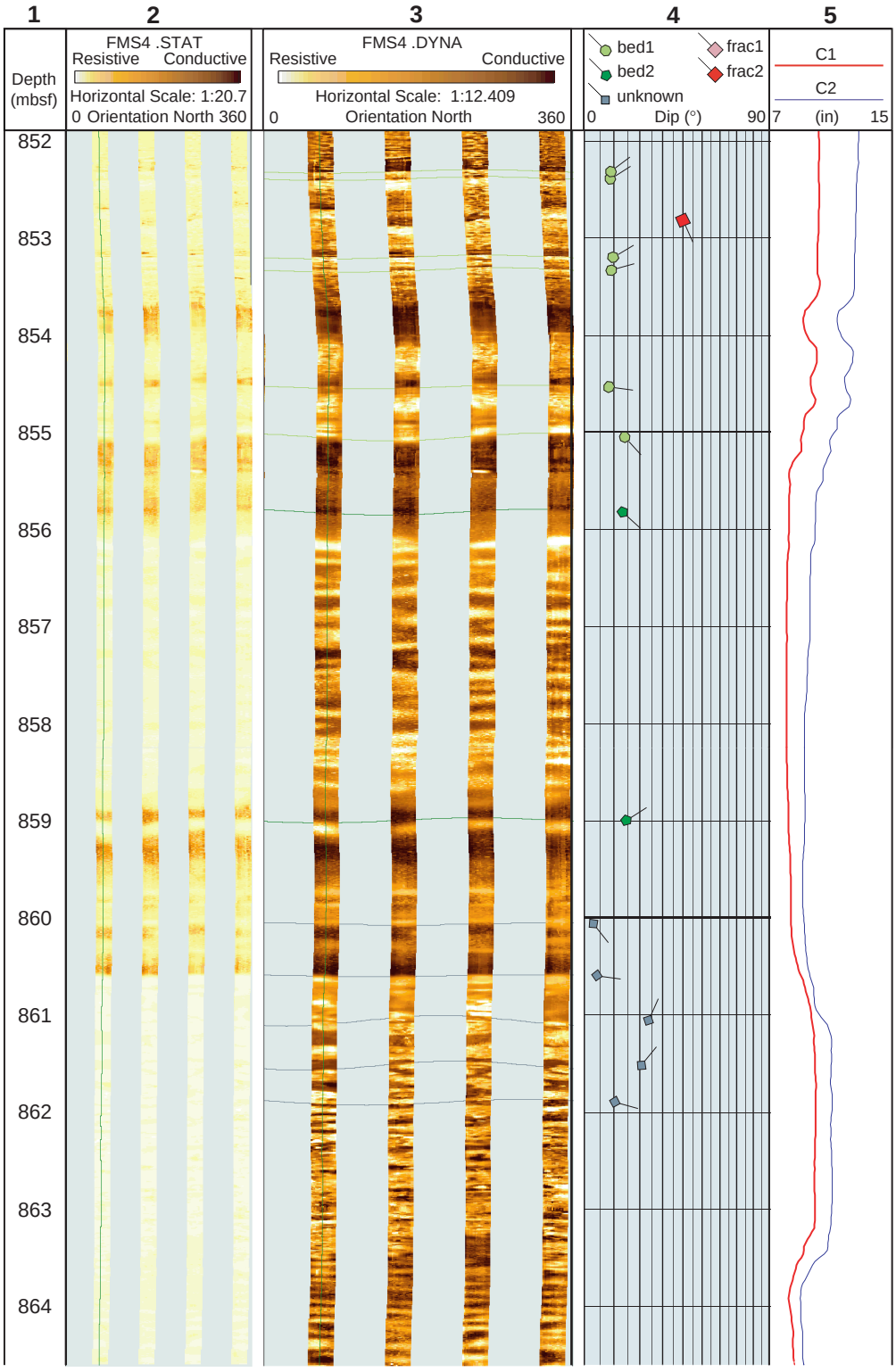

Figure F26. FMS image and analysis, Hole 1118A, 868–880.5 mbsf, reduced to ~70%. From left: (1) depth, (2) static FMS image, (3) dynamic FMS image with a 2-m color equalization sliding window; sinusoids correspond to the structural measurements, (4) structural measurement tadpoles, and (5) caliper measurements. The thin vertical green line on the FMS images indicates the orientation of pad 1, which corresponds to the C1 caliper reading. The tadpole position on the horizontal axis indicates the dip magnitude, and its tail points toward the dip direction.

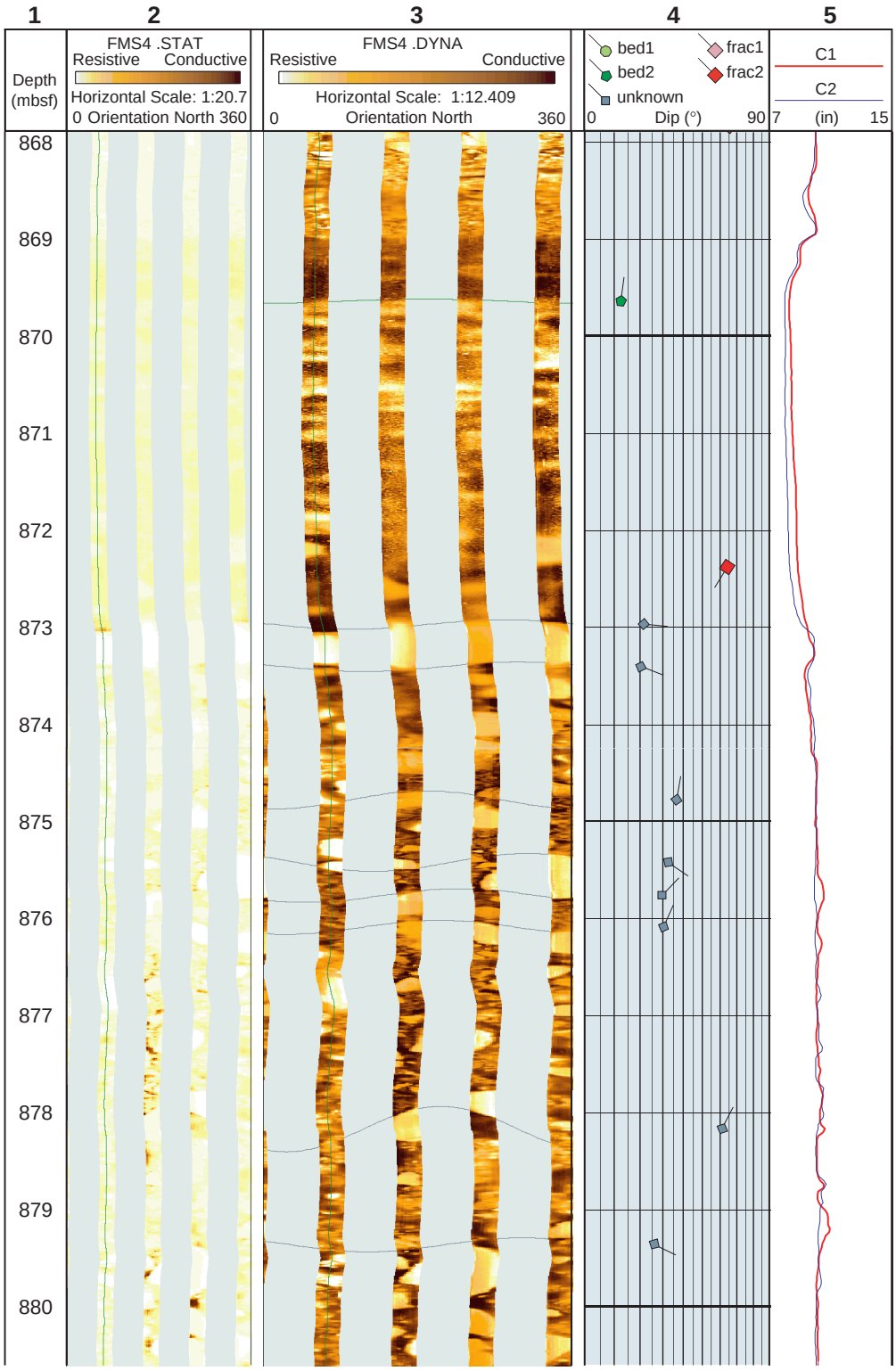

Figure F27. Structure orientations, Hole 1118A, 840–890 mbsf. Stereographic projection of poles to bed 1, bed 2, frac 2, and unknown structures (light green circles, darker green pentagons, red squares, and gray diamonds, respectively). Equal area stereographic projection, lower hemisphere. Strike and dip histograms of bedding only, where bed 1 and bed 2 are stacked with same color code as stereonet poles. Histograms use 5° bins. Strike is normalized so that the dip direction is 90° clockwise from strike. Fracture 4 is located at 853 mbsf. A partial 5° stereonet is shown in the background to highlight a cylindrical structure.

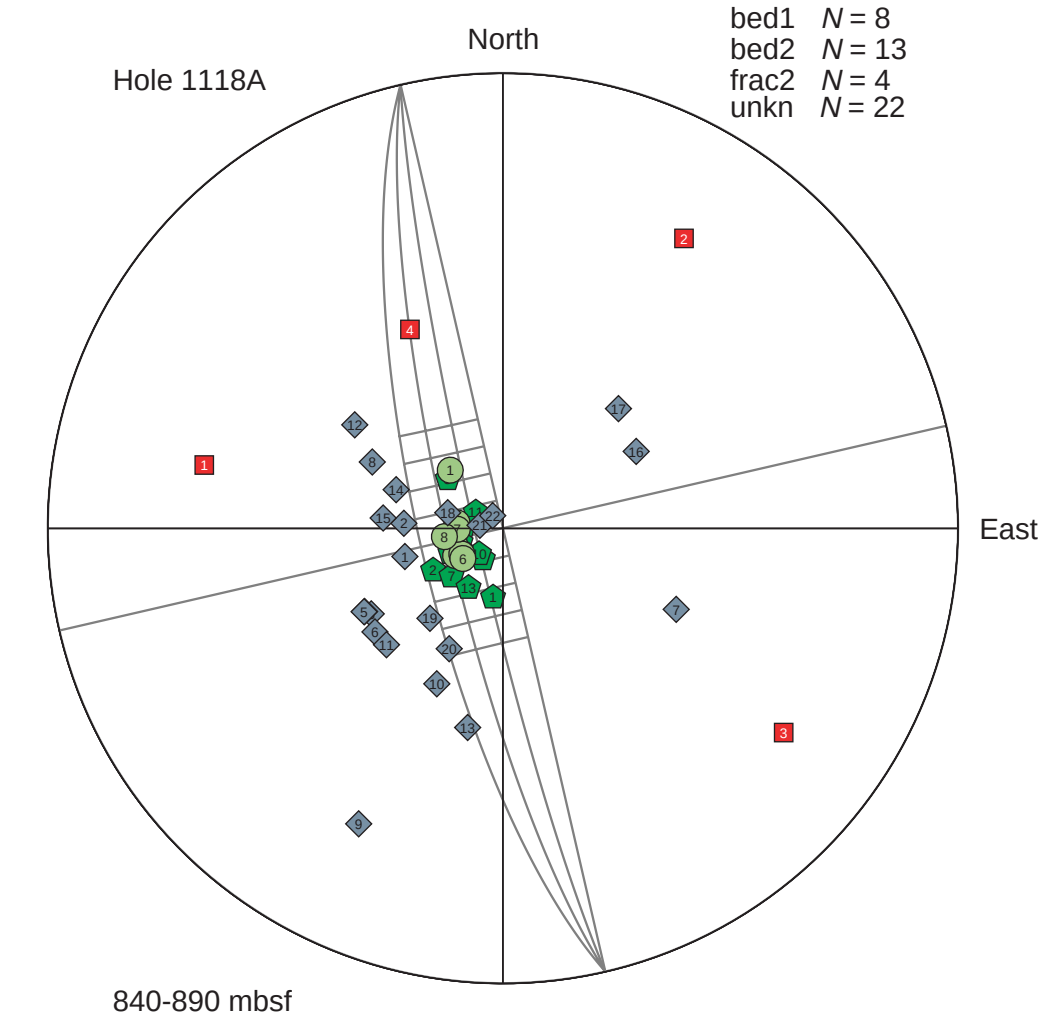

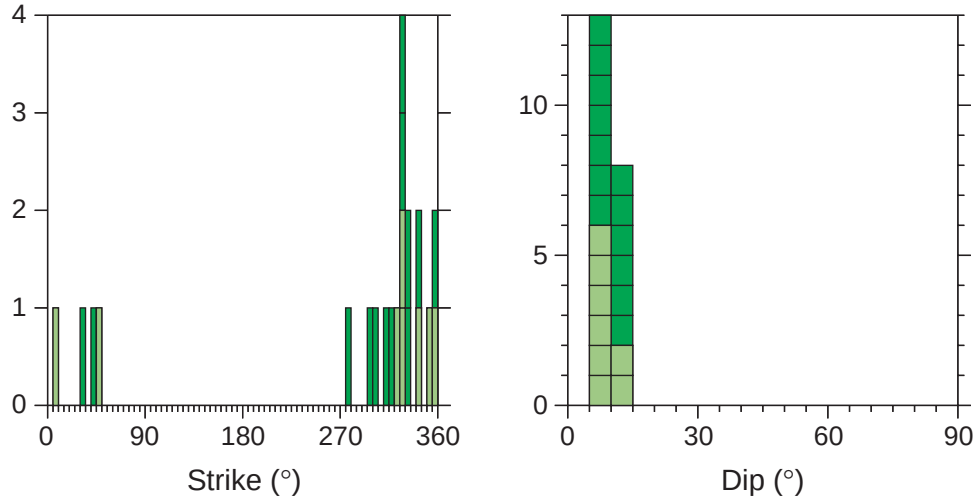

Figure F28. Composite log of Hole 1109D. From left: (1) core number, (2) core recovery, (3) depth, (4) static FMS image, (5) location of detailed FMS figures, (6) structural interpretation tadpoles, (7) depth intervals of detailed orientation plots, (8) lithologic units (summarized in Table T2, p. 112), (9) logging units, (10) structural domains, and (11) caliper measurements. The thin vertical green line on the FMS images indicates the orientation of pad 1 that corresponds to the C1 caliper reading. The tadpole position on the horizontal axis indicates the dip magnitude, and its tail points toward the dip direction. In the structure column (10), deformed zones are highlighted in pink. CID = core induced deformation. BD = boudinage, FZ = fracture zone. (Continued on next two pages.)

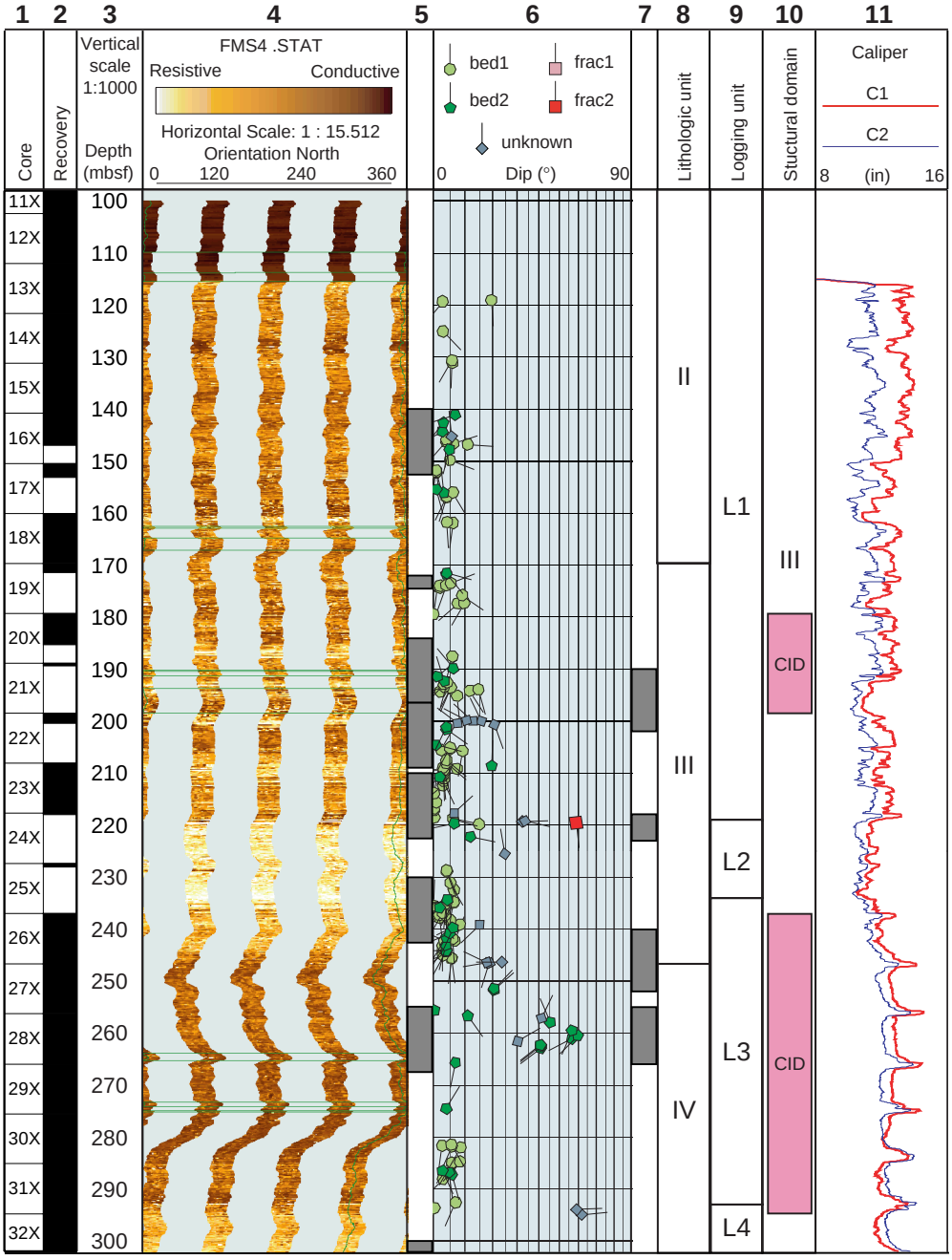

Figure F28 (continued).

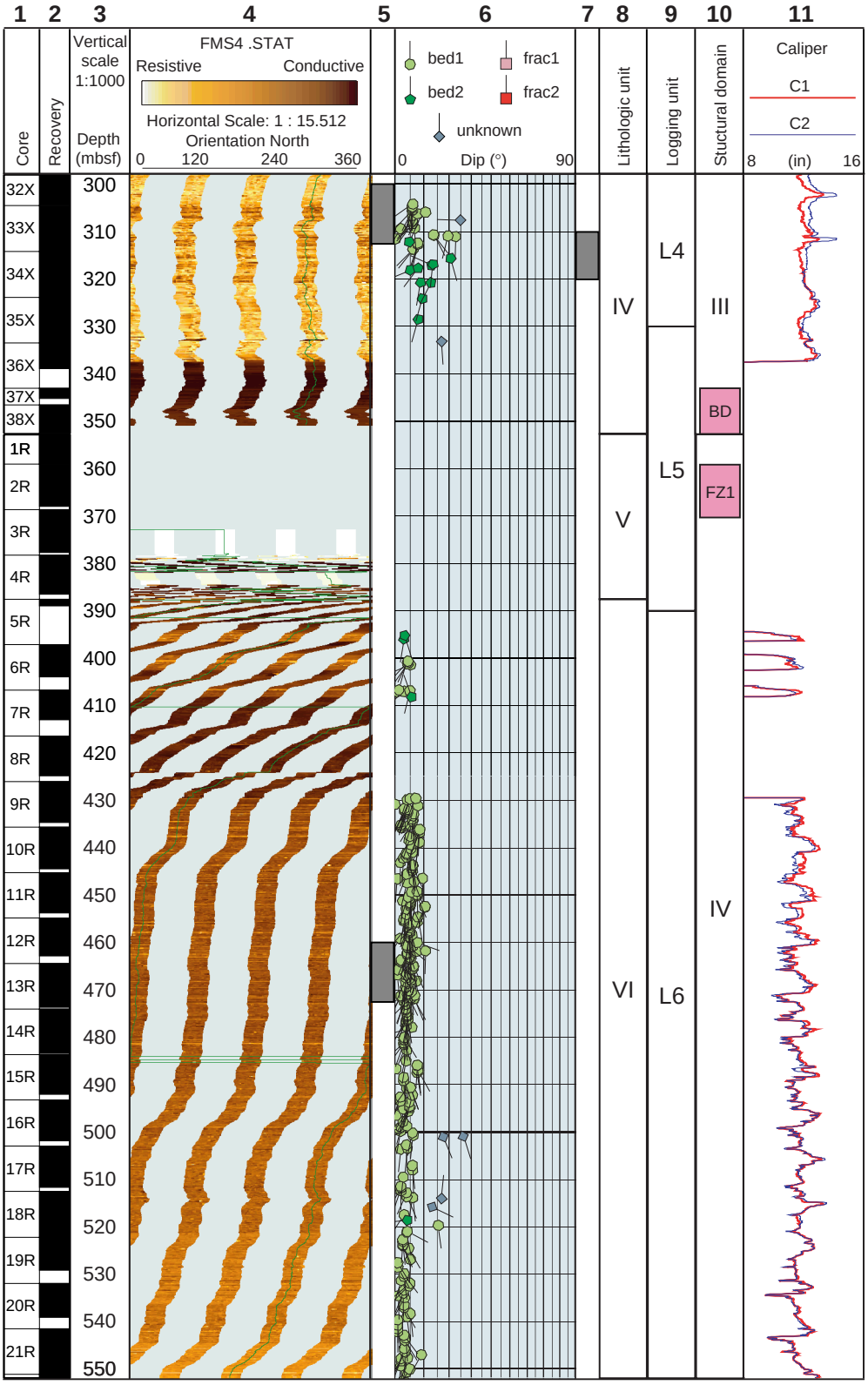

Figure F28 (continued).

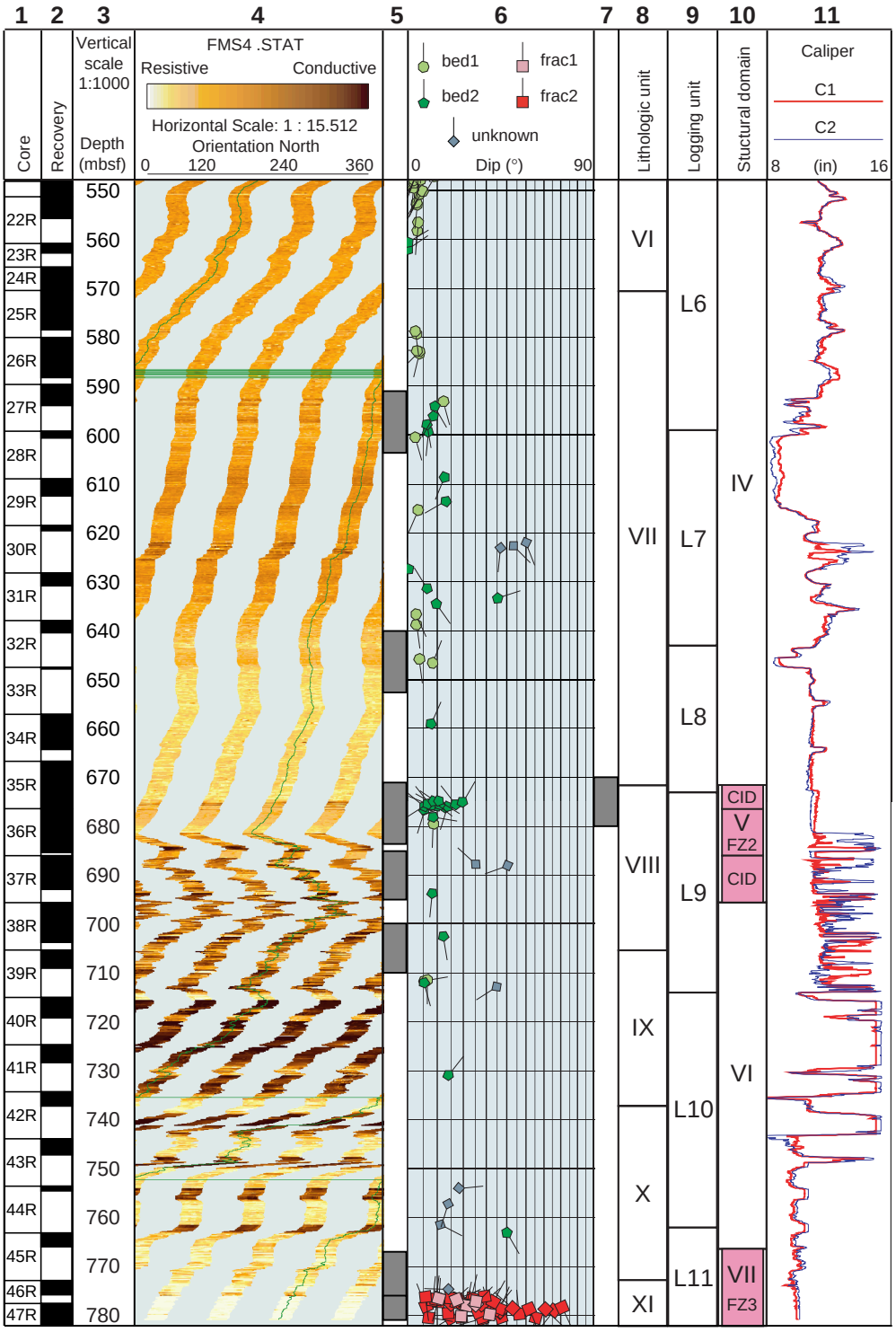

Figure F29. Hole 1109D global bed orientations. Equal area stereographic projection, lower hemisphere. Poles to bed 1 and bed 2 are shown as light green circles and darker green pentagons, respectively. Strike and dip histograms use 5° bins. Strike is normalized so that the dip direction is 90° clockwise from strike. Bed 1 and bed 2 histograms are stacked with same color code as stereonet poles.

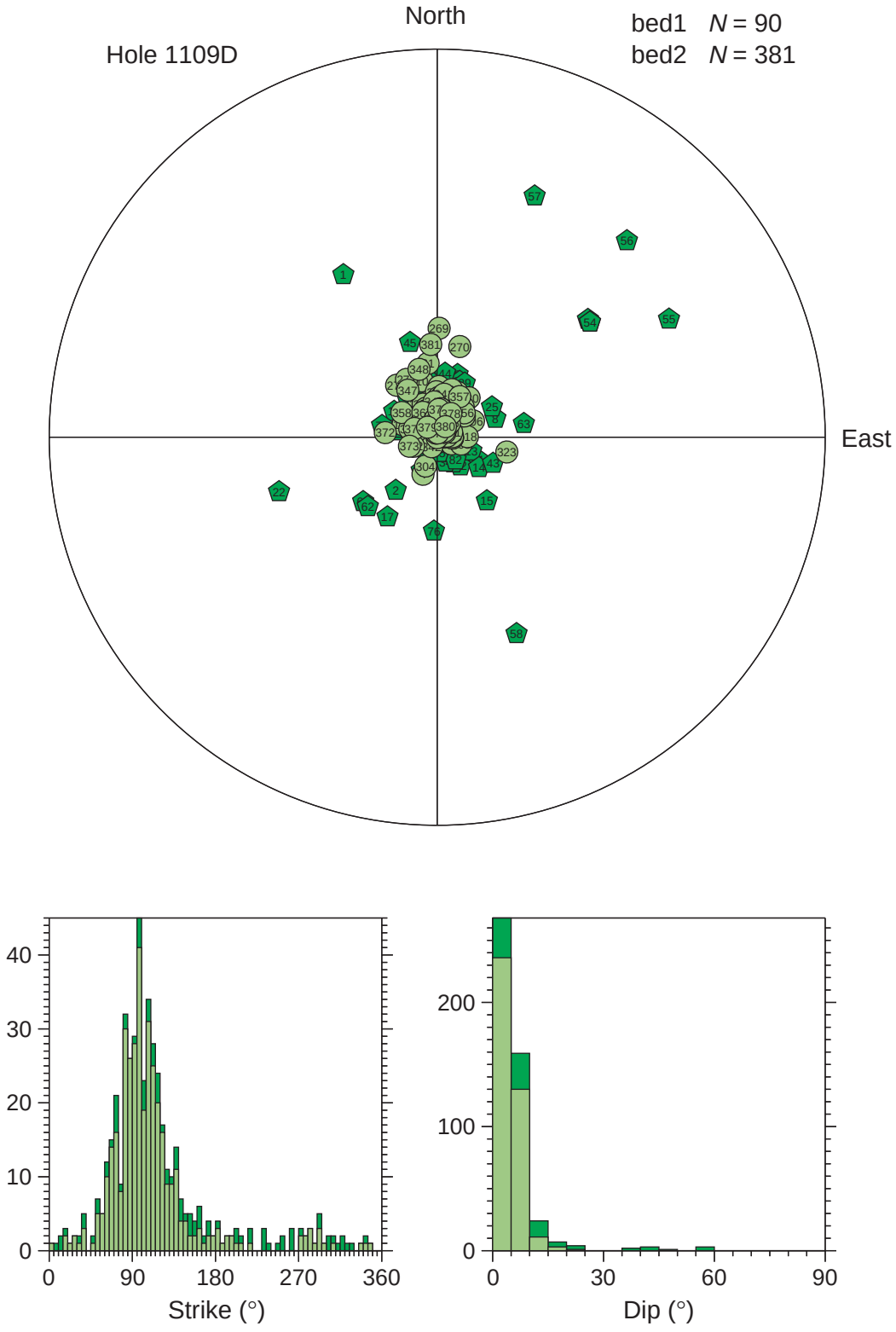

Figure F30. Hole 1109D global fracture orientations. Equal area stereographic projection, lower hemisphere. Poles to frac 1 and frac 2 are shown as pink and red squares, respectively. Strike and dip histograms use 5° bins. Strike is normalized so that the dip direction is 90° clockwise from strike. Frac 1 and frac 2 histograms are stacked with same color code as stereonet poles. All these fractures are located within the bottom dolerite (Fig. F28, p. 57) except that labeled #37 (orange), which is within the sediments at 220 mbsf (Fig. F28, p. 55) and belongs to the frac 2 set.

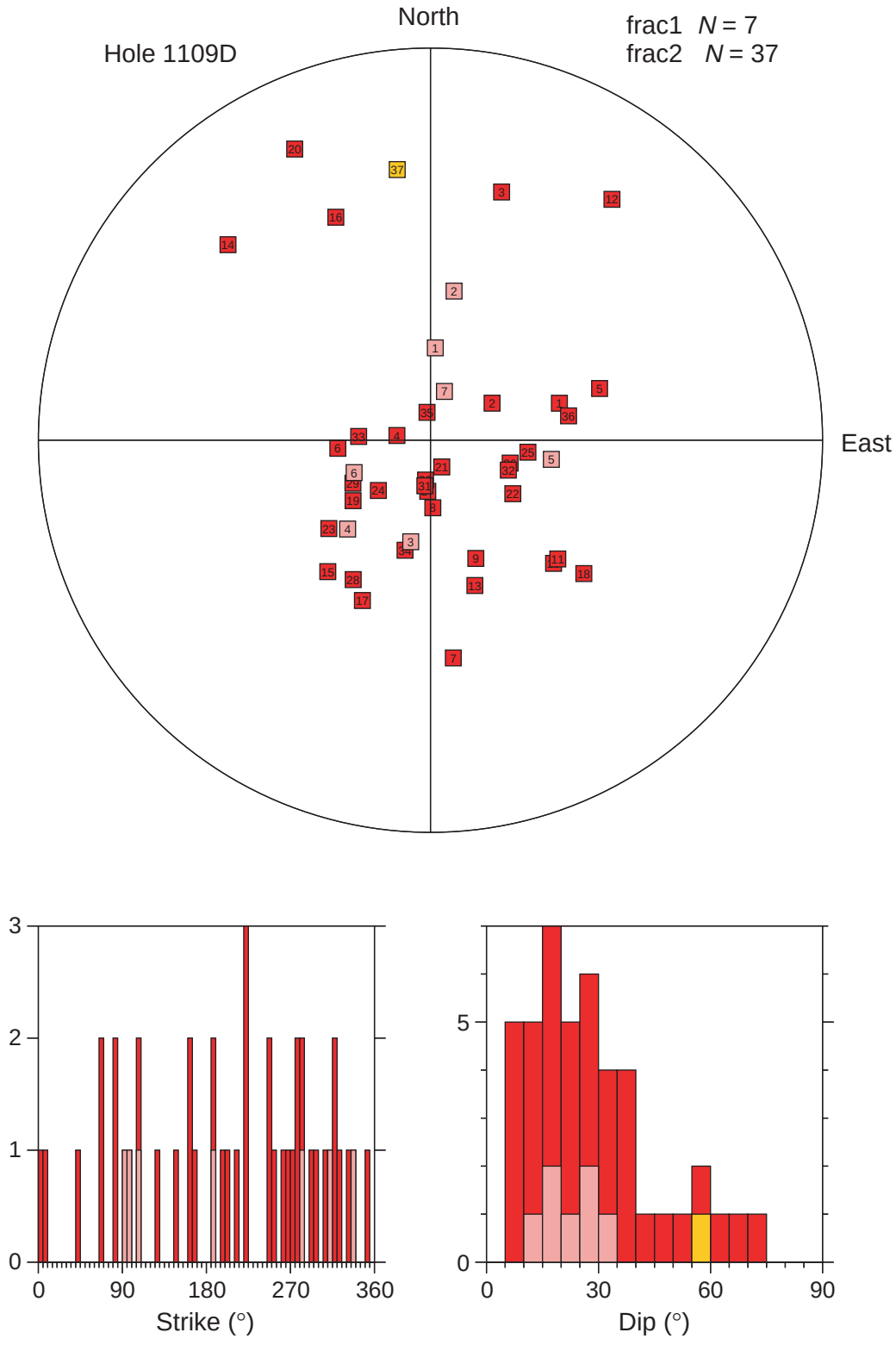

Figure F31. Hole 1109D global unknown planar structure orientations. Equal area stereographic projection, lower hemisphere. Poles are shown as gray diamonds. Strike and dip histograms use 5° bins. Strike is normalized so that the dip direction is 90° clockwise from strike.

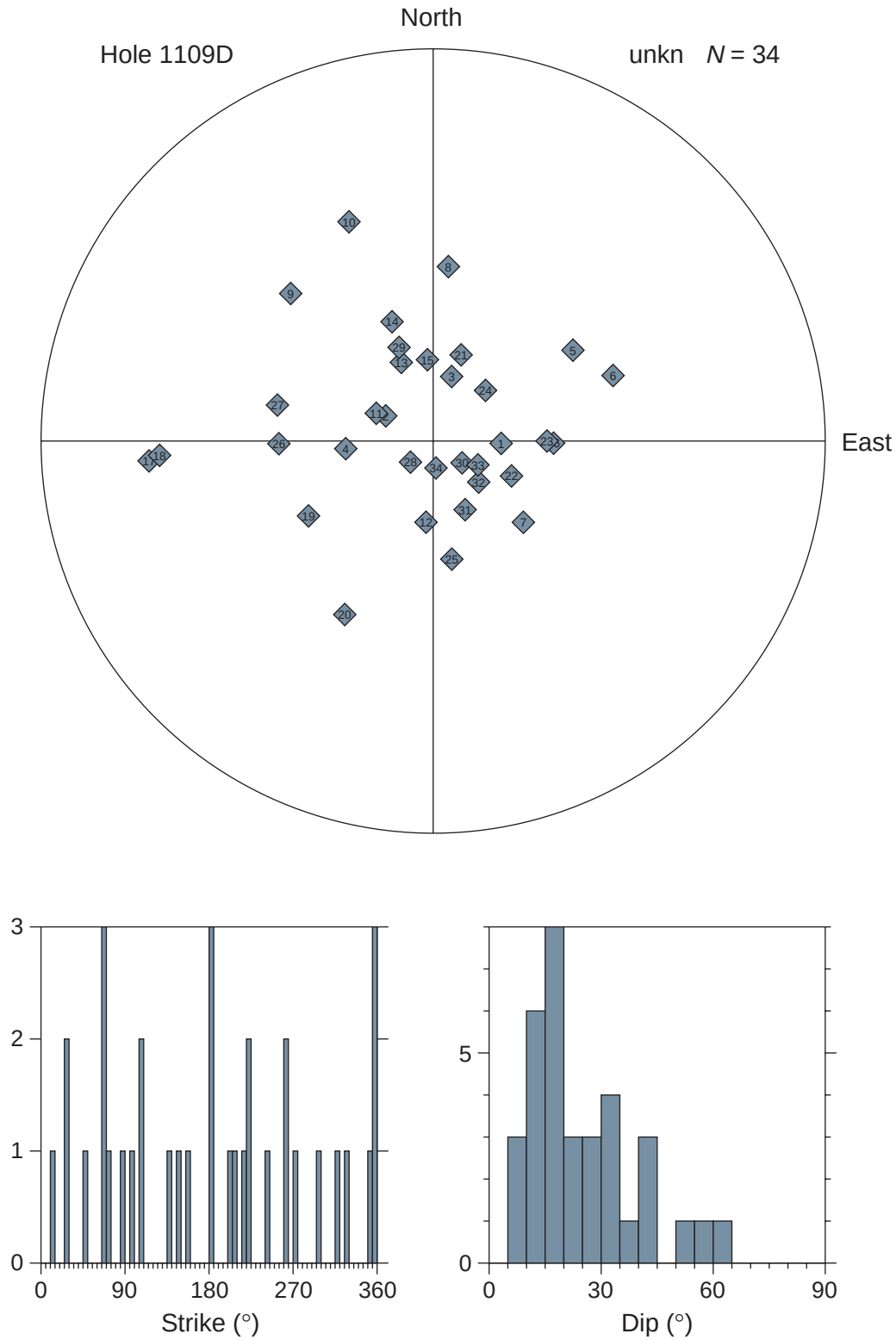

Figure F32. FMS image and analysis, Hole 1109D, 140–152.5 mbsf, reduced to ~70%. From left: (1) depth, (2) static FMS image, (3) dynamic FMS image with a 2-m color equalization sliding window; sinusoids correspond to the structural measurements, (4) structural measurement tadpoles, and (5) caliper measurements. The thin vertical green line on the FMS images indicates the orientation of pad 1, which corresponds to the C1 caliper reading. The tadpole position on the horizontal axis indicates the dip magnitude, and its tail points toward the dip direction.

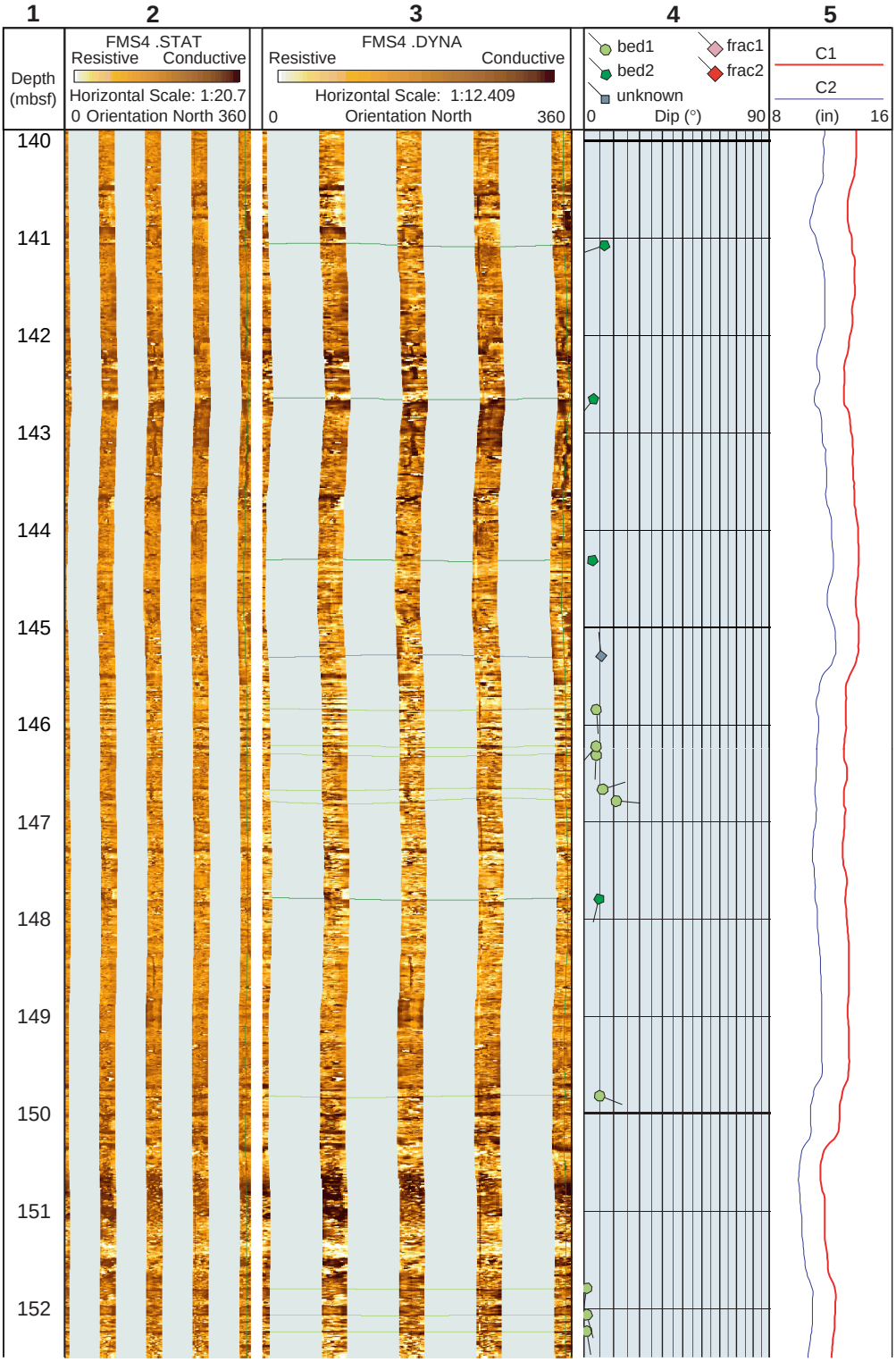

Figure F33. FMS image and analysis, Hole 1109D, 172–174.5 mbsf, reduced to ~70%. From left: (1) depth, (2) static FMS image, (3) dynamic FMS image with a 2-m color equalization sliding window; sinusoids correspond to the structural measurements, (4) structural measurement tadpoles, and (5) caliper measurements. The thin vertical green line on the FMS images indicates the orientation of pad 1, which corresponds to the C1 caliper reading. The tadpole position on the horizontal axis indicates the dip magnitude, and its tail points toward the dip direction.

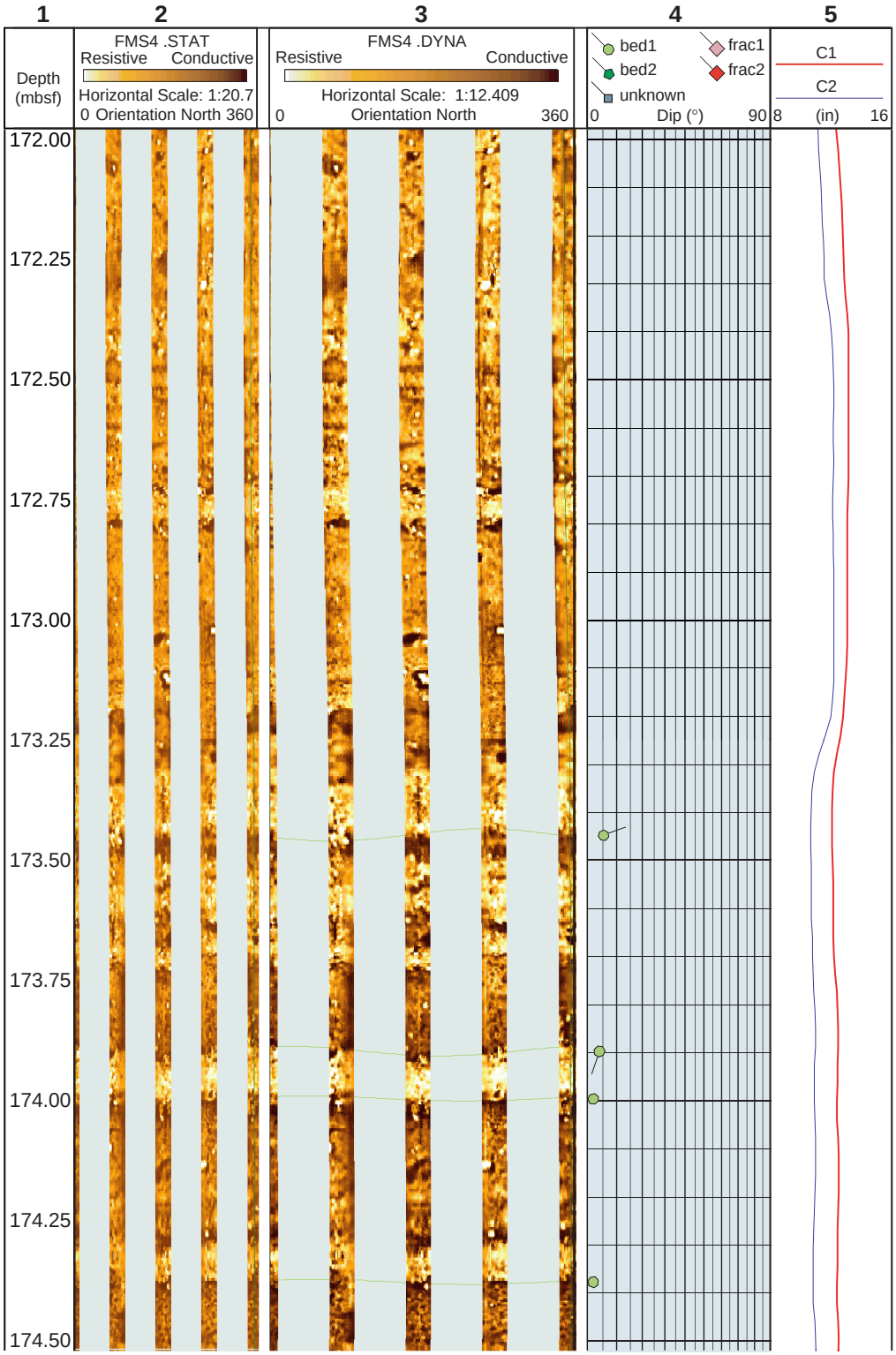

Figure F34. FMS image and analysis, Hole 1109D, 184–196.5 mbsf, reduced to ~70%. From left: (1) depth, (2) static FMS image, (3) dynamic FMS image with a 2-m color equalization sliding window; sinusoids correspond to the structural measurements, (4) structural measurement tadpoles, and (5) caliper measurements. The thin vertical green line on the FMS images indicates the orientation of pad 1, which corresponds to the C1 caliper reading. The tadpole position on the horizontal axis indicates the dip magnitude, and its tail points toward the dip direction.

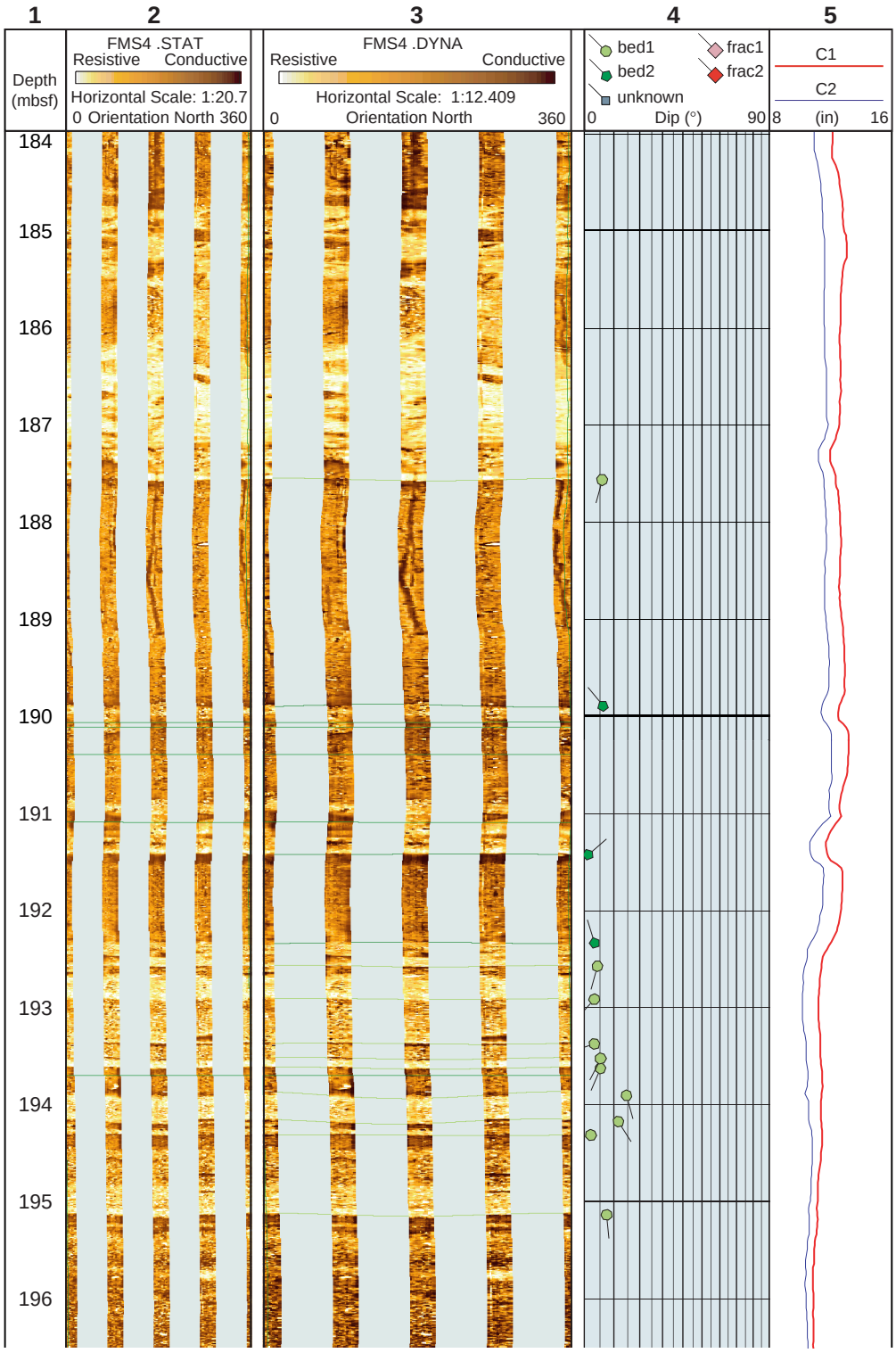

Figure F35. FMS image and analysis, Hole 1109D, 196.5–209 mbsf, reduced to ~70%. From left: (1) depth, (2) static FMS image, (3) dynamic FMS image with a 2-m color equalization sliding window; sinusoids correspond to the structural measurements, (4) structural measurement tadpoles, and (5) caliper measurements. The thin vertical green line on the FMS images indicates the orientation of pad 1, which corresponds to the C1 caliper reading. The tadpole position on the horizontal axis indicates the dip magnitude, and its tail points toward the dip direction.

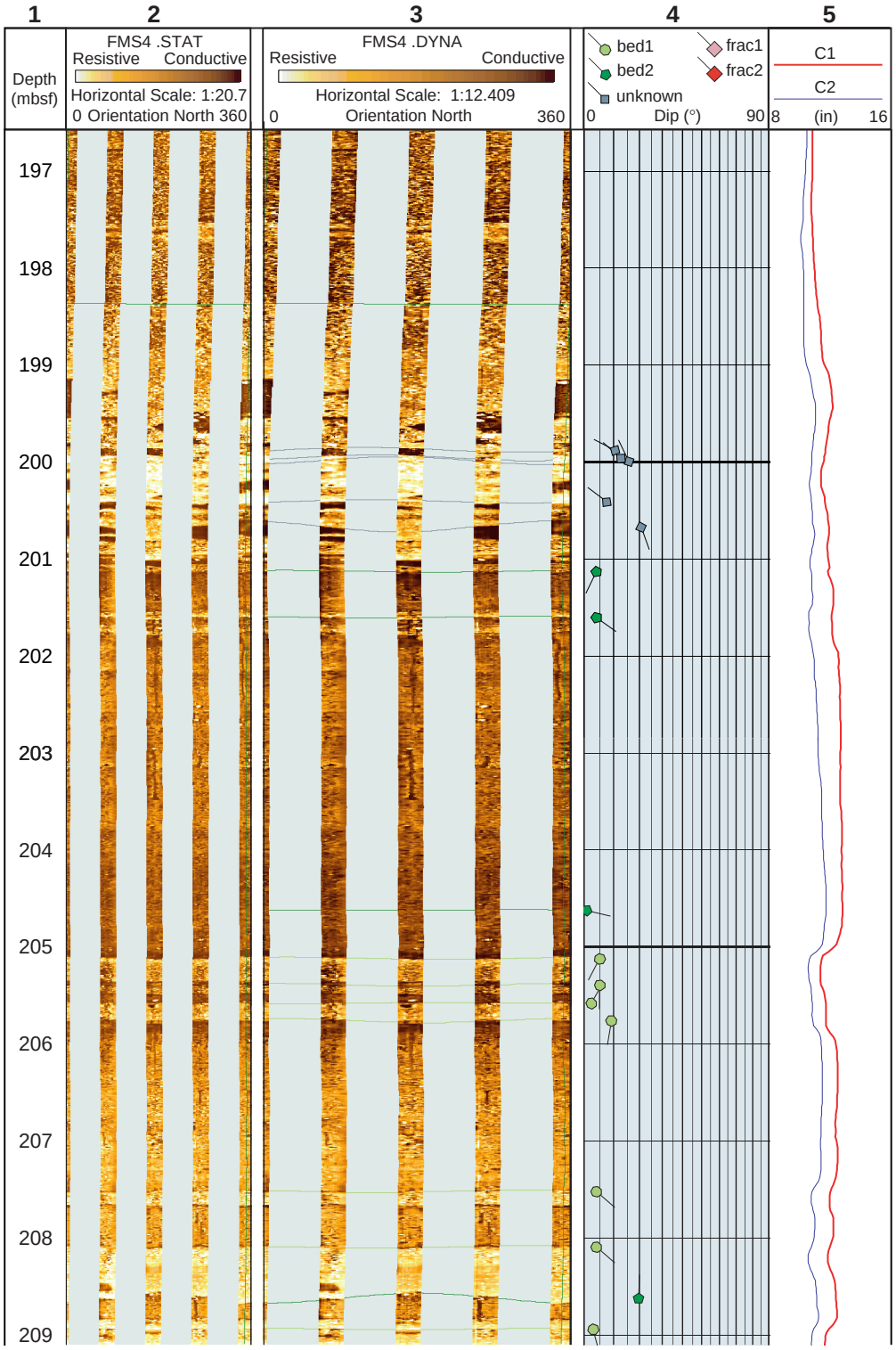

Figure F36. Structure orientations, Hole 1109D, 190–202 mbsf. Stereographic projection of poles to bed 1, bed 2, frac 2, and unknown structures (light green circles, darker green pentagons, red squares, and gray diamonds, respectively). Equal area stereographic projection, lower hemisphere. Strike and dip histograms of bedding only, where bed 1 and bed 2 are stacked with same color code as stereonet poles. Histograms use 5° bins. Strike is normalized so that the dip direction is 90° clockwise from strike. A partial 5° stereonet is shown in the background to highlight a cylindrical structure.

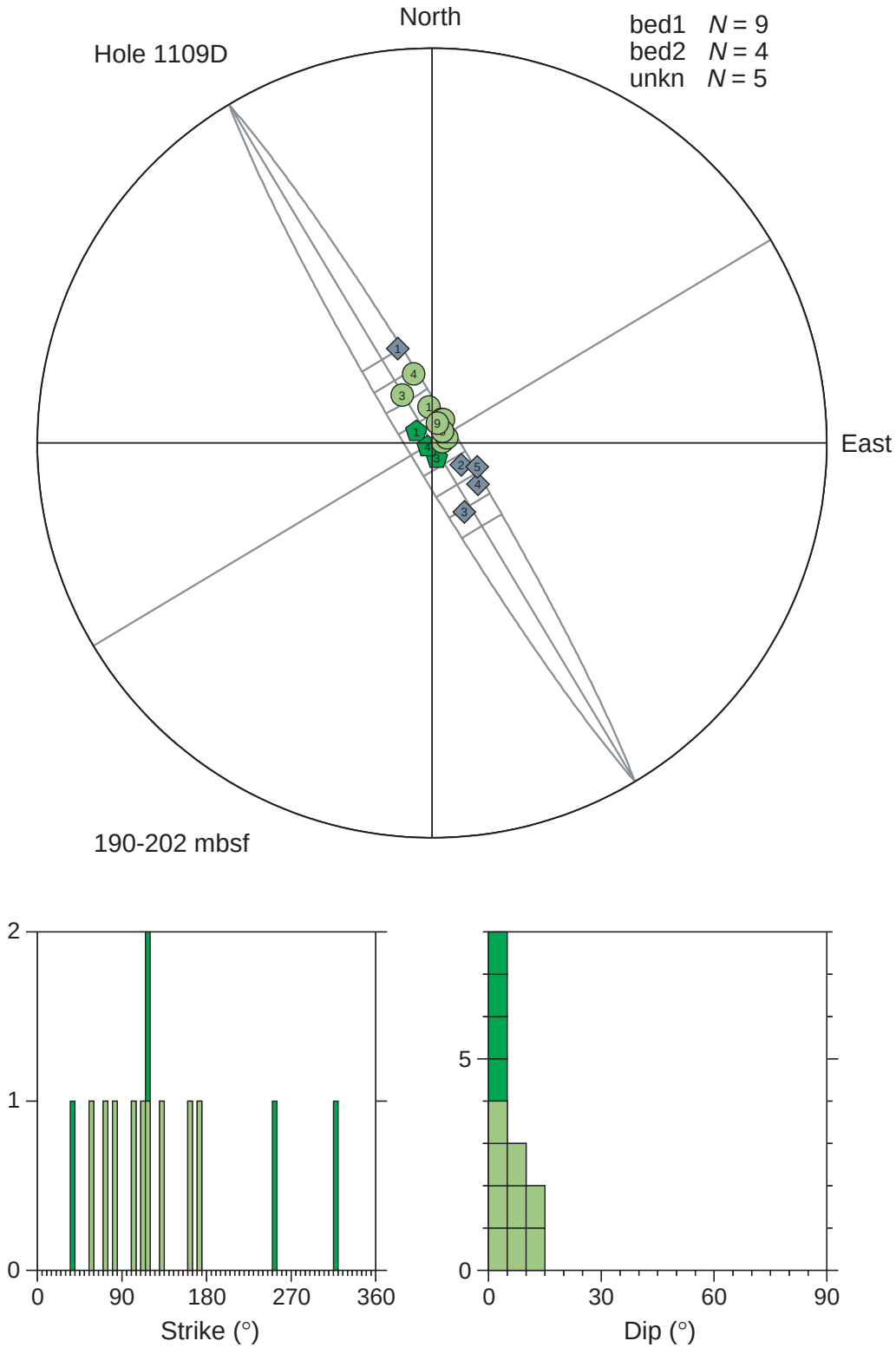

Figure F37. FMS image and analysis, Hole 1109D, 210–222.5 mbsf, reduced to ~70%. From left: (1) depth, (2) static FMS image, (3) dynamic FMS image with a 2-m color equalization sliding window; sinusoids correspond to the structural measurements, (4) structural measurement tadpoles, and (5) caliper measurements. The thin vertical green line on the FMS images indicates the orientation of pad 1, which corresponds to the C1 caliper reading. The tadpole position on the horizontal axis indicates the dip magnitude, and its tail points toward the dip direction.

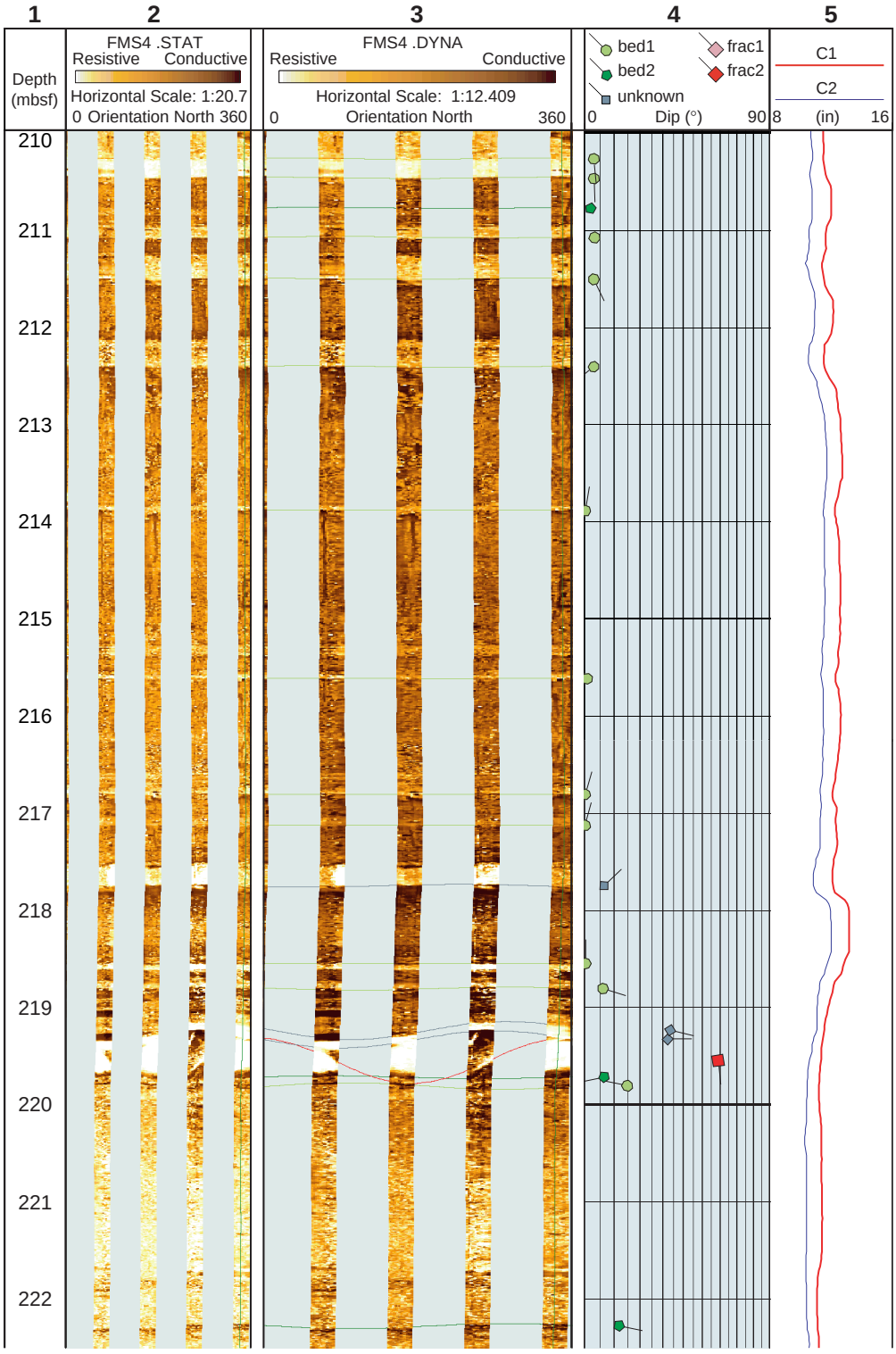

Figure F38. FMS image and analysis, Hole 1109D, 230–242.5 mbsf, reduced to ~70%. From left: (1) depth, (2) static FMS image, (3) dynamic FMS image with a 2-m color equalization sliding window; sinusoids correspond to the structural measurements, (4) structural measurement tadpoles, and (5) caliper measurements. The thin vertical green line on the FMS images indicates the orientation of pad 1, which corresponds to the C1 caliper reading. The tadpole position on the horizontal axis indicates the dip magnitude, and its tail points toward the dip direction.

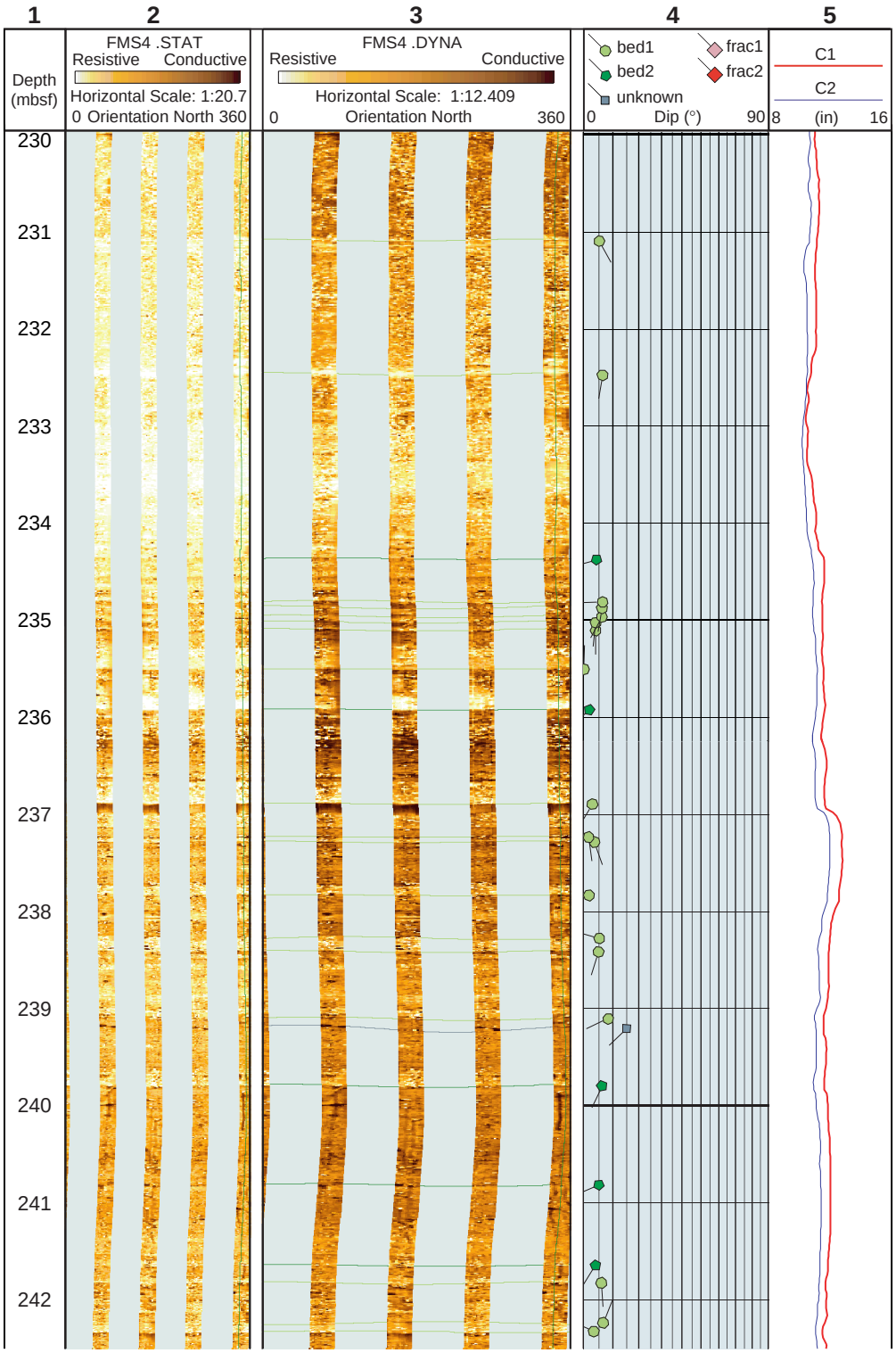

Figure F39. Structure orientations, Hole 1109D, 218–223 mbsf. Stereographic projection of poles to bed 1, bed 2, frac 2, and unknown structures (light green circles, darker green pentagons, red squares, and gray diamonds, respectively). Equal area stereographic projection, lower hemisphere. Strike and dip histograms of bedding only, where bed 1 and bed 2 are stacked with same color code as stereonet poles. Histograms use 5° bins. Strike is normalized so that the dip direction is 90° clockwise from strike. A partial 5° stereonet is shown in the background to highlight a cylindrical structure.

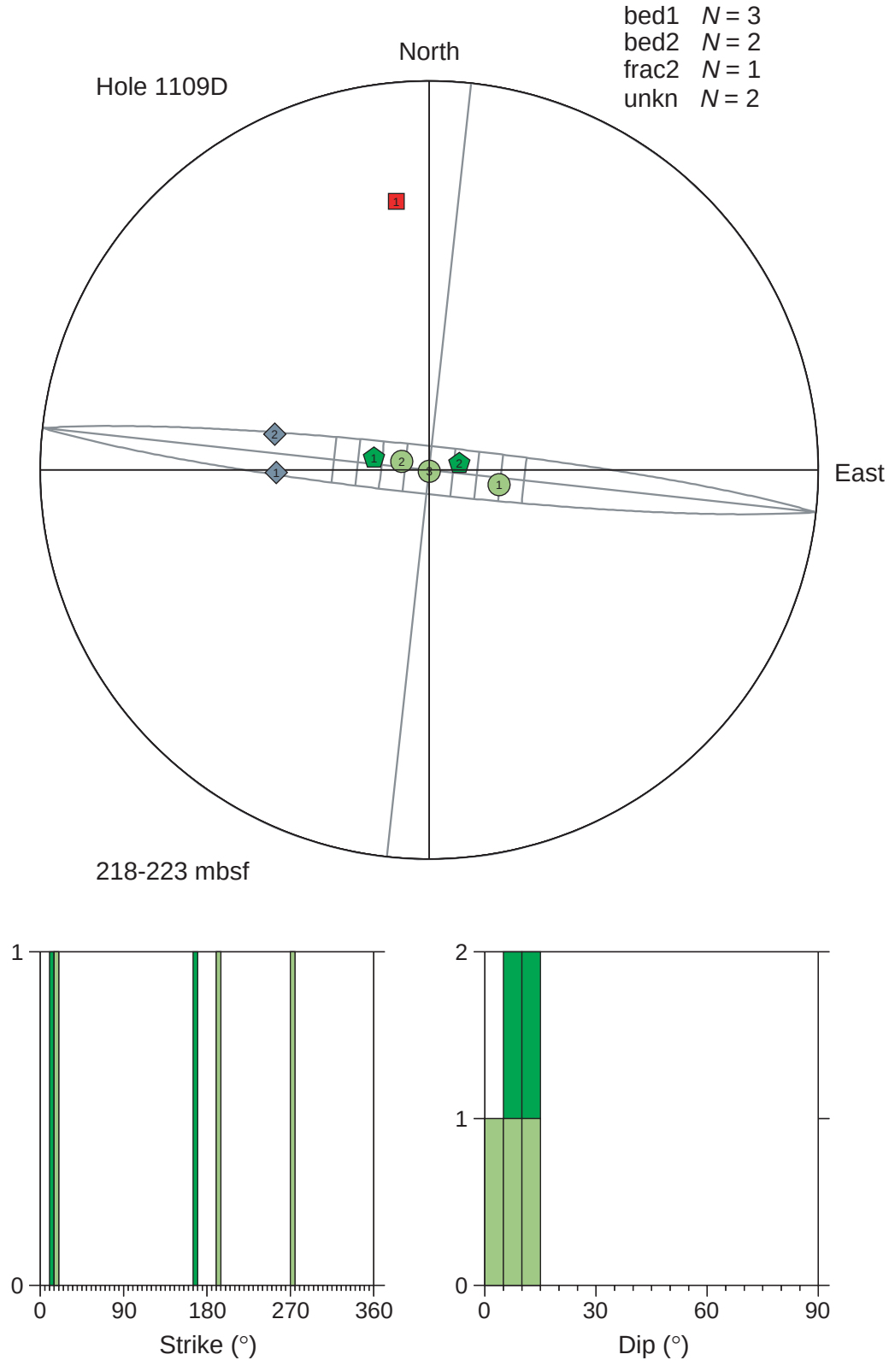

Figure F40. FMS image and analysis, Hole 1109D, 255–267.5 mbsf, reduced to ~70%. From left: (1) depth, (2) static FMS image, (3) dynamic FMS image with a 2-m color equalization sliding window; sinusoids correspond to the structural measurements, (4) structural measurement tadpoles, and (5) caliper measurements. The thin vertical green line on the FMS images indicates the orientation of pad 1, which corresponds to the C1 caliper reading. The tadpole position on the horizontal axis indicates the dip magnitude, and its tail points toward the dip direction.

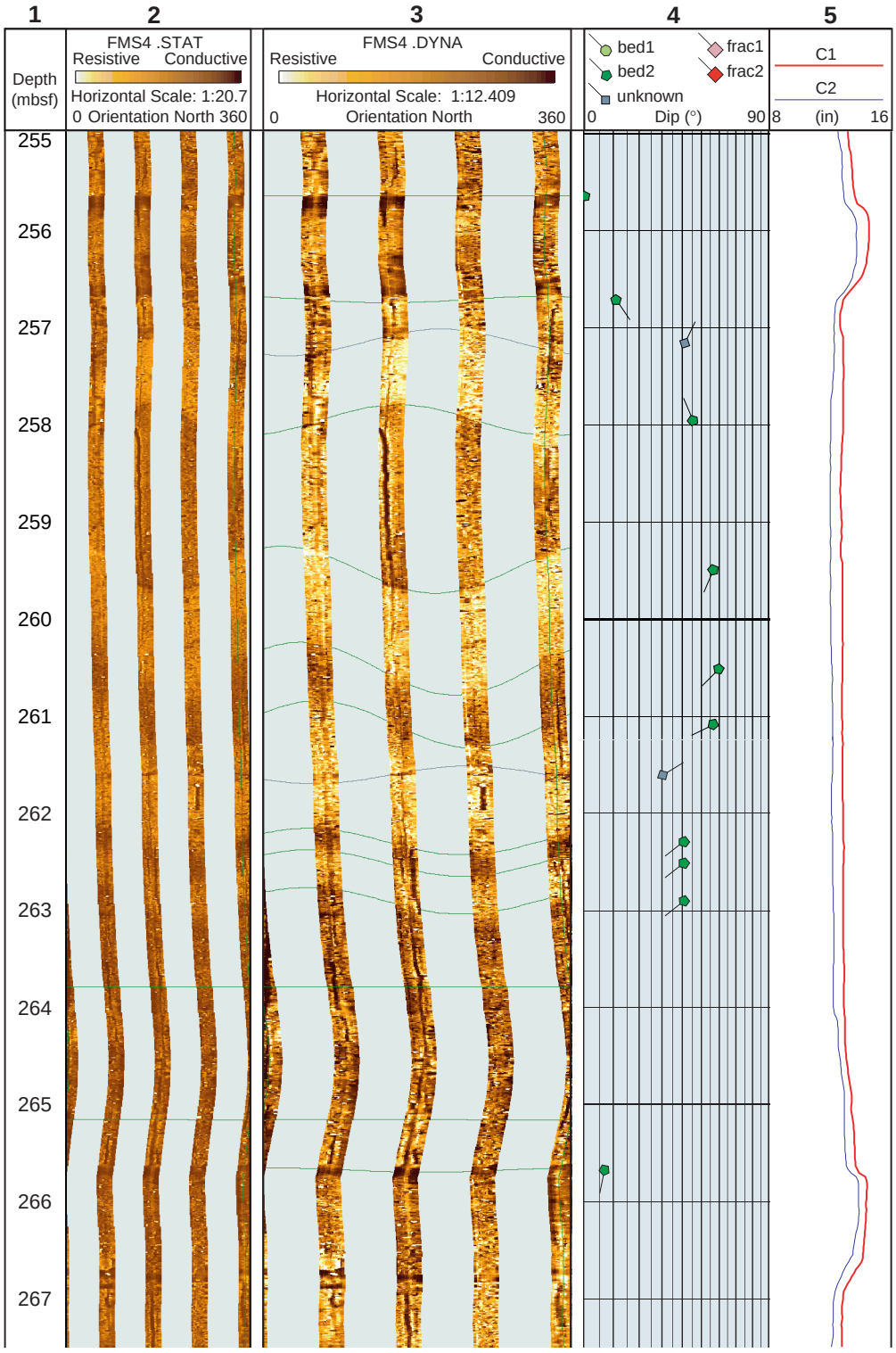

Figure F41. Structure orientations, Hole 1109D, 240–252 mbsf. Stereographic projection of poles to bed 1, bed 2, frac 2, and unknown structures (light green circles, darker green pentagons, red squares, and gray diamonds, respectively). Equal area stereographic projection, lower hemisphere. Strike and dip histograms of bedding only, where bed 1 and bed 2 are stacked with same color code as stereonet poles. Histograms use 5° bins. Strike is normalized so that the dip direction is 90° clockwise from strike. A partial 5° stereonet is shown in the background to highlight a cylindrical structure.

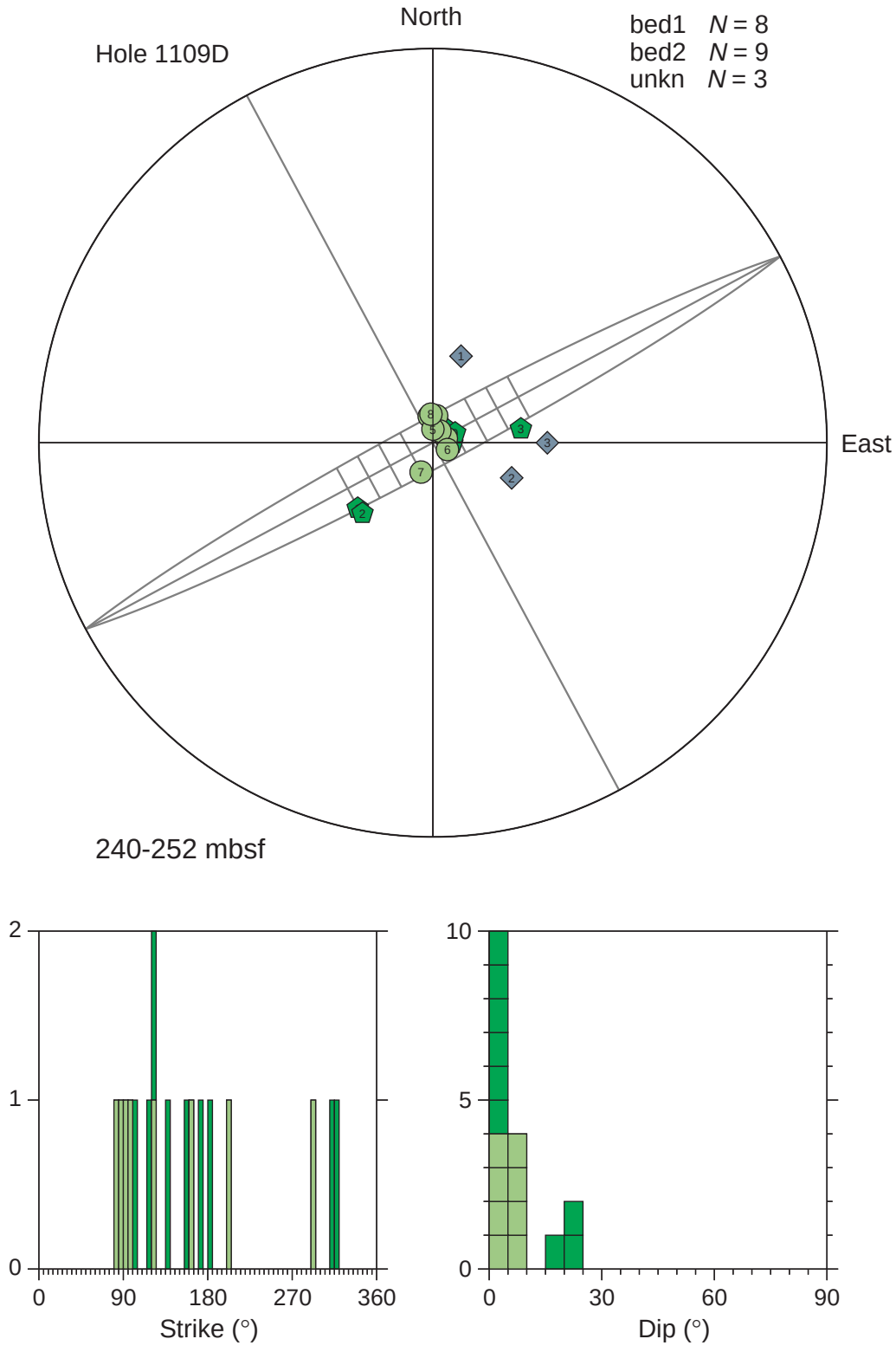

Figure F42. Structure orientations, Hole 1109D, 255–266 mbsf. Stereographic projection of poles to bed 1, bed 2, frac 2, and unknown structures (light green circles, darker green pentagons, red squares, and gray diamonds, respectively). Equal area stereographic projection, lower hemisphere. Strike and dip histograms of bedding only, where bed 1 and bed 2 are stacked with same color code as stereonet poles. Histograms use 5° bins. Strike is normalized so that the dip direction is 90° clockwise from strike.

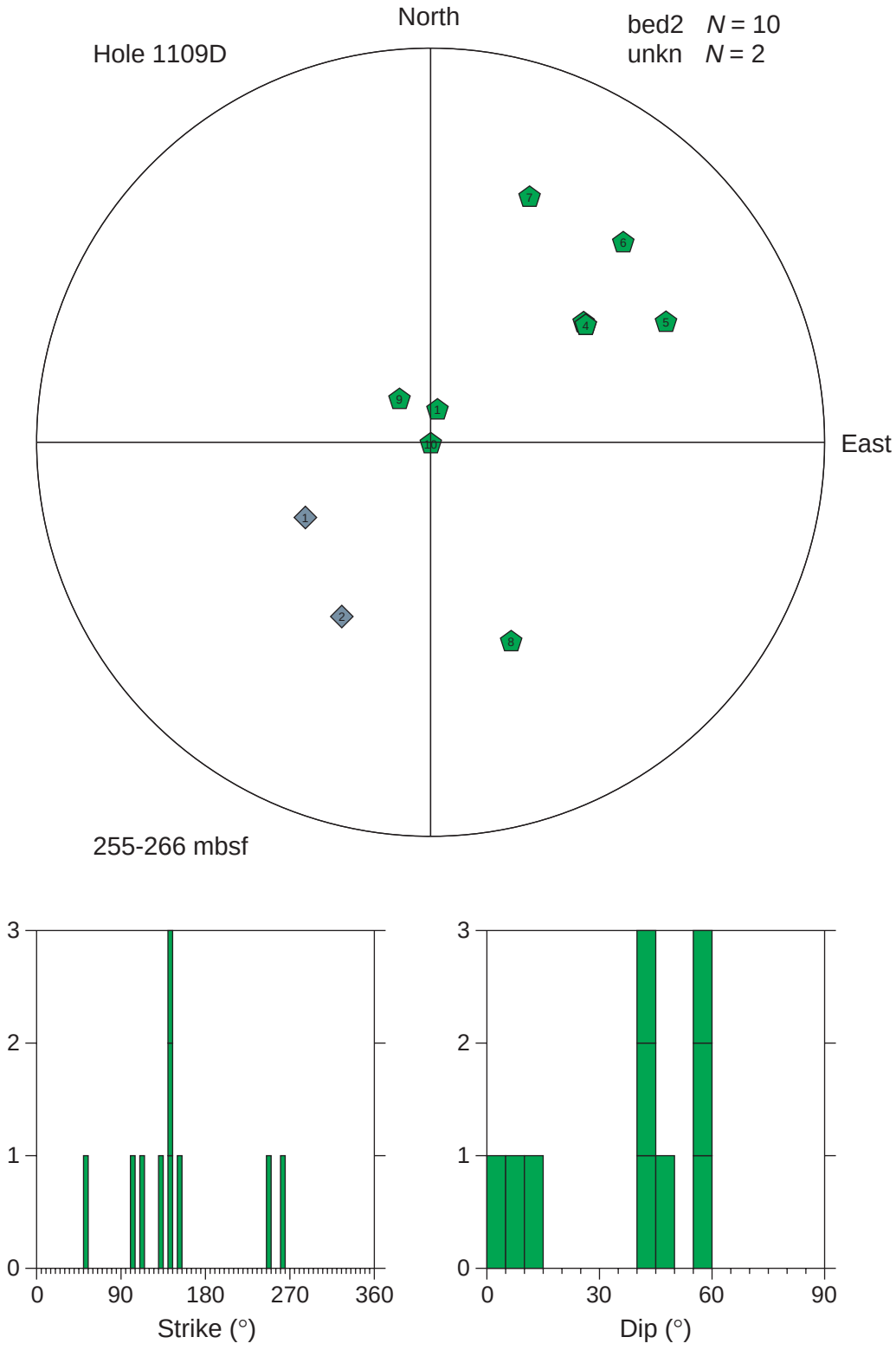

Figure F43. FMS image and analysis, Hole 1109D, 300–312.5 mbsf, reduced to ~70%. From left: (1) depth, (2) static FMS image, (3) dynamic FMS image with a 2-m color equalization sliding window; sinusoids correspond to the structural measurements, (4) structural measurement tadpoles, and (5) caliper measurements. The thin vertical green line on the FMS images indicates the orientation of pad 1, which corresponds to the C1 caliper reading. The tadpole position on the horizontal axis indicates the dip magnitude, and its tail points toward the dip direction.

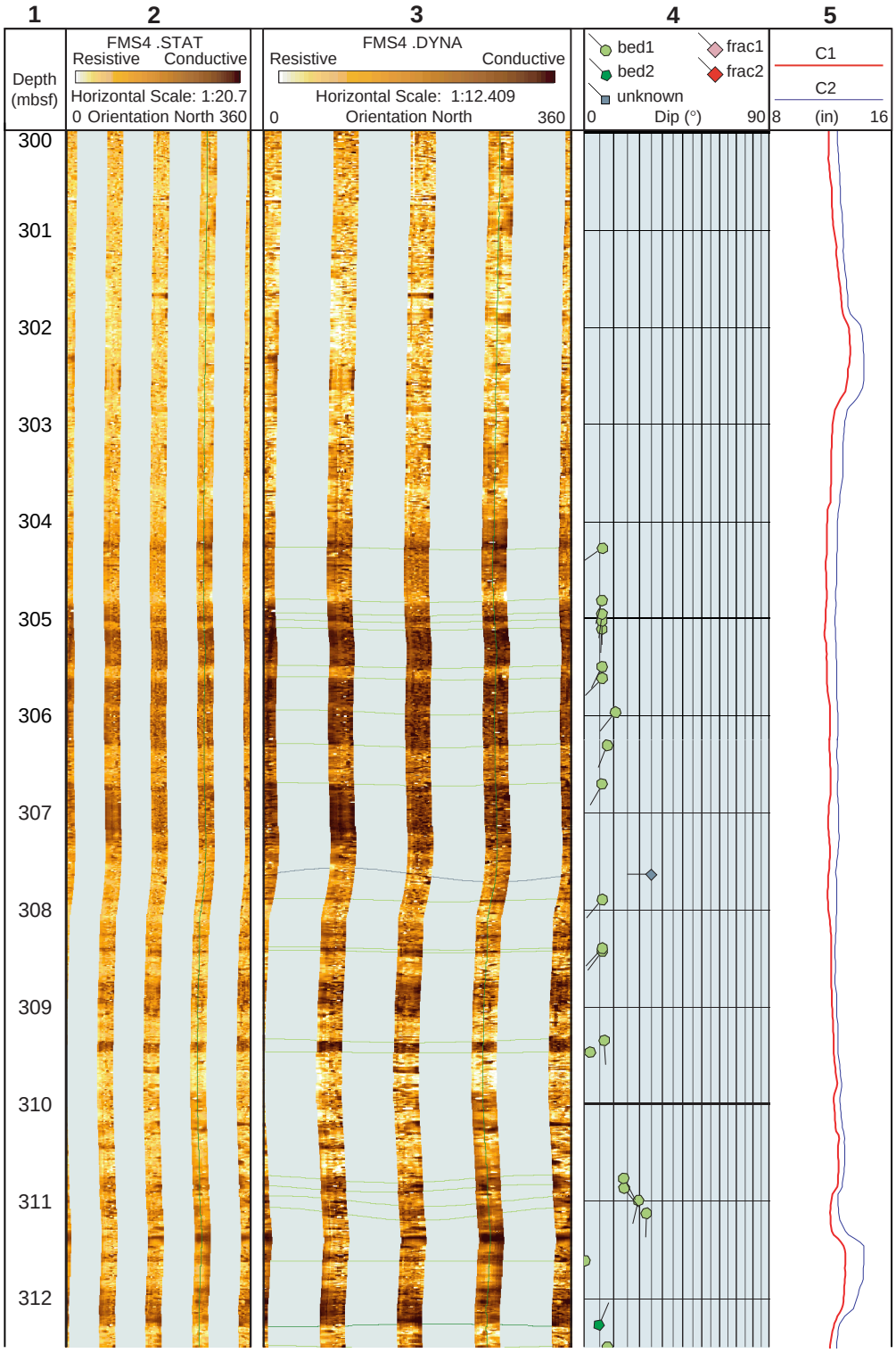

Figure F44. Structure orientations, Hole 1109D, 310–320 mbsf. Stereographic projection of poles to bed 1, bed 2, frac 2, and unknown structures (light green circles, darker green pentagons, red squares, and gray diamonds, respectively). Equal area stereographic projection, lower hemisphere. Strike and dip histograms of bedding only, where bed 1 and bed 2 are stacked with same color code as stereonet poles. Histograms use 5° bins. Strike is normalized so that the dip direction is 90° clockwise from strike. A partial 5° stereonet is shown in the background to highlight a cylindrical structure.

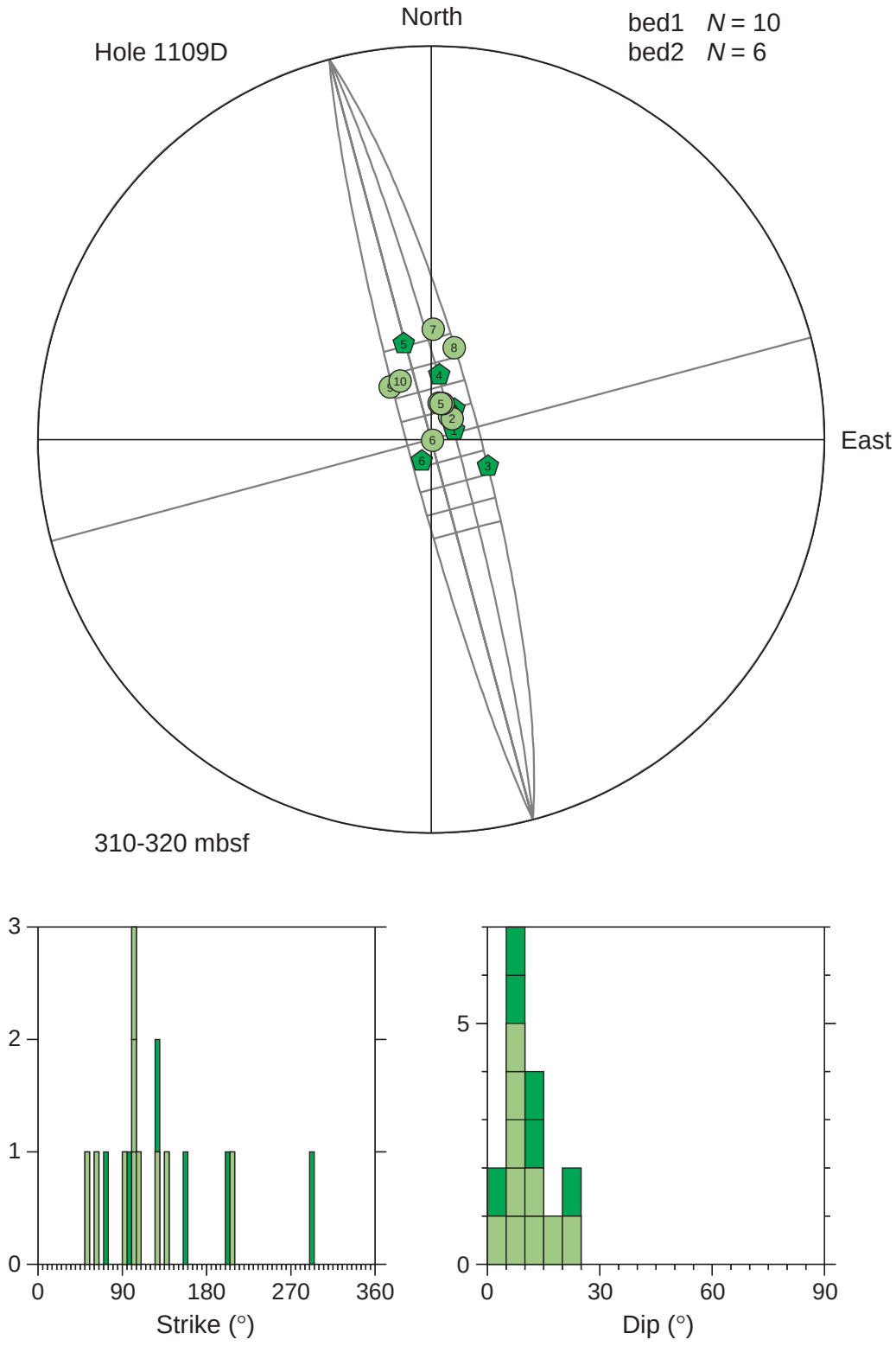

Figure F45. FMS image and analysis, Hole 1109D, 460–472.5 mbsf, reduced to ~70%. From left: (1) depth, (2) static FMS image, (3) dynamic FMS image with a 2-m color equalization sliding window; sinusoids correspond to the structural measurements, (4) structural measurement tadpoles, and (5) caliper measurements. The thin vertical green line on the FMS images indicates the orientation of pad 1, which corresponds to the C1 caliper reading. The tadpole position on the horizontal axis indicates the dip magnitude, and its tail points toward the dip direction.

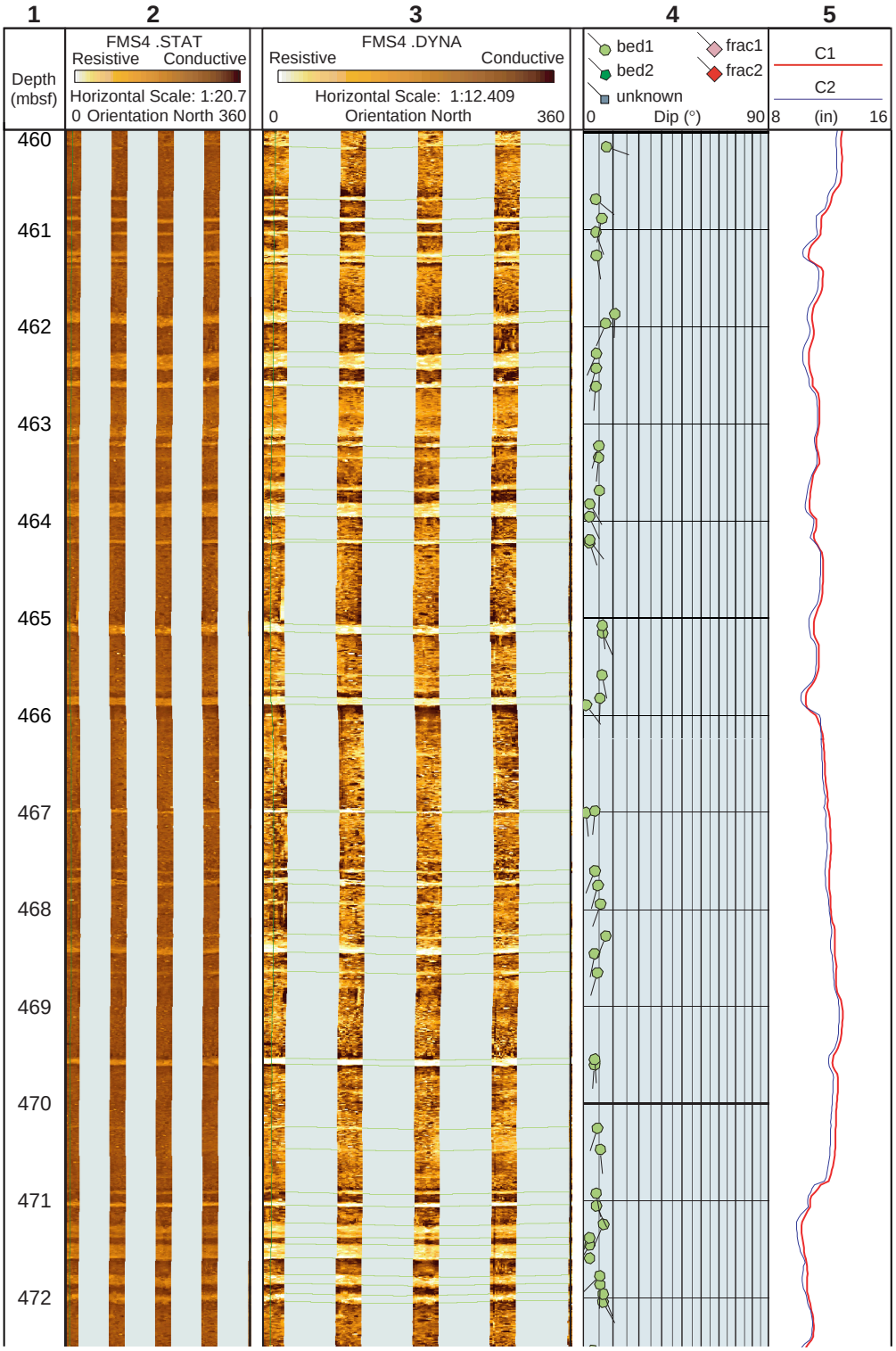

Figure F46. FMS image and analysis, Hole 1109D, 591–603.5 mbsf, reduced to ~70%. From left: (1) depth, (2) static FMS image, (3) dynamic FMS image with a 2-m color equalization sliding window; sinusoids correspond to the structural measurements, (4) structural measurement tadpoles, and (5) caliper measurements. The thin vertical green line on the FMS images indicates the orientation of pad 1, which corresponds to the C1 caliper reading. The tadpole position on the horizontal axis indicates the dip magnitude, and its tail points toward the dip direction.

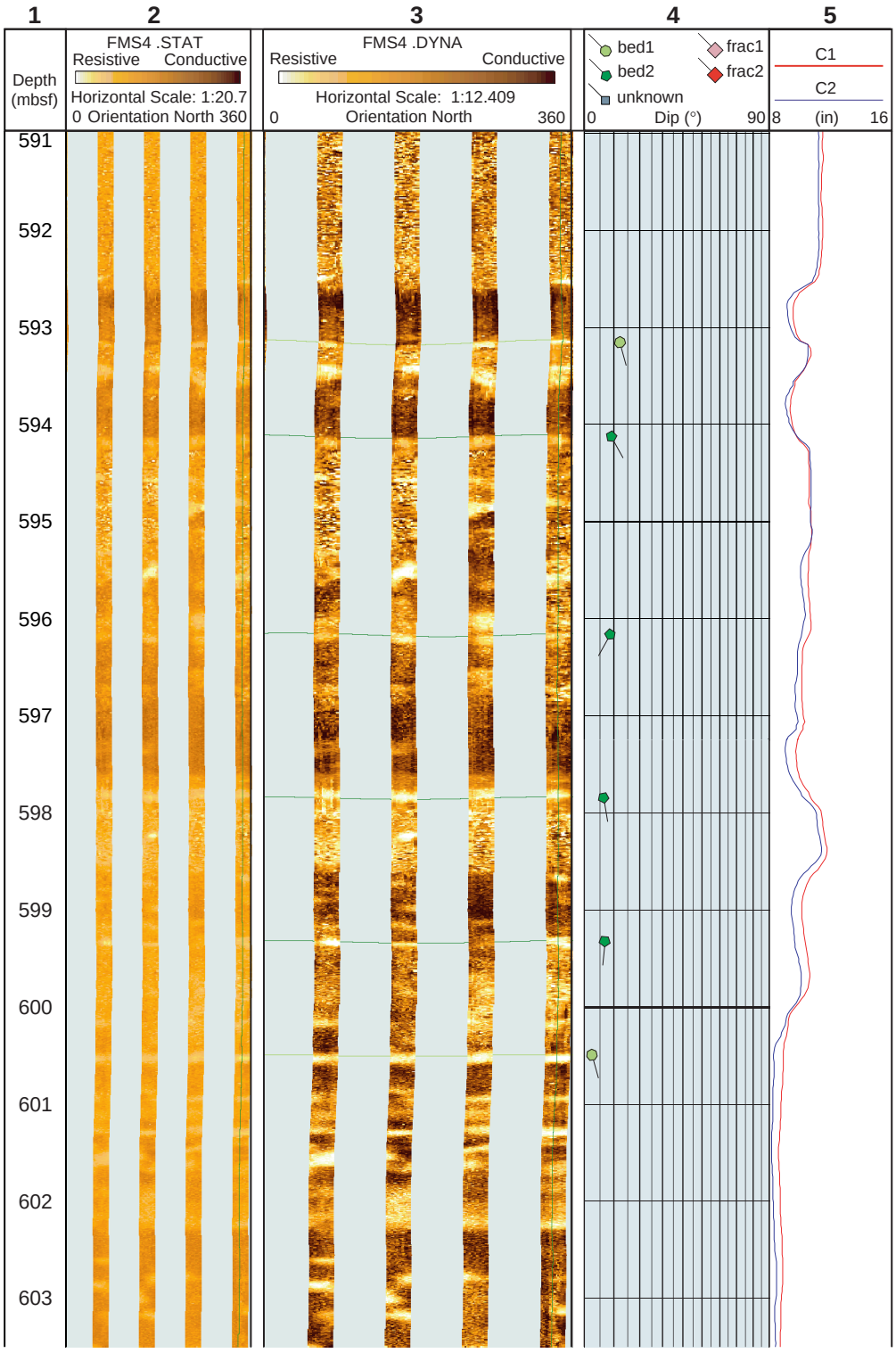

Figure F47. FMS image and analysis, Hole 1109D, 640–652.5 mbsf, reduced to ~70%. From left: (1) depth, (2) static FMS image, (3) dynamic FMS image with a 2-m color equalization sliding window; sinusoids correspond to the structural measurements, (4) structural measurement tadpoles, and (5) caliper measurements. The thin vertical green line on the FMS images indicates the orientation of pad 1, which corresponds to the C1 caliper reading. The tadpole position on the horizontal axis indicates the dip magnitude, and its tail points toward the dip direction.

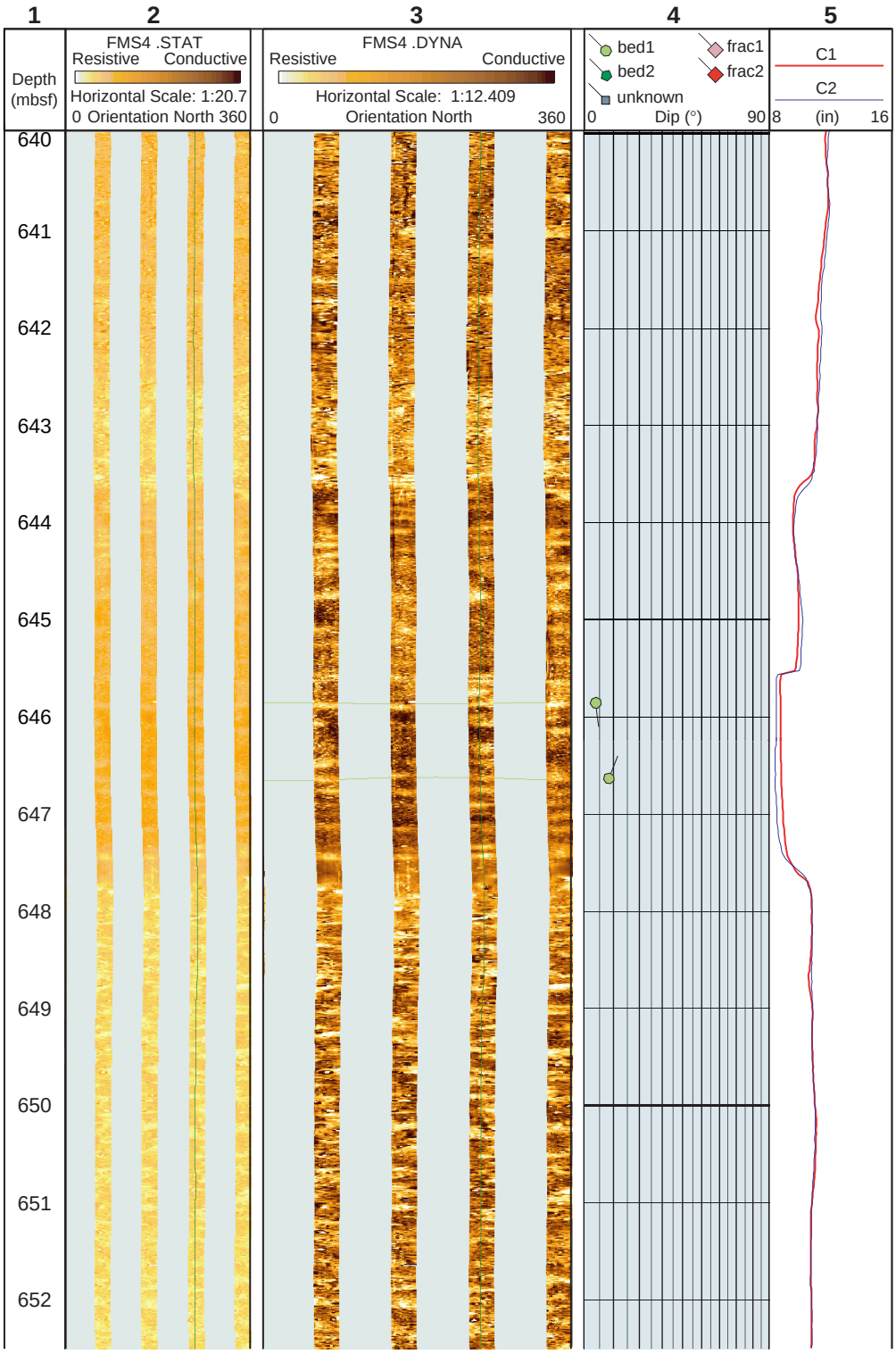

Figure F48. FMS image and analysis, Hole 1109D, 671–683.5 mbsf, reduced to ~70%. From left: (1) depth, (2) static FMS image, (3) dynamic FMS image with a 2-m color equalization sliding window; sinusoids correspond to the structural measurements, (4) structural measurement tadpoles, and (5) caliper measurements. The thin vertical green line on the FMS images indicates the orientation of pad 1, which corresponds to the C1 caliper reading. The tadpole position on the horizontal axis indicates the dip magnitude, and its tail points toward the dip direction.

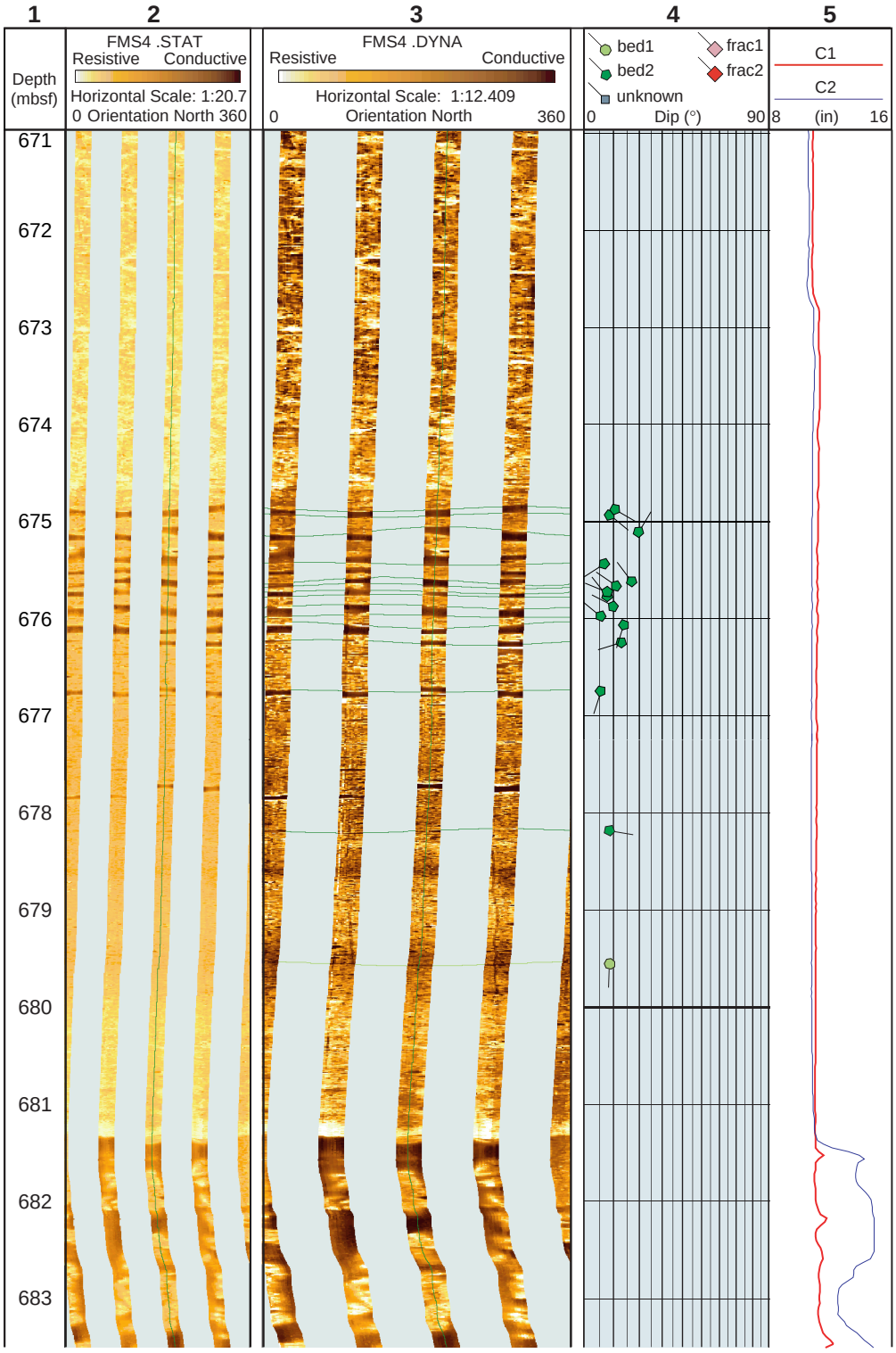

Figure F49. Structure orientations, Hole 1109D, 670–680 mbsf. Stereographic projection of poles to bed 1, bed 2, frac 2, and unknown structures (light green circles, darker green pentagons, red squares, and gray diamonds, respectively). Equal area stereographic projection, lower hemisphere. Strike and dip histograms of bedding only, where bed 1 and bed 2 are stacked with same color code as stereonet poles. Histograms use 5° bins. Strike is normalized so that the dip direction is 90° clockwise from strike.

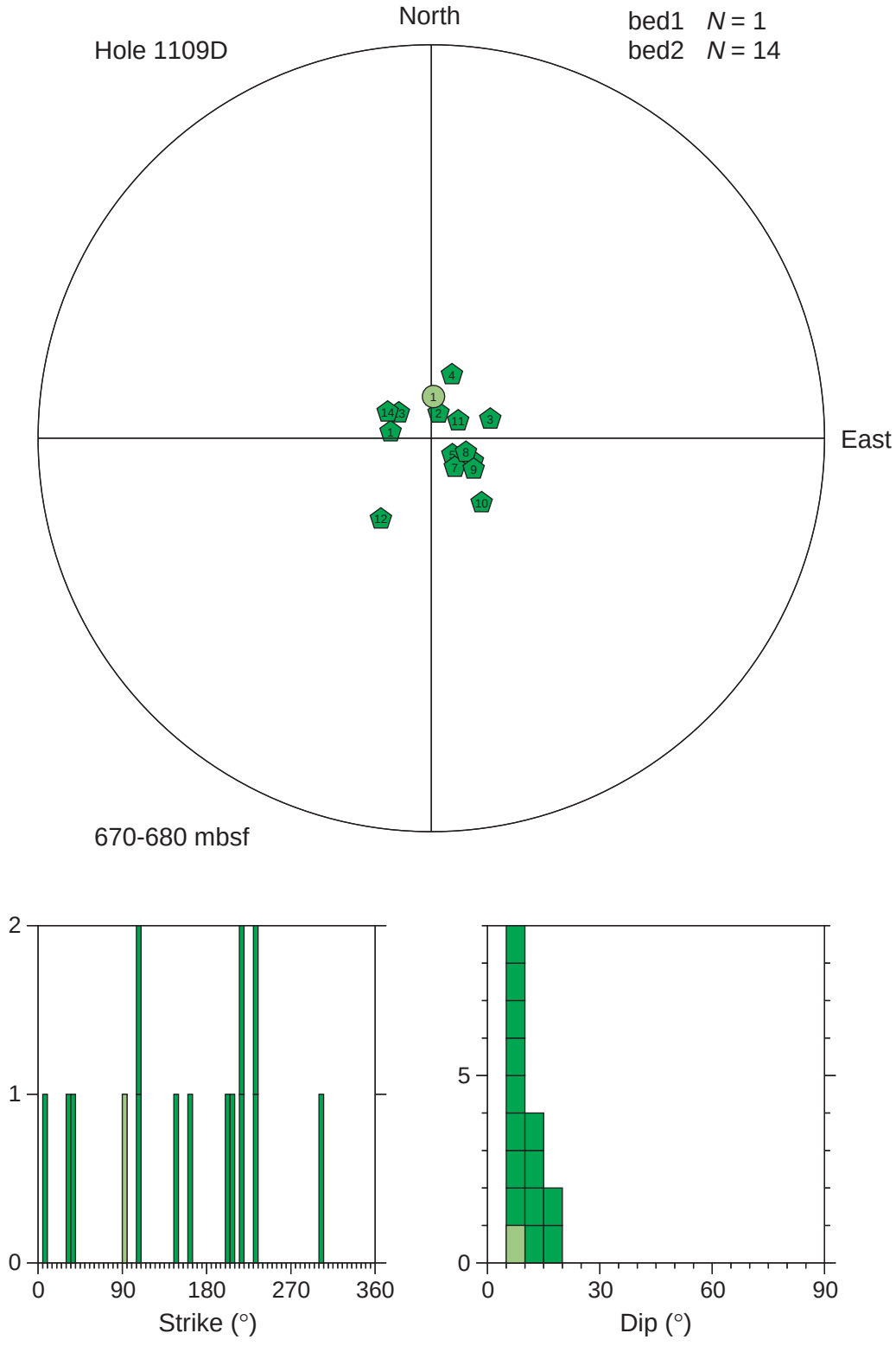

Figure F50. FMS image and analysis, Hole 1109D, 685–695 mbsf, reduced to ~70%. From left: (1) depth, (2) static FMS image, (3) dynamic FMS image with a 2-m color equalization sliding window; sinusoids correspond to the structural measurements, (4) structural measurement tadpoles, and (5) caliper measurements. The thin vertical green line on the FMS images indicates the orientation of pad 1, which corresponds to the C1 caliper reading. The tadpole position on the horizontal axis indicates the dip magnitude, and its tail points toward the dip direction.

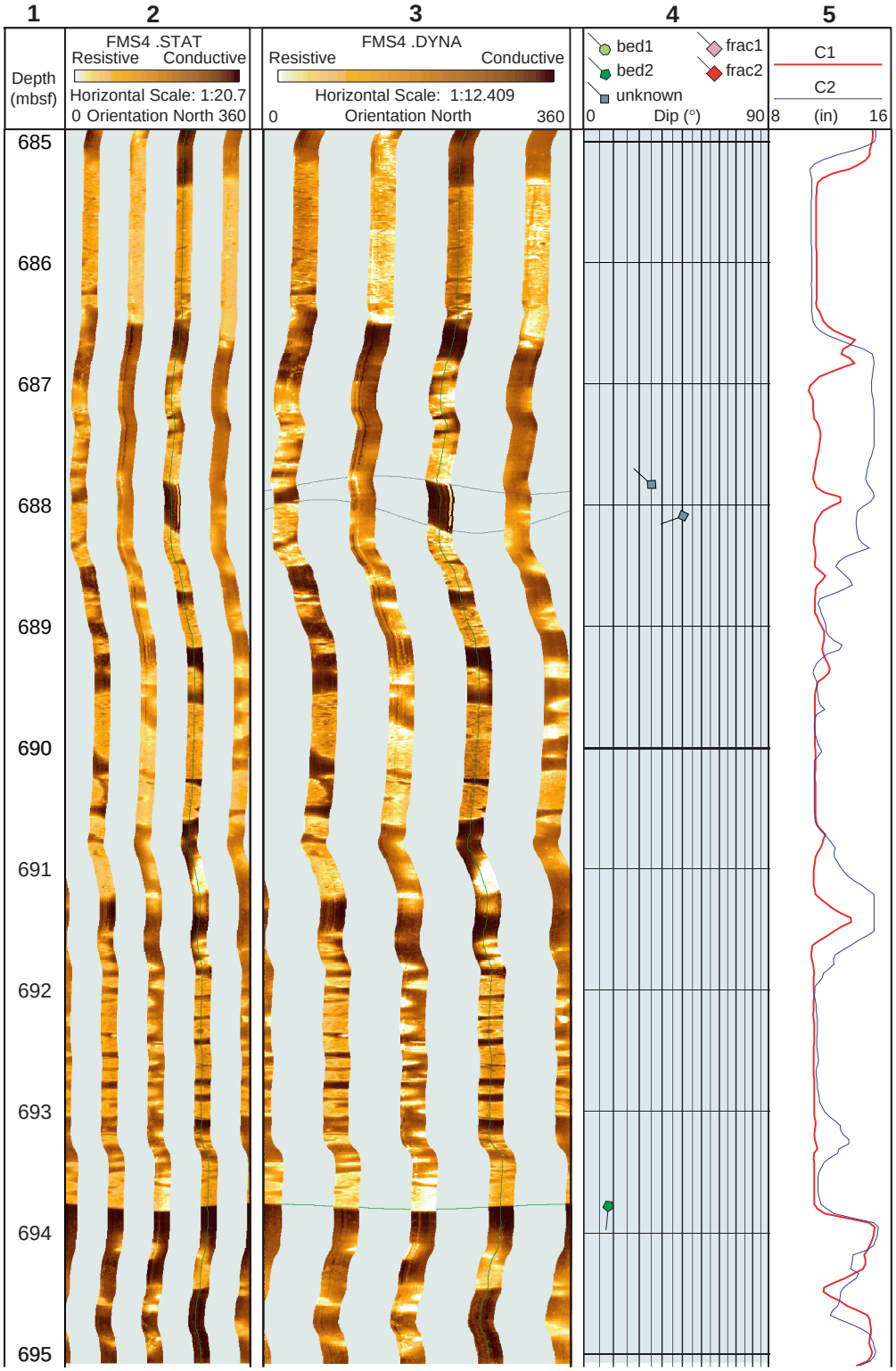

Figure F51. FMS image and analysis, Hole 1109D, 700–710 mbsf, reduced to ~70%. From left: (1) depth, (2) static FMS image, (3) dynamic FMS image with a 2-m color equalization sliding window; sinusoids correspond to the structural measurements, (4) structural measurement tadpoles, and (5) caliper measurements. The thin vertical green line on the FMS images indicates the orientation of pad 1, which corresponds to the C1 caliper reading. The tadpole position on the horizontal axis indicates the dip magnitude, and its tail points toward the dip direction.

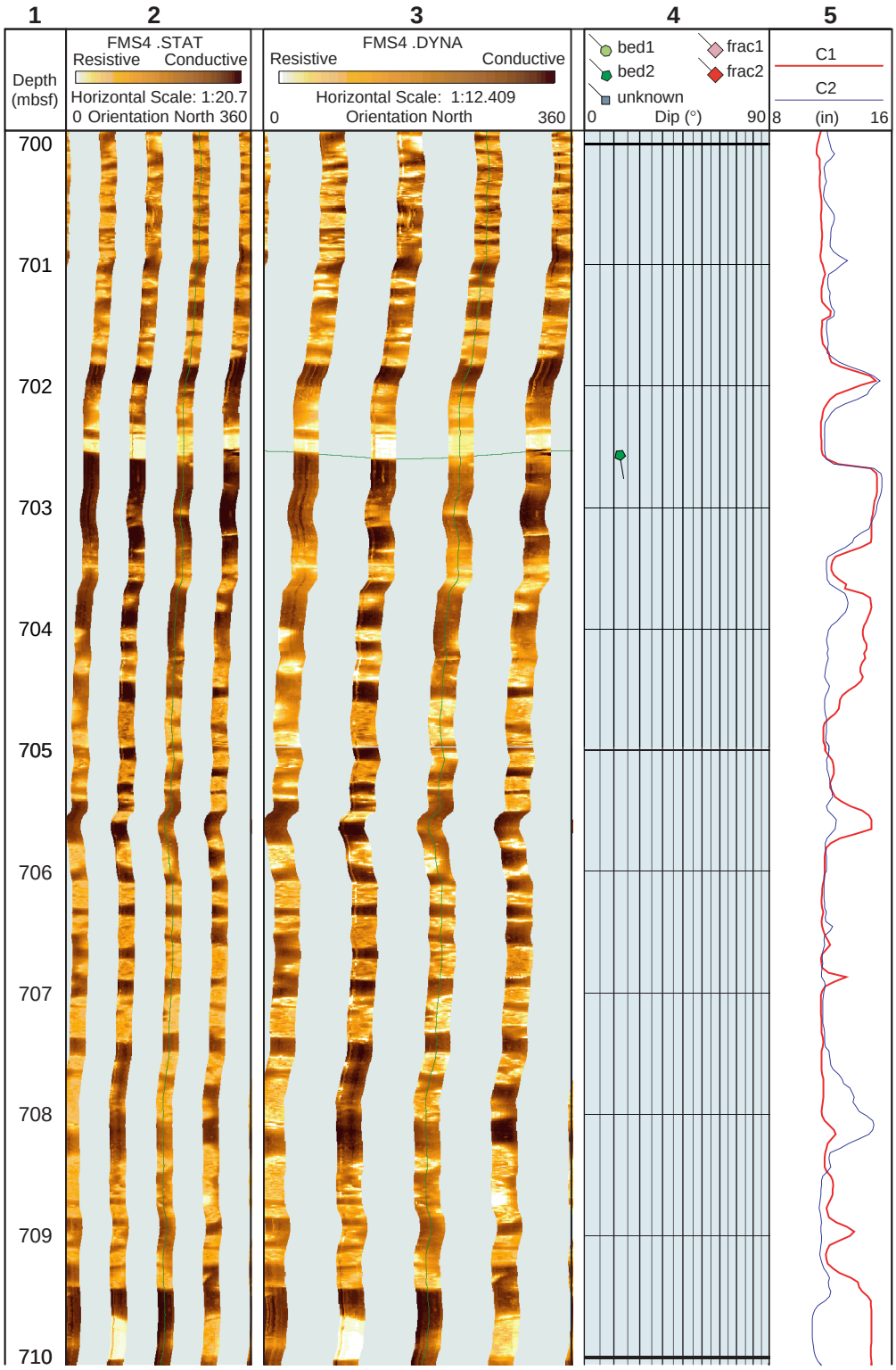

Figure F52. FMS image and analysis, Hole 1109D, 767–777 mbsf, reduced to ~70%. From left: (1) depth, (2) static FMS image, (3) dynamic FMS image with a 2-m color equalization sliding window; sinusoids correspond to the structural measurements, (4) structural measurement tadpoles, and (5) caliper measurements. The thin vertical green line on the FMS images indicates the orientation of pad 1, which corresponds to the C1 caliper reading. The tadpole position on the horizontal axis indicates the dip magnitude, and its tail points toward the dip direction.

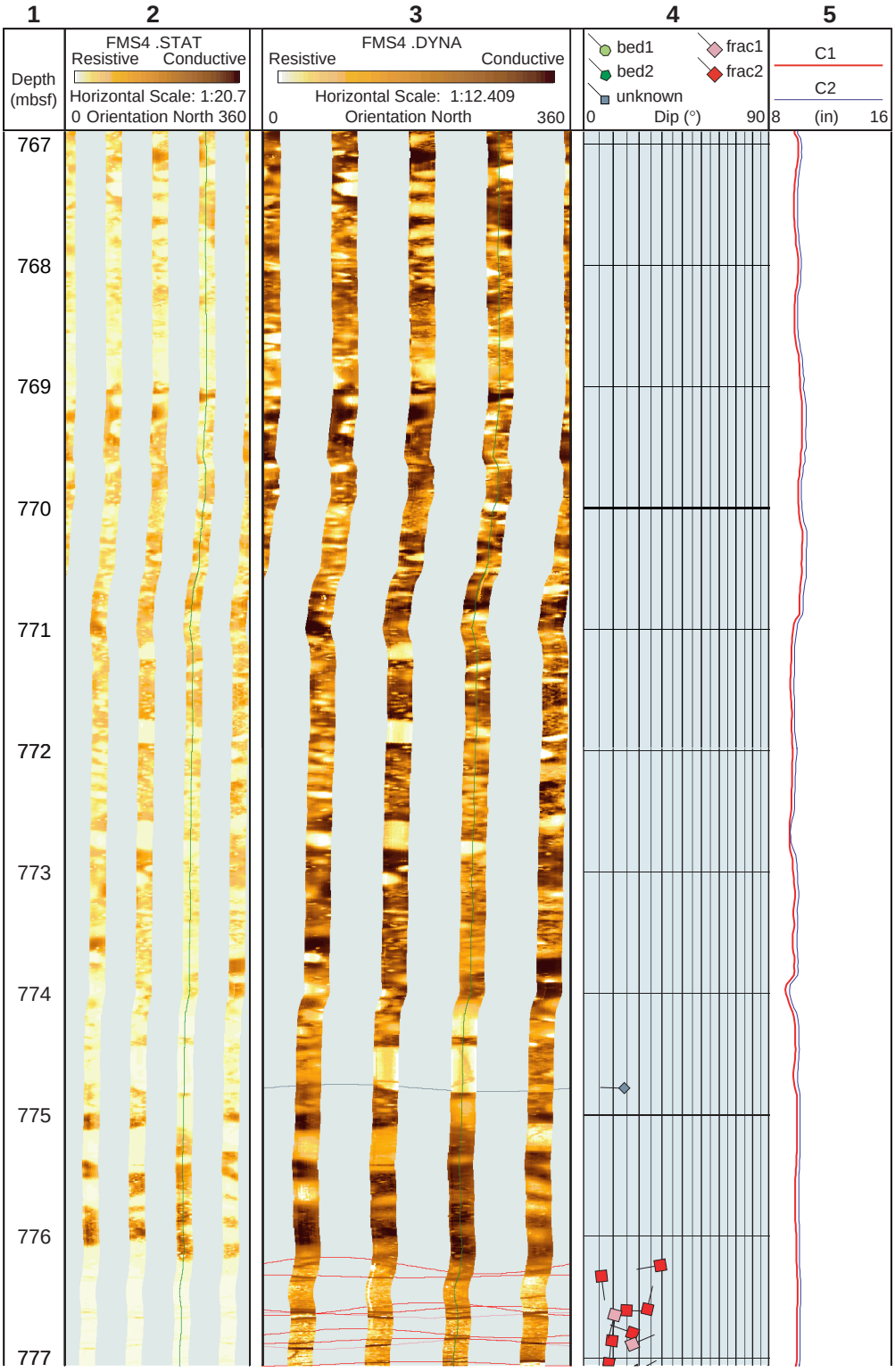

Figure F53. FMS image and analysis, Hole 1109D, 776–781 mbsf, reduced to ~70%. The color range of the static image has been shifted towards darker values so as to better reveal the fracturation. From left: (1) depth, (2) static FMS image, (3) dynamic FMS image with a 2-m color equalization sliding window; sinusoids correspond to the structural measurements, (4) structural measurement tadpoles, and (5) caliper measurements. The thin vertical green line on the FMS images indicates the orientation of pad 1, which corresponds to the C1 caliper reading. The tadpole position on the horizontal axis indicates the dip magnitude, and its tail points toward the dip direction.

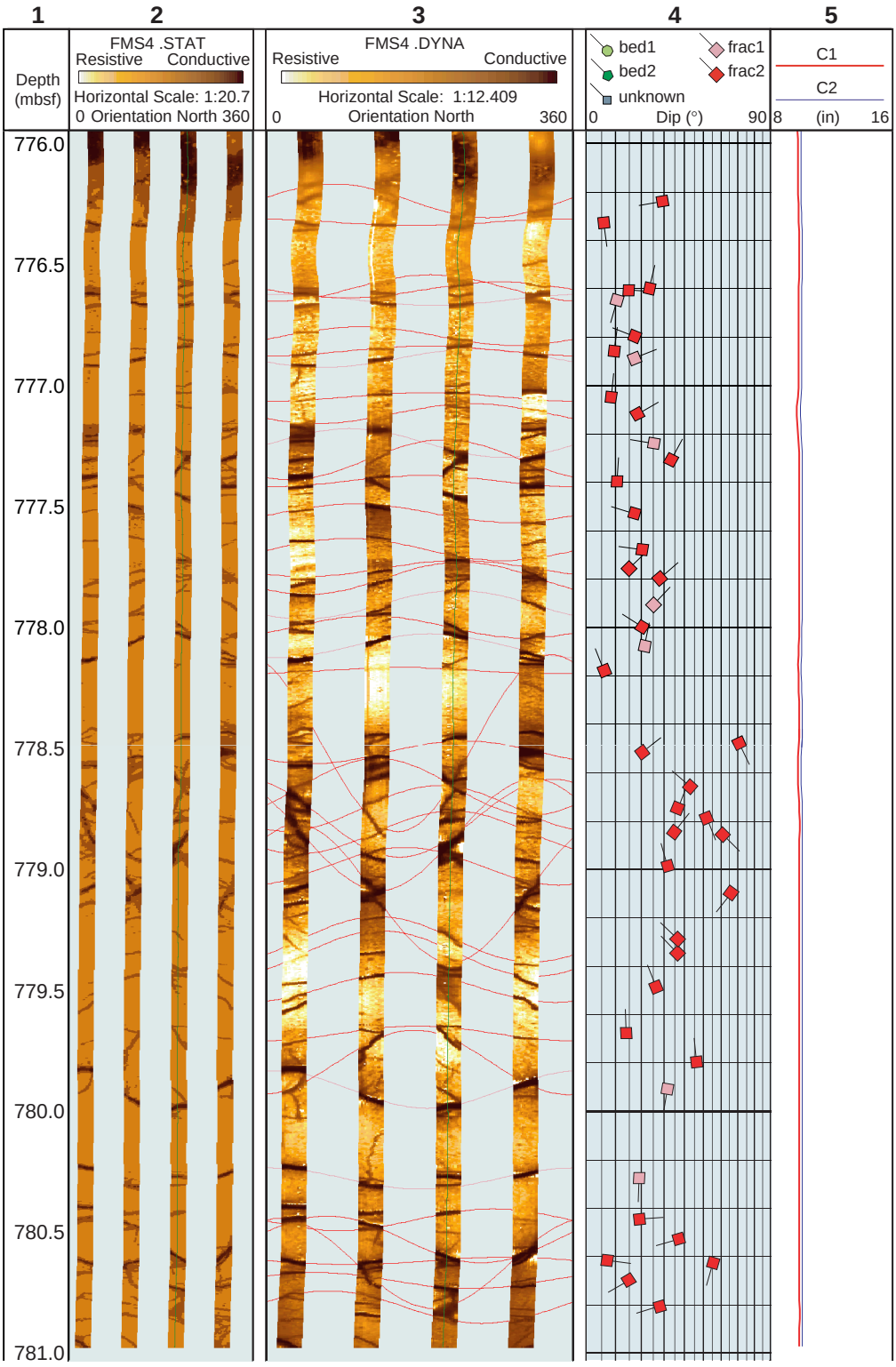

Figure F54. Composite log of Hole 1115C. From left: (1) core number, (2) core recovery, (3) depth, (4) static FMS image, (5) location of detailed FMS figures, (6) structural interpretation tadpoles, (7) depth intervals of detailed orientation plots, (8) lithologic units (summarized in Table T2, p. 112), (9) logging units, (10) structural domains, and (11) caliper measurements. The thin vertical green line on the FMS images indicates the orientation of pad 1 that corresponds to the C1 caliper reading. The tadpole position on the horizontal axis indicates the dip magnitude, and its tail points toward the dip direction. In the structure column (10), deformed zones are highlighted in pink. CID = core induced deformation, FZ = fracture zone. (Continued on next two pages.)

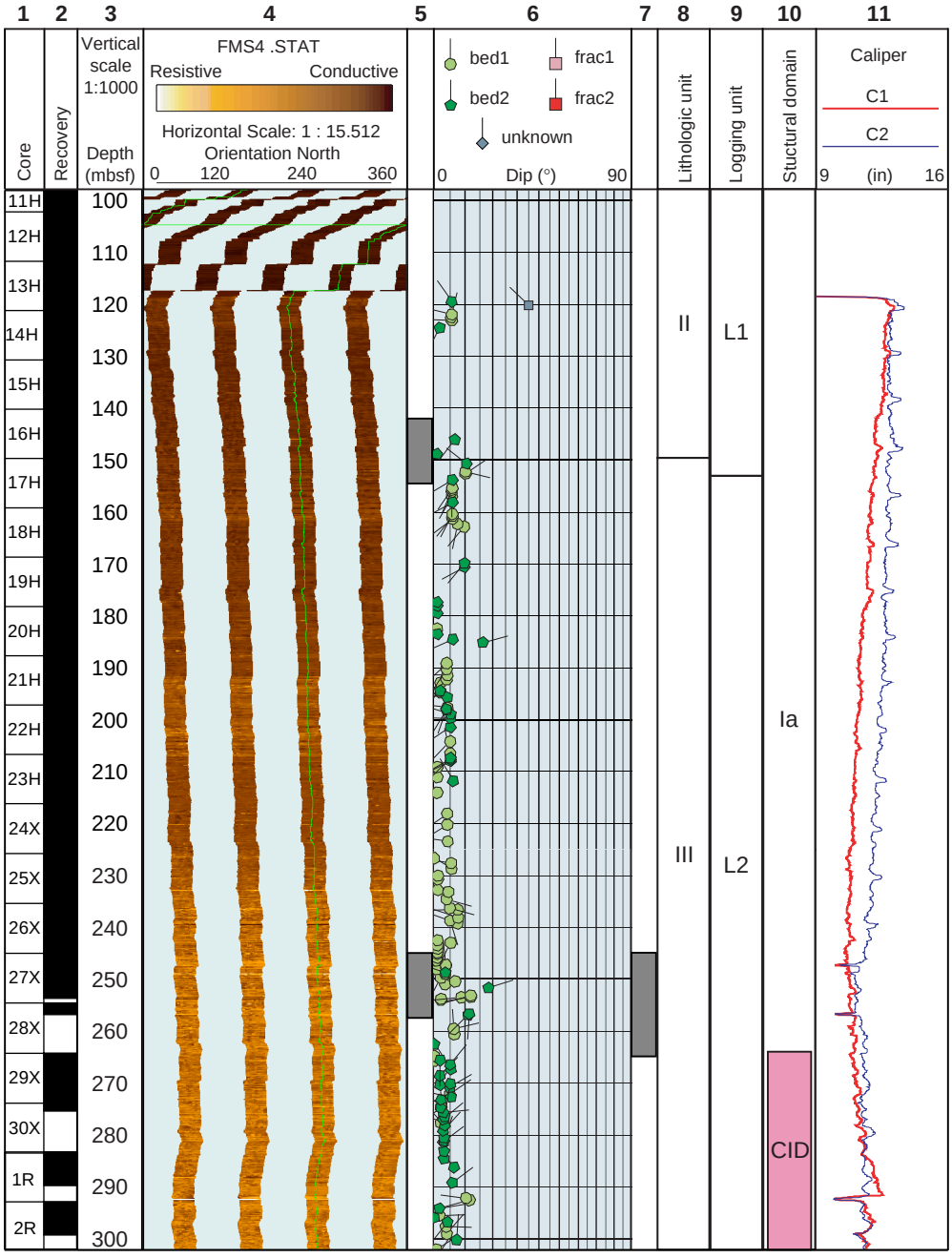

Figure F54 (continued).

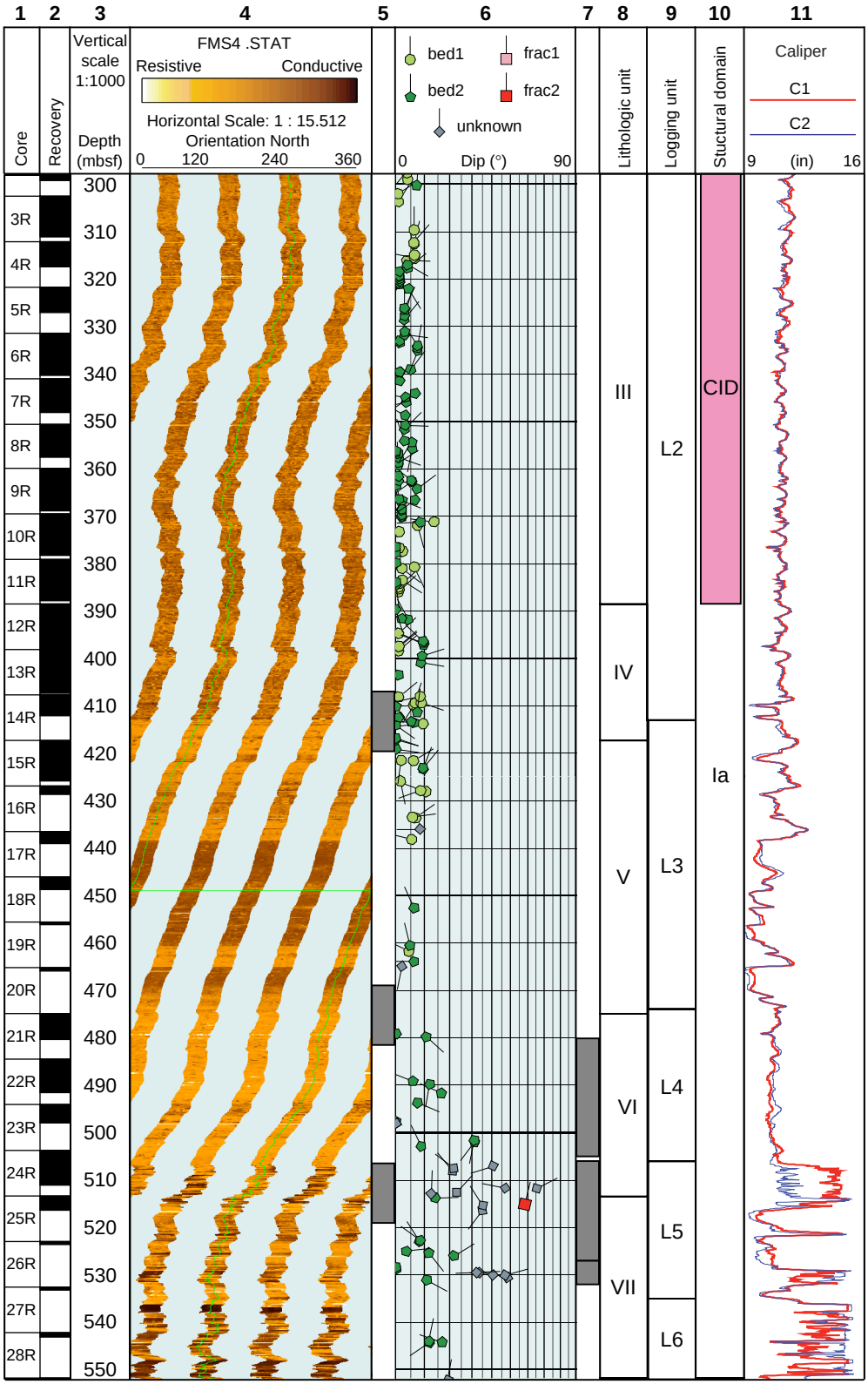

Figure F54 (continued).

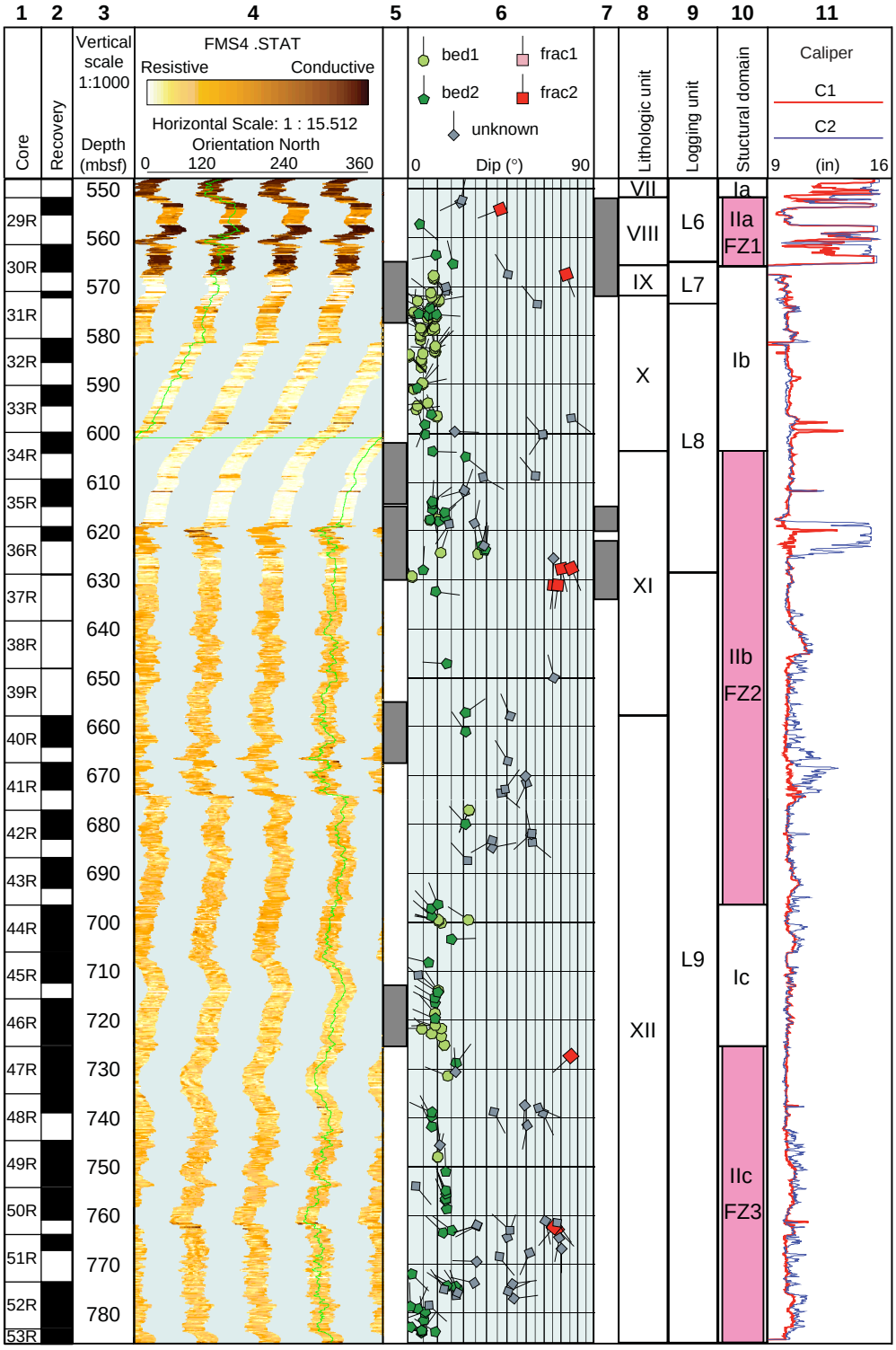

Figure F55. Hole 1115C global bed orientations. Equal area stereographic projection, lower hemisphere. Poles to bed 1 and bed 2 are shown as light green circles and darker green pentagons, respectively. Strike and dip histograms use 5° bins. Strike is normalized so that the dip direction is 90° clockwise from strike. Bed 1 and bed 2 histograms are stacked with same color code as stereonet poles.

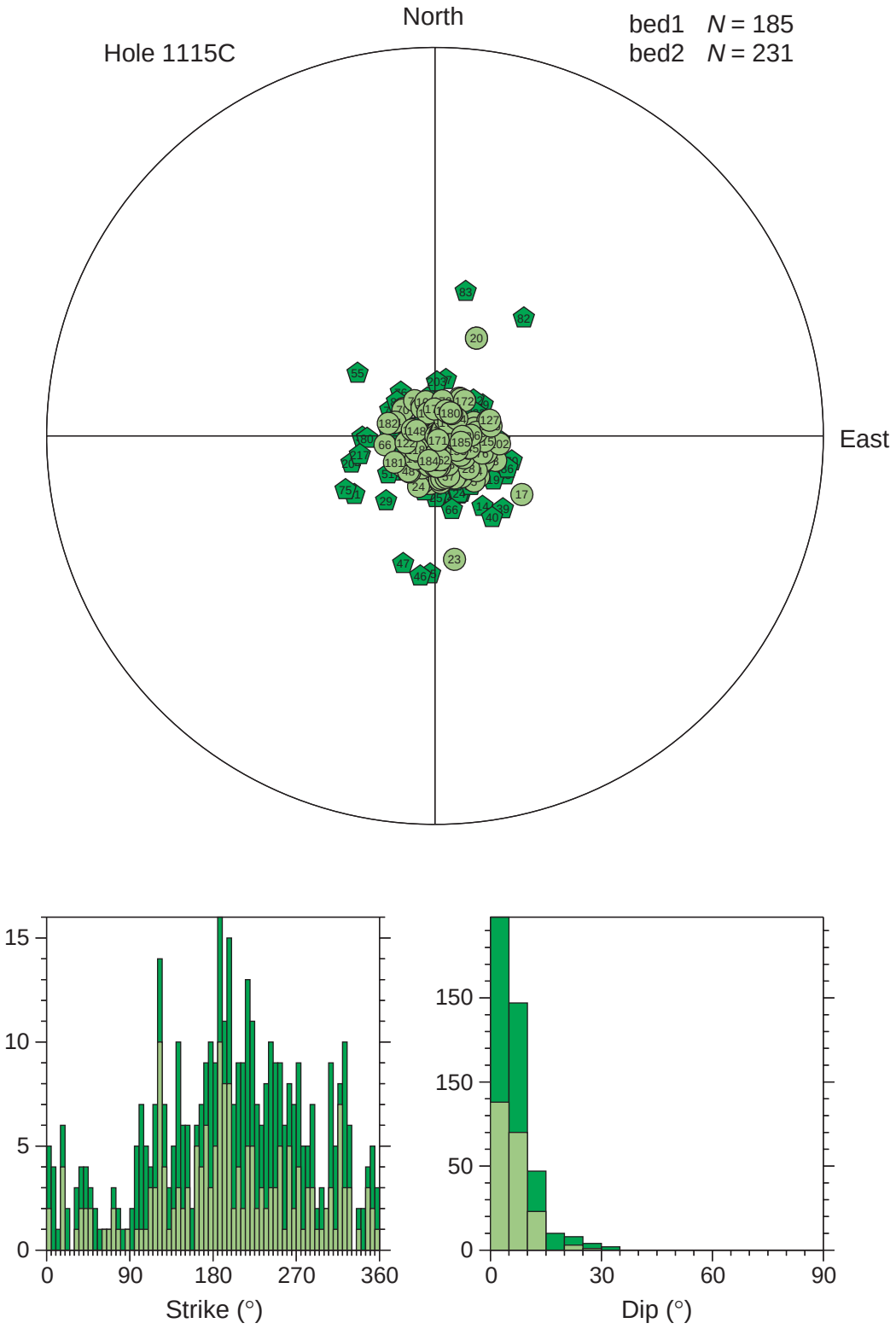

Figure F56. Hole 1115C global fracture orientations. Equal area stereographic projection, lower hemisphere. Poles to frac 1 (none here) and frac 2 are shown as pink and red squares, respectively. Strike and dip histograms use 5° bins. Strike is normalized so that the dip direction is 90° clockwise from strike. Frac 1 and frac 2 histograms are stacked with same color code as stereonet poles. Fractures 8–9, 4–7, and 1–3 are located in core-defined fracture zones 1, 2, and 3, respectively.

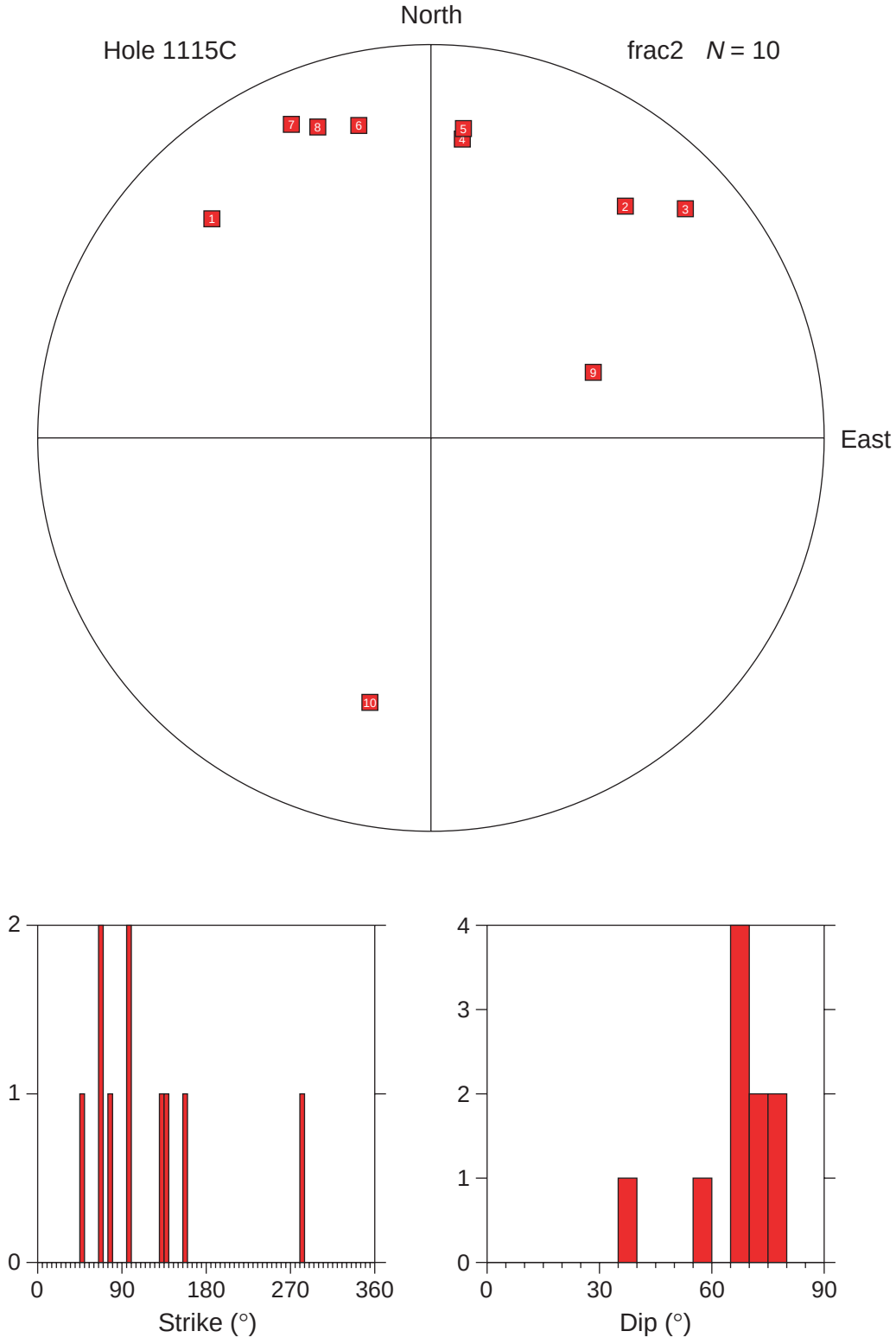

Figure F57. Hole 1115C unknown planar structures orientations. Equal area stereographic projection, lower hemisphere. Poles are shown as gray diamonds. Strike and dip histograms use 5° bins. Strike is normalized so that the dip direction is 90° clockwise from strike.

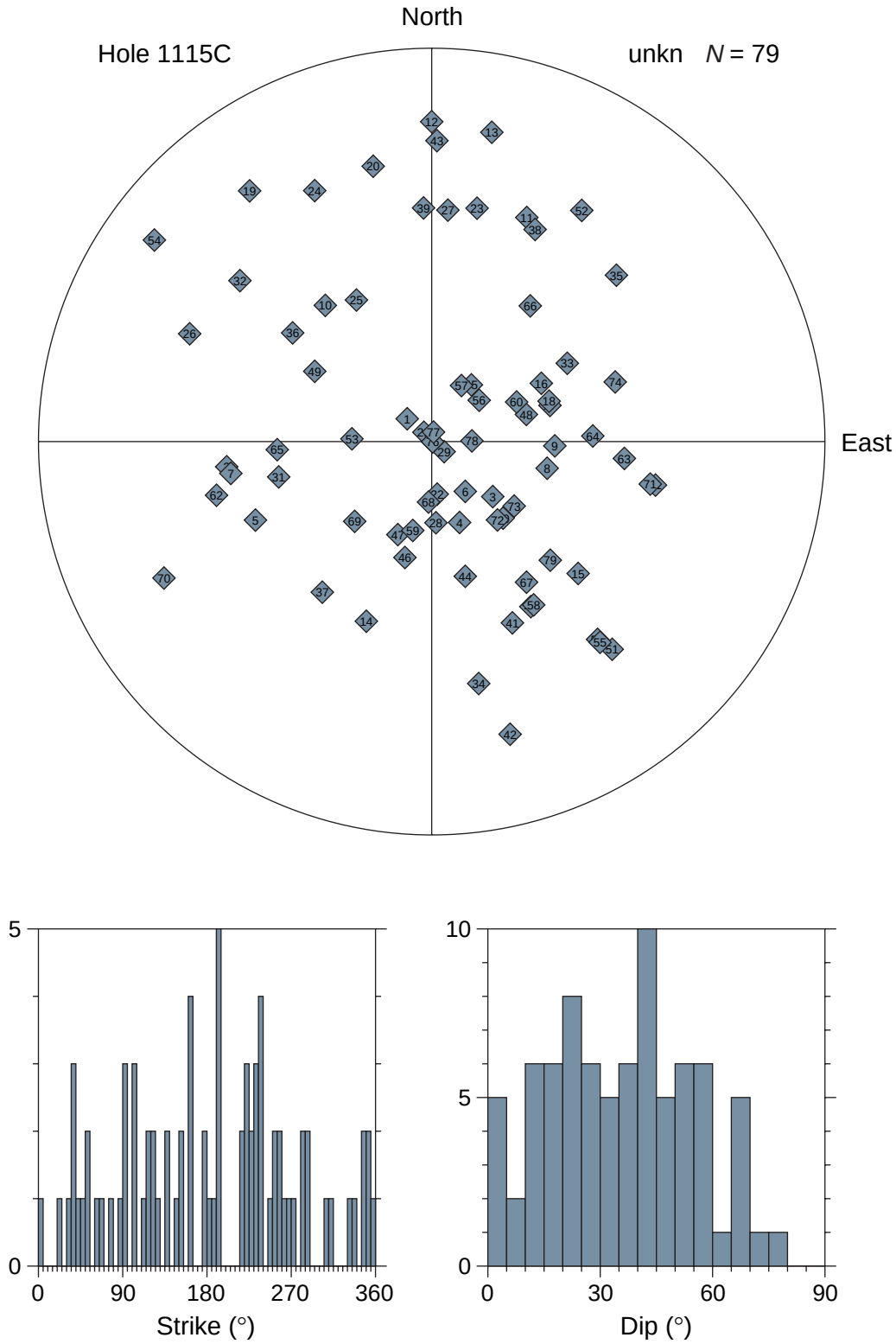

Figure F58. Prerift bed orientations, Hole 1115C, 573.5–790 mbsf. Equal area stereographic projection, lower hemisphere. Poles to bed 1 and bed 2 are shown as light green circles and darker green pentagons, respectively. Strike and dip histograms use 5° bins. Strike is normalized so that the dip direction is 90° clockwise from strike. Bed 1 and bed 2 histograms are stacked with same color code as stereonet poles.

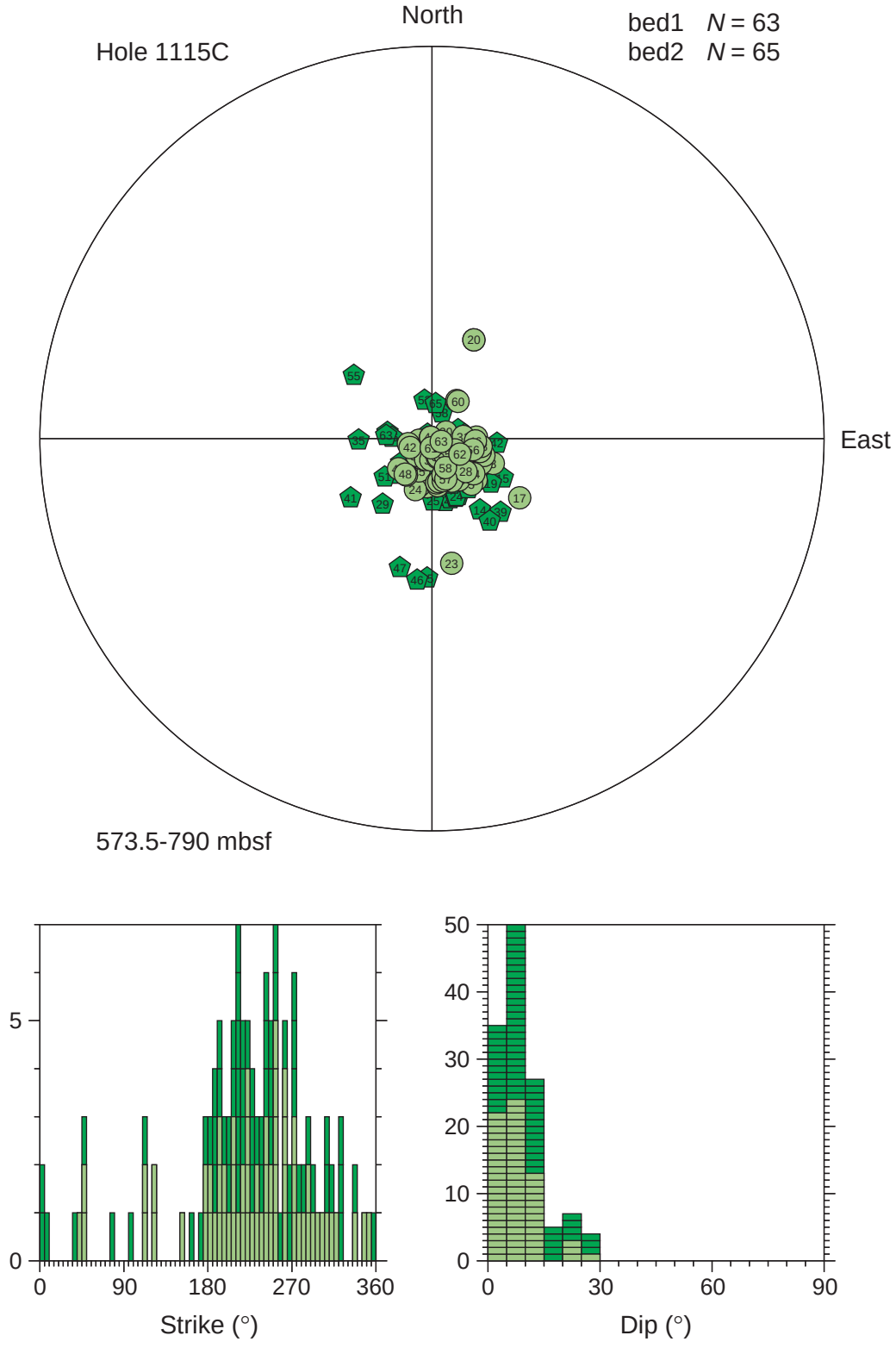

Figure F59. Synrift bed orientations, Hole 1115C, 119–573.5 mbsf. Equal area stereographic projection, lower hemisphere. Poles to bed 1 and bed 2 are shown as light green circles and darker green pentagons, respectively. Strike and dip histograms use 5° bins. Strike is normalized so that the dip direction is 90° clockwise from strike. Bed 1 and bed 2 histograms are stacked with same color code as stereonet poles.

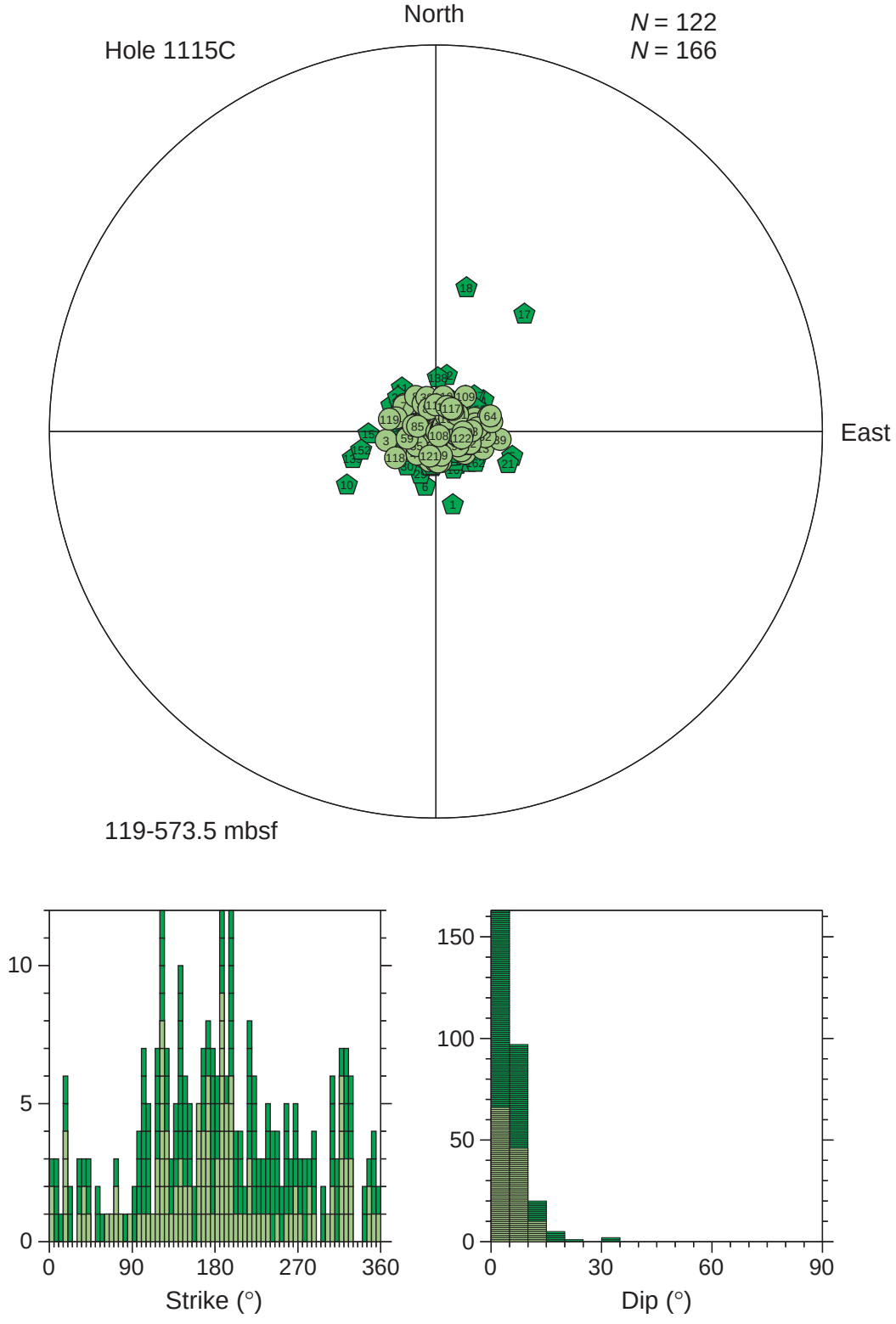

Figure F60. FMS image and analysis, Hole 1115C, 142–154.5 mbsf, reduced to ~70%. From left: (1) depth, (2) static FMS image, (3) dynamic FMS image with a 2-m color equalization sliding window; sinusoids correspond to the structural measurements, (4) structural measurement tadpoles, and (5) caliper measurements. The thin vertical green line on the FMS images indicates the orientation of pad 1, which corresponds to the C1 caliper reading. The tadpole position on the horizontal axis indicates the dip magnitude, and its tail points toward the dip direction.

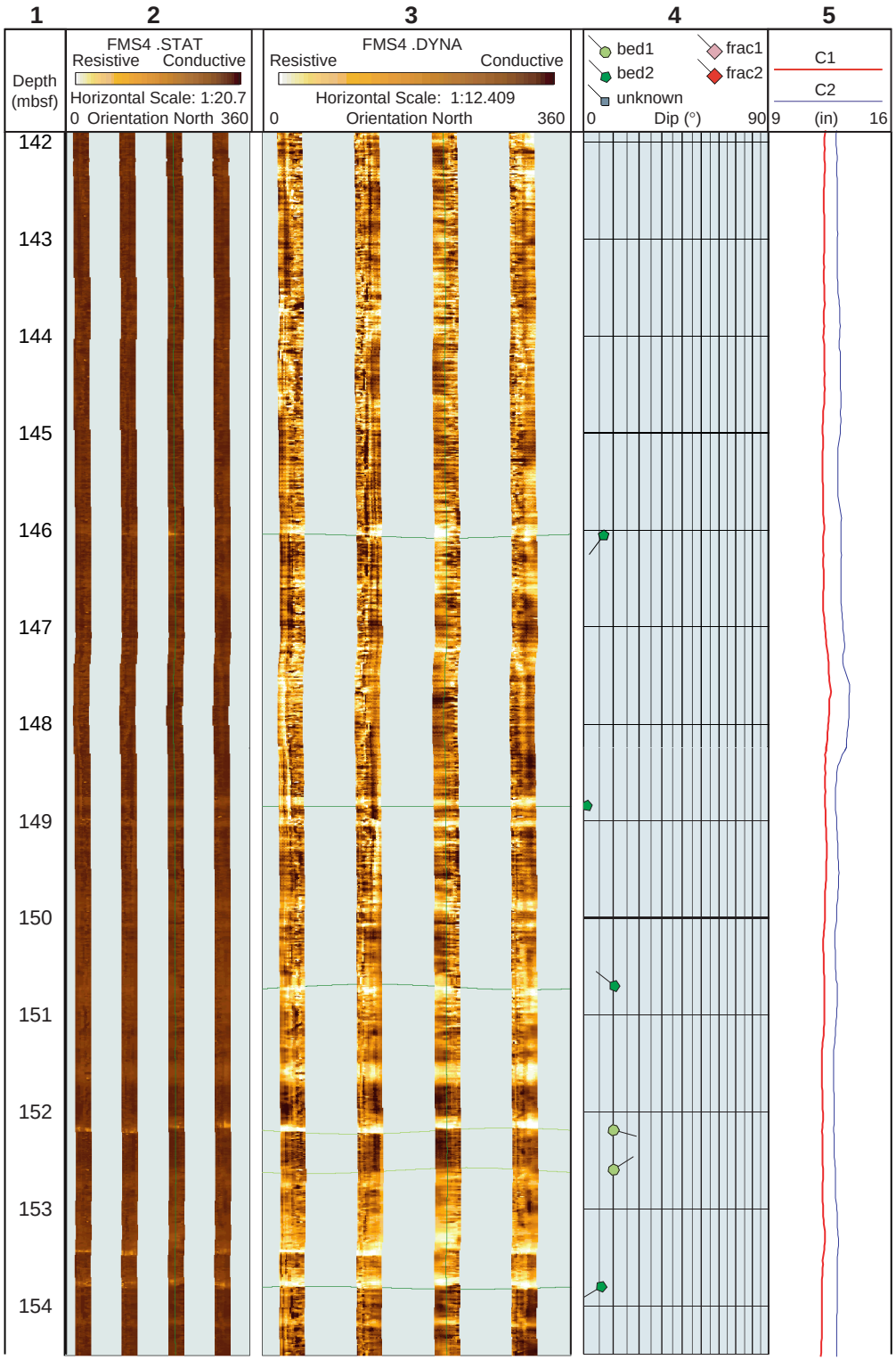

Figure F61. FMS image and analysis, Hole 1115C, 245–257.5 mbsf, reduced to ~70%. From left: (1) depth, (2) static FMS image, (3) dynamic FMS image with a 2-m color equalization sliding window; sinusoids correspond to the structural measurements, (4) structural measurement tadpoles, and (5) caliper measurements. The thin vertical green line on the FMS images indicates the orientation of pad 1, which corresponds to the C1 caliper reading. The tadpole position on the horizontal axis indicates the dip magnitude, and its tail points toward the dip direction.

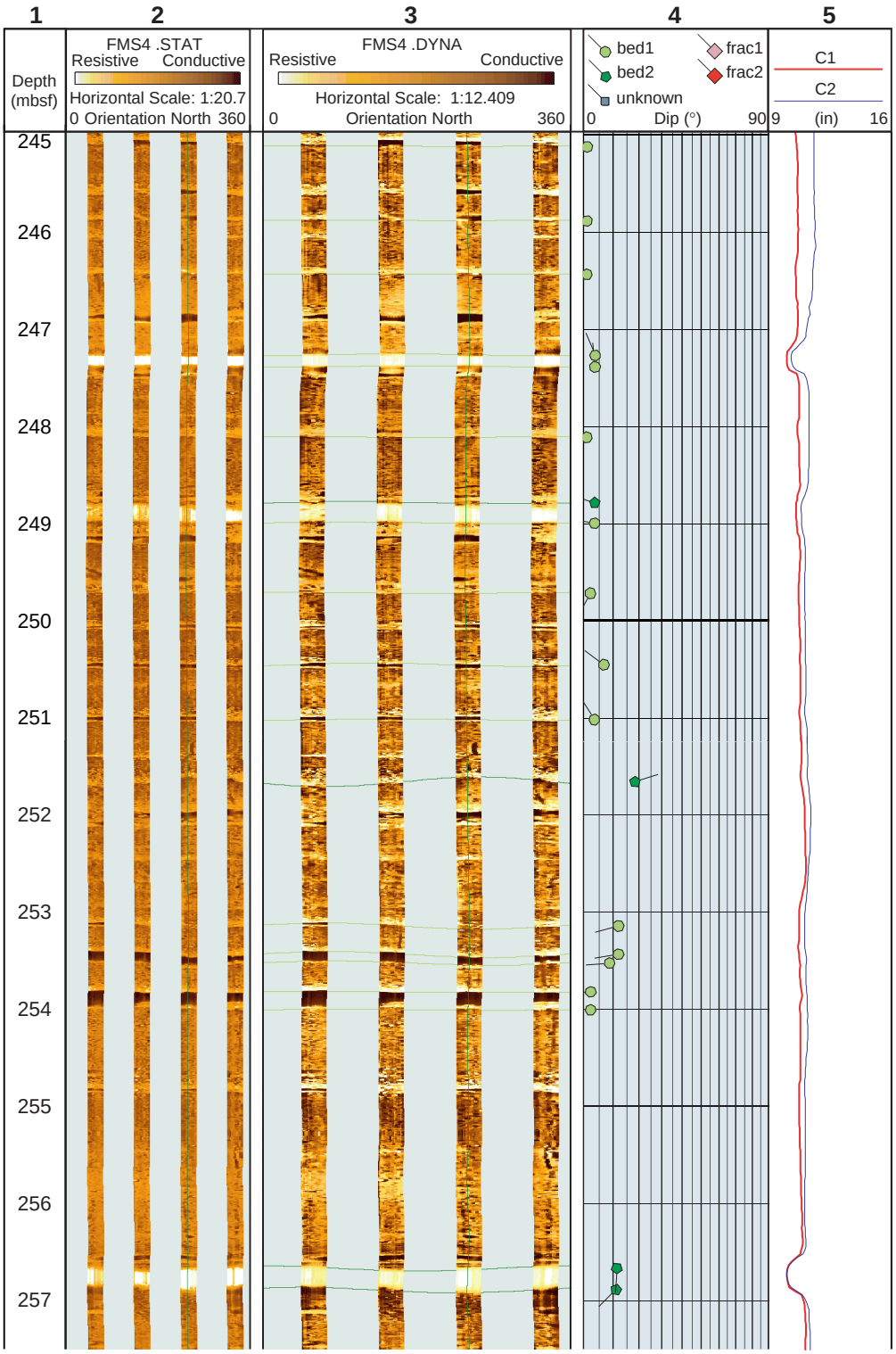

Figure F62. Structure orientation, Hole 1115C, 245–265 mbsf. Stereographic projection of poles to bed 1, bed 2, frac 2, and unknown structures (light green circles, darker green pentagons, red squares, and gray diamonds, respectively). Equal area stereographic projection, lower hemisphere. Strike and dip histograms of bedding only, where bed 1 and bed 2 are stacked with same color code as stereonet poles. Histograms use 5° bins. Strike is normalized so that the dip direction is 90° clockwise from strike. A partial 5° stereonet is shown in the background to highlight a cylindrical structure.

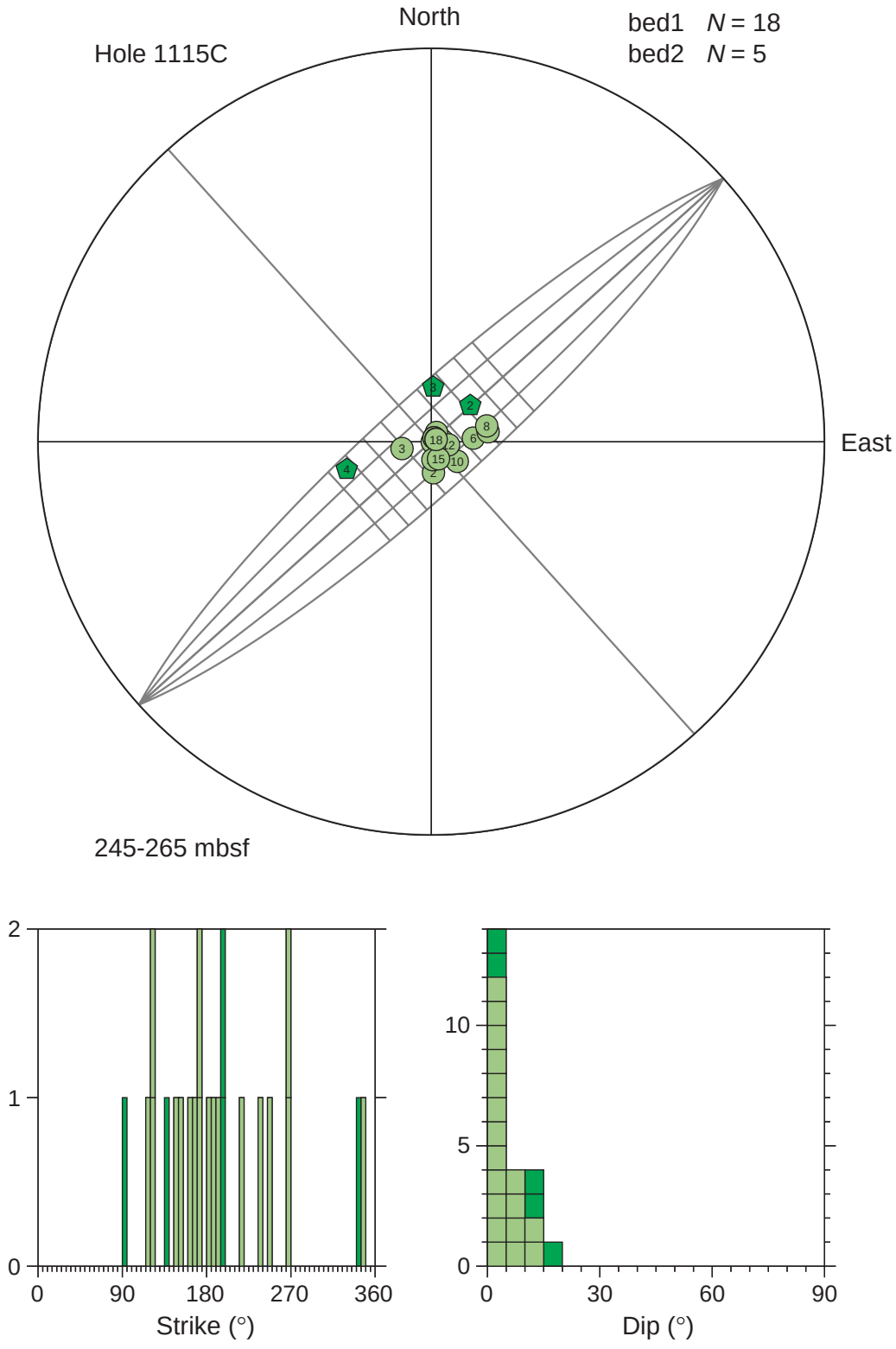

Figure F63. FMS image and analysis, Hole 1115C, 407–419.5 mbsf, reduced to ~70%. From left: (1) depth, (2) static FMS image, (3) dynamic FMS image with a 2-m color equalization sliding window; sinusoids correspond to the structural measurements, (4) structural measurement tadpoles, and (5) caliper measurements. The thin vertical green line on the FMS images indicates the orientation of pad 1, which corresponds to the C1 caliper reading. The tadpole position on the horizontal axis indicates the dip magnitude, and its tail points toward the dip direction.

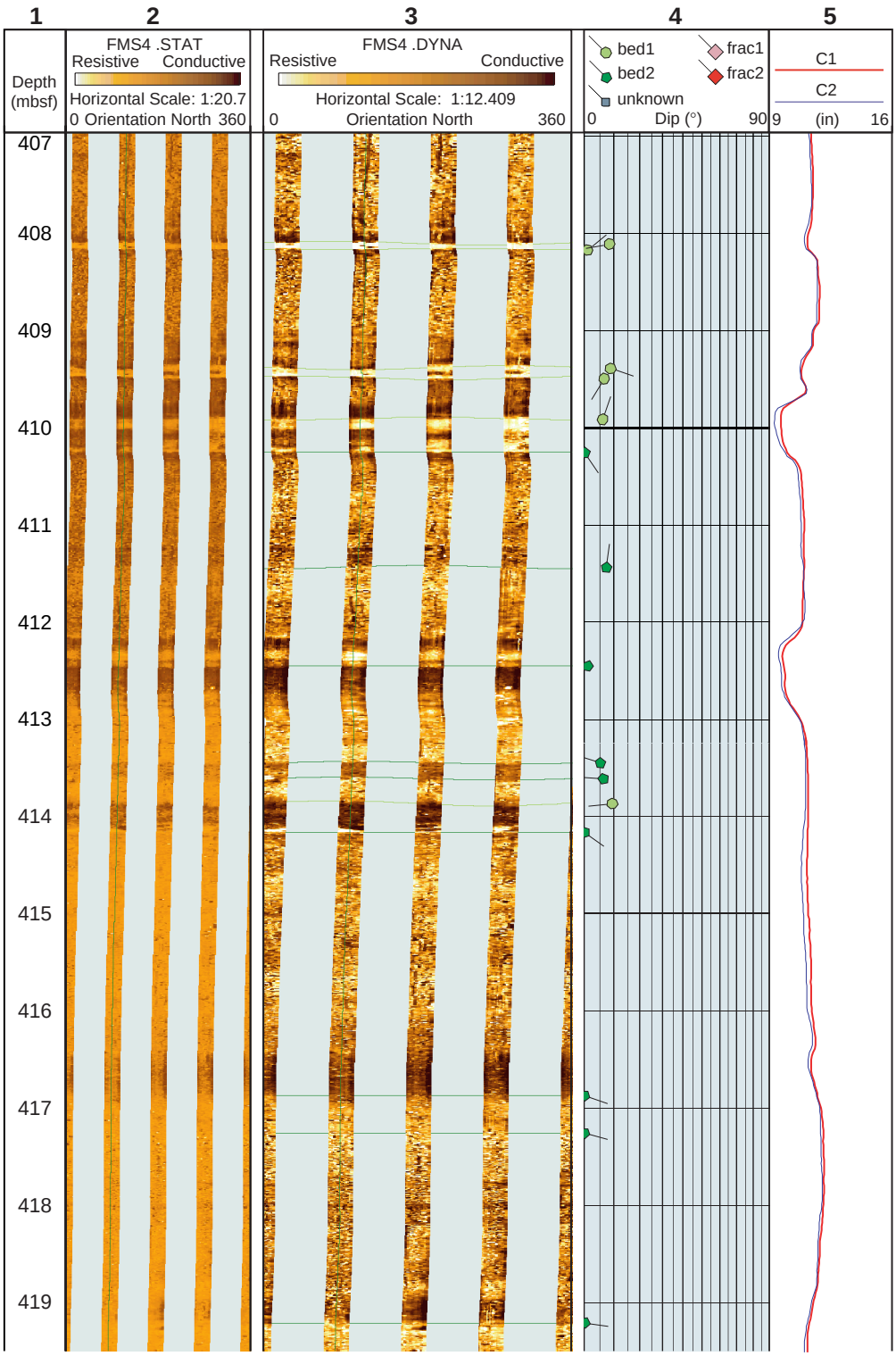

Figure F64. FMS image and analysis, Hole 1115C, 469–4815 mbsf, reduced to ~70%. From left: (1) depth, (2) static FMS image, (3) dynamic FMS image with a 2-m color equalization sliding window; sinusoids correspond to the structural measurements, (4) structural measurement tadpoles, and (5) caliper measurements. The thin vertical green line on the FMS images indicates the orientation of pad 1, which corresponds to the C1 caliper reading. The tadpole position on the horizontal axis indicates the dip magnitude, and its tail points toward the dip direction.

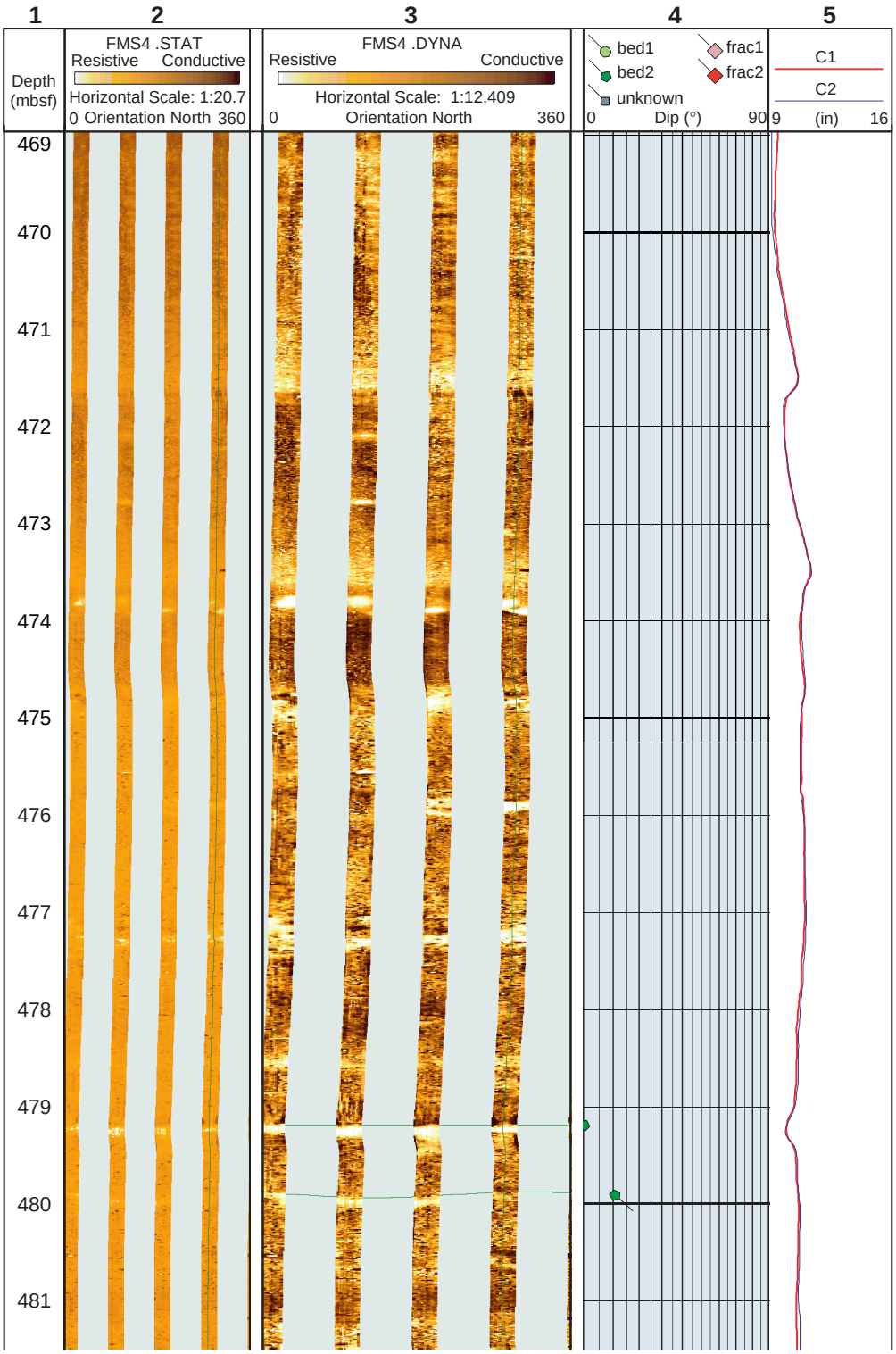

Figure F65. Structure orientation, Hole 1115C, 480–505 mbsf. Stereographic projection of poles to bed 1, bed 2, frac 2, and unknown structures (light green circles, darker green pentagons, red squares, and gray diamonds, respectively). Equal area stereographic projection, lower hemisphere. Strike and dip histograms of bedding only, where bed 1 and bed 2 are stacked with same color code as stereonet poles. Histograms use 5° bins. Strike is normalized so that the dip direction is 90° clockwise from strike.

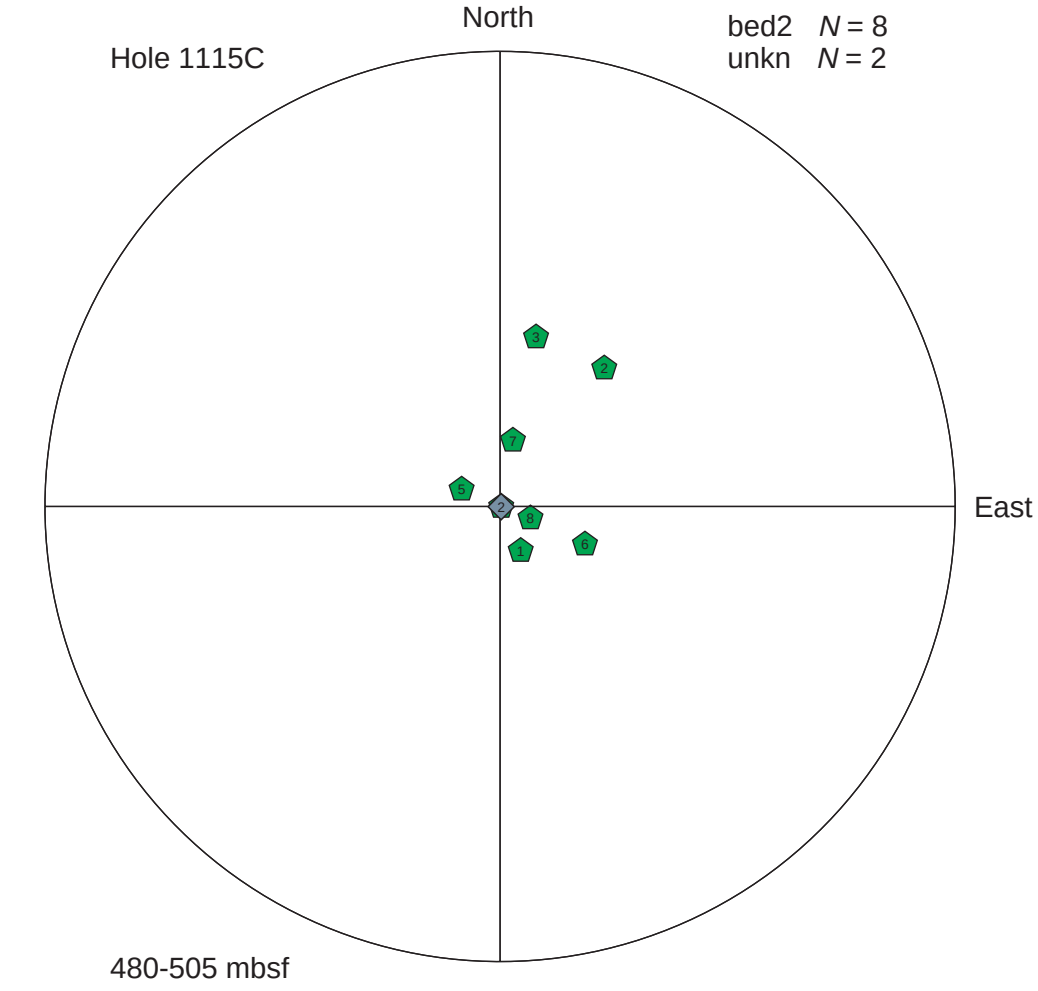

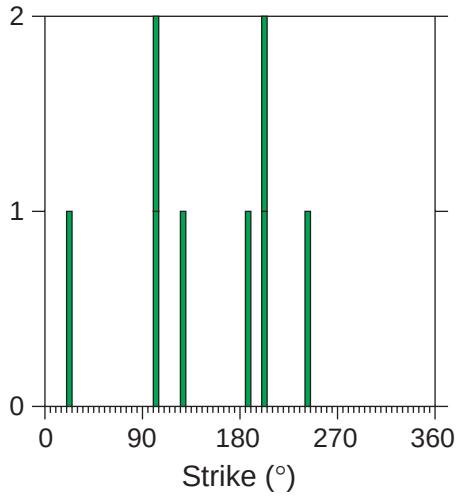

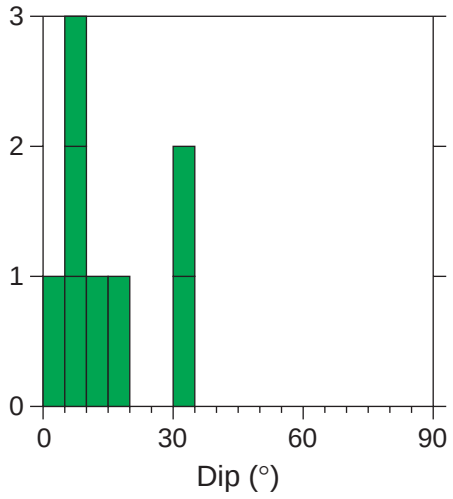

Figure F66. FMS image and analysis, Hole 1115C, 506.5–519 mbsf, reduced to ~70%. From left: (1) depth, (2) static FMS image, (3) dynamic FMS image with a 2-m color equalization sliding window; sinusoids correspond to the structural measurements, (4) structural measurement tadpoles, and (5) caliper measurements. The thin vertical green line on the FMS images indicates the orientation of pad 1, which corresponds to the C1 caliper reading. The tadpole position on the horizontal axis indicates the dip magnitude, and its tail points toward the dip direction.

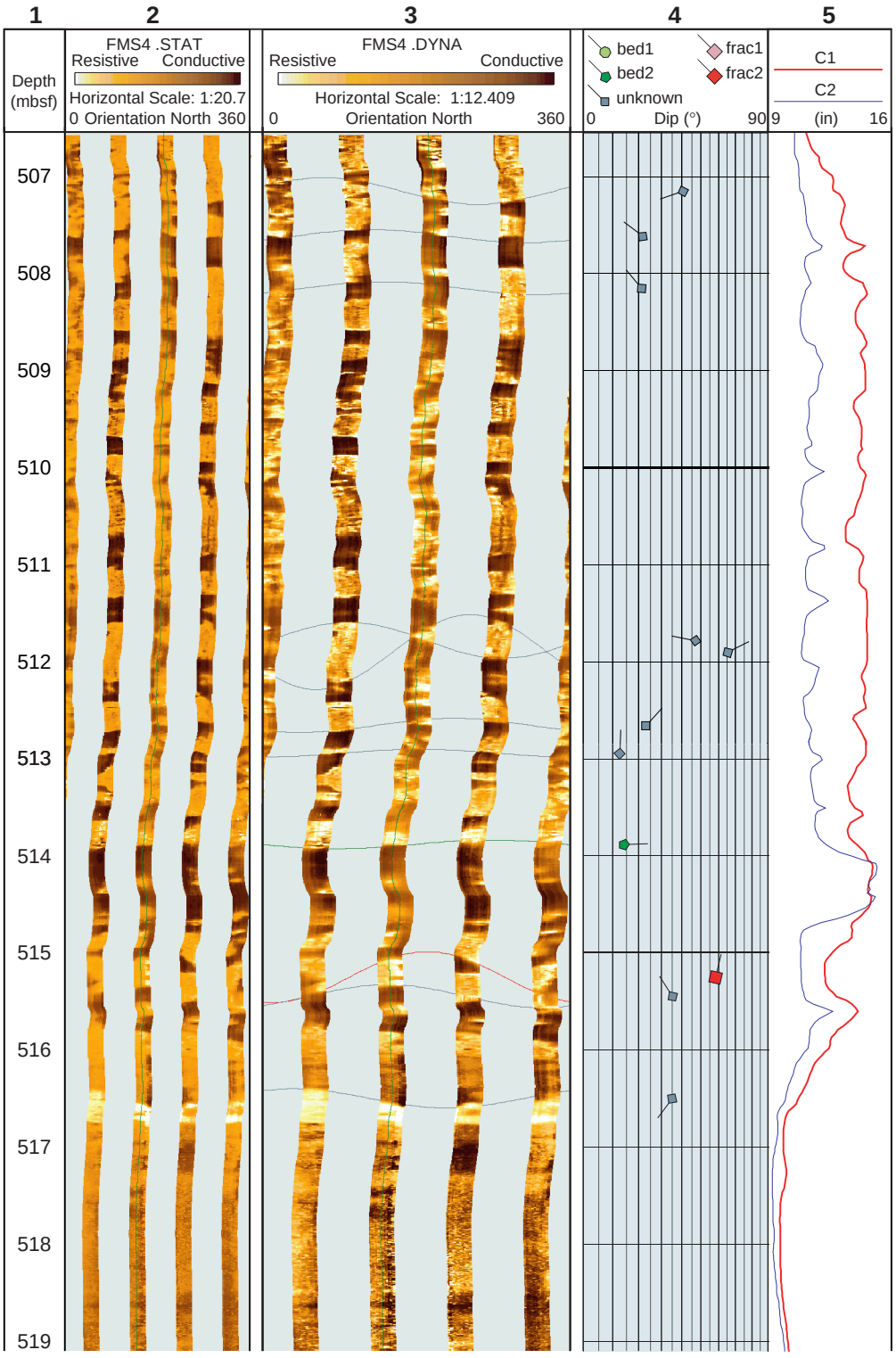

Figure F67. Structure orientation, Hole 1115C, 506–527 mbsf. Stereographic projection of poles to bed 1, bed 2, frac 2, and unknown structures (light green circles, darker green pentagons, red squares, and gray diamonds, respectively). Equal area stereographic projection, lower hemisphere. Strike and dip histograms of bedding only, where bed 1 and bed 2 are stacked with same color code as stereonet poles. Histograms use 5° bins. Strike is normalized so that the dip direction is 90° clockwise from strike.

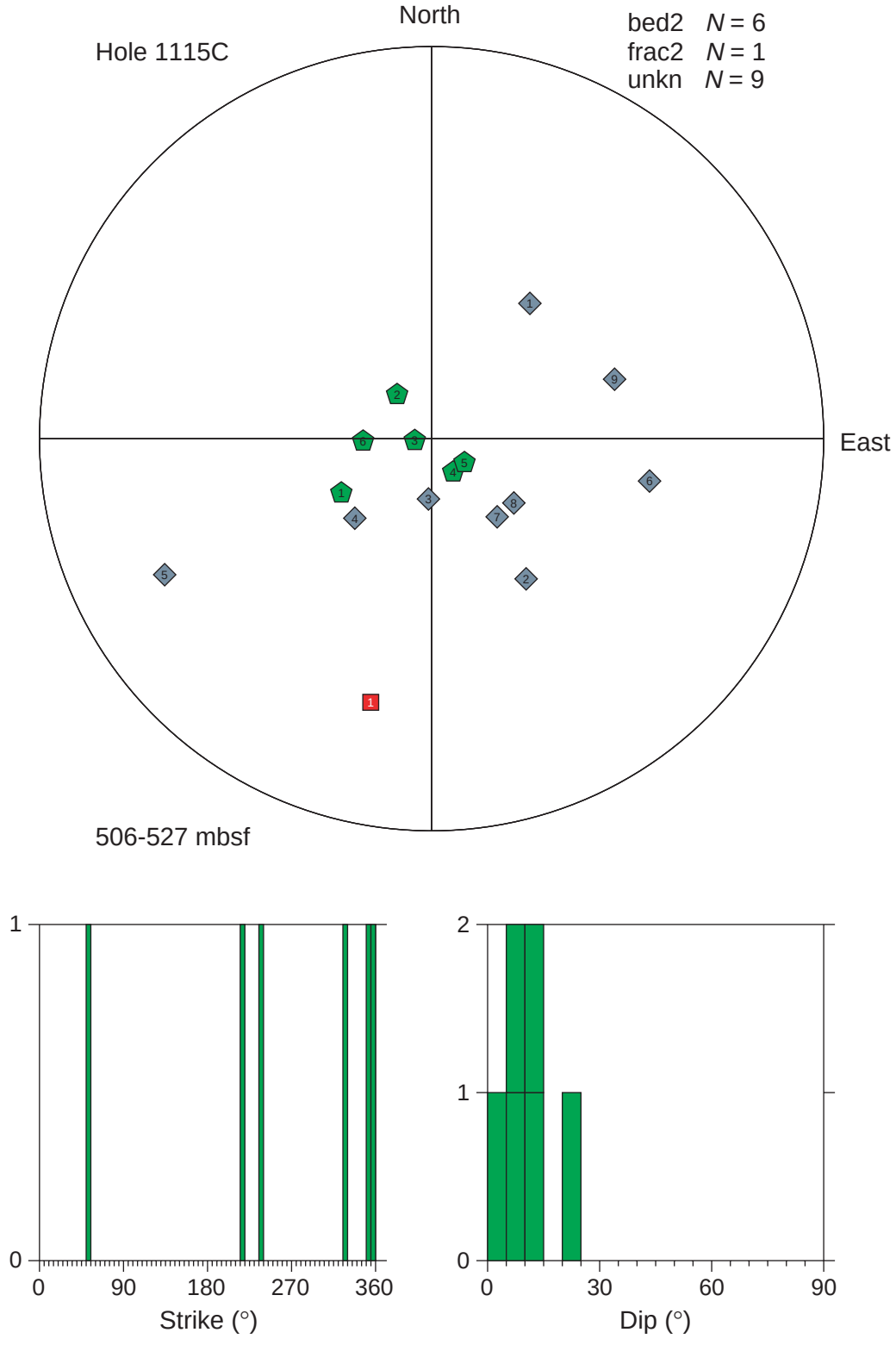

Figure F68. Structure orientation, Hole 1115C, 527–532 mbsf. Stereographic projection of poles to bed 1, bed 2, frac 2, and unknown structures (light green circles, darker green pentagons, red squares, and gray diamonds, respectively). Equal area stereographic projection, lower hemisphere. Strike and dip histograms of bedding only, where bed 1 and bed 2 are stacked with same color code as stereonet poles. Histograms use 5° bins. Strike is normalized so that the dip direction is 90° clockwise from strike. A partial 5° stereonet is shown in the background to highlight a cylindrical structure.

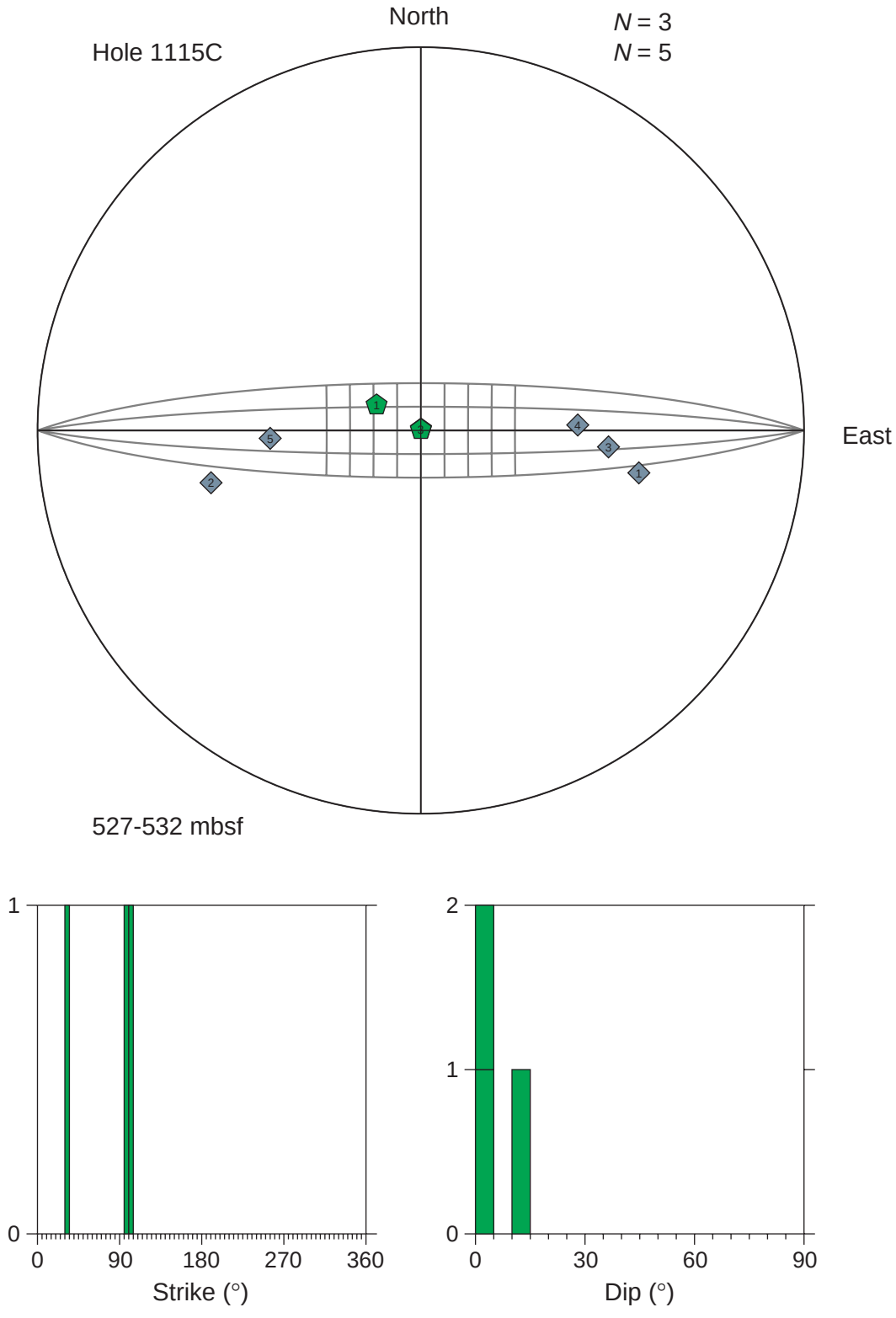

Figure F69. FMS image and analysis, Hole 1115C, 565–577.5 mbsf, reduced to ~70%. From left: (1) depth, (2) static FMS image, (3) dynamic FMS image with a 2-m color equalization sliding window; sinusoids correspond to the structural measurements, (4) structural measurement tadpoles, and (5) caliper measurements. The thin vertical green line on the FMS images indicates the orientation of pad 1, which corresponds to the C1 caliper reading. The tadpole position on the horizontal axis indicates the dip magnitude, and its tail points toward the dip direction.

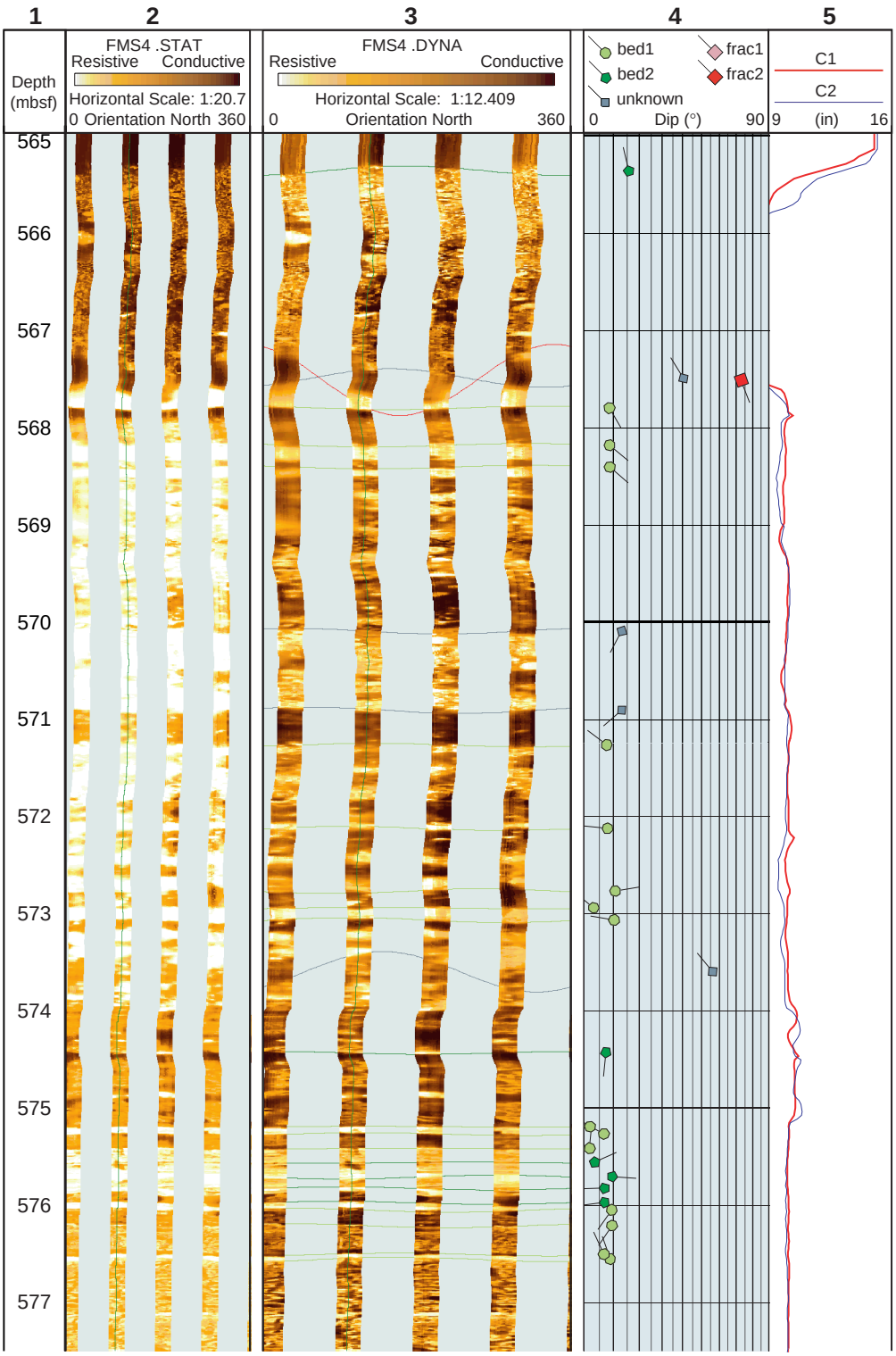

Figure F70. Structure orientation, Hole 1115C, 552–572 mbsf. Stereographic projection of poles to bed 1, bed 2, frac 2, and unknown structures (light green circles, darker green pentagons, red squares, and gray diamonds, respectively). Equal area stereographic projection, lower hemisphere. Strike and dip histograms of bedding only, where bed 1 and bed 2 are stacked with same color code as stereonet poles. Histograms use 5° bins. Strike is normalized so that the dip direction is 90° clockwise from strike.

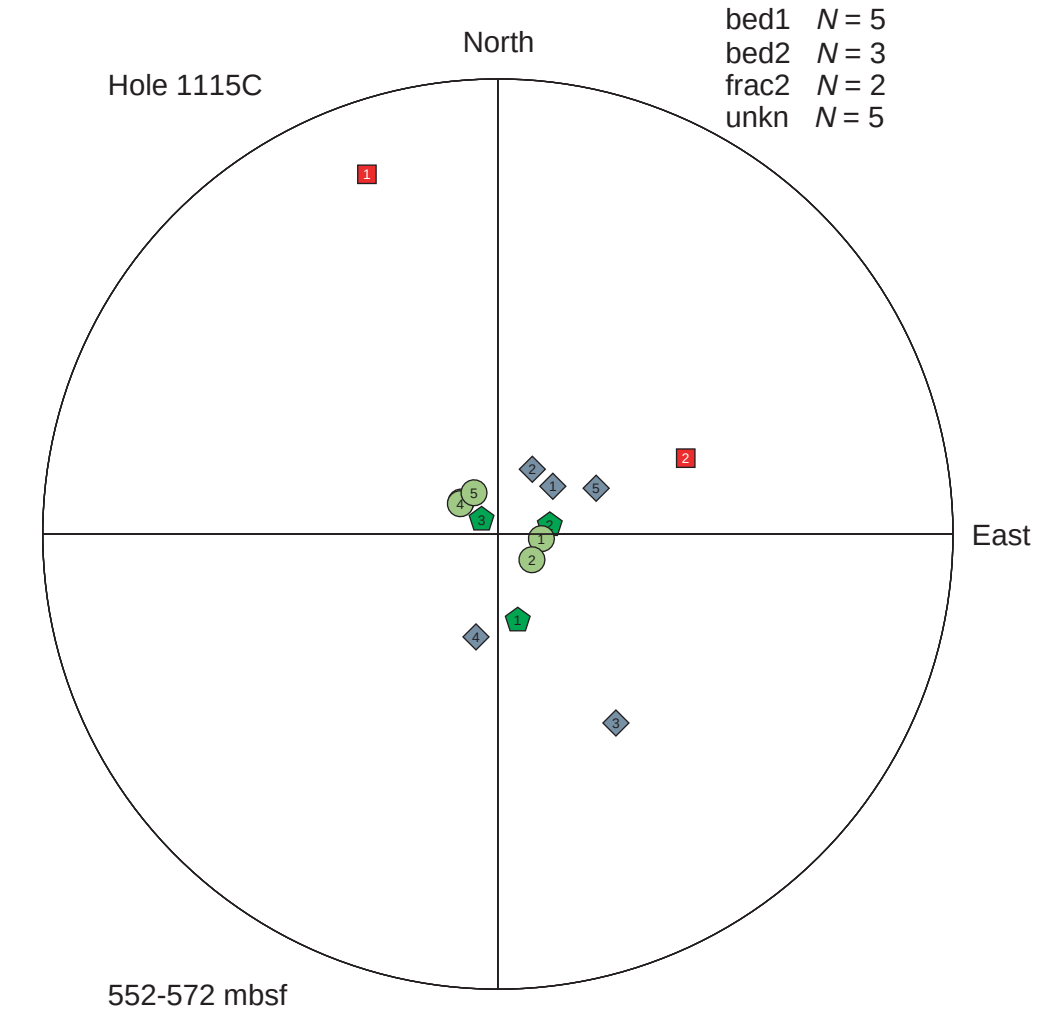

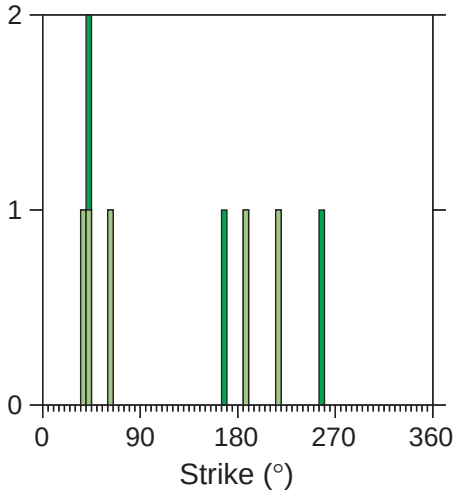

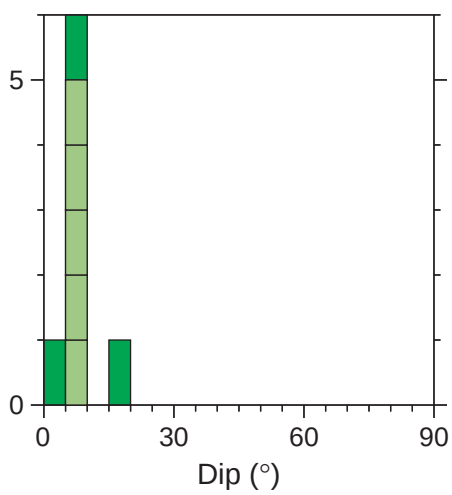

Figure F71. FMS image and analysis, Hole 1115C, 602–614.5 mbsf, reduced to ~70%. From left: (1) depth, (2) static FMS image, (3) dynamic FMS image with a 2-m color equalization sliding window; sinusoids correspond to the structural measurements, (4) structural measurement tadpoles, and (5) caliper measurements. The thin vertical green line on the FMS images indicates the orientation of pad 1, which corresponds to the C1 caliper reading. The tadpole position on the horizontal axis indicates the dip magnitude, and its tail points toward the dip direction.

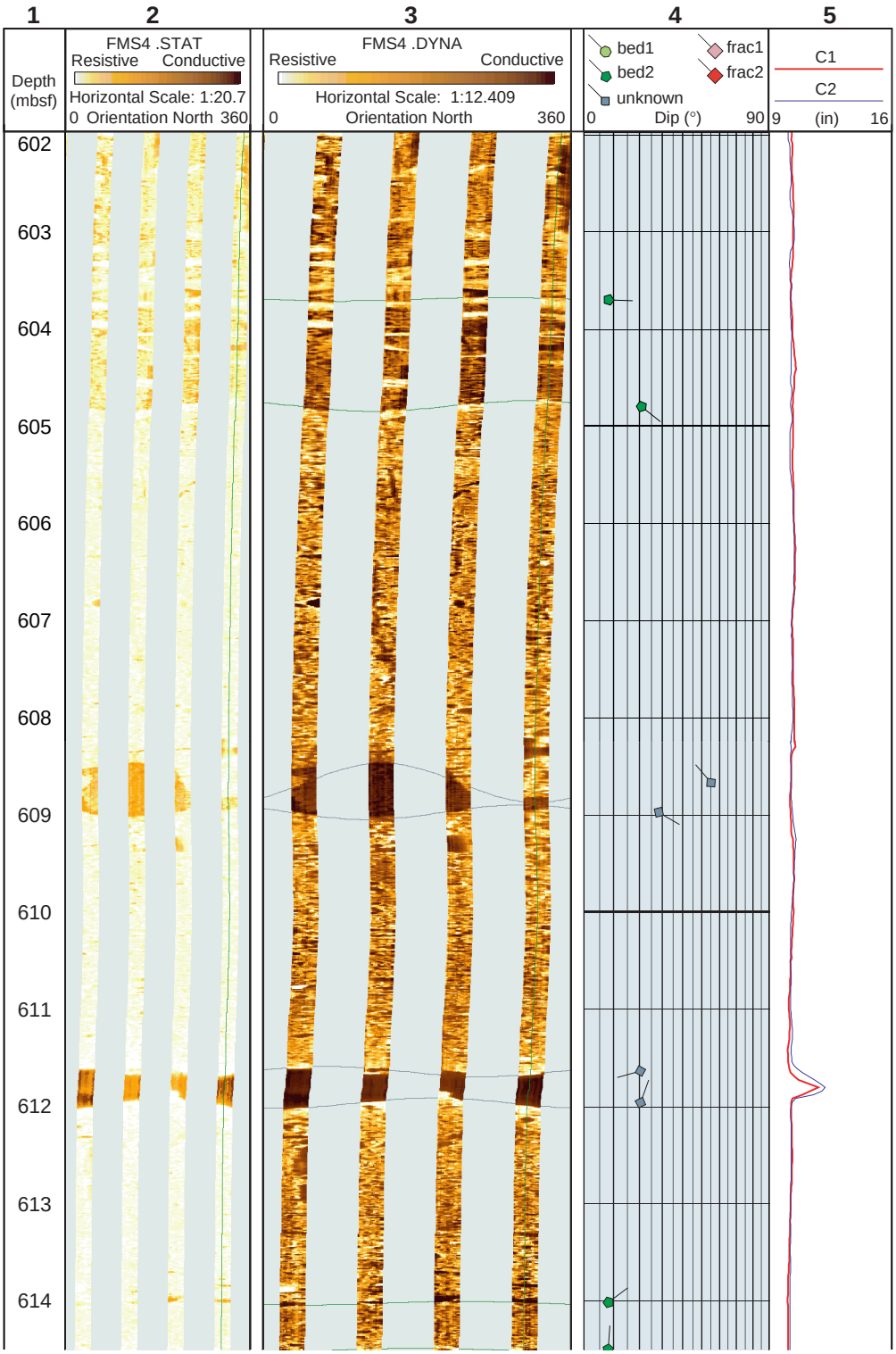

Figure F72. FMS image and analysis, Hole 1115C, 615–630 mbsf, reduced to ~70%. From left: (1) depth, (2) static FMS image, (3) dynamic FMS image with a 2-m color equalization sliding window; sinusoids correspond to the structural measurements, (4) structural measurement tadpoles, and (5) caliper measurements. The thin vertical green line on the FMS images indicates the orientation of pad 1, which corresponds to the C1 caliper reading. The tadpole position on the horizontal axis indicates the dip magnitude, and its tail points toward the dip direction.

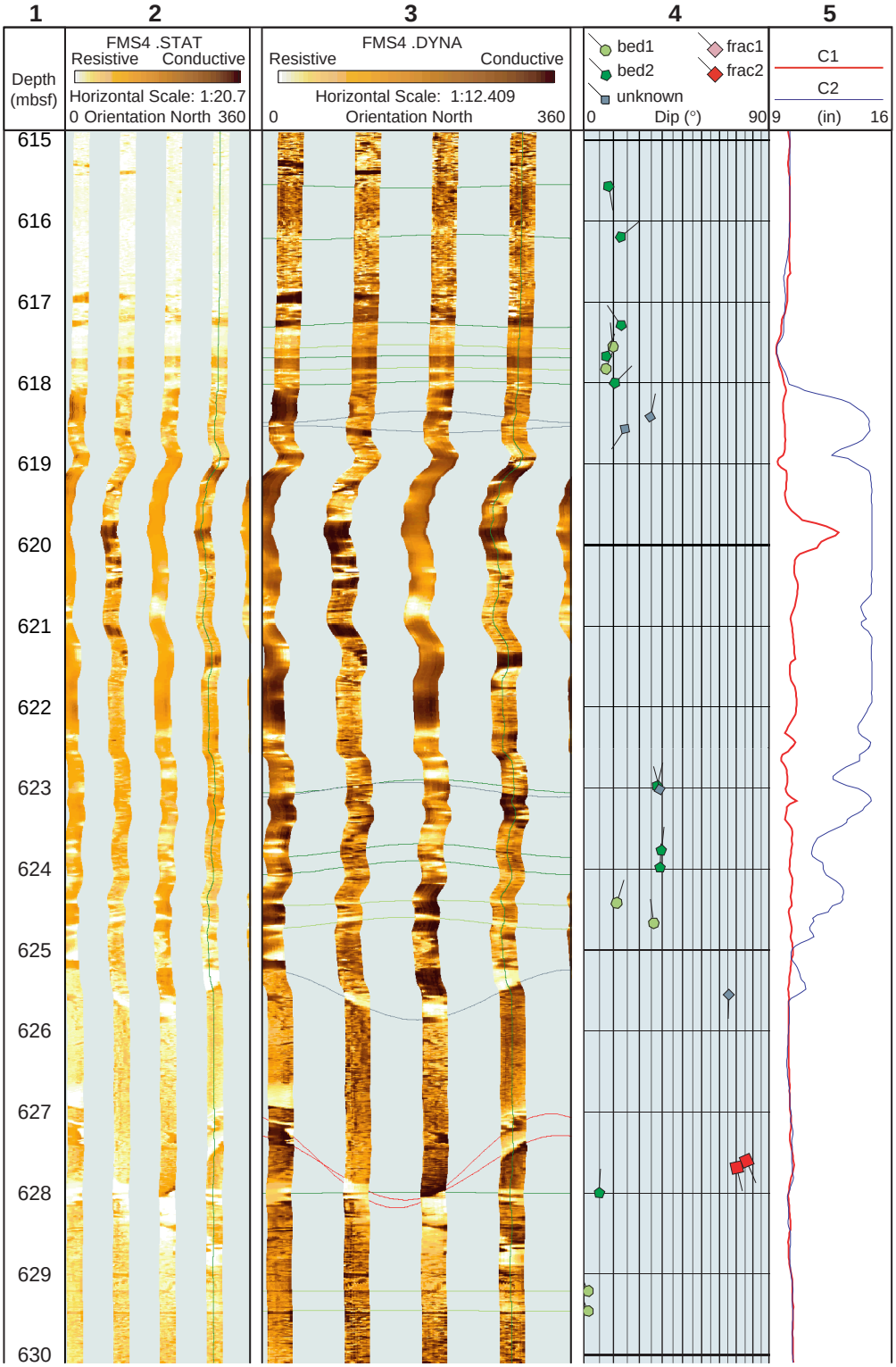

Figure F73. Structure orientation, Hole 1115C, 615–620 mbsf. Stereographic projection of poles to bed 1, bed 2, frac 2, and unknown structures (light green circles, darker green pentagons, red squares, and gray diamonds, respectively). Equal area stereographic projection, lower hemisphere. Strike and dip histograms of bedding only, where bed 1 and bed 2 are stacked with same color code as stereonet poles. Histograms use 5° bins. Strike is normalized so that the dip direction is 90° clockwise from strike.

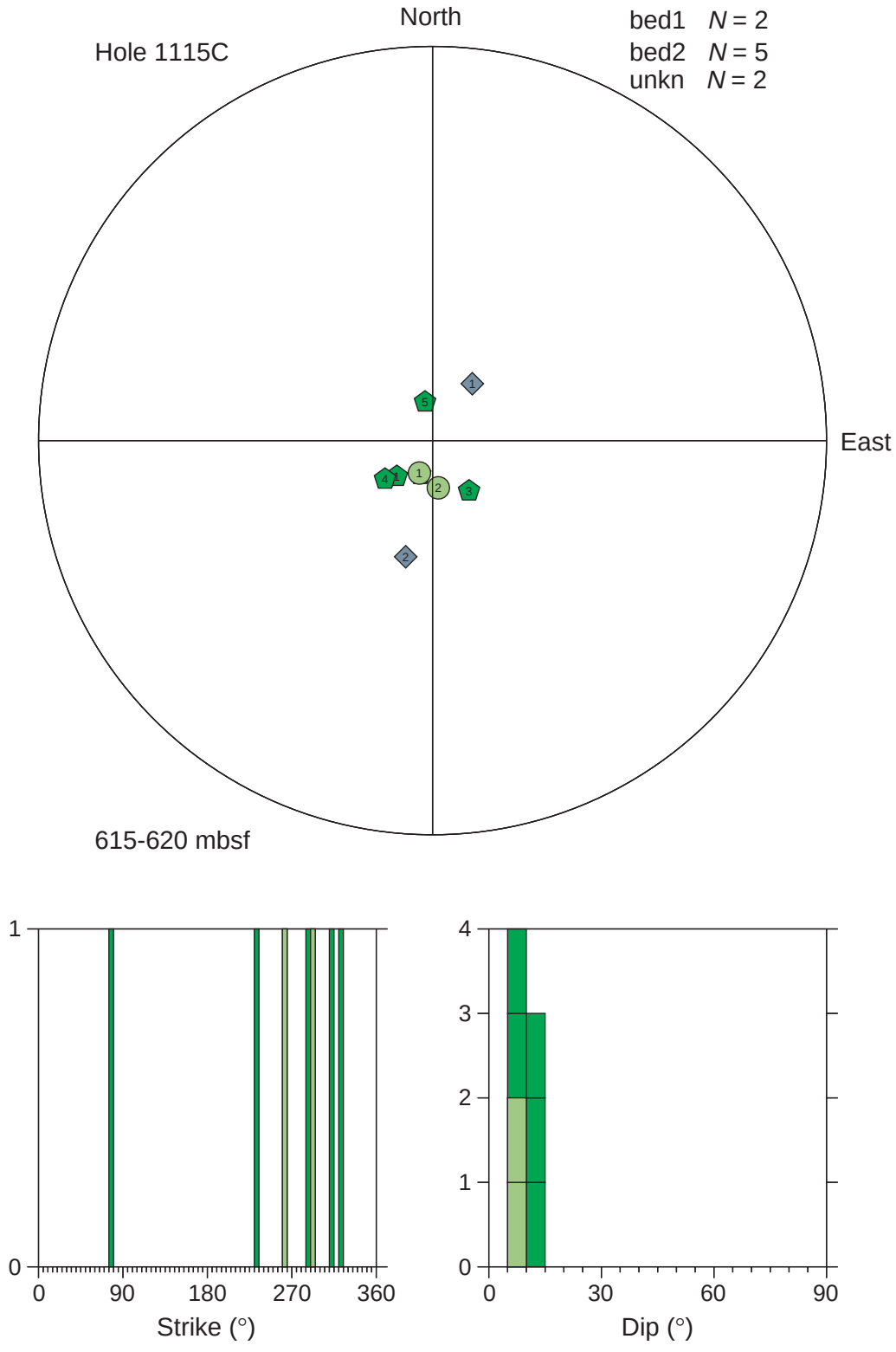

Figure F74. Structure orientation, Hole 1115C, 622–634 mbsf. Stereographic projection of poles to bed 1, bed 2, frac 2, and unknown structures (light green circles, darker green pentagons, red squares, and gray diamonds, respectively). Equal area stereographic projection, lower hemisphere. Strike and dip histograms of bedding only, where bed 1 and bed 2 are stacked with same color code as stereonet poles. Histograms use 5° bins. Strike is normalized so that the dip direction is 90° clockwise from strike. A partial 5° stereonet is shown in the background to highlight a cylindrical structure.

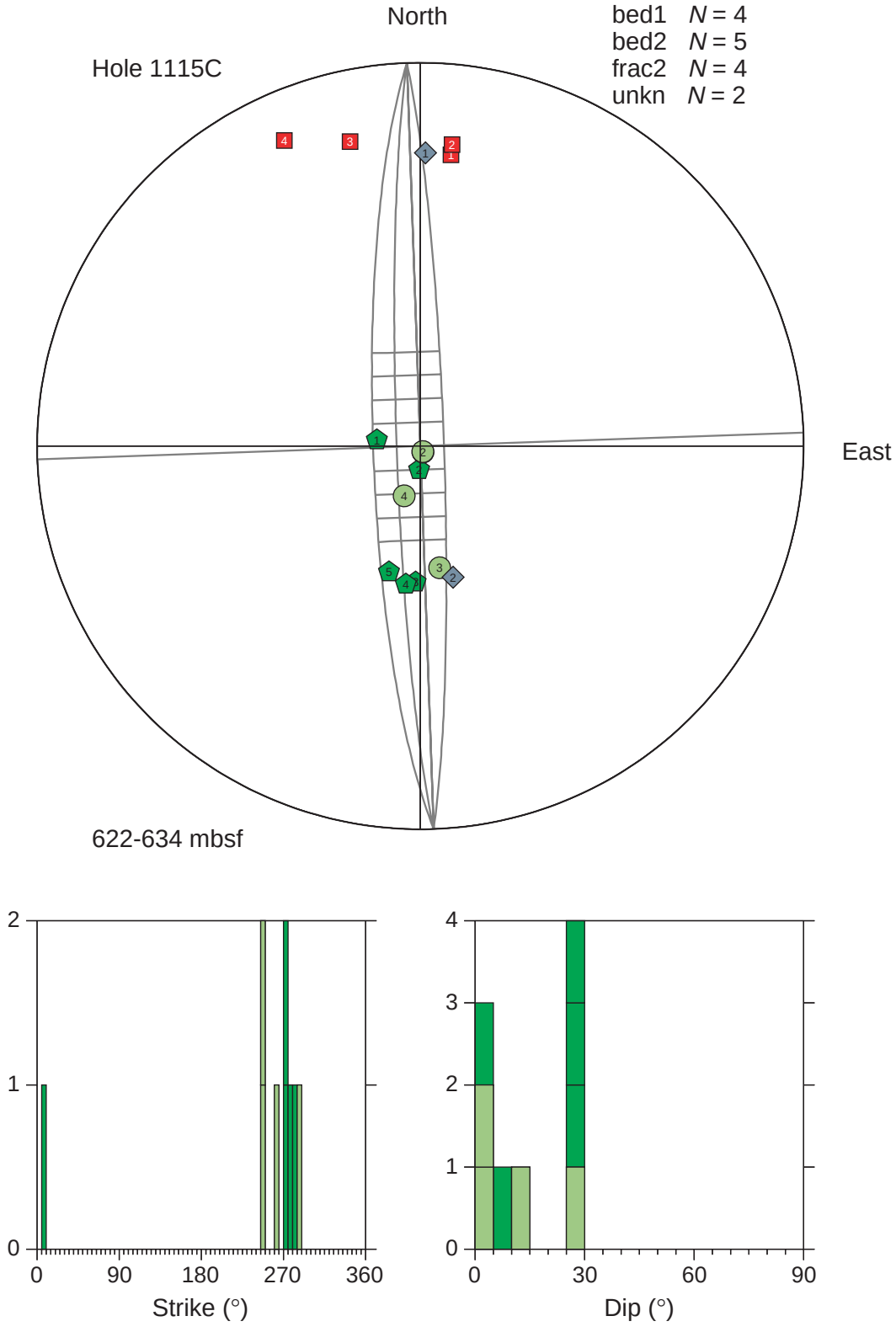

Figure F75. FMS image and analysis, Hole 1115C, 655–667.5 mbsf, reduced to ~70%. From left: (1) depth, (2) static FMS image, (3) dynamic FMS image with a 2-m color equalization sliding window; sinusoids correspond to the structural measurements, (4) structural measurement tadpoles, and (5) caliper measurements. The thin vertical green line on the FMS images indicates the orientation of pad 1, which corresponds to the C1 caliper reading. The tadpole position on the horizontal axis indicates the dip magnitude, and its tail points toward the dip direction.

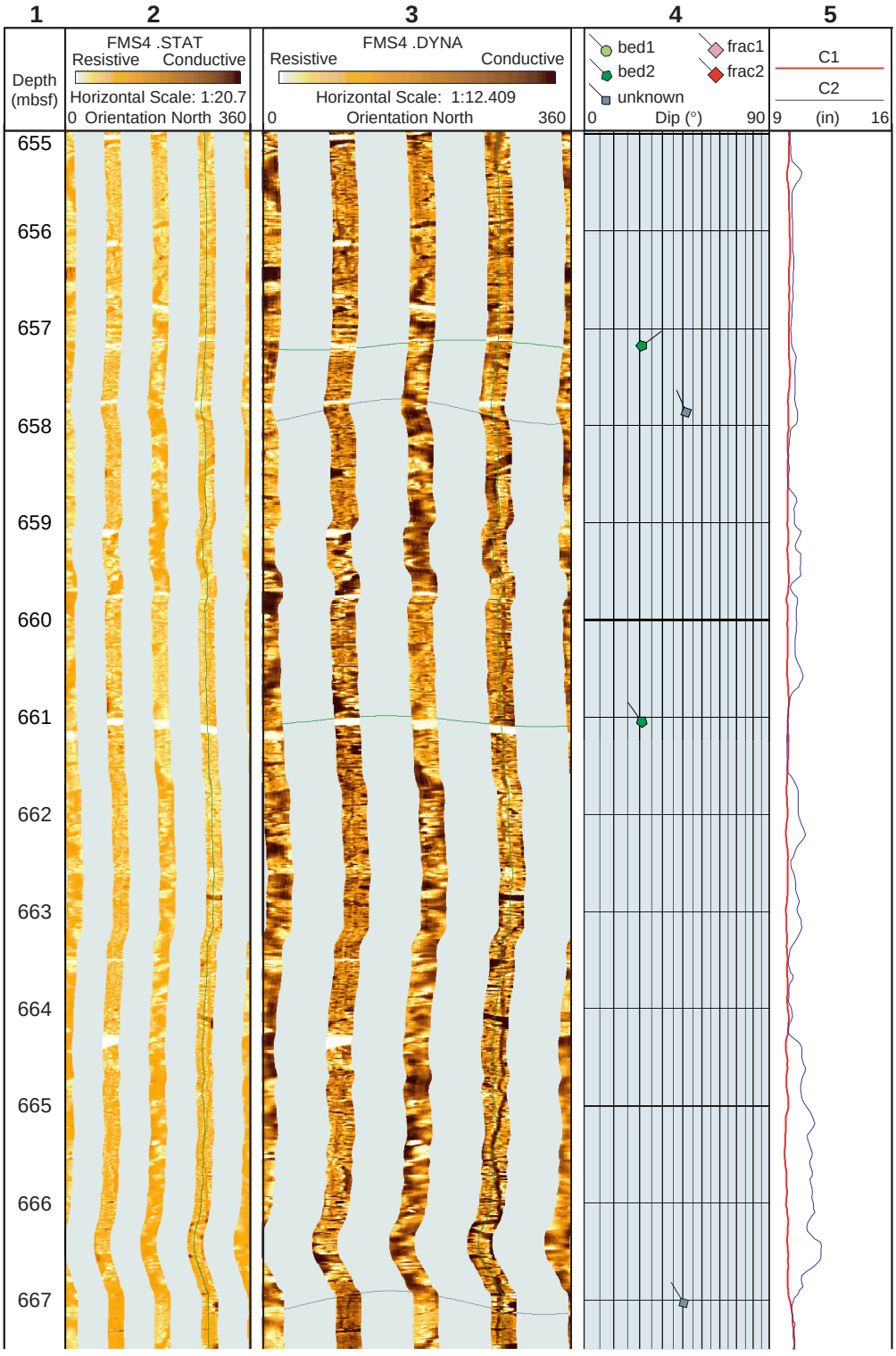

Figure F76. FMS image and analysis, Hole 1115C, 713–725.5 mbsf, reduced to ~70%. From left: (1) depth, (2) static FMS image, (3) dynamic FMS image with a 2-m color equalization sliding window; sinusoids correspond to the structural measurements, (4) structural measurement tadpoles, and (5) caliper measurements. The thin vertical green line on the FMS images indicates the orientation of pad 1, which corresponds to the C1 caliper reading. The tadpole position on the horizontal axis indicates the dip magnitude, and its tail points toward the dip direction.

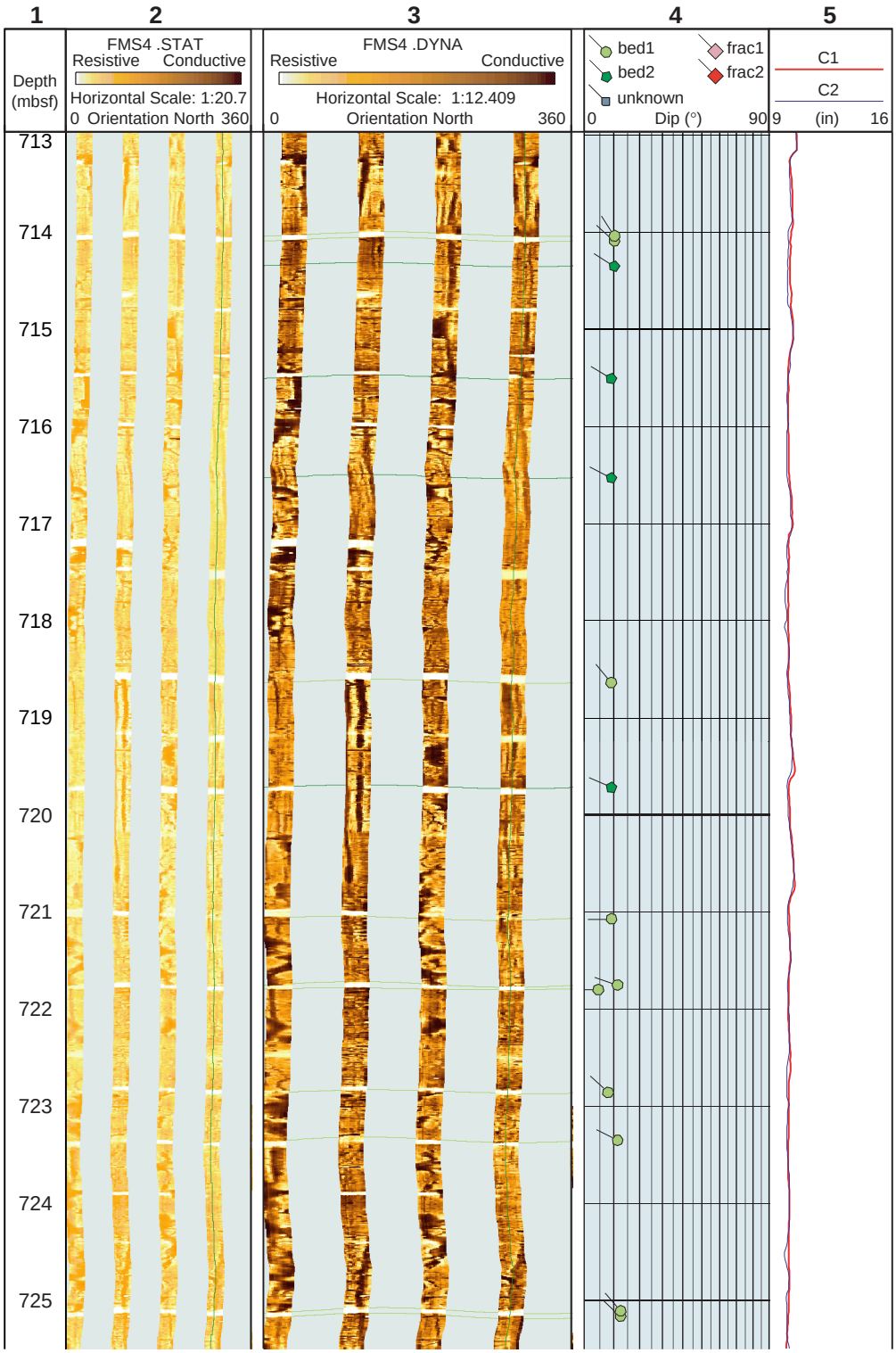

Figure F77. Structure orientation, Hole 1115C, 695–785 mbsf. Stereographic projection of poles to bed 1, bed 2, frac 2, and unknown structures (light green circles, darker green pentagons, red squares, and gray diamonds, respectively). Equal area stereographic projection, lower hemisphere. Strike and dip histograms of bedding only, where bed 1 and bed 2 are stacked with same color code as stereonet poles. Histograms use 5° bins. Strike is normalized so that the dip direction is 90° clockwise from strike.

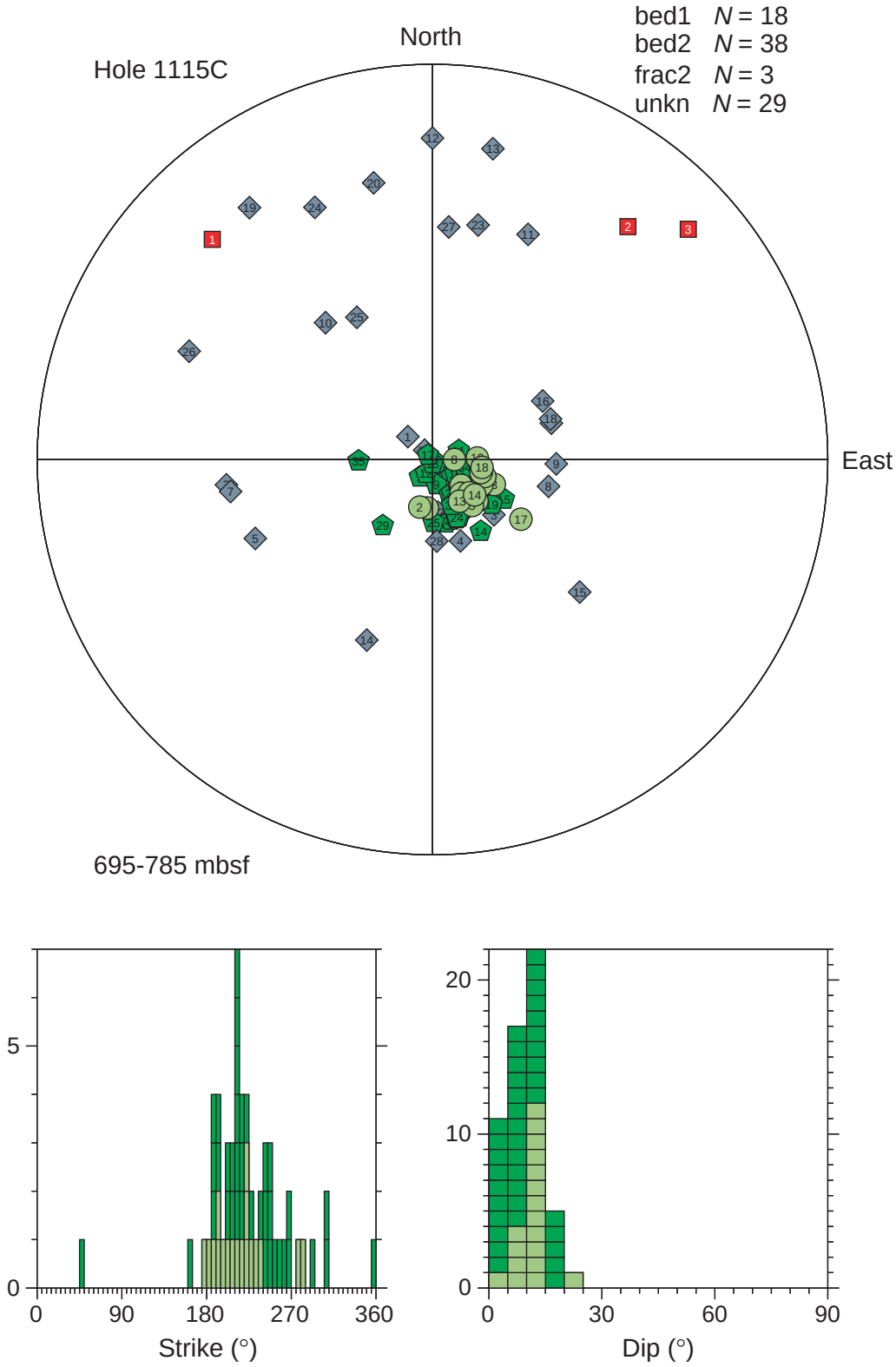

Figure F78. Bedding orientation, Hole 1115C, 573.5–695 mbsf. Equal area stereographic projection, lower hemisphere. Poles to bed 1 and bed 2 are shown as light green circles and darker green pentagons, respectively. Strike and dip histograms use 5° bins. Strike is normalized so that the dip direction is 90° clockwise from strike. Bed 1 and bed 2 histograms are stacked with same color code as stereonet poles.

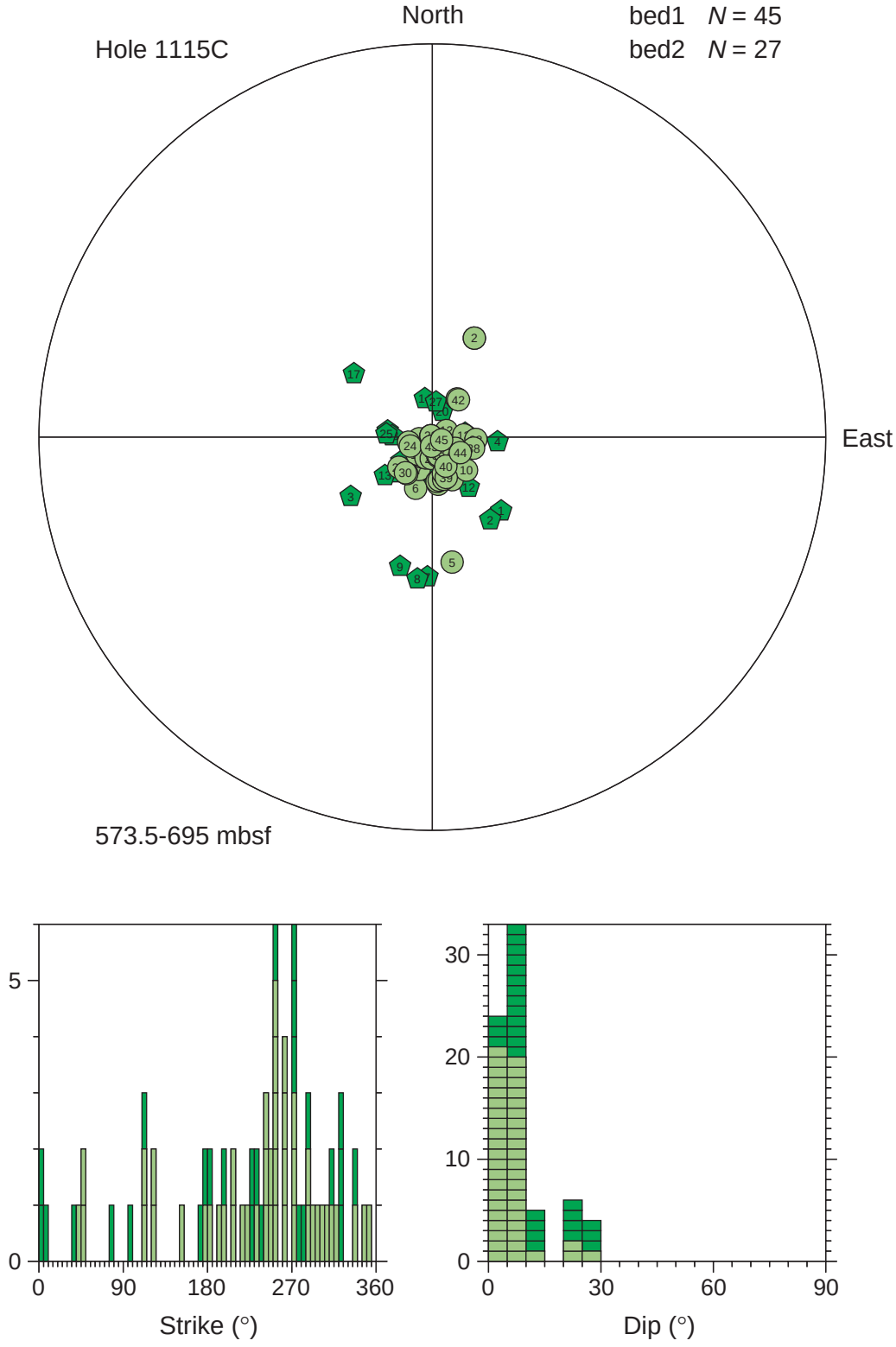

Figure F79. Spherically focused resistivity (SFLU) vs. photoelectric effect (PEFL) and neutron lithodensity porosity difference (DPORO) in Holes 1118A, 1109D, and 1115C.

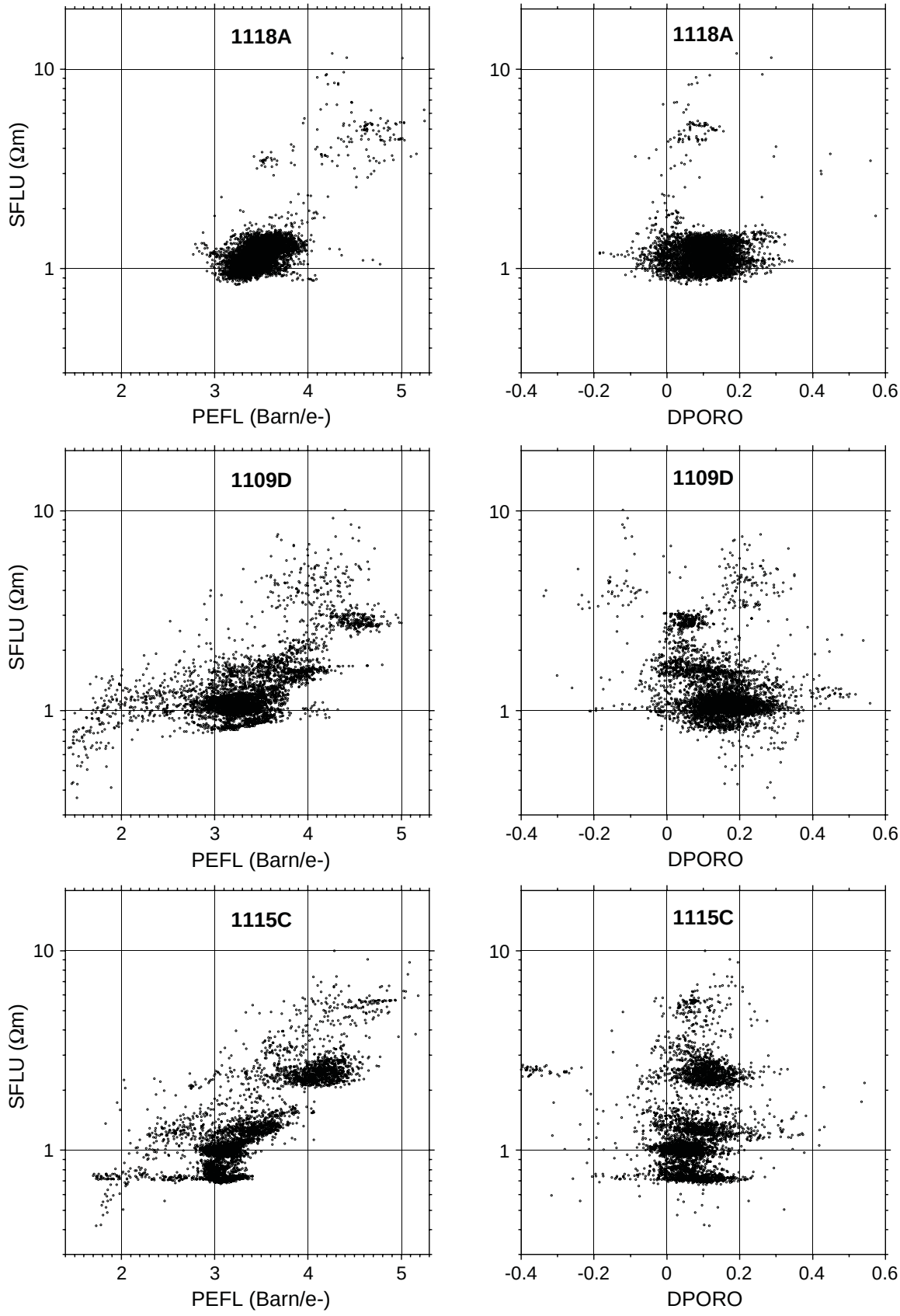

Table T1. Core and log data coverage, Leg 180.

Hole:	1114A	1118A	1109C and 1109D	1115B and 1115C
Maximum penetration (m):	352.8	926.6	802.0	802.5
Cored section length (m):	352.8	721.6	824.9	812.4
Recovered core length (m):	43.8	466.2	623.0	578.5
Core recovery (%):	12	65	75	71
FMS section (mbsf):	106–296	138–889	116–781	119–785
FMS section length (m):	190	751	665	666
(FMS/core) length ratio:	4.3	1.6	1.1	1.2

Table T2. Lithologic unit intervals and summary descriptions.

Lithologic unit	Site 1118	Site 1109	Site 1115
I	Silty claystone and clayey siltstone interbedded with sandstone and siltstone 205–377.8 mbsf	Calcareous sand, silt, and clay with volcaniclastic sand and volcanic ash 0–83.4 mbsf	Nannofossil ooze with volcanic ash 0–35.7 mbsf
II	Claystone, siltstone, and sandstone 377.8–492.4 mbsf	Greenish gray clay interbedded with abundant volcaniclastic sand 83.4–169.7 mbsf	Nannofossil-rich silty clay with volcanic ash layers 35.7–149.7 mbsf
III	Silty claystone and clayey siltstone interbedded with sandstone and siltstone 492.4–679.3 mbsf	Clayey silt and silty clay interbedded with clayey silt to coarse sand 169.7–246.7 mbsf	Calcareous silty clay/claystone with volcaniclastic sand/sandstone layers 149.7–388.5 mbsf
IV	Silty claystone and clayey siltstone interbedded with volcaniclastic sandstone 679.3–810.8 mbsf	Clayey silt and silty clay 246.7–352.8 mbsf	Calcareous sandy silty claystone 388.5–417.3 mbsf
V	Mixed sandstone, siltstone, volcaniclastic sandstone 810.8–857.1 mbsf	Clayey siltstone and silty claystone interbedded with volcaniclastic sand 352.8–387.6 mbsf	Mixed silty sandstone 417.3–474.9 mbsf
VI	Limestone 857.1–859mbsf	Clayey siltstone and silty claystone interlayered with clayey siltstone to coarse-grained sandstone 387.6–570.4 mbsf	Sandy siltstone and silty sandstone 474.9–513.4 mbsf
VII	Paraconglomerate 859–873.1 mbsf	Sandstone, packstone, and grainstone 570.4–671.8 mbsf	Siltstone 513.4–551.8 mbsf
VIII	Dolerite conglomerate 873.1–929.6 mbsf	Silty claystone and clayey siltstone 671.8–705.3 mbsf	Organic-rich silty claystone and limestone 551.8–565.7 mbsf
IX	NA	Clayey siltstone and sandstone 705.3–737.1 mbsf	Conglomerate, sandstone, and siltstone 565.7–571.9 mbsf
X	NA	Dolerite pebbles and conglomerate 737.1–772.9 mbsf	Sandstone, siltstone, claystone, and conglomerate 571.9–603.9 mbsf
XI	NA	Dolerite 772.9–802.5 mbsf	Calcareous sandstone, packstone, siltstone, and silty claystone 603.9–657.8 mbsf
XII	NA	NA	Sandy siltstone and silty sandstone 657.8–802.5 mbsf
First induration	Above Core 180-1118A-1R Above 205 mbsf	Core 180-1109C-4H 36 mbsf	Core 180-1115B-28X 256 mbsf
Reference	Fig. F1 (Shipboard Scientific Party, 1999e)	Fig. F1 (Shipboard Scientific Party, 1999c)	Fig. F1 (Shipboard Scientific Party, 1999d)

Table T3. Number of planar structure measurements.

Hole:	1118A	1109D	1115C
Bedding 1	253	381	185
Bedding 2	336	90	231
Total bed	589	471	416
Fracture1	0	7	0
Fracture 2	24	37	10
Total fracture	24	44	10
Unknown	72	34	79

Table T4. Bedding folding axis.

Depth range (mbsf)	Axis trend	Number of faults	Number of compatible faults	Dip direction of compatible fault	Core observations	Possible interpretation
Hole 1118A						
250–280	67	0	0		Soft sediment deformation	Slump
275–340	52	3	1	S	Soft sediment deformation, slump	Roll over
390–410	104	0	0		Soft sediment deformation, slump	Slump
570–596	97	6	2	NNW, NNE	Fracture zone 1, Soft sediment deformation	Drag fold
840–890	77	4	1	SSE	Breccia	Roll over
Hole 1109A						
190–202	59	0	0		Core induced deformation	Depositional structure
218–223	6	1	0			Slump
240–252	152	0	0		Core induced deformation	Depositional structure
310–320	75	0	0			Depositional structure
Hole 1115C						
622–634	88	4	2	S	Fracture zone 2	Roll over

Table T5. Sand and carbonate FMS image facies.

Hole:	1118A	1109D	1115C
Sand	Figure **F23,** p. 50	Figure **F46,** p. 75 (593–603 mbsf)	Figure **F66,** p. 97 (517–519 mbsf)
	Figure **F24,** p. 51	Figure **F47,** p. 76 (644–647 mbsf)	Figure **F72,** p. 103 (618–625 mbsf)
Calcareous sand	Figure **F13,** p. 40	Figure **F37,** p. 66 (220–222 mbsf)	Figure **F64,** p. 95 (469–474 mbsf)
	Figure **F25,** p. 52 (859–860 mbsf)	Figure **F38,** p. 67 (230–232 mbsf)	Figure **F71,** p. 102 (602–604 mbsf)
		Figure **F47,** p. 76 (640–642 mbsf)	
Sandy carbonate		Figure **F35,** p. 64 (197–200 mbsf)	Figure **F64,** p. 95 (475–479 mbsf)
Carbonate	Figure **F25,** p. 52 (856–858 mbsf)	Figure **F38,** p. 67 (233–234 mbsf)	Figure **F71,** p. 102 (605–614 mbsf)
		Figure **F47,** p. 76 (642–643 mbsf)	
		Figure **F47,** p. 76 (648–652 mbsf)	
		Figure **F48,** p. 77 (671–674 mbsf)	

Figure AF1. FMS image and analysis, Hole 1118A. From left: (1) depth, (2) static FMS image, (3) dynamic FMS image with a 2-m color equalization sliding window with sinusoids corresponding to the structural measurements, (4) structural interpretation tadpoles, and (5) caliper measurements. The thin vertical green line on the FMS images indicates the orientation of pad 1, which corresponds to the C1 caliper reading. The tadpole position on the horizontal axis indicates the dip magnitude, and its tail points toward the dip direction. The global image is cut in consecutive page size pieces. (Continued on next 15 pages.)

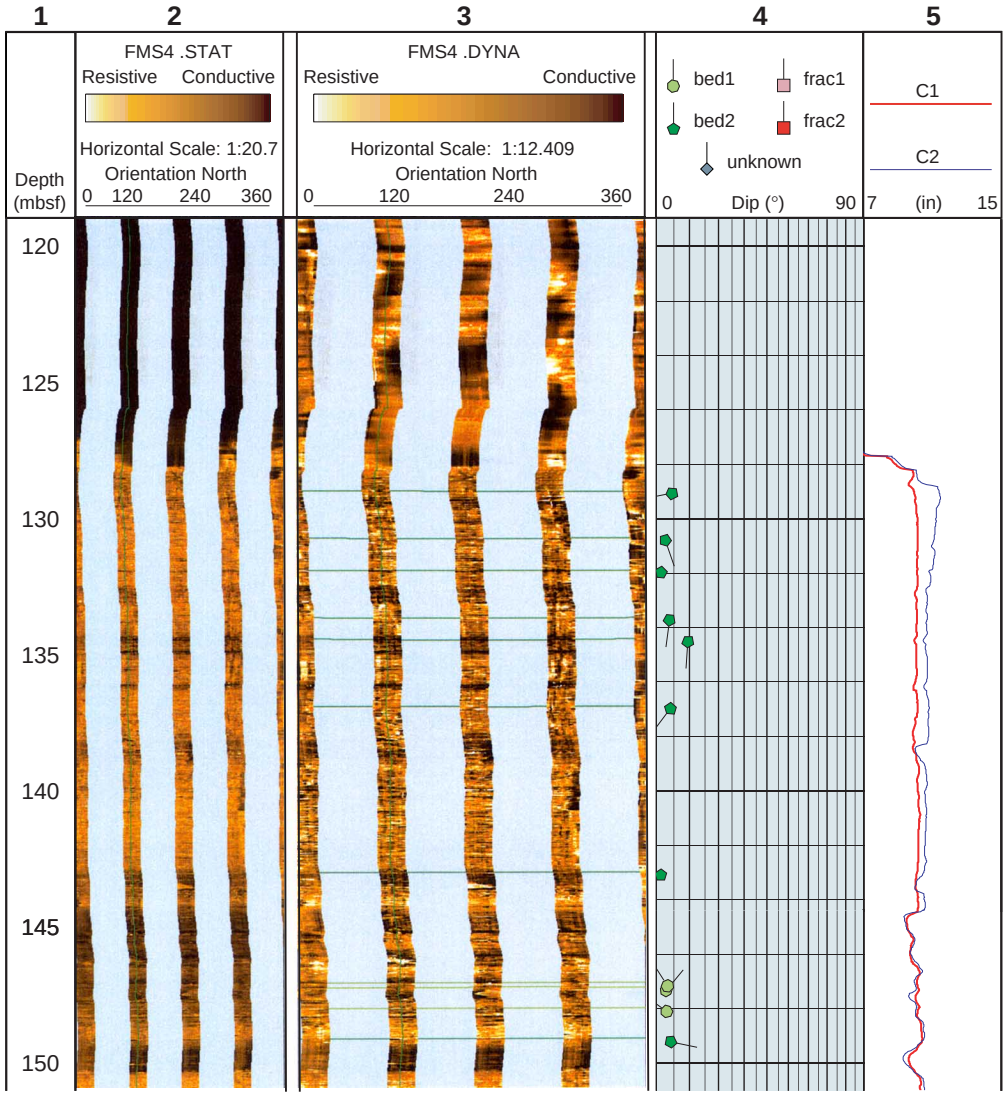

Figure AF1 (continued).

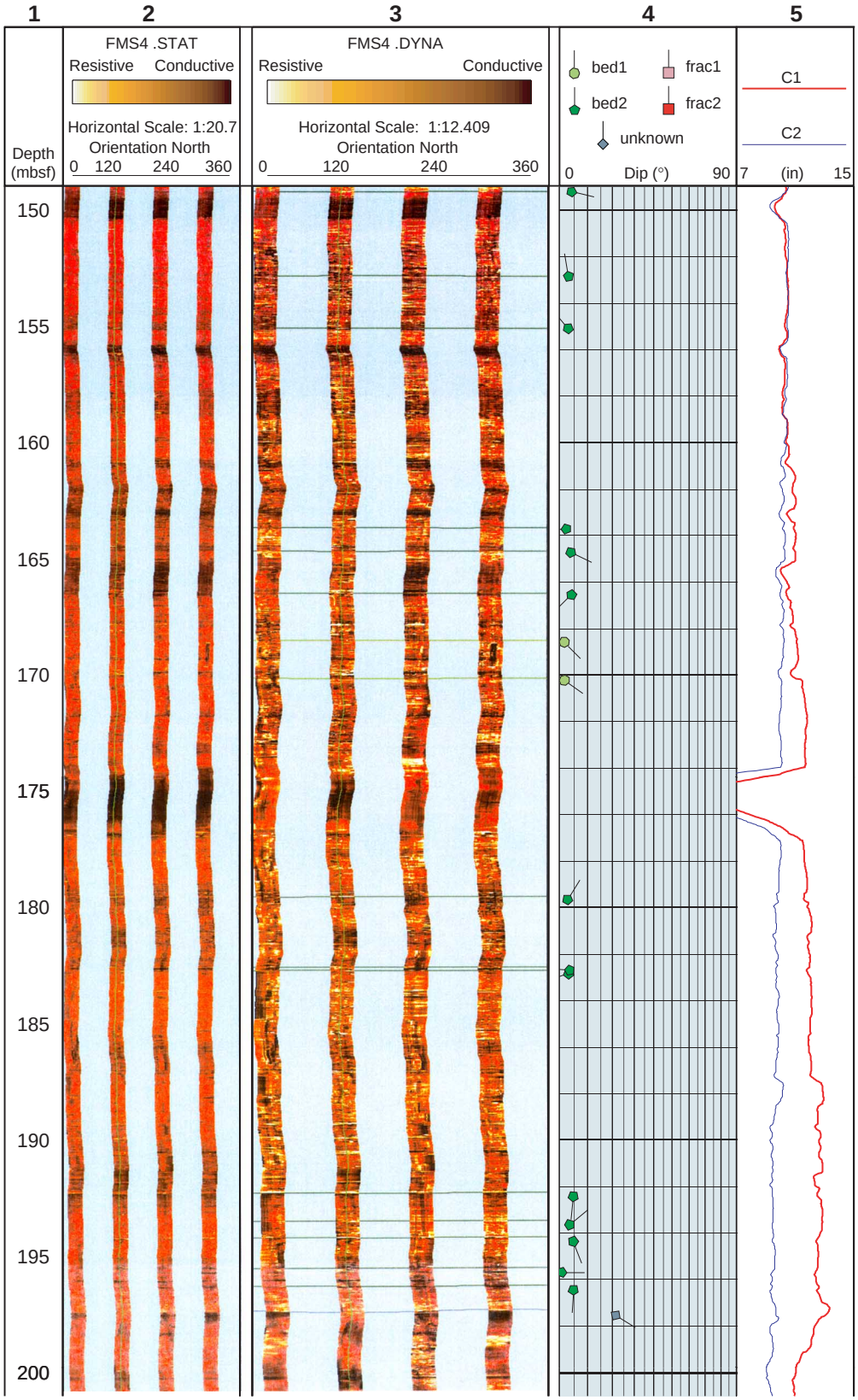

Figure AF1 (continued).

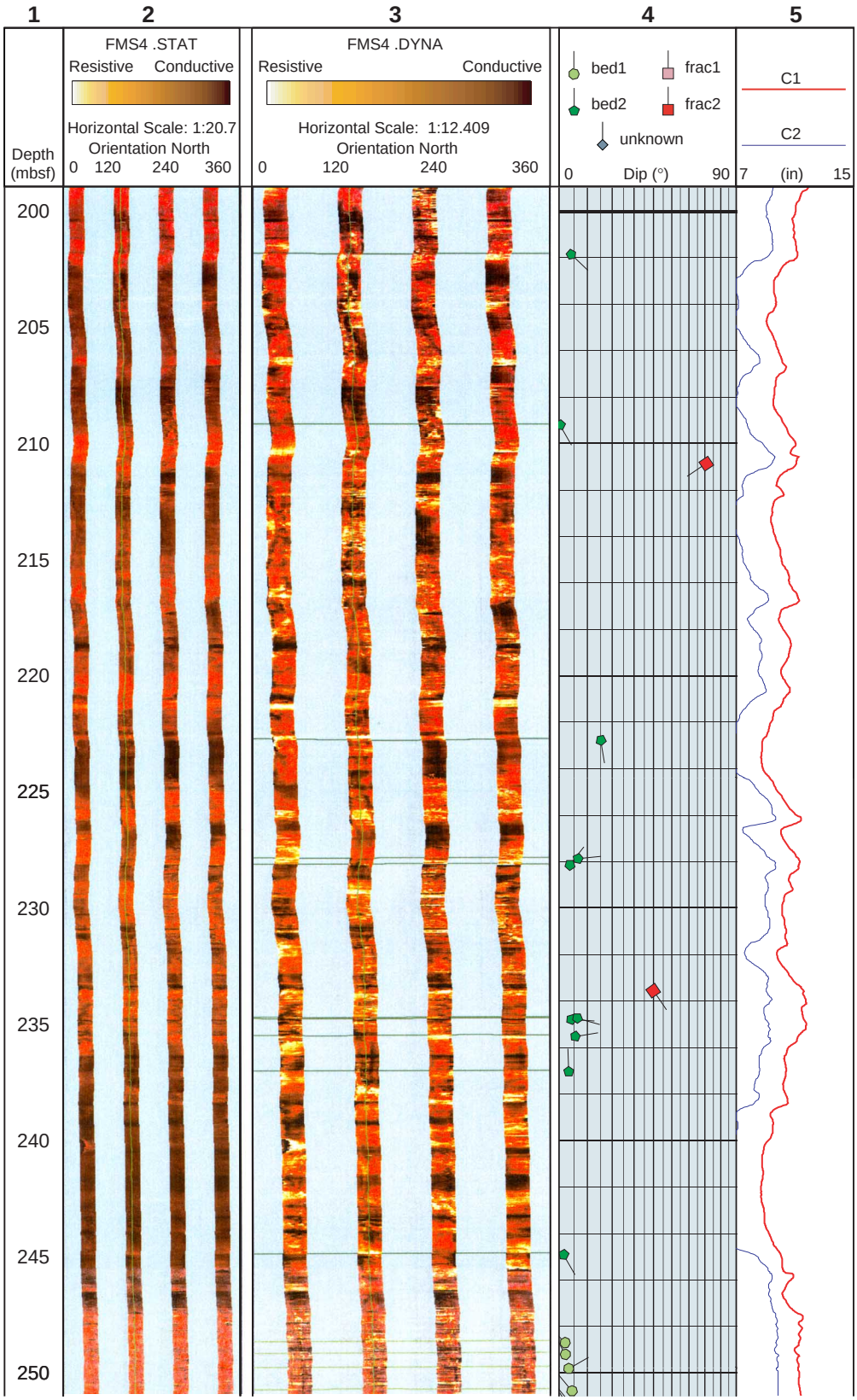

Figure AF1 (continued).

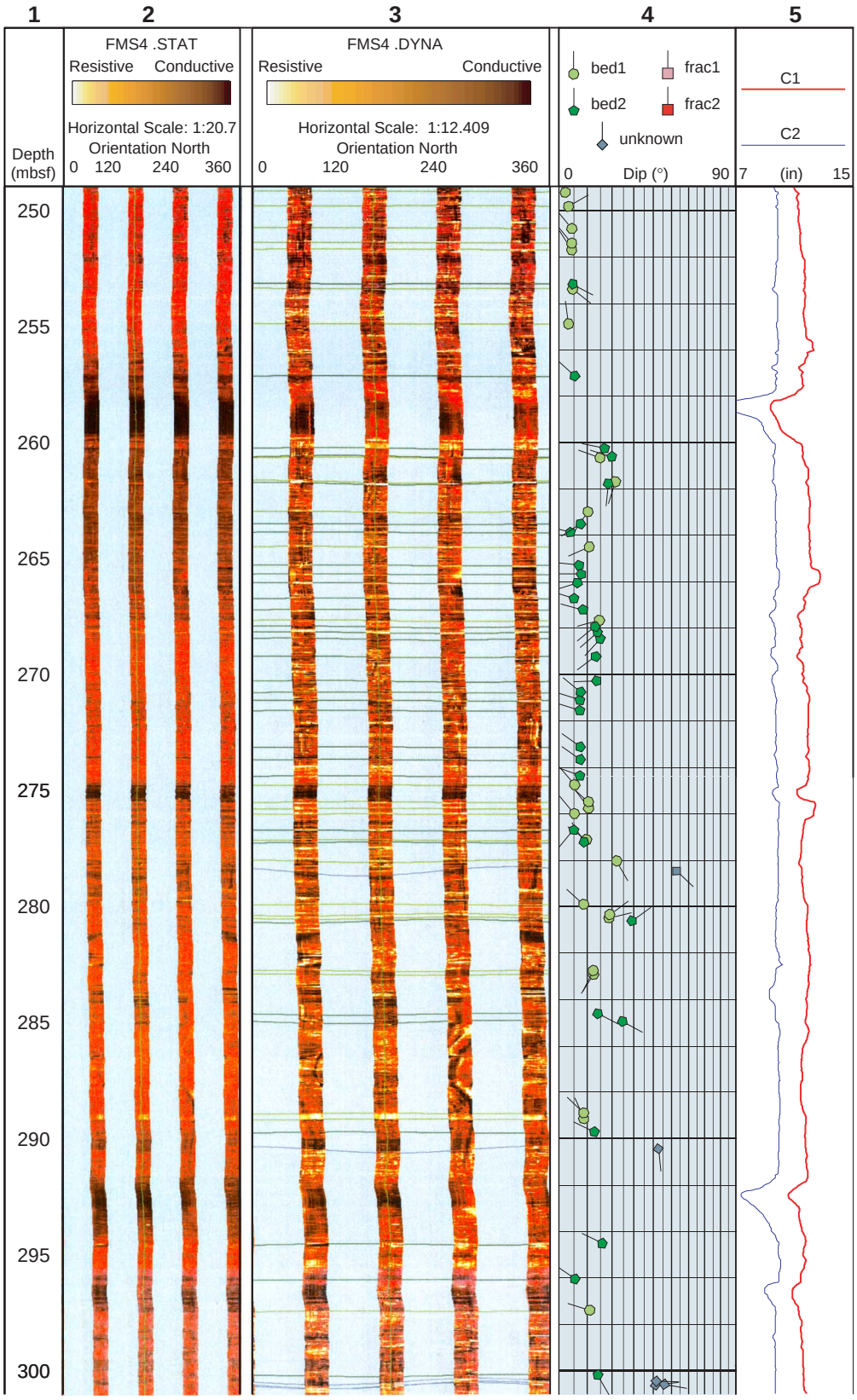

Figure AF1 (continued).

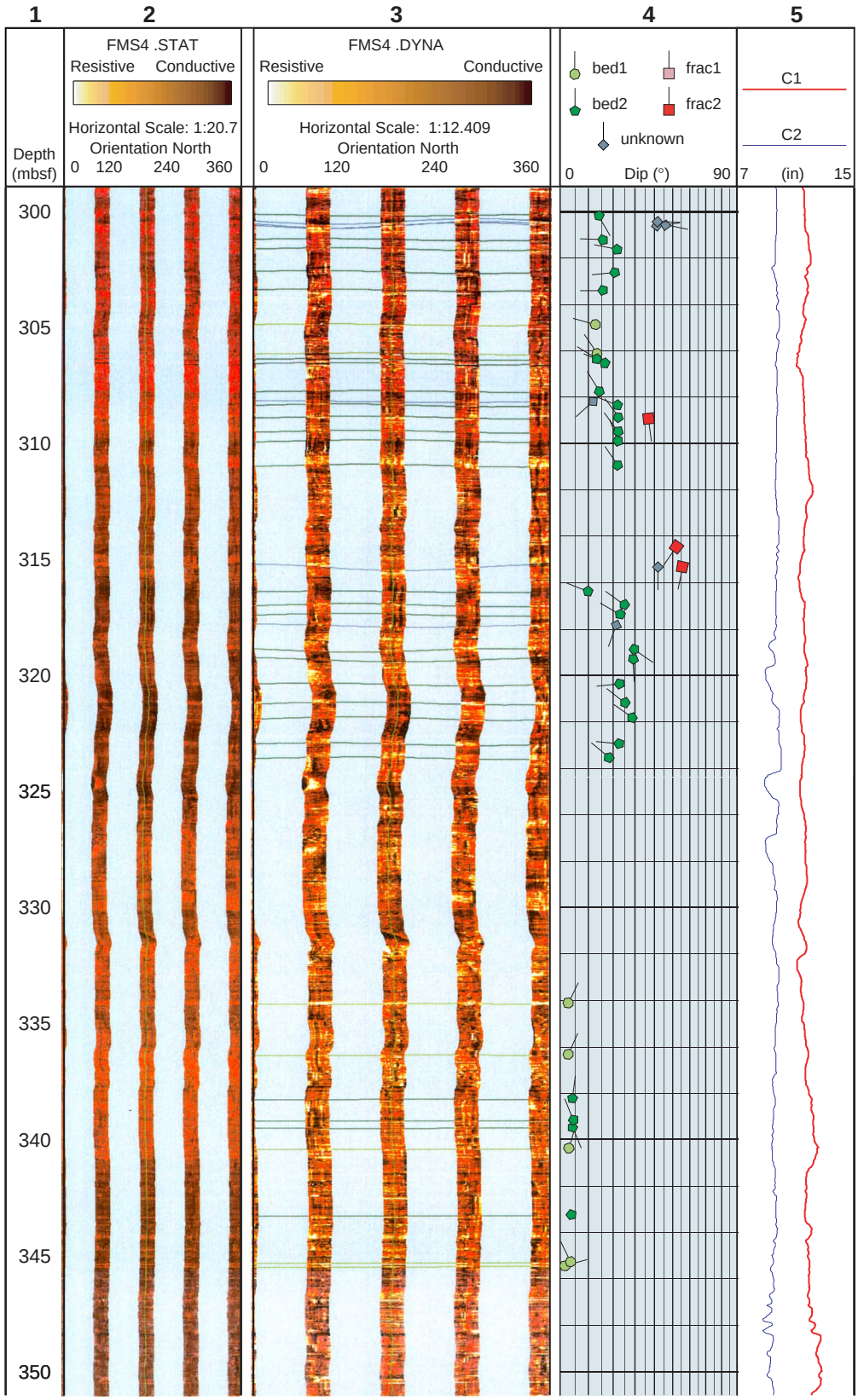

Figure AF1 (continued).

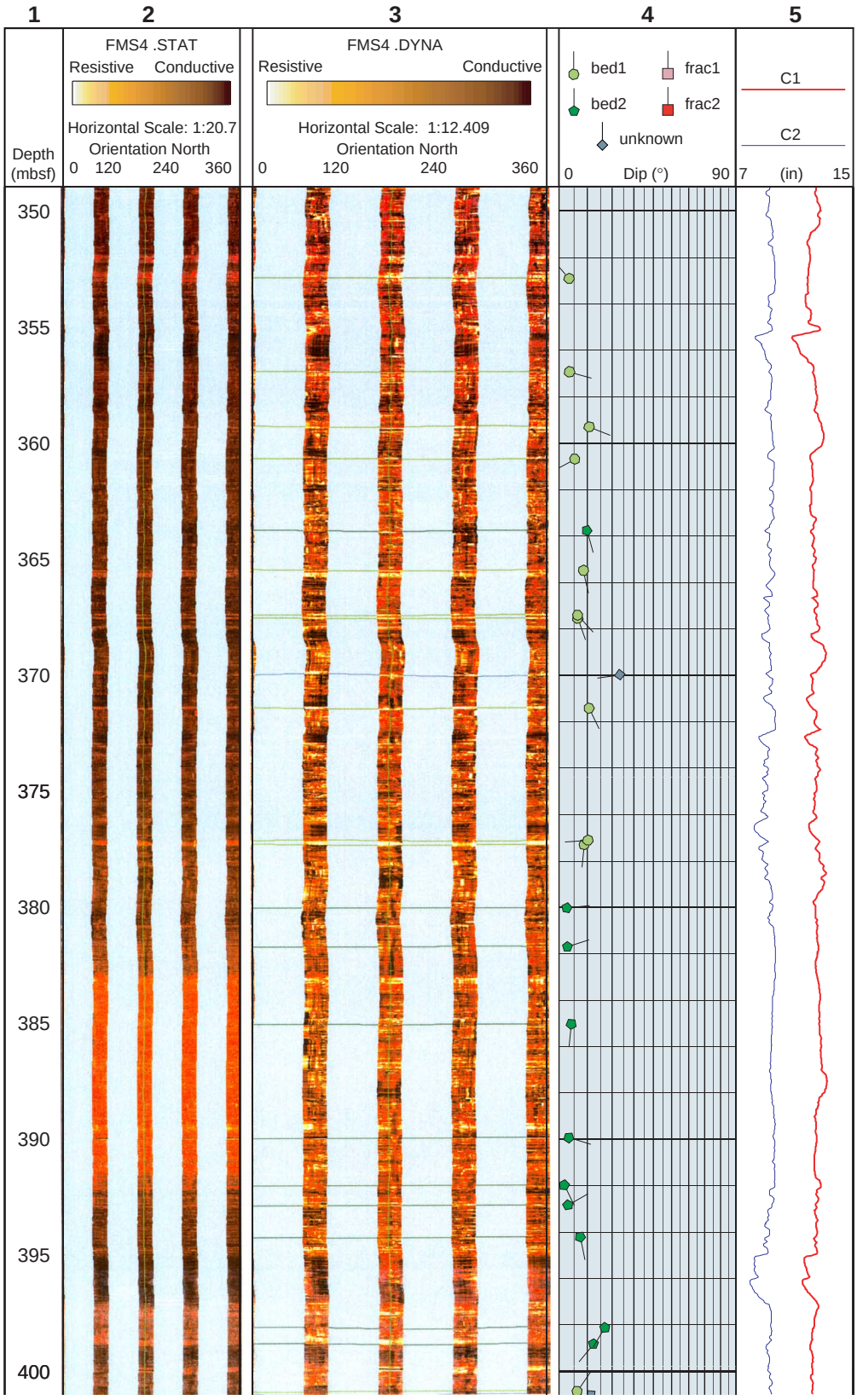

Figure AF1 (continued).

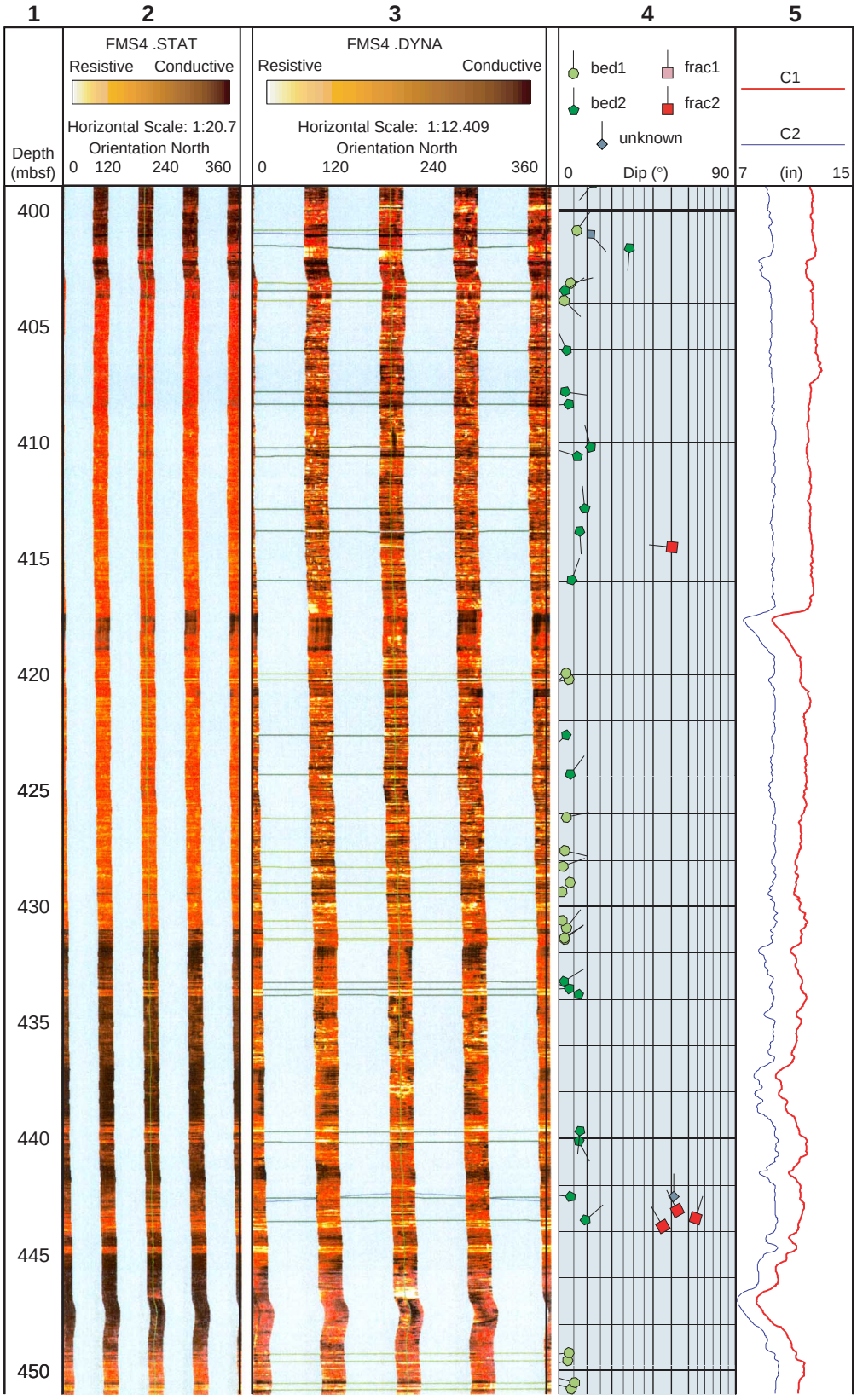

Figure AF1 (continued).

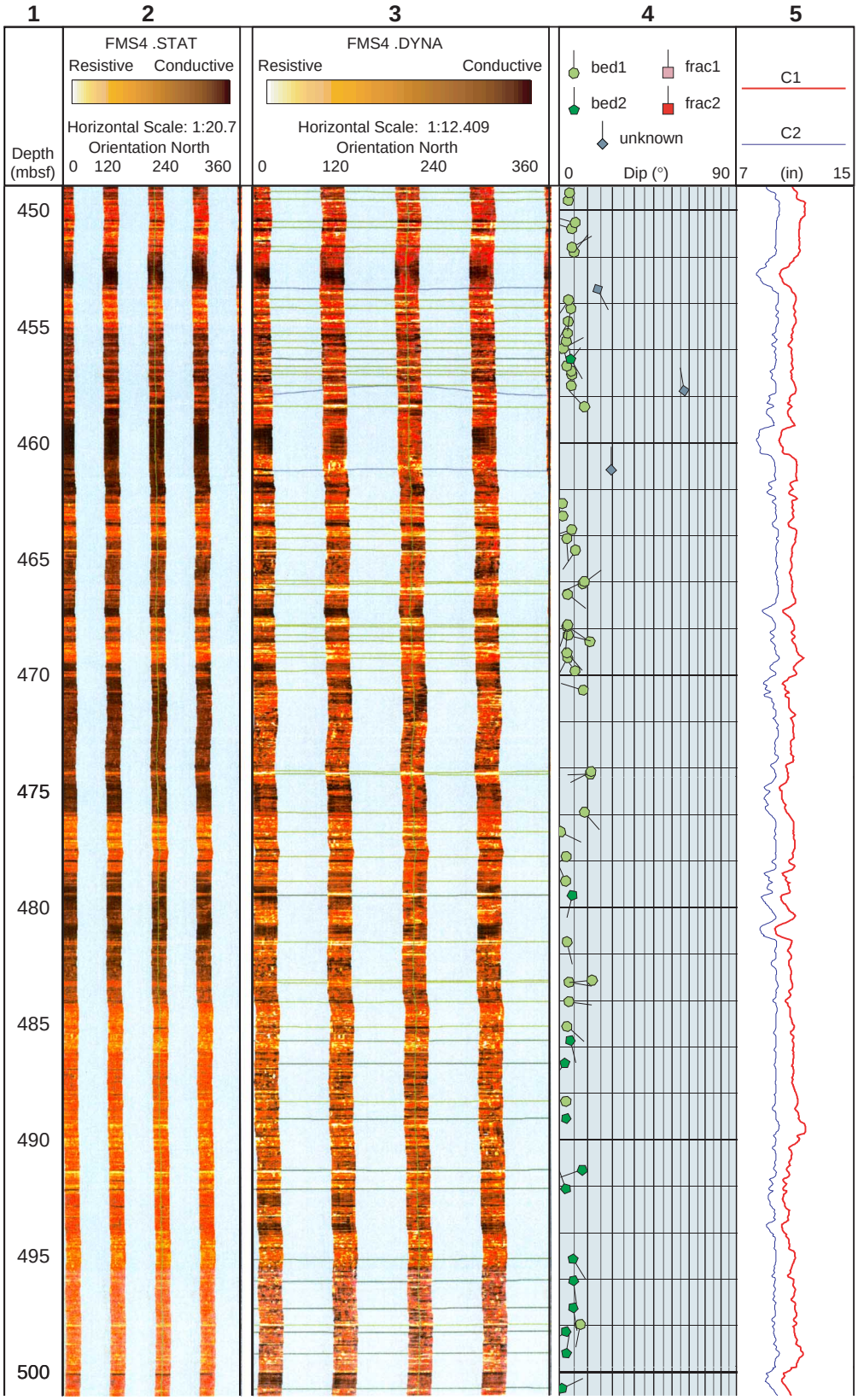

Figure AF1 (continued).

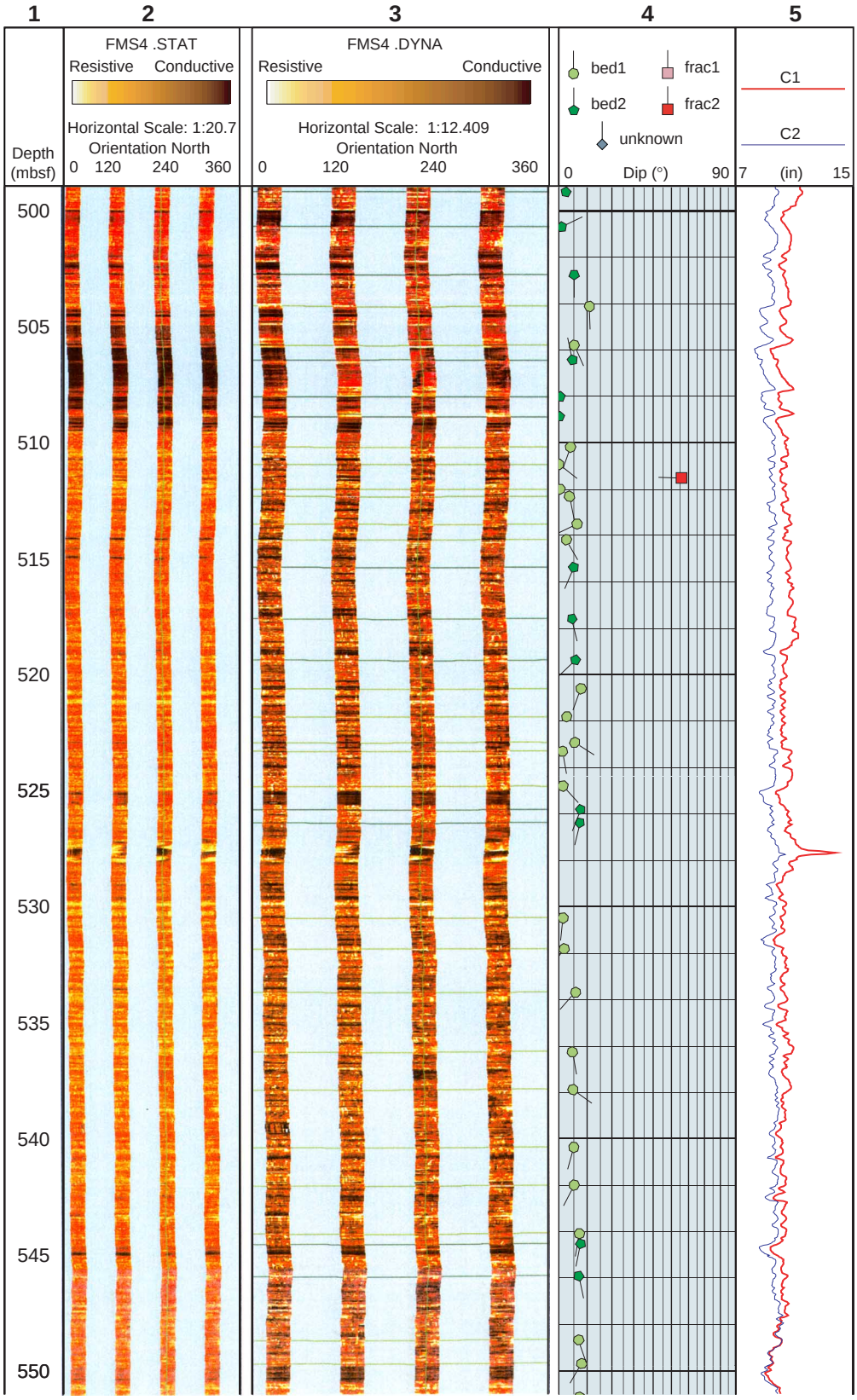

Figure AF1 (continued).

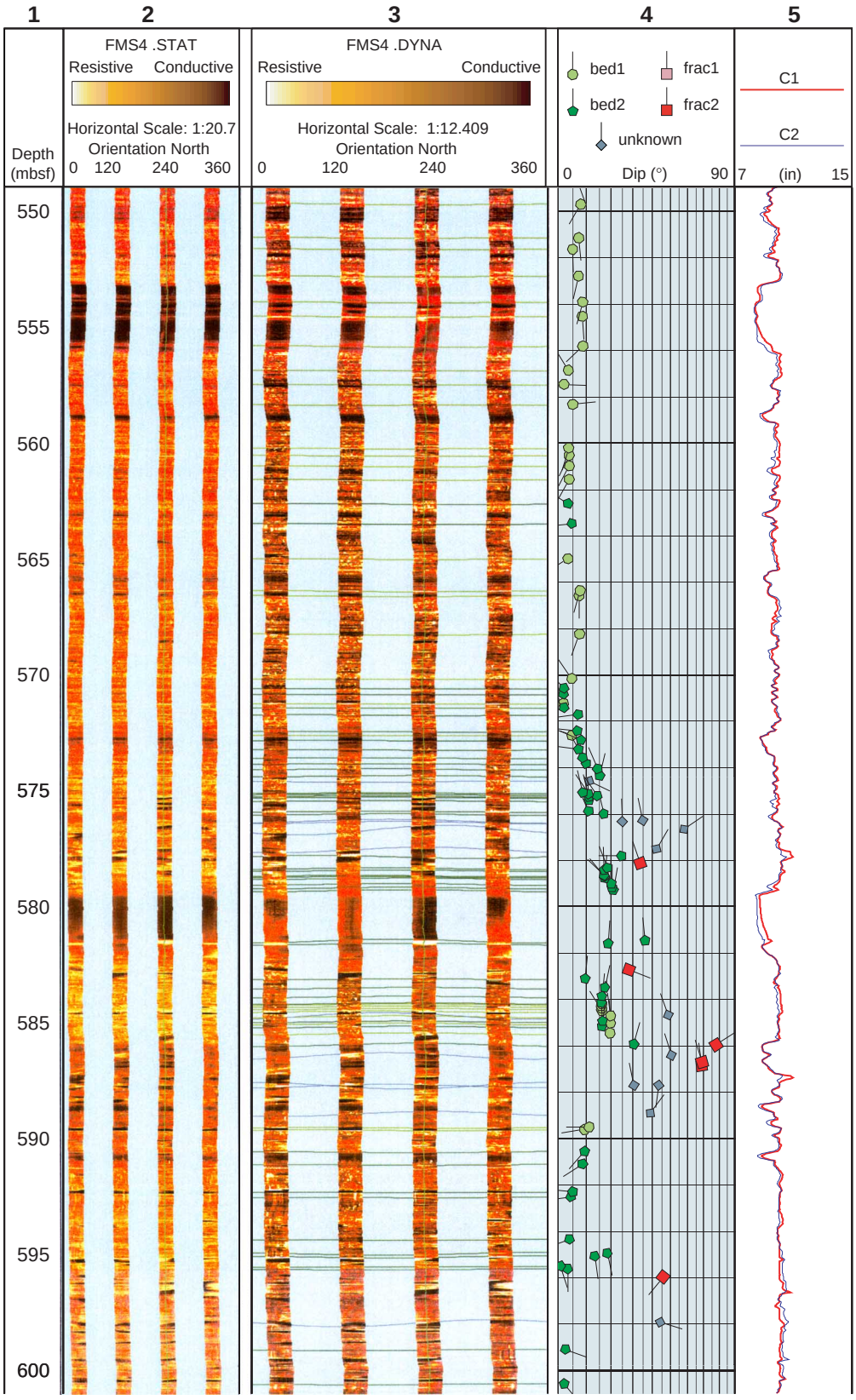

Figure AF1 (continued).

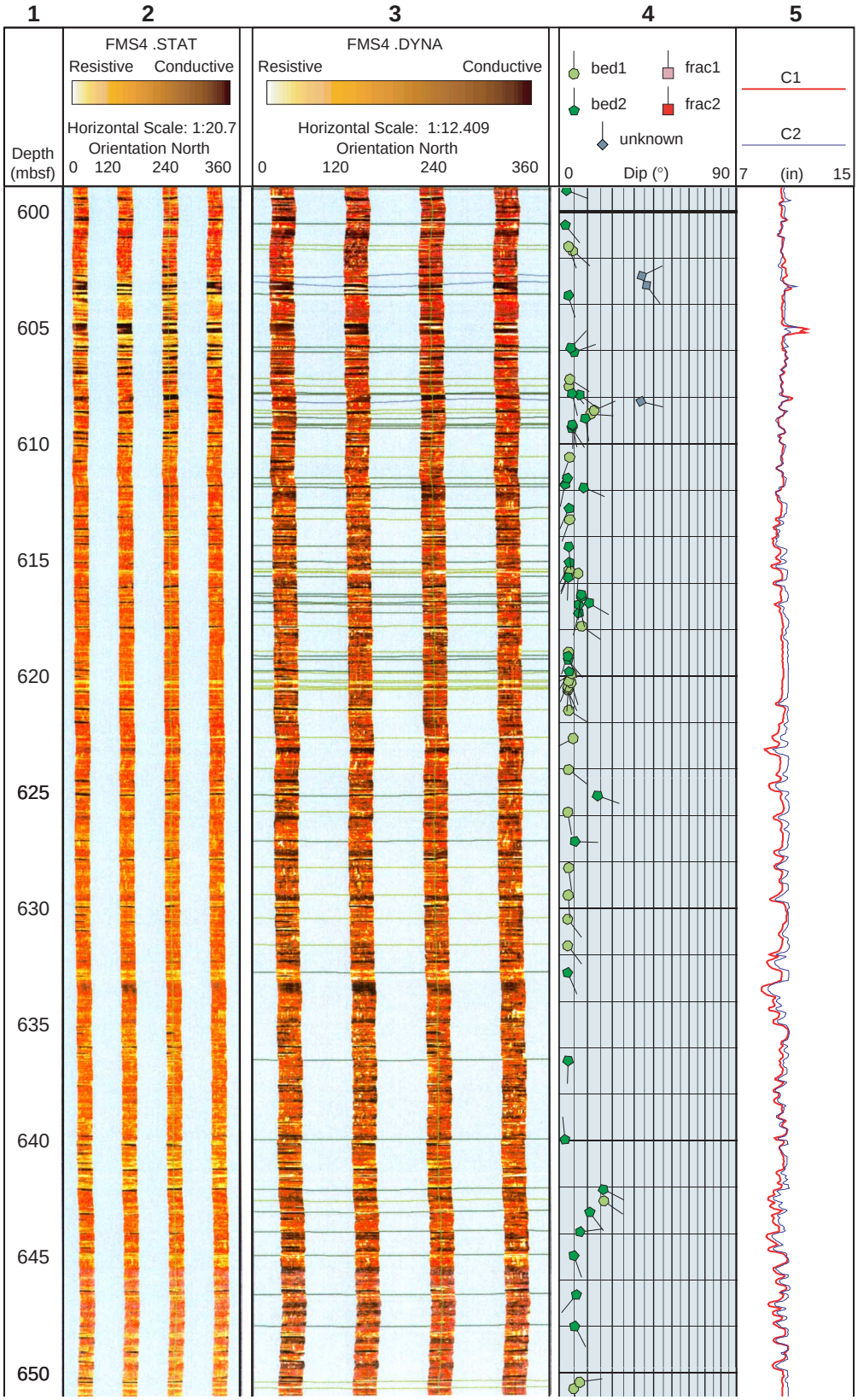

Figure AF1 (continued).

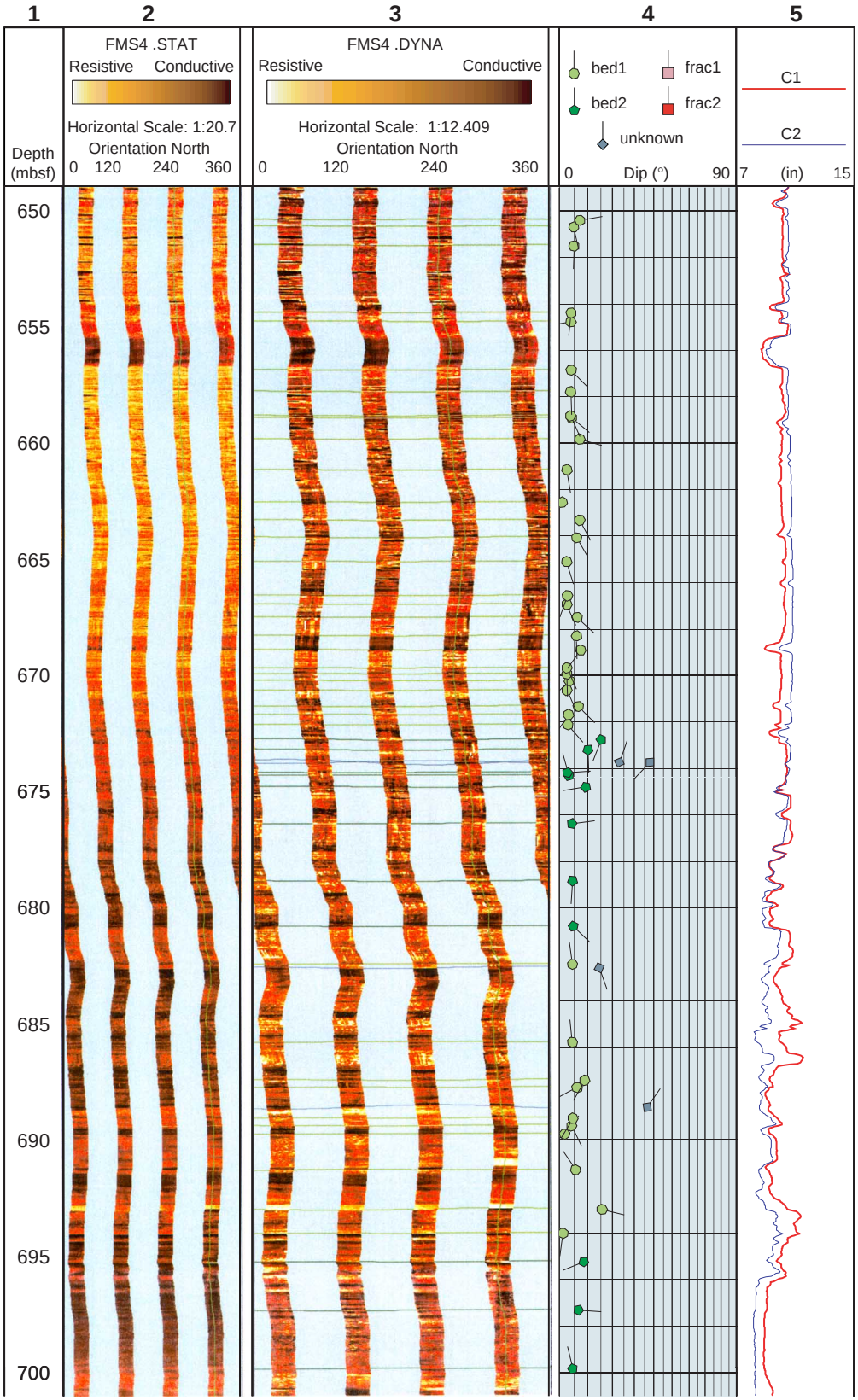

Figure AF1 (continued).

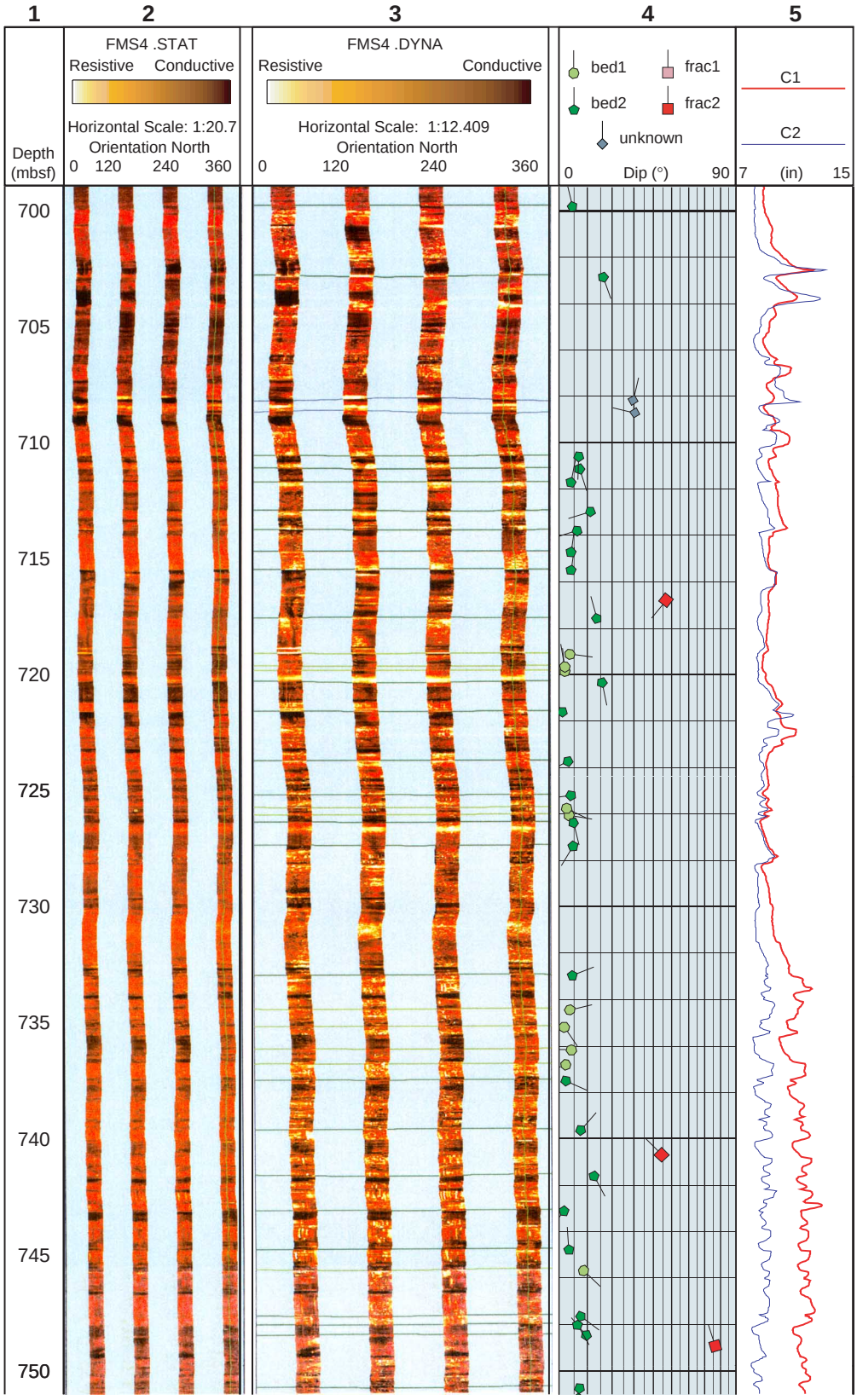

Figure AF1 (continued).

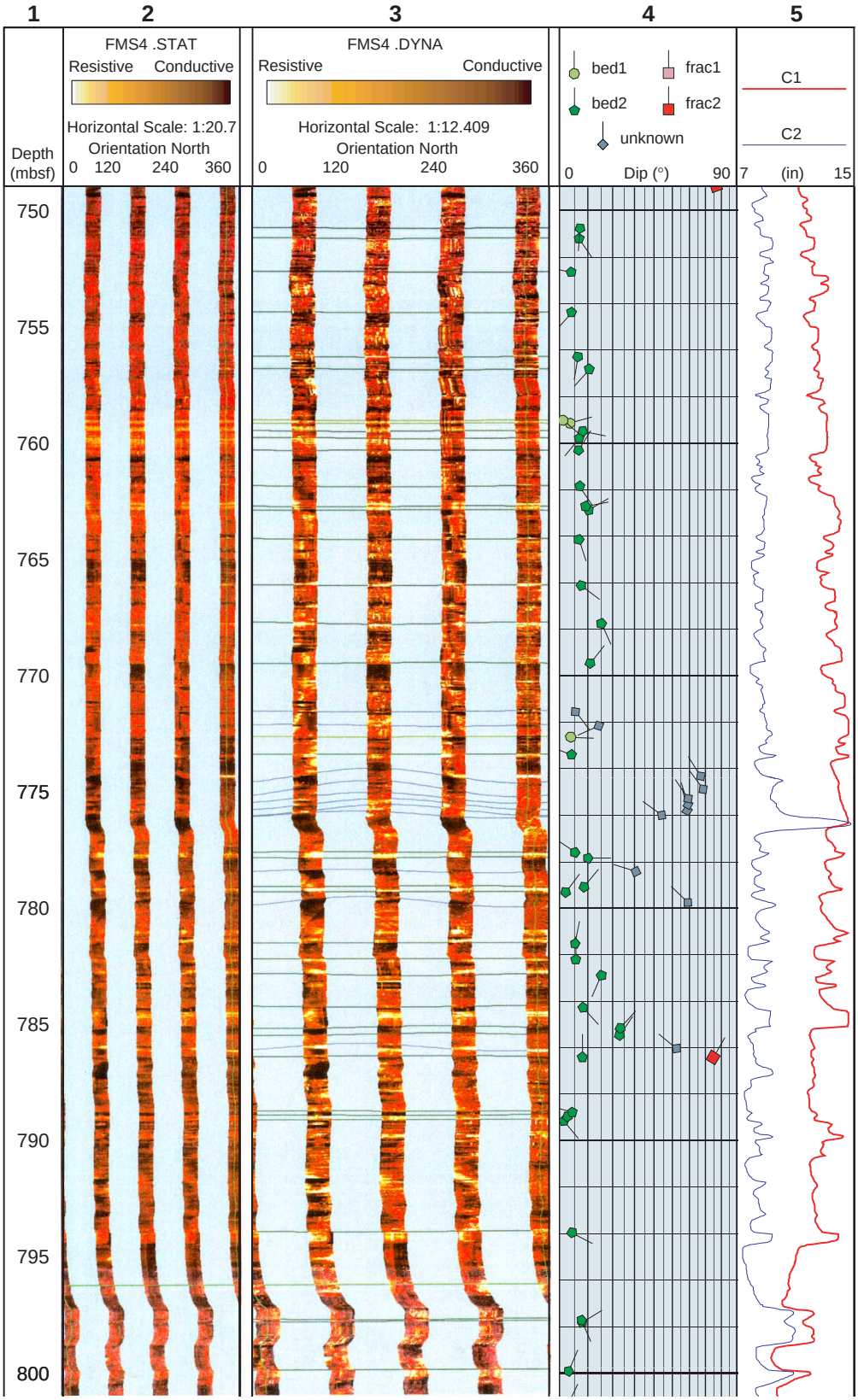

Figure AF1 (continued).

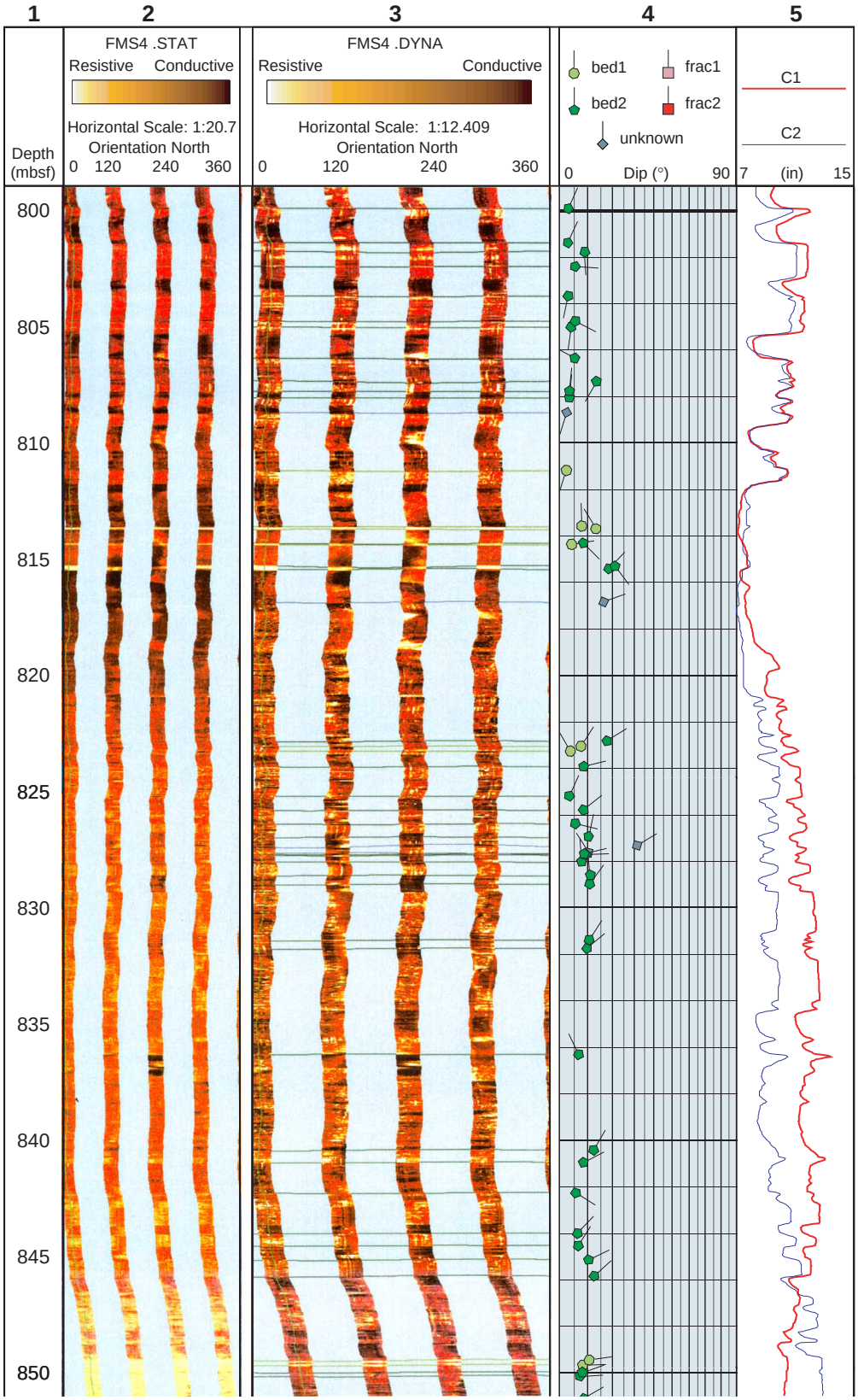

Figure AF1 (continued).

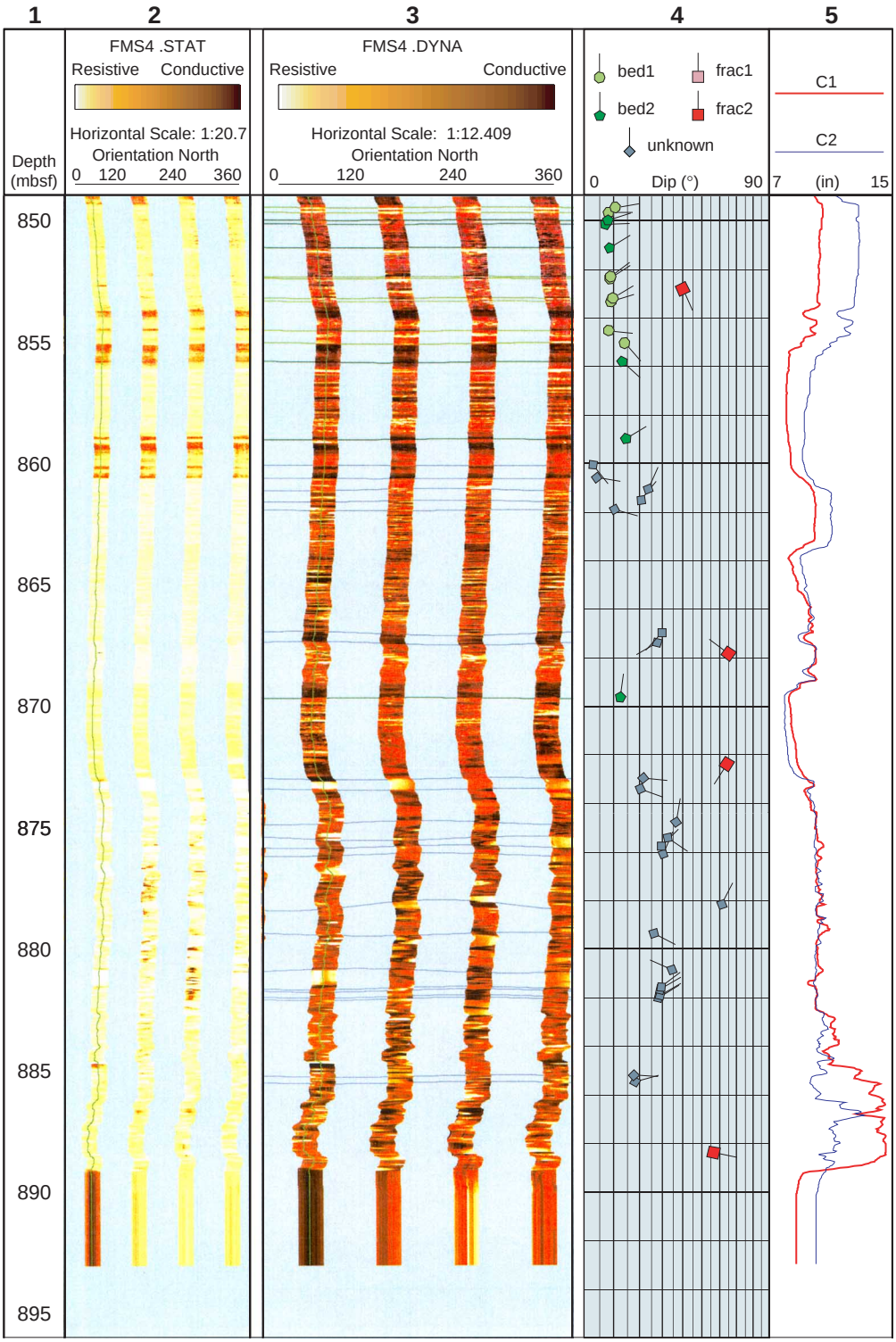

Figure AF2. FMS image and analysis, Hole 1109D. From left: (1) depth, (2) static FMS image, (3) dynamic FMS image with a 2-m color equalization sliding window with sinusoids corresponding to the structural measurements, (4) structural interpretation tadpoles, and (5) caliper measurements. The thin vertical green line on the FMS images indicates the orientation of pad 1, which correspond to the C1 caliper reading. The tadpole position on the horizontal axis indicates the dip magnitude, and its tail points toward the dip direction. (Continued on next 13 pages.)

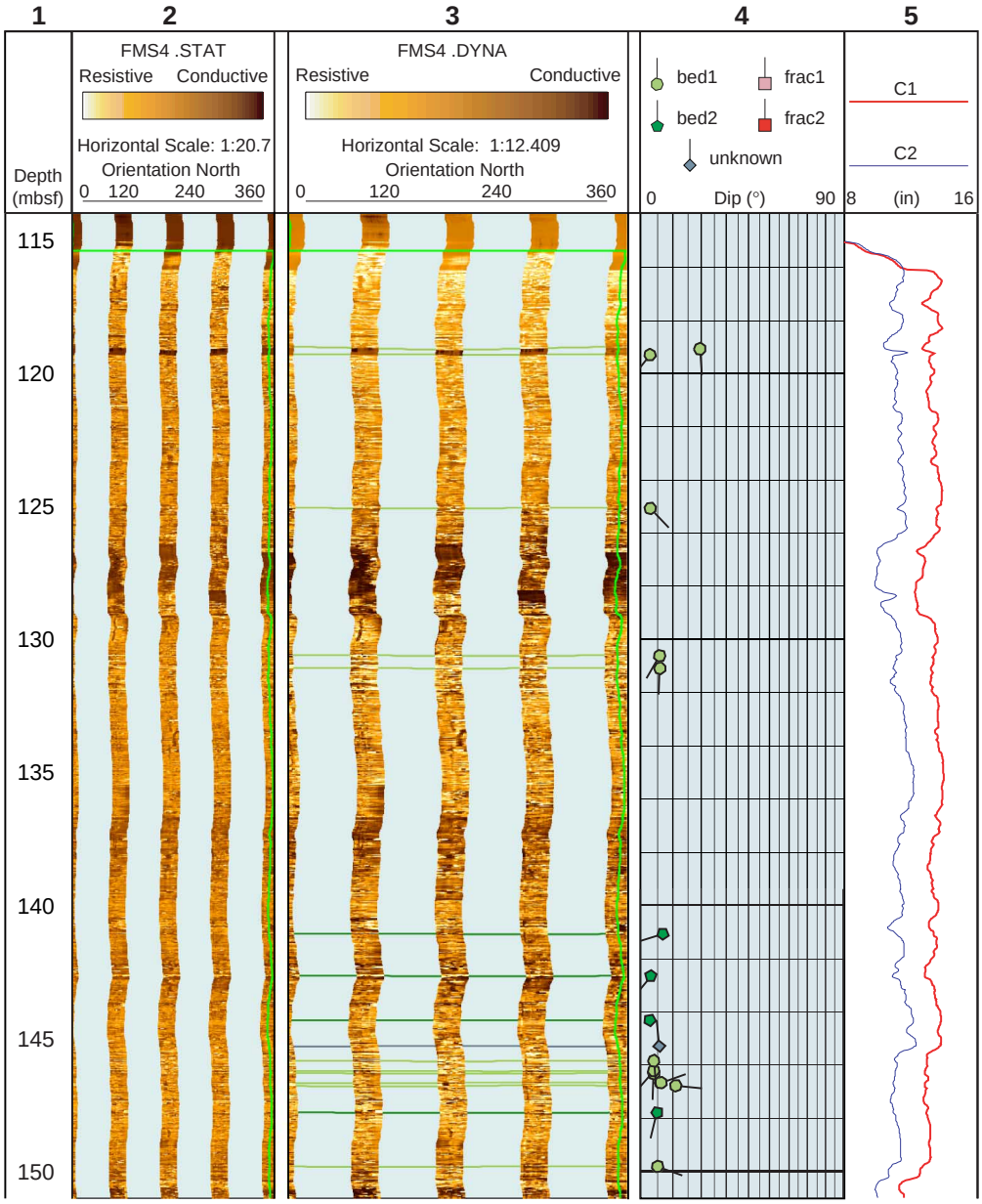

Figure AF2 (continued).

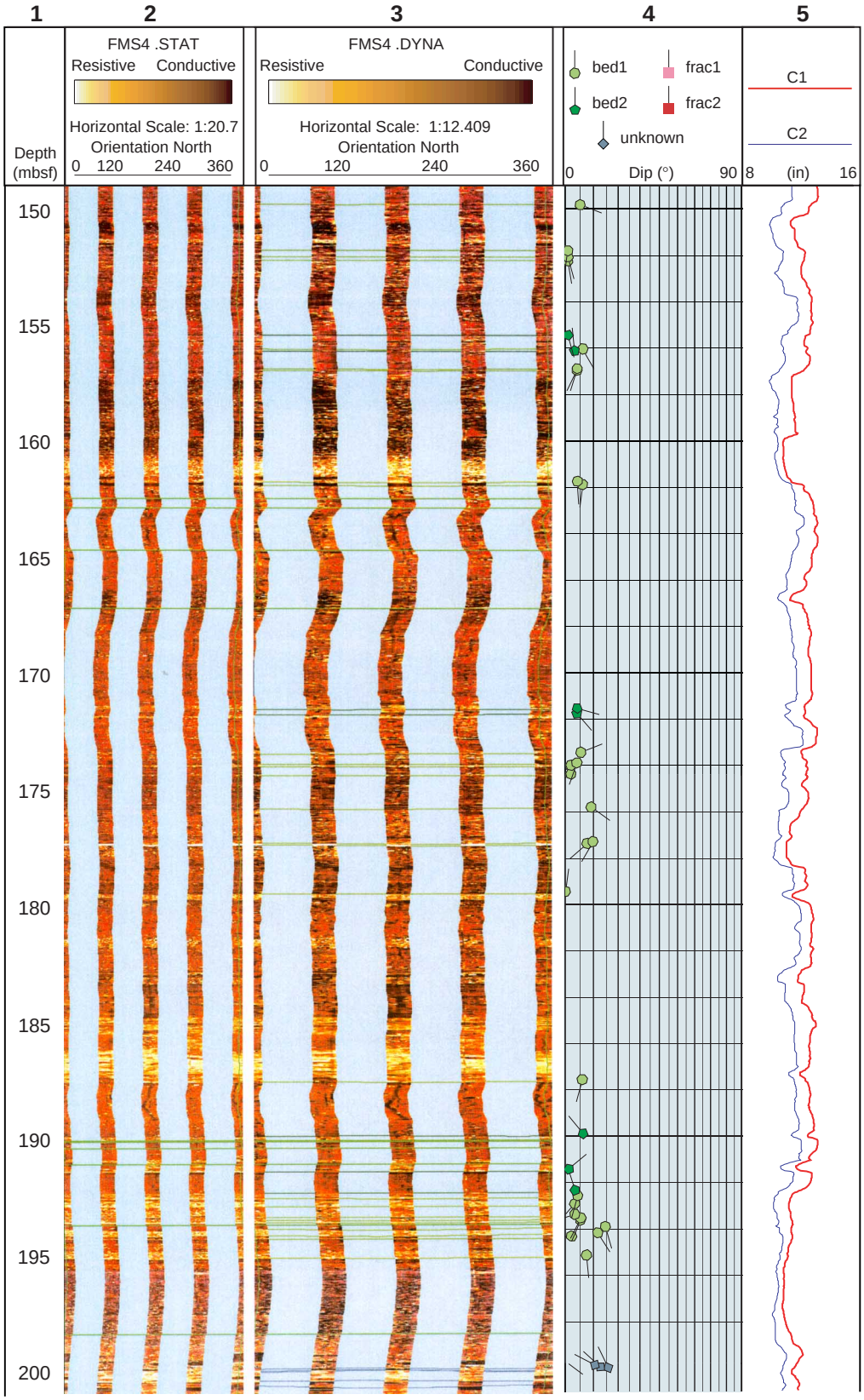

Figure AF2 (continued).

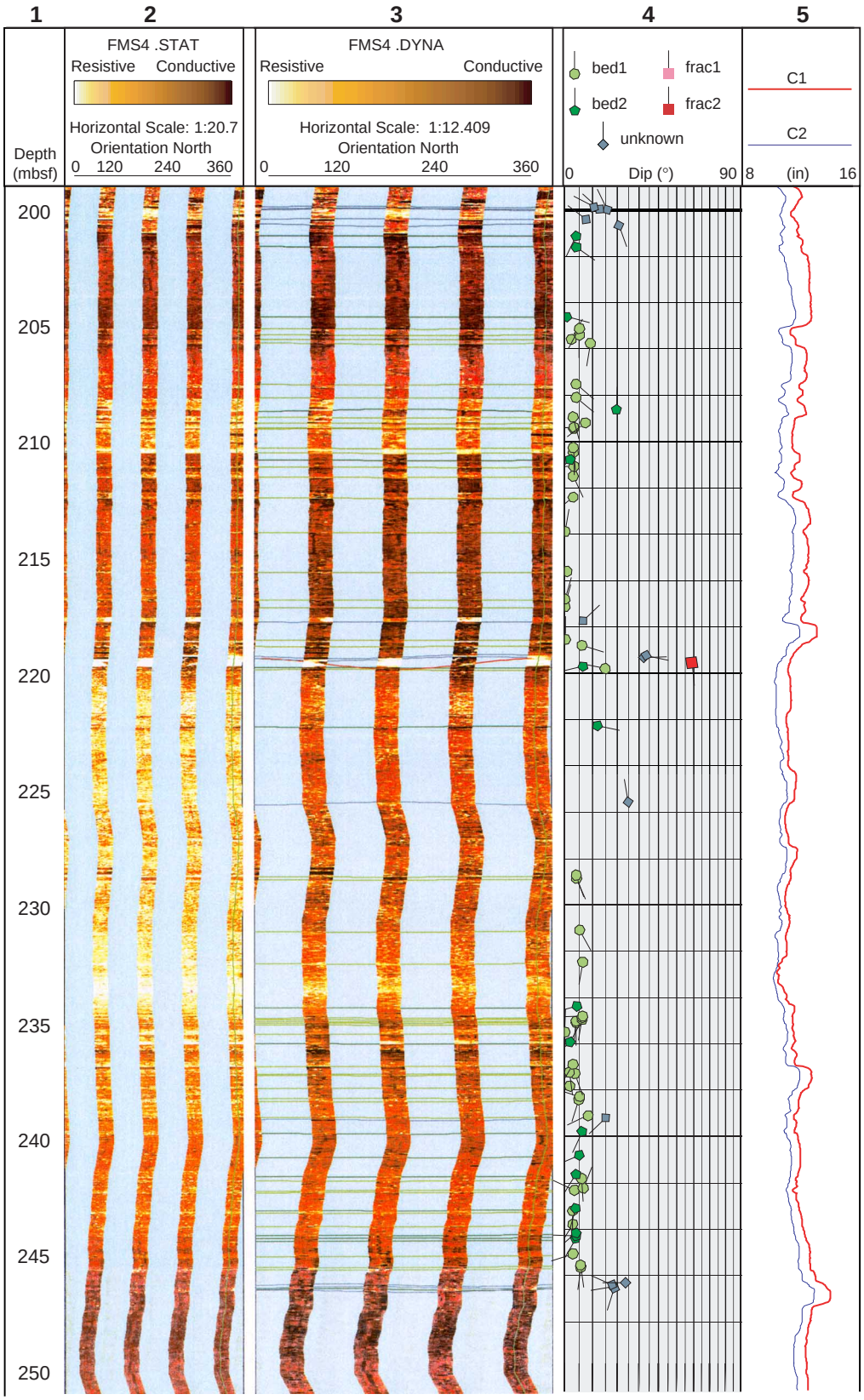

Figure AF2 (continued).

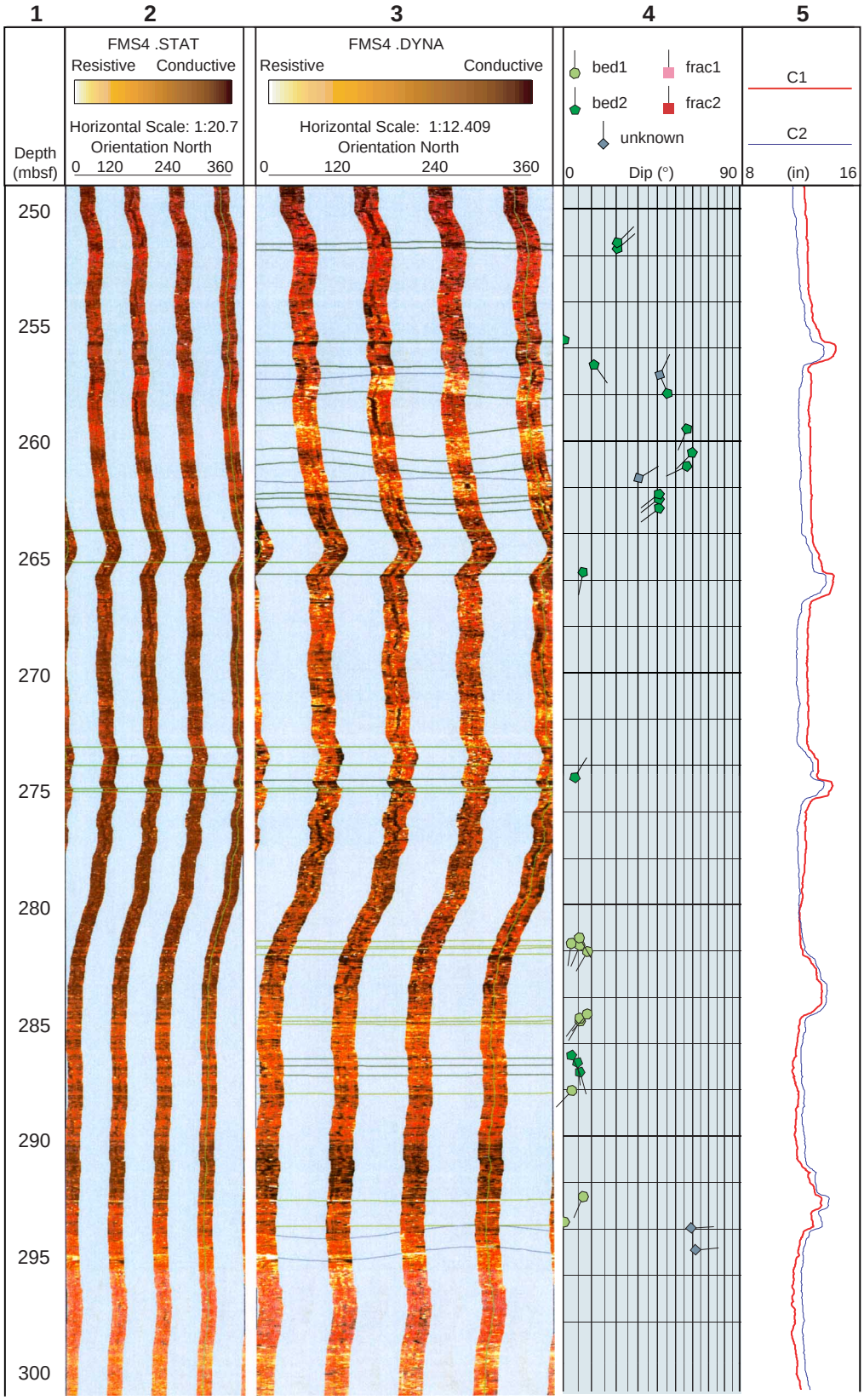

Figure AF2 (continued).

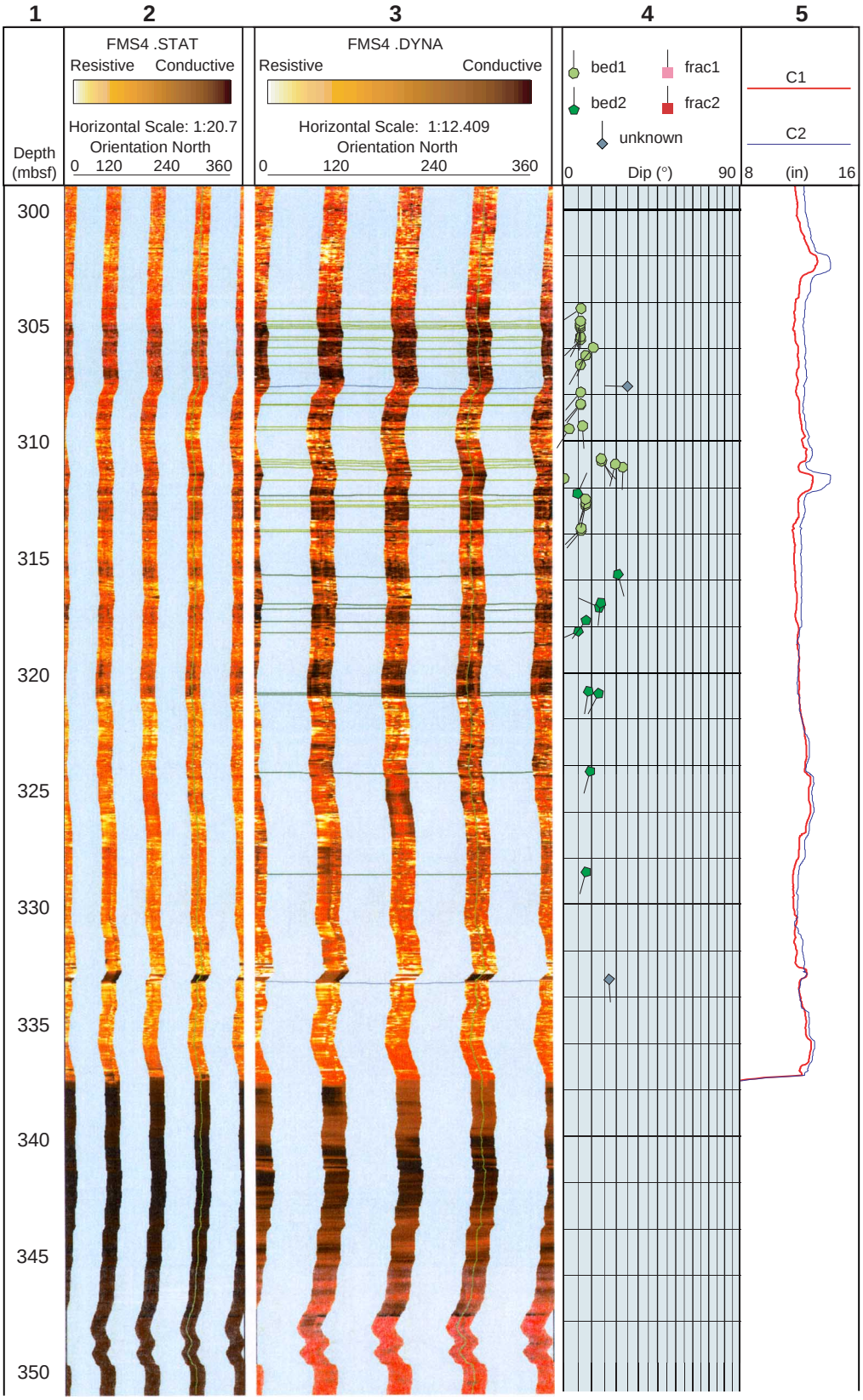

Figure AF2 (continued).

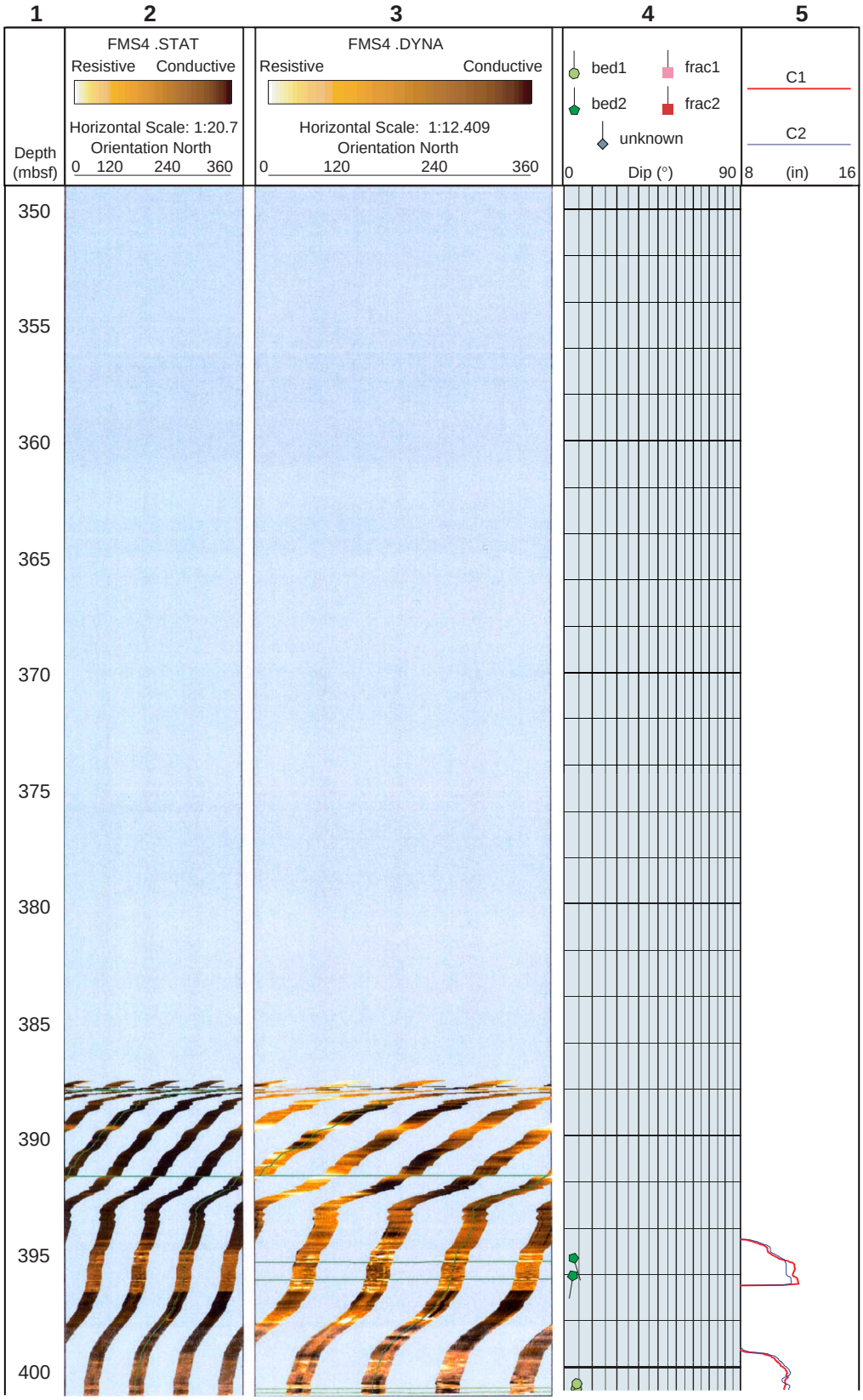

Figure AF2 (continued).

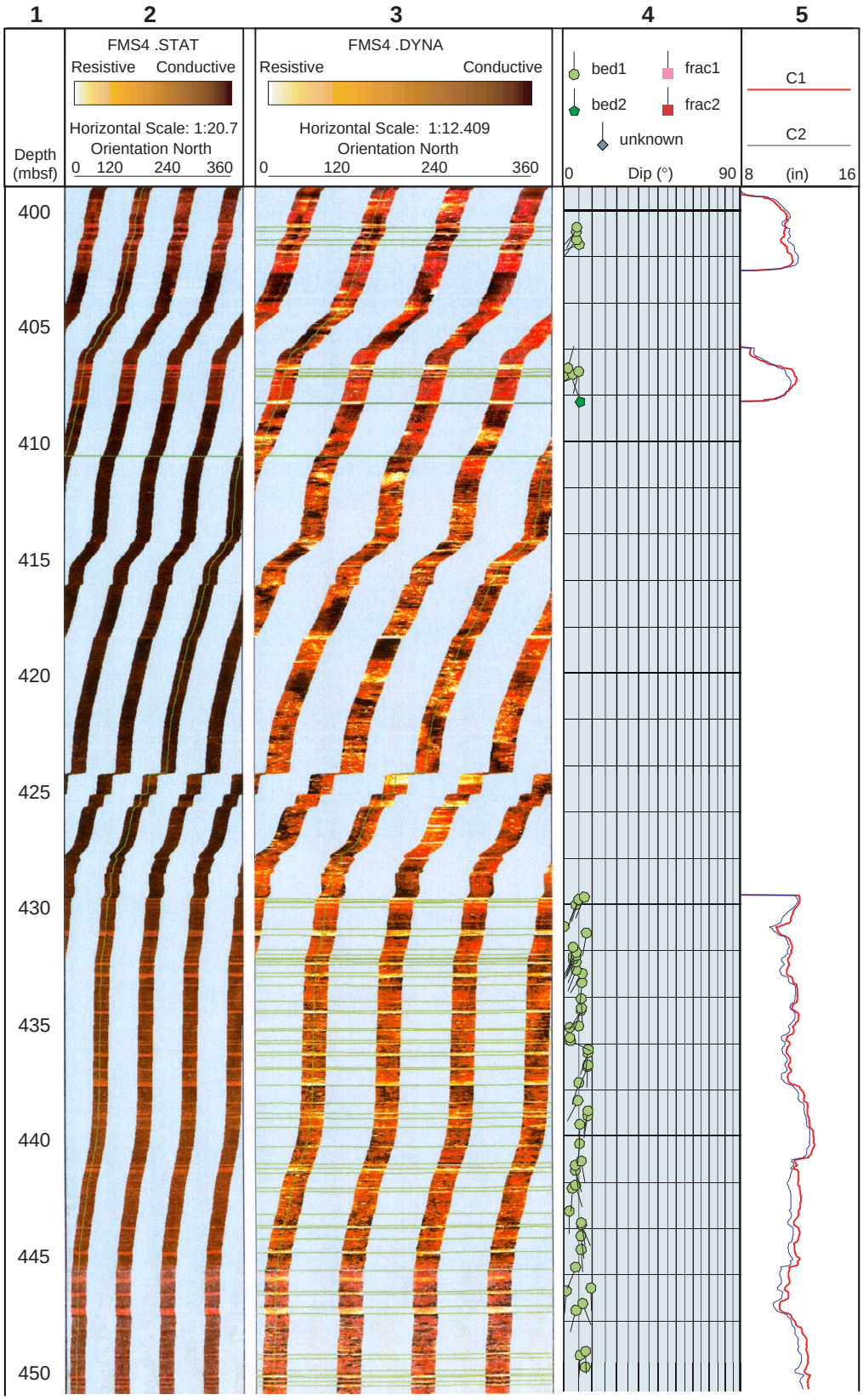

Figure AF2 (continued).

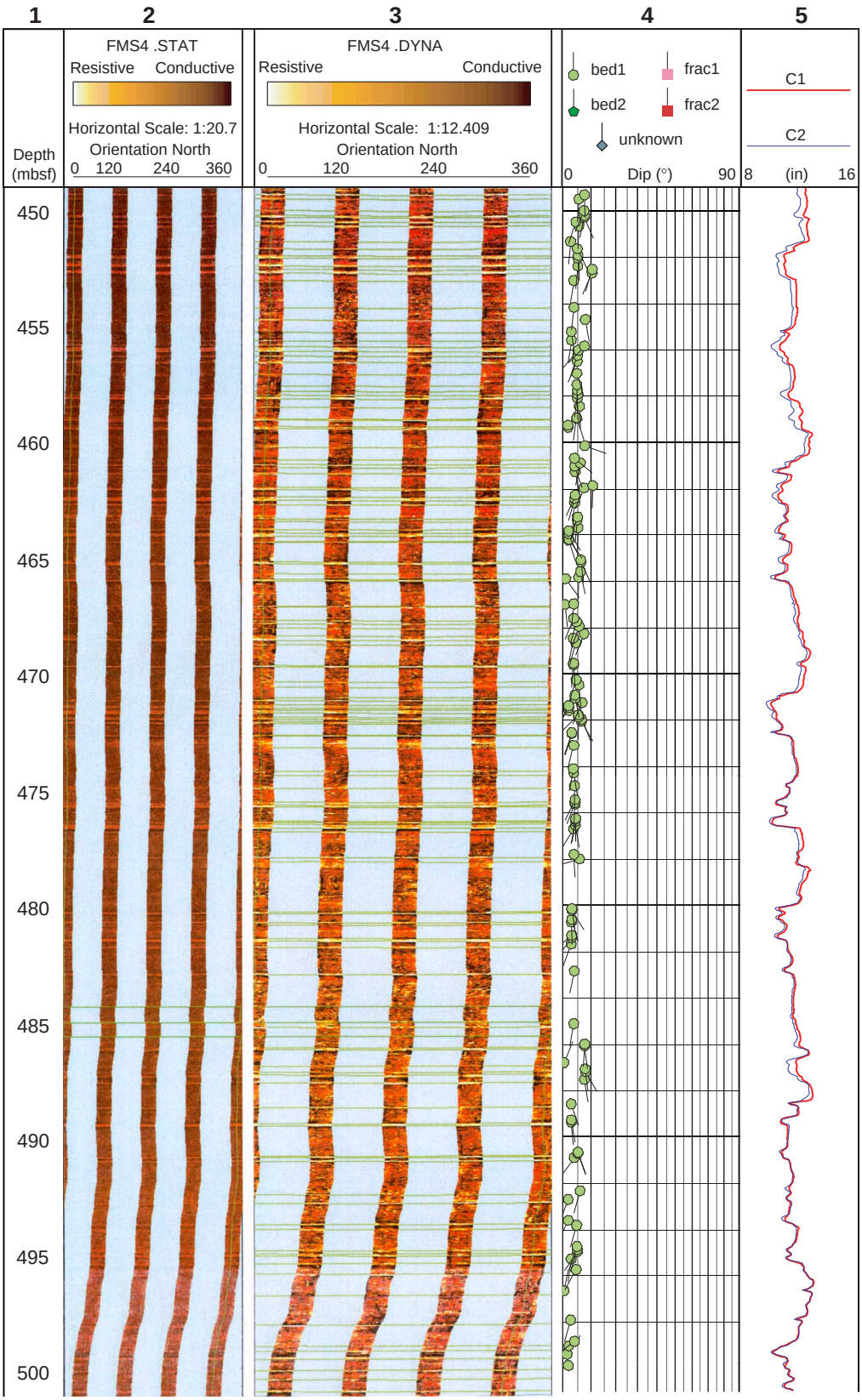

Figure AF2 (continued).

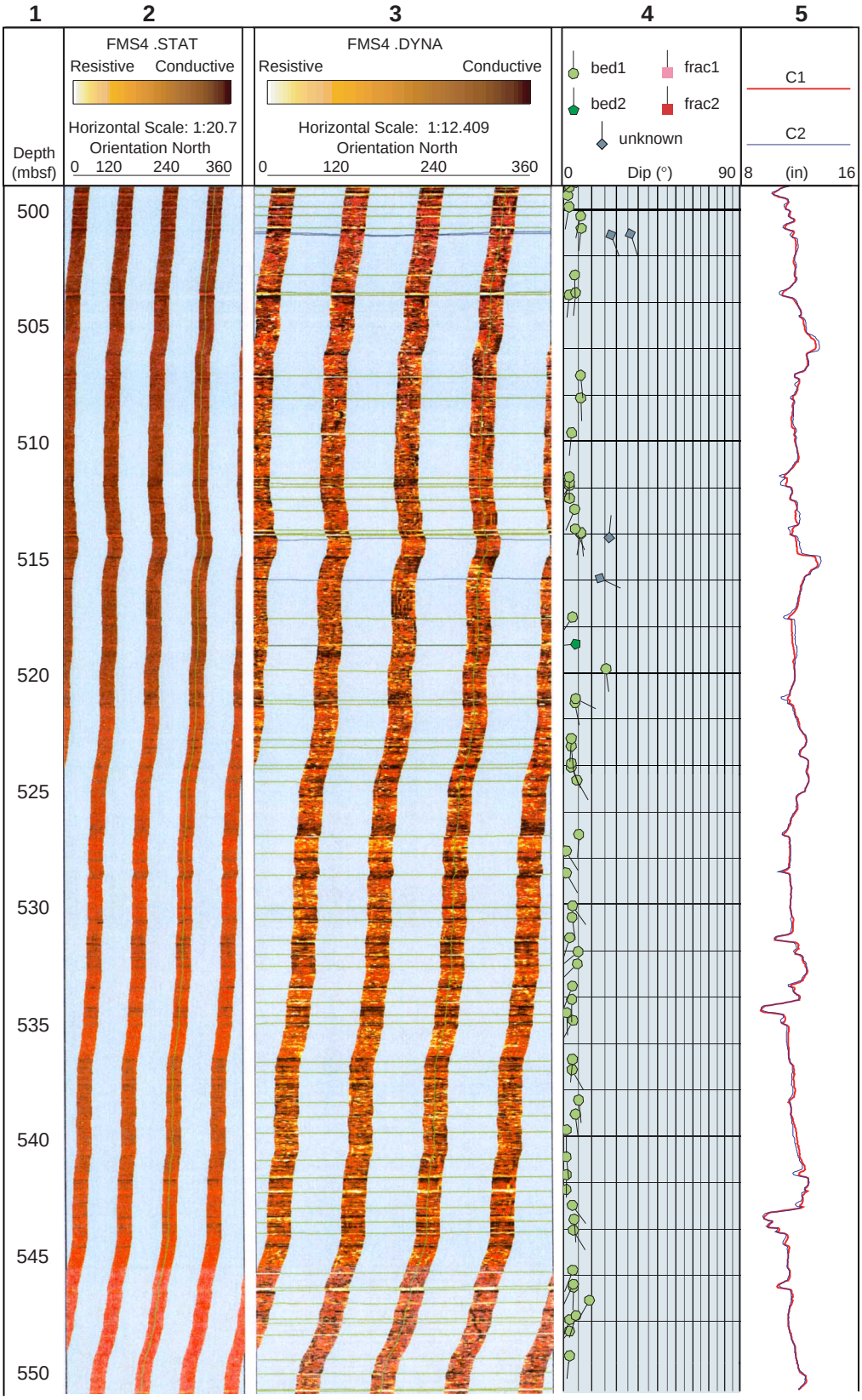

Figure AF2 (continued).

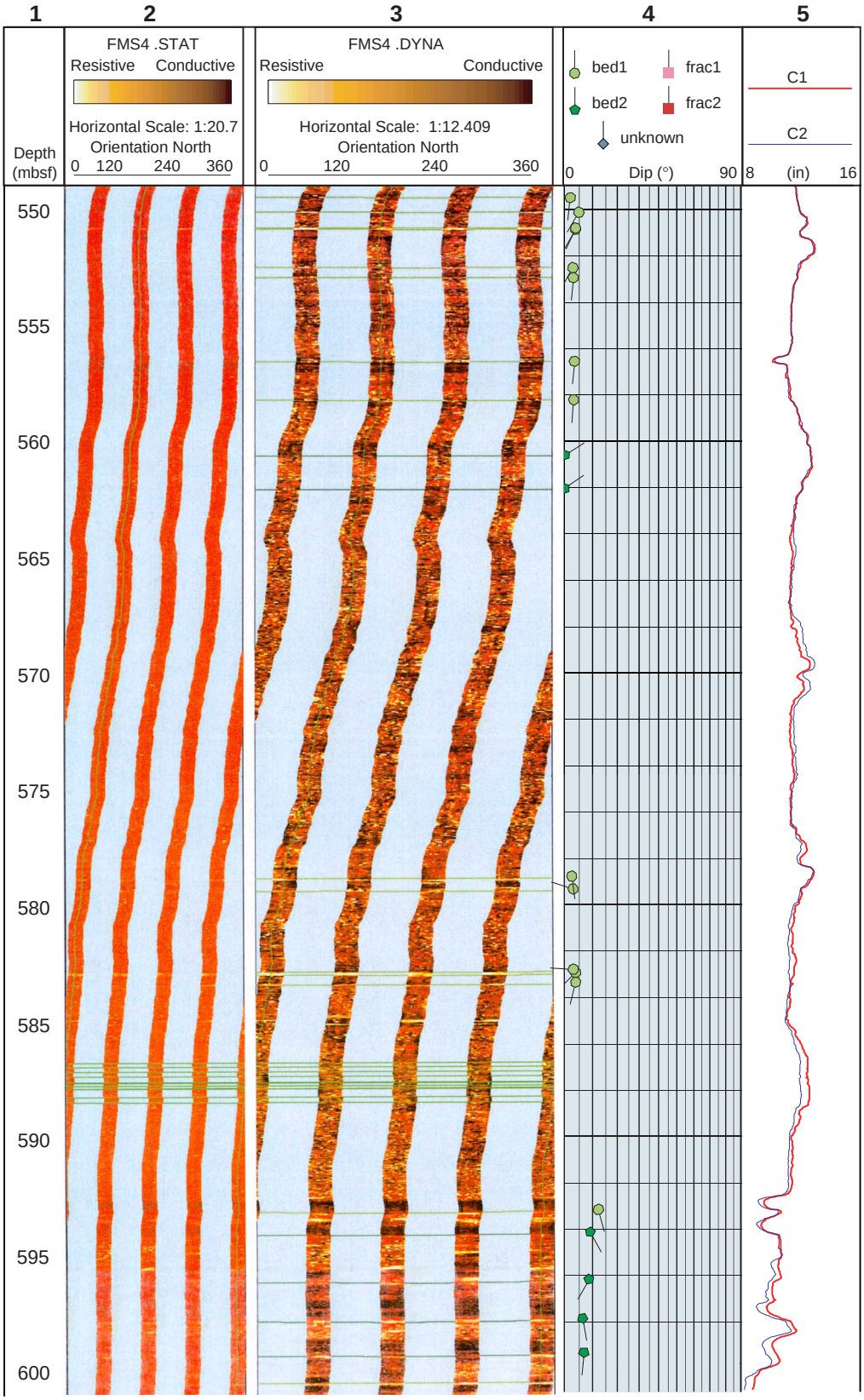

Figure AF2 (continued).

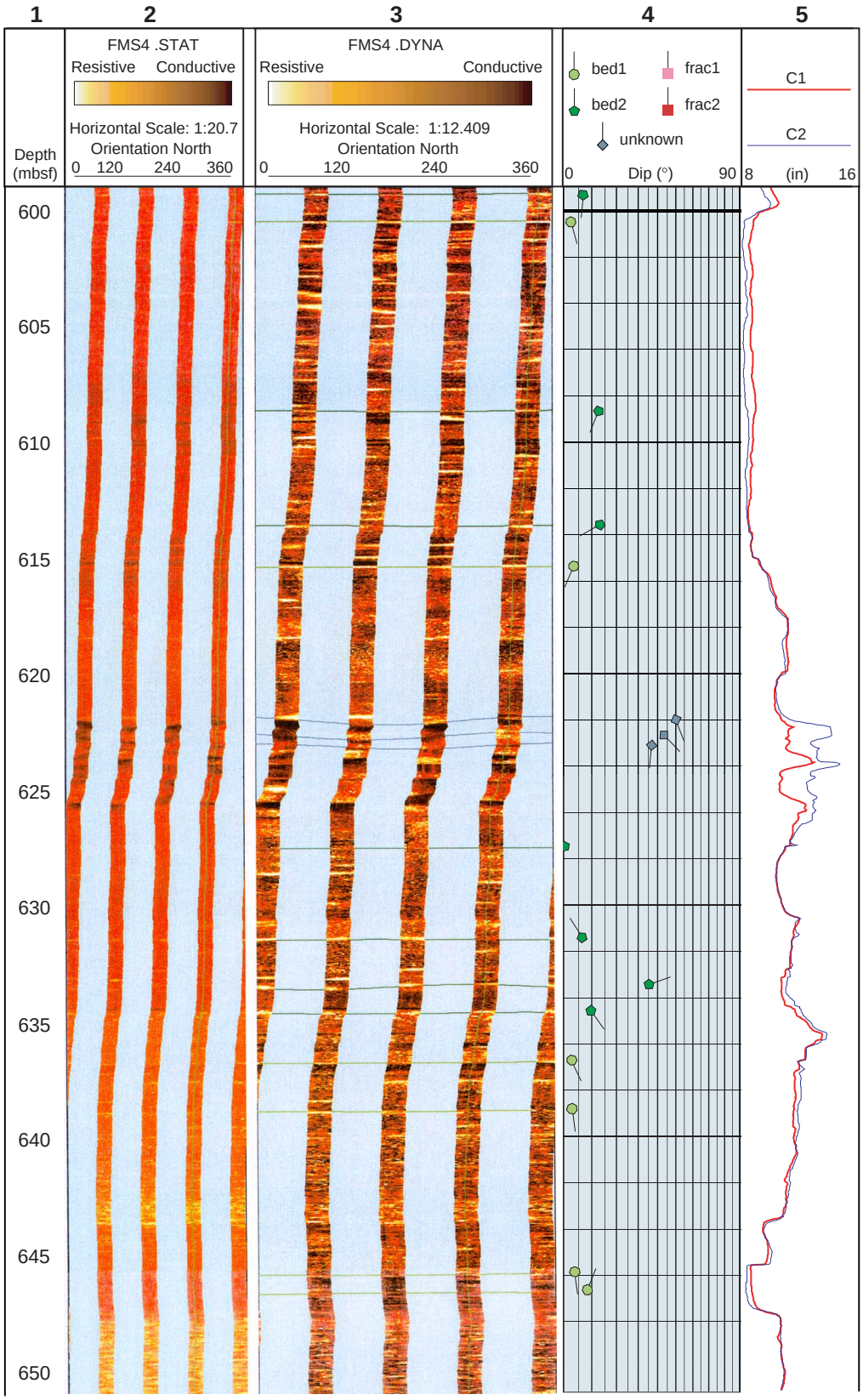

Figure AF2 (continued).

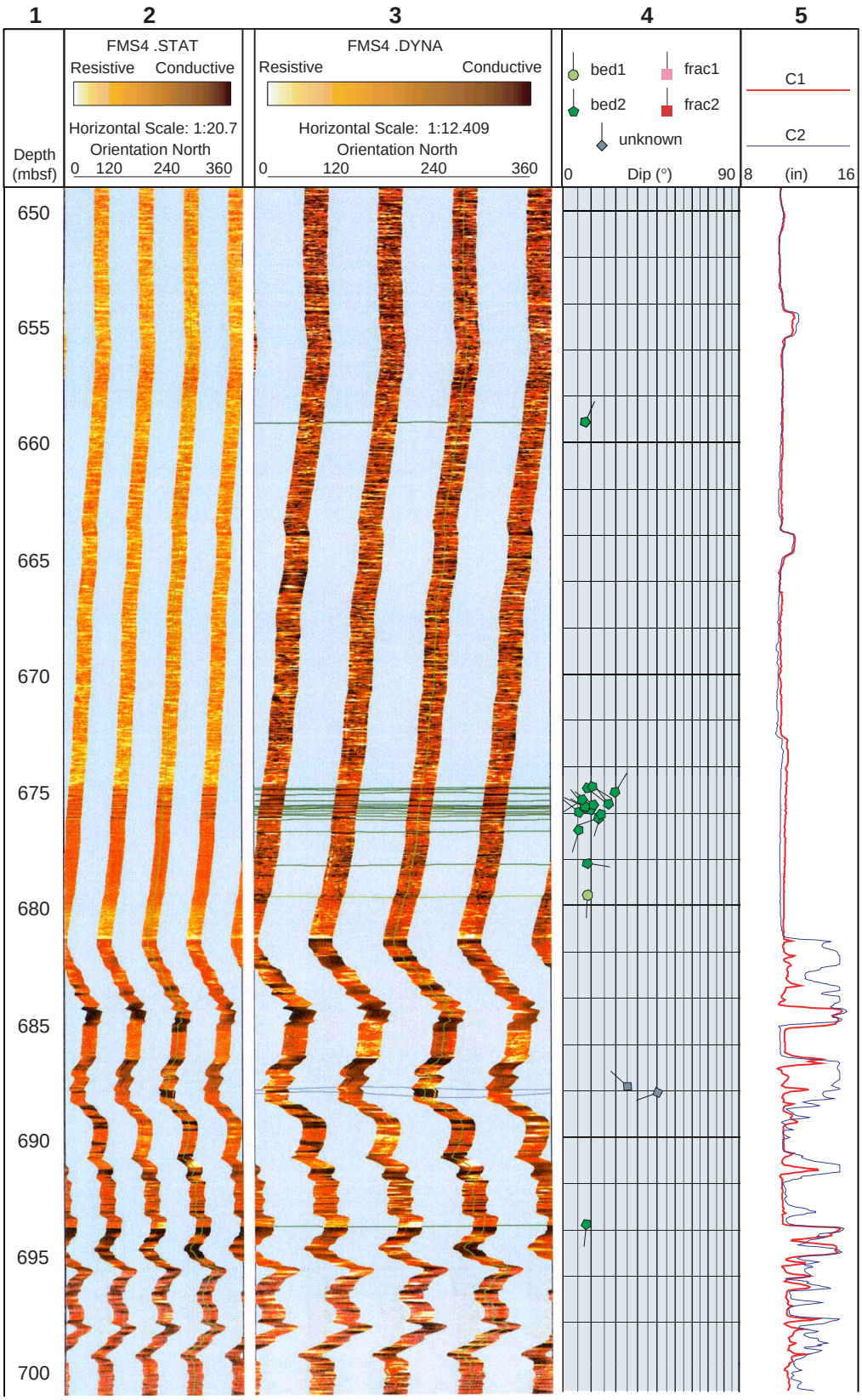

Figure AF2 (continued).

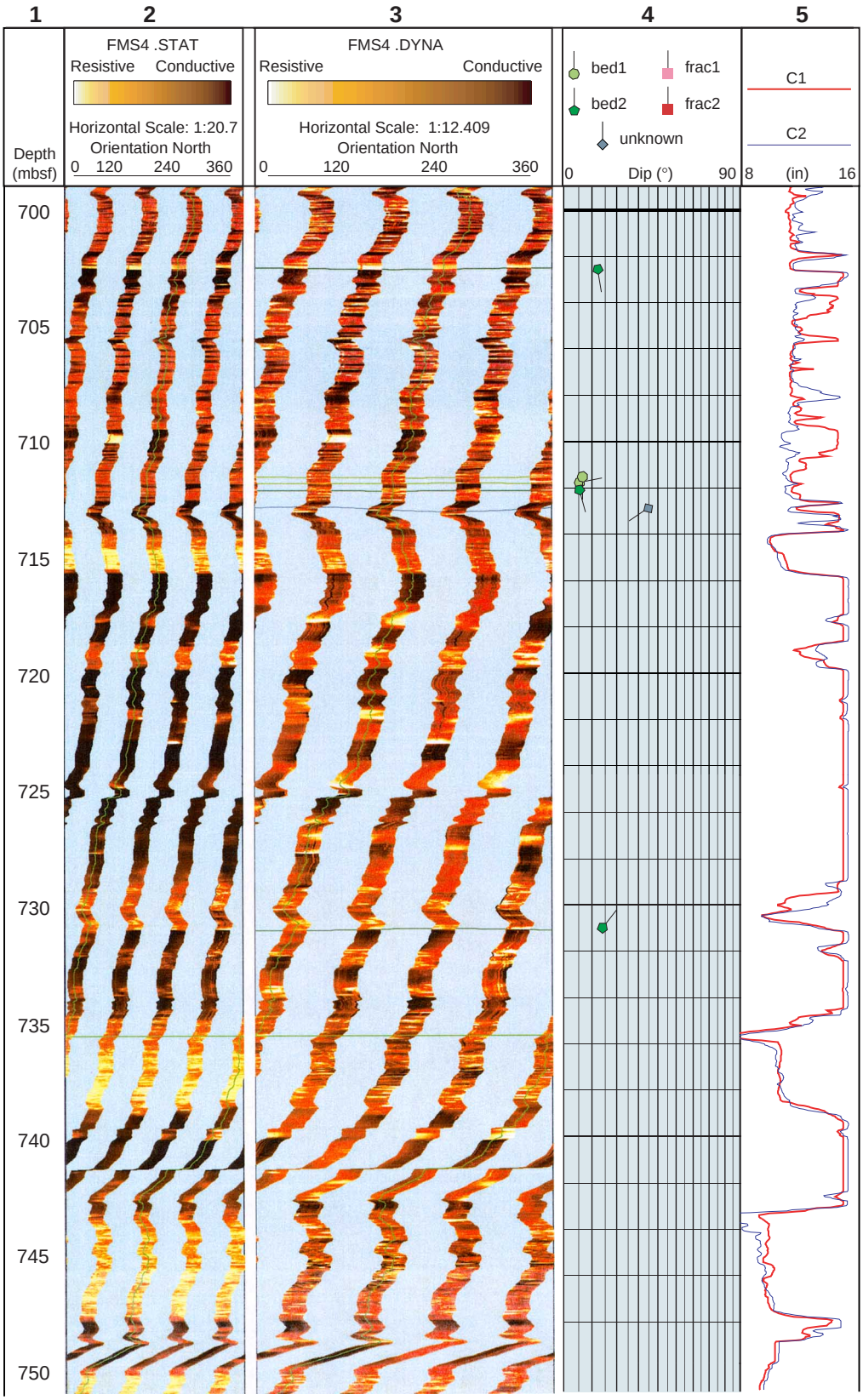

Figure AF2 (continued).

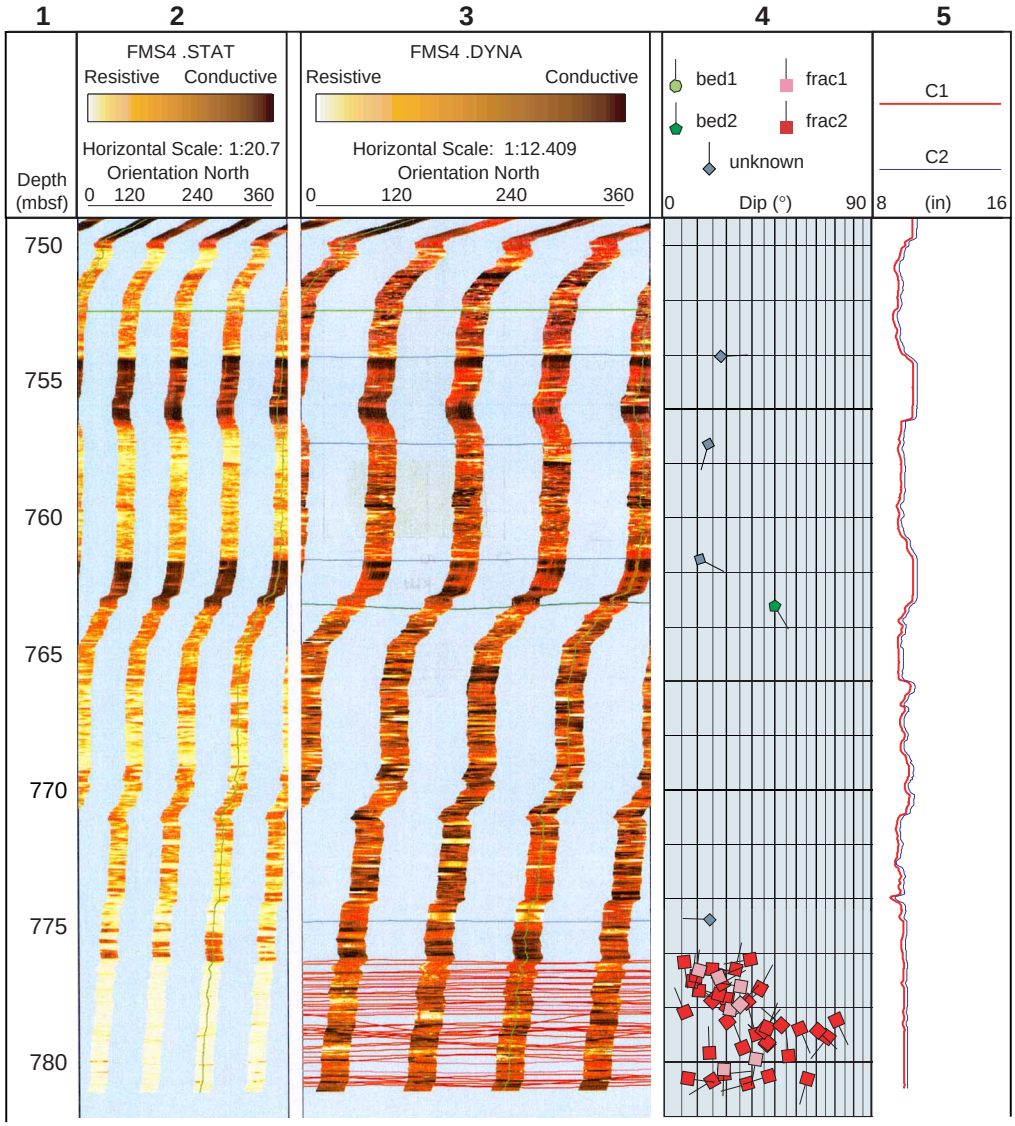

Figure AF3. FMS image and analysis, Hole 1115C. From left: (1) depth, (2) static FMS image, (3) dynamic FMS image with a 2-m color equalization sliding window with sinusoids corresponding to the structural measurements, (4) structural interpretation tadpoles, and (5) caliper measurements. The thin vertical green line on the FMS images indicates the orientation of pad 1, which correspond to the C1 caliper reading. The tadpole position on the horizontal axis indicates the dip magnitude, and its tail points toward the dip direction. (Continued on next 13 pages.)

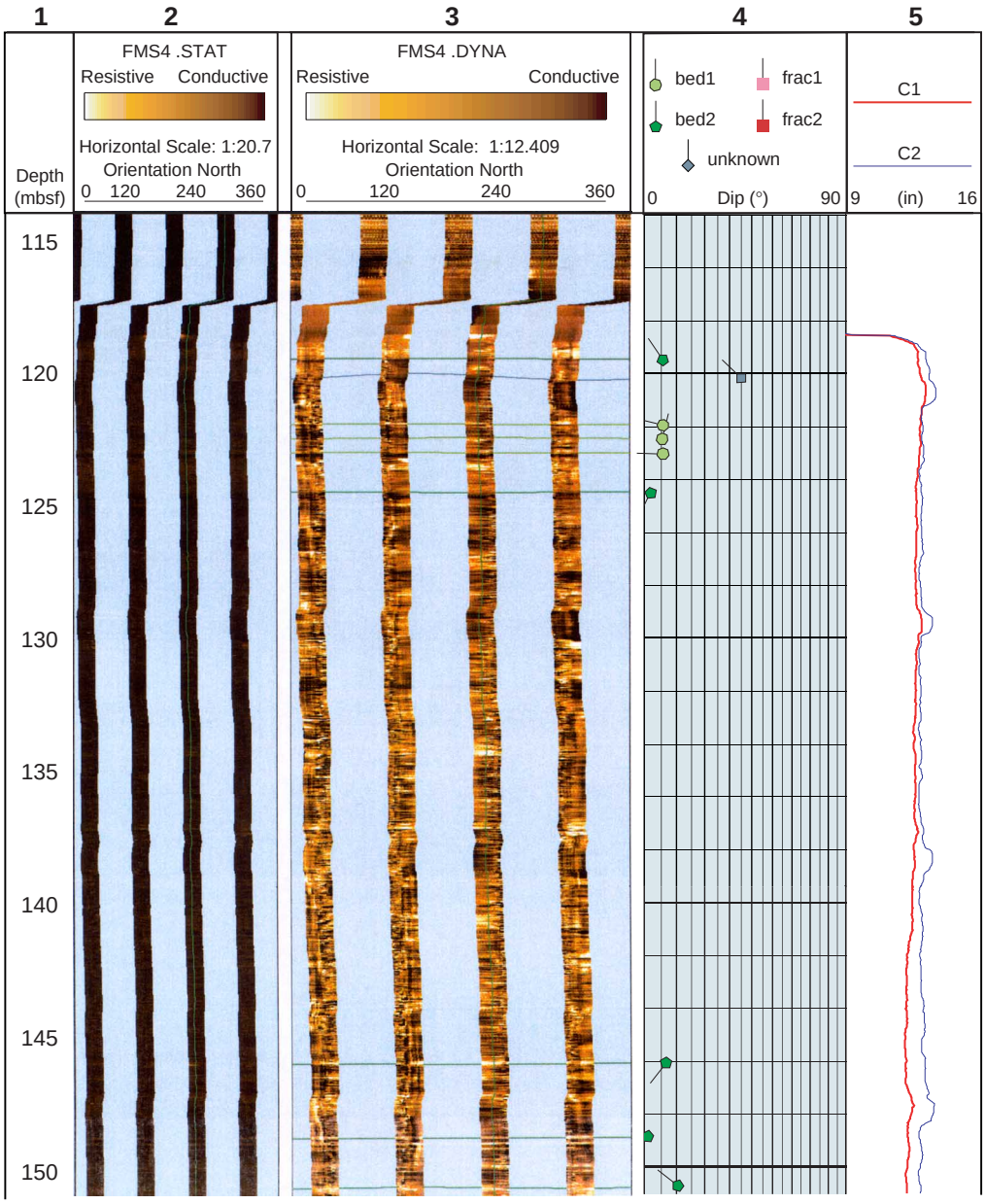

Figure AF3 (continued).

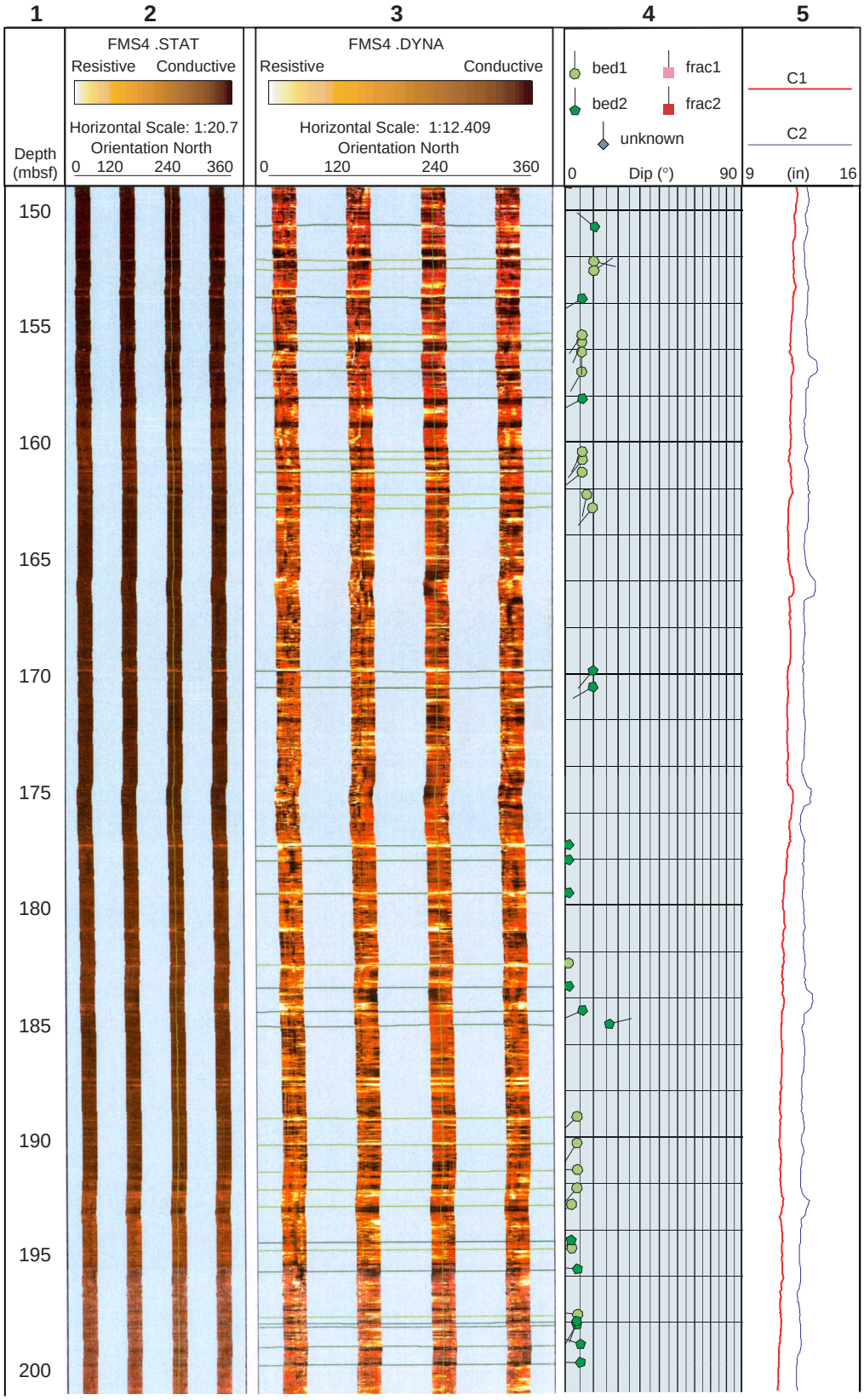

Figure AF3 (continued).

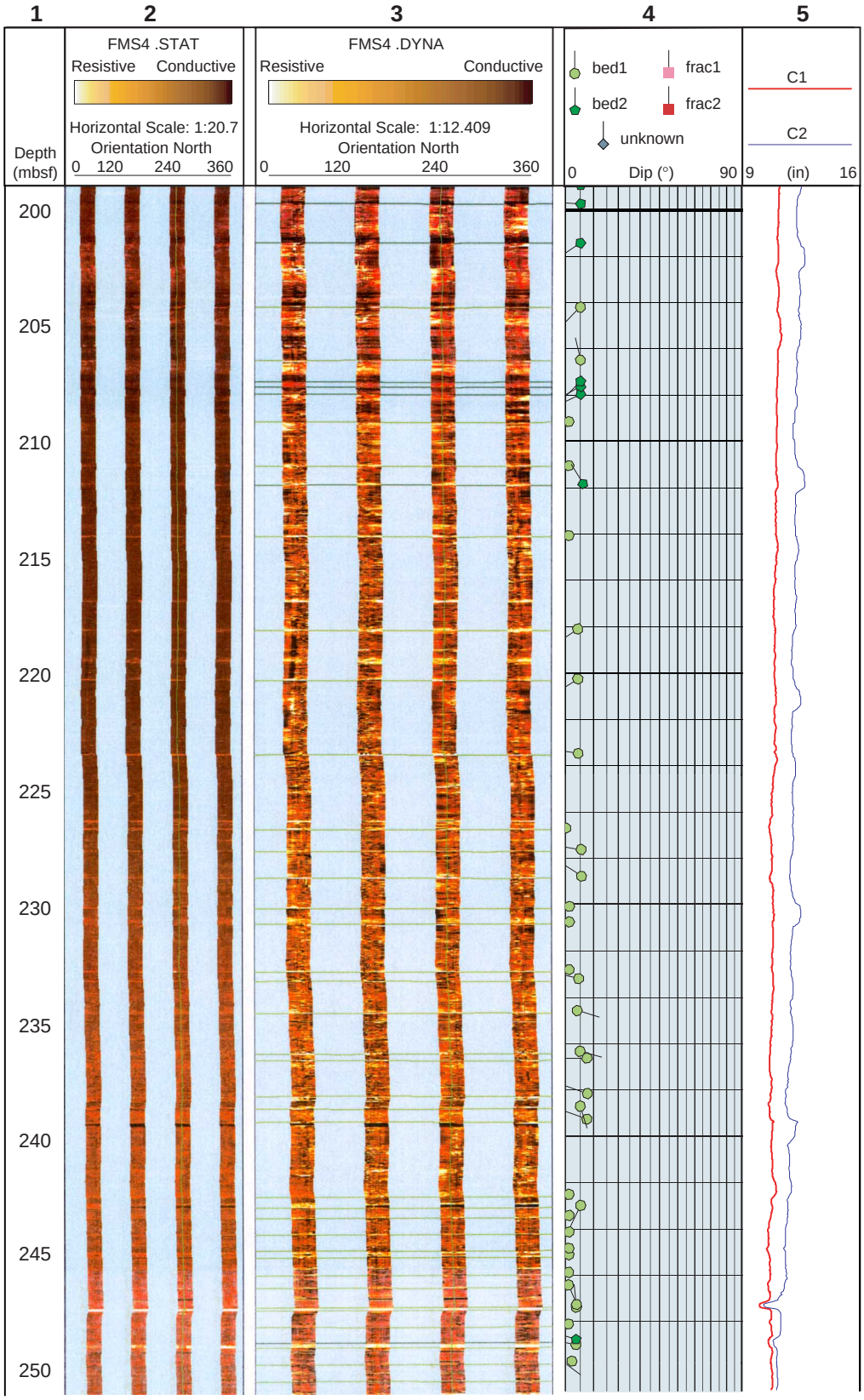

Figure AF3 (continued).

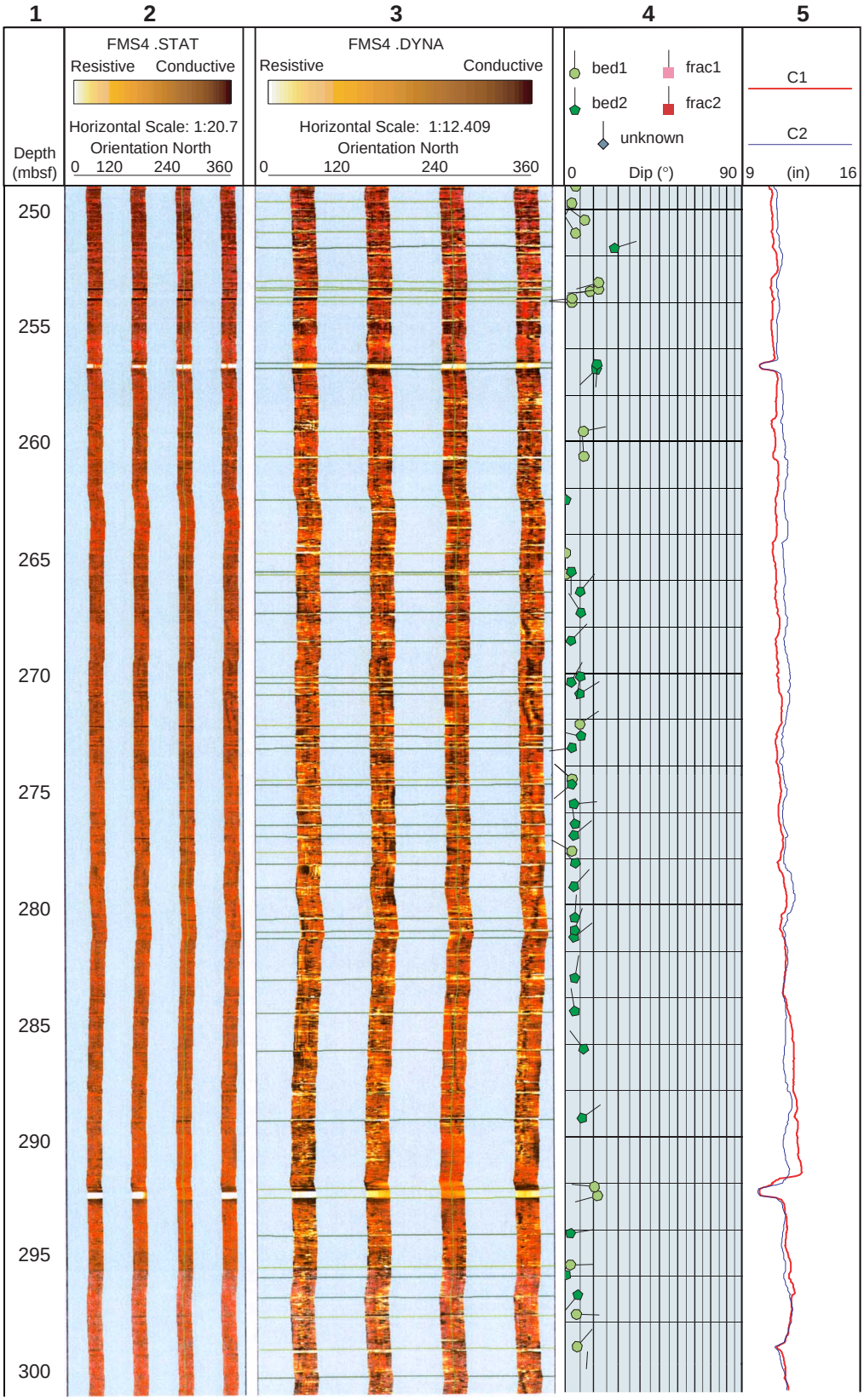

Figure AF3 (continued).

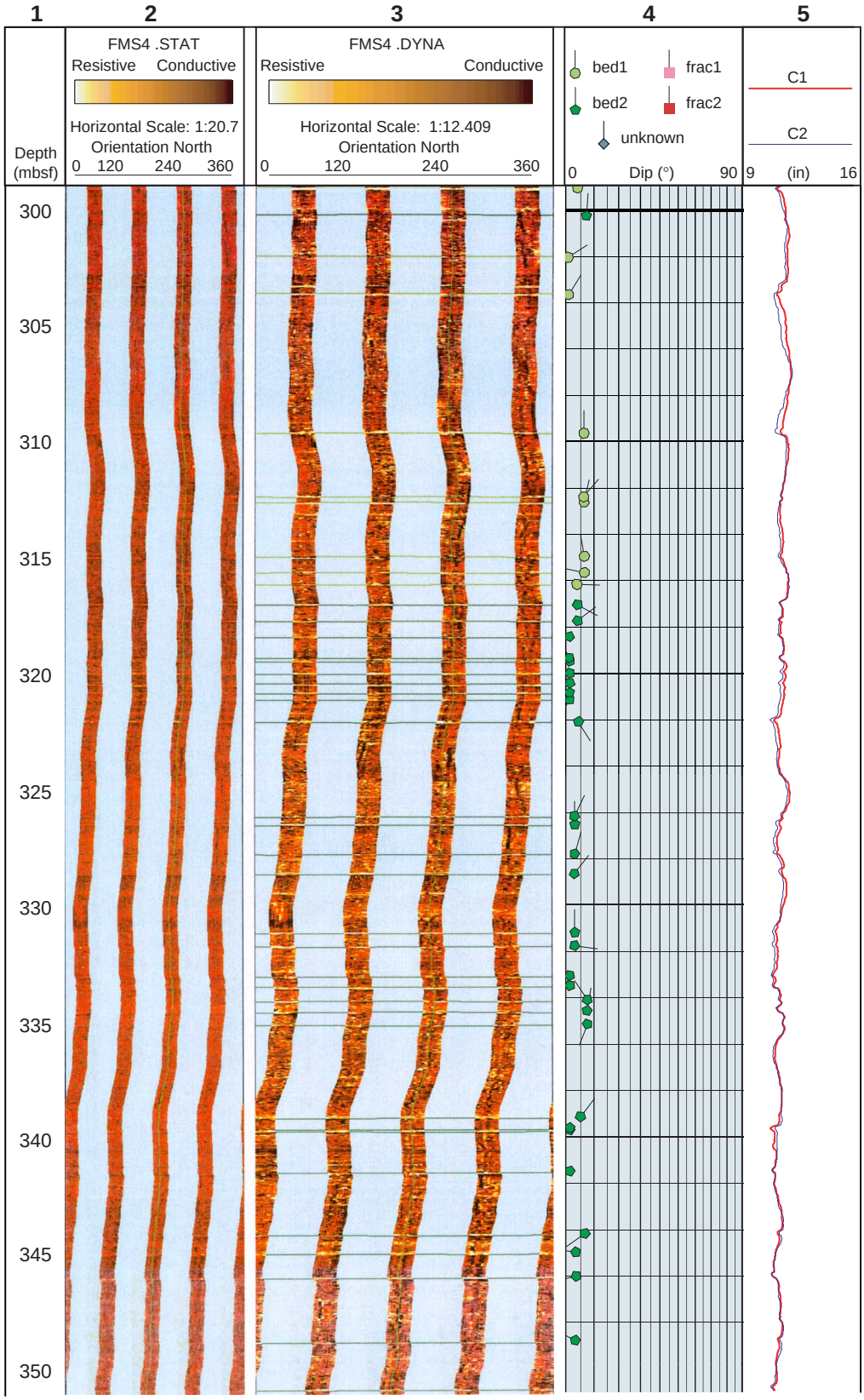

Figure AF3 (continued).

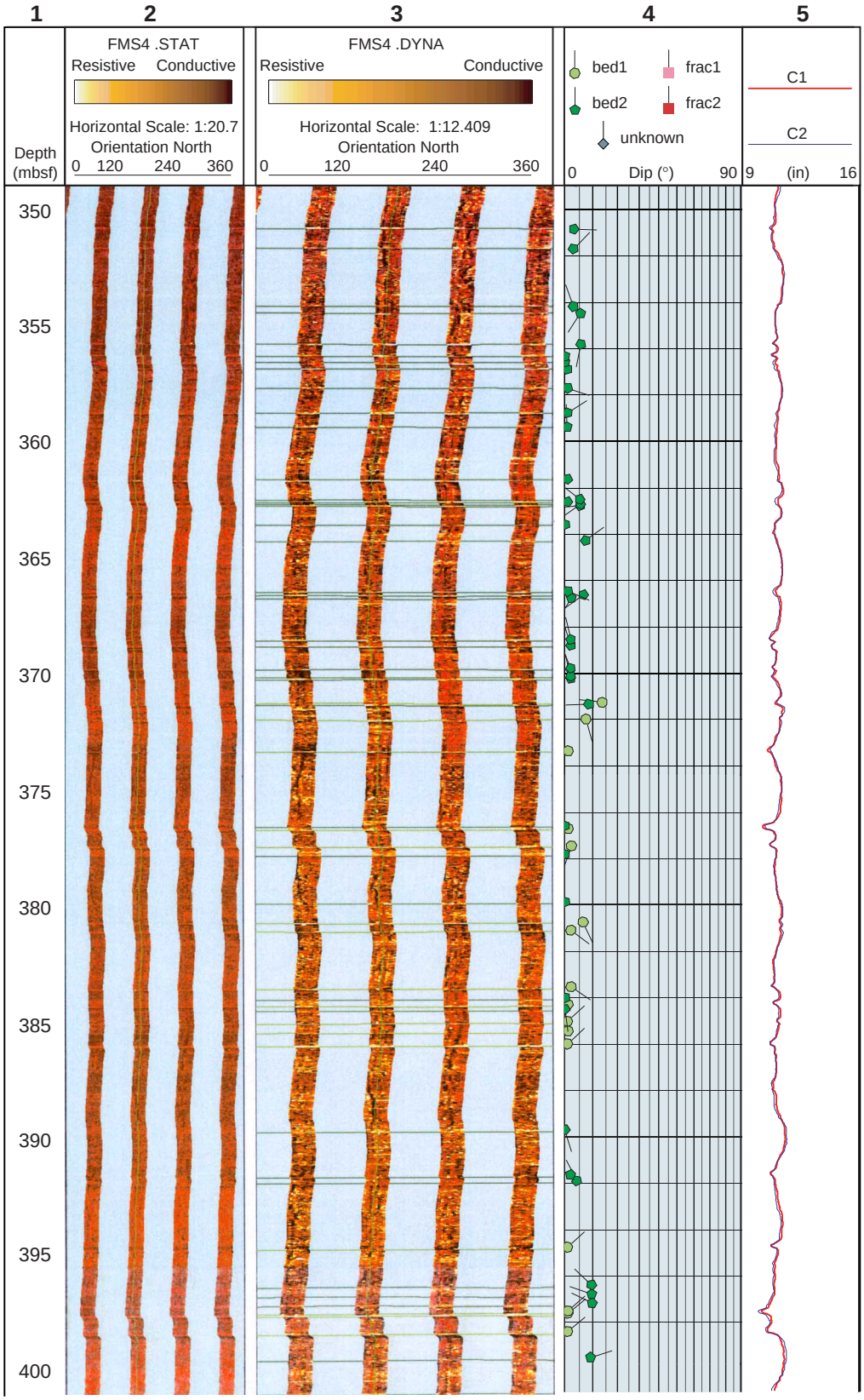

Figure AF3 (continued).

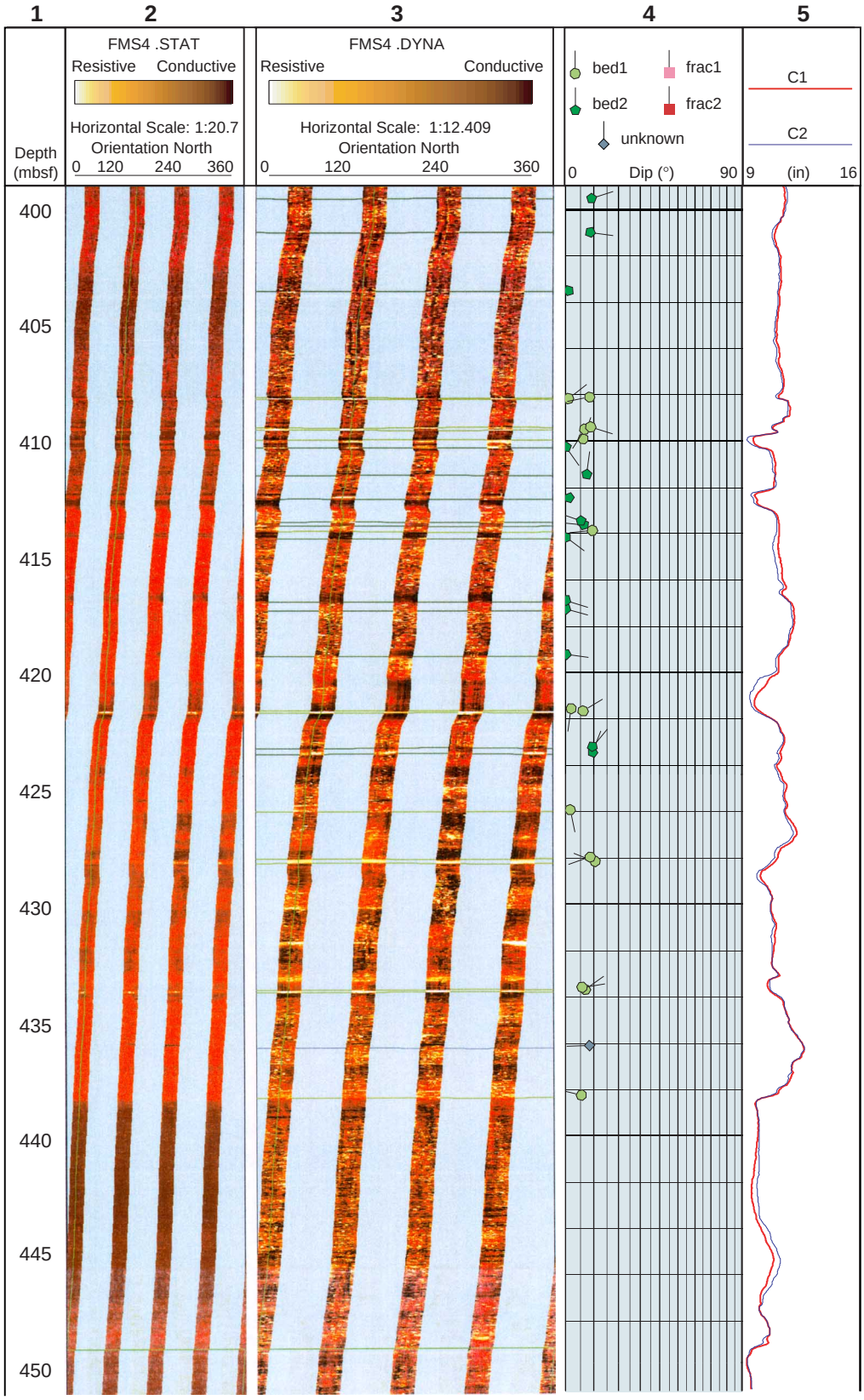

Figure AF3 (continued).

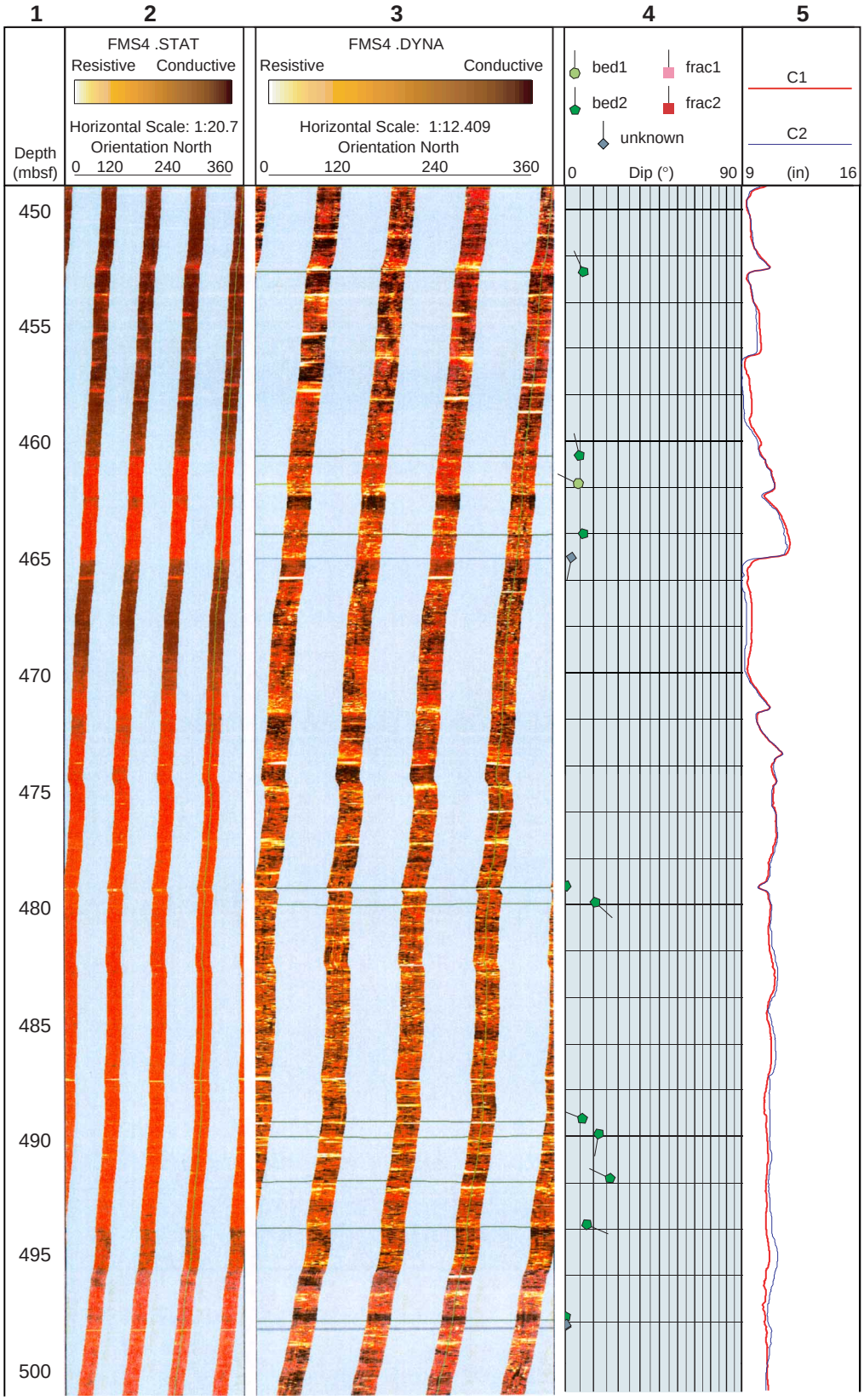

Figure AF3 (continued).

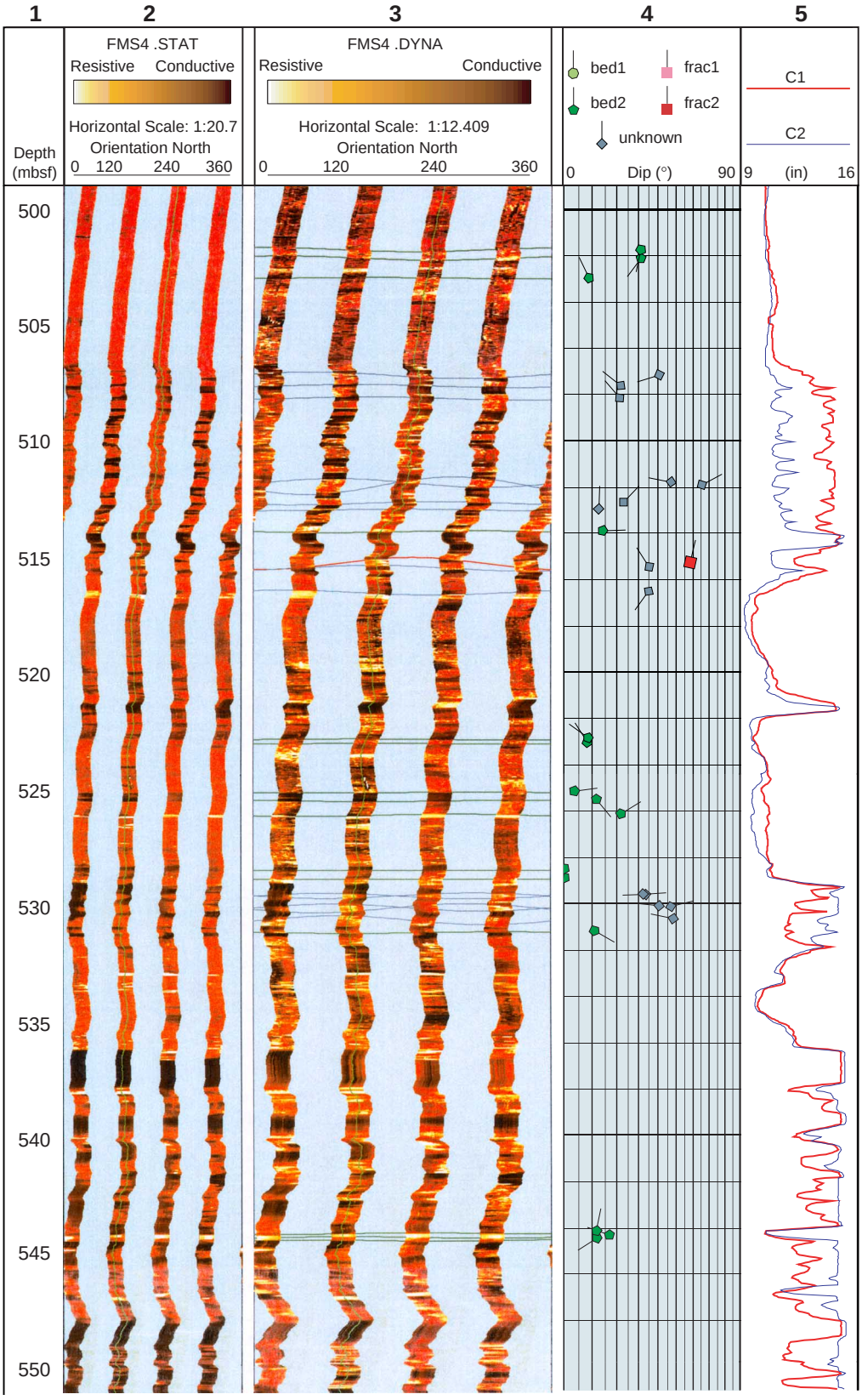

Figure AF3 (continued).

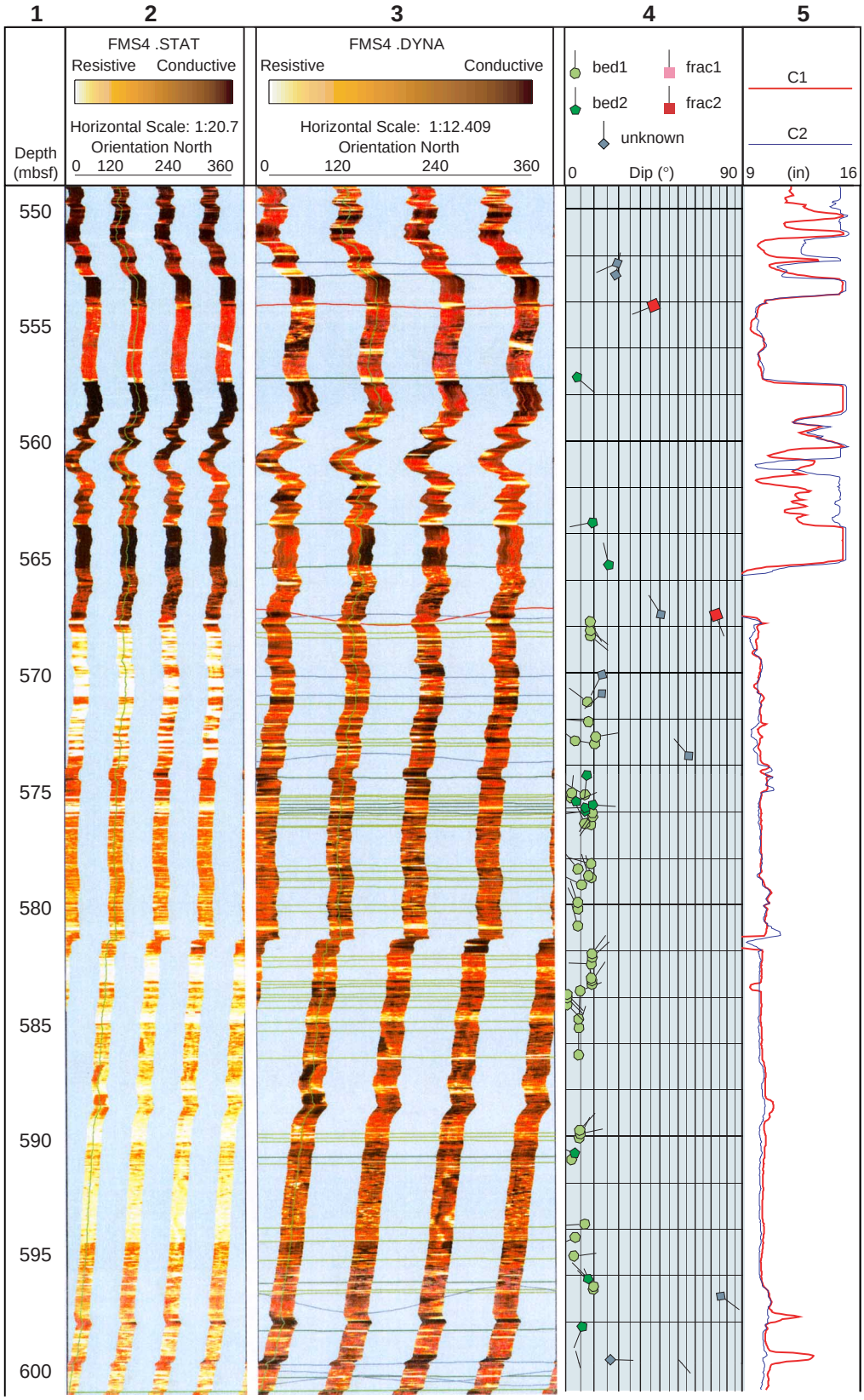

Figure AF3 (continued).

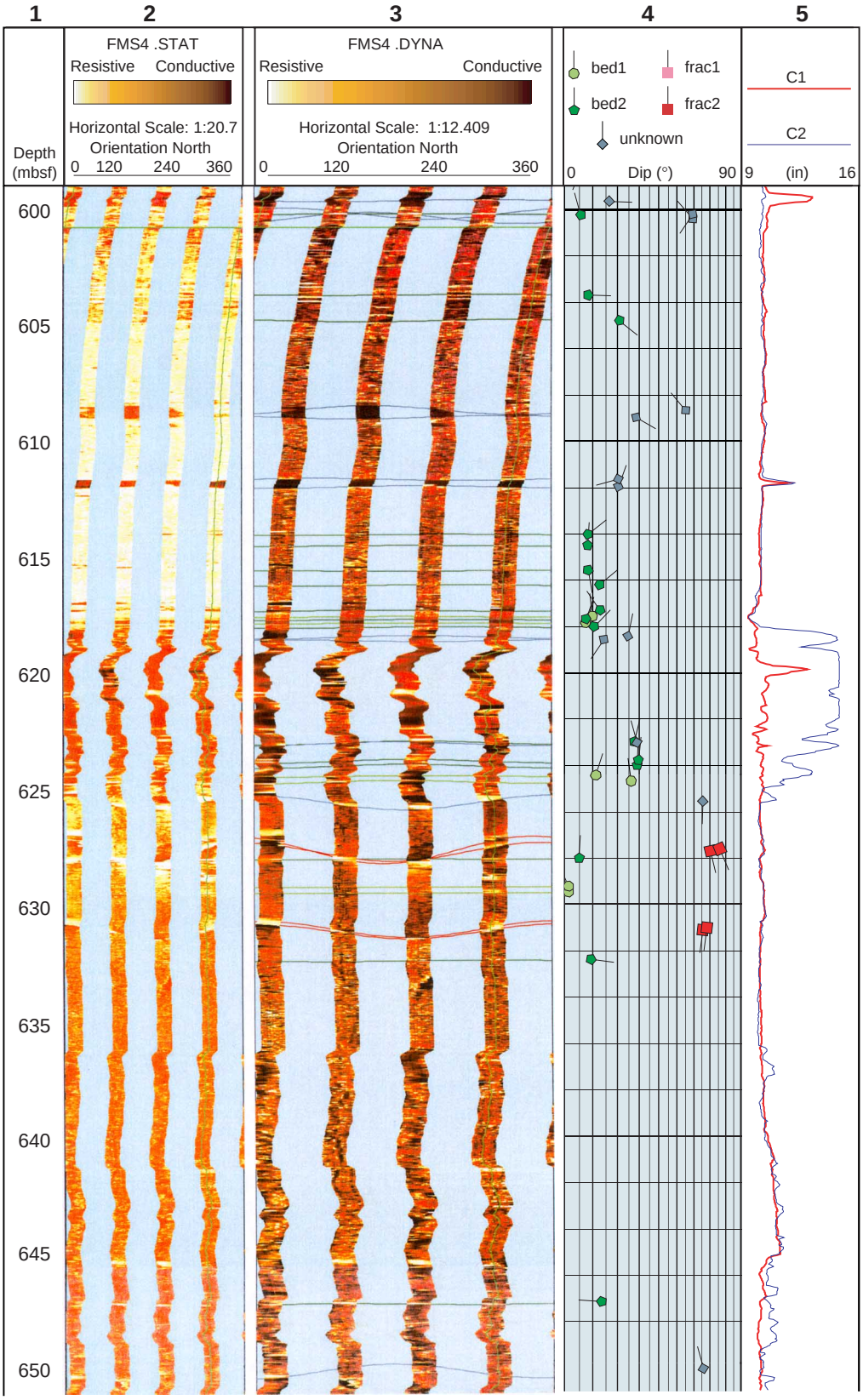

Figure AF3 (continued).

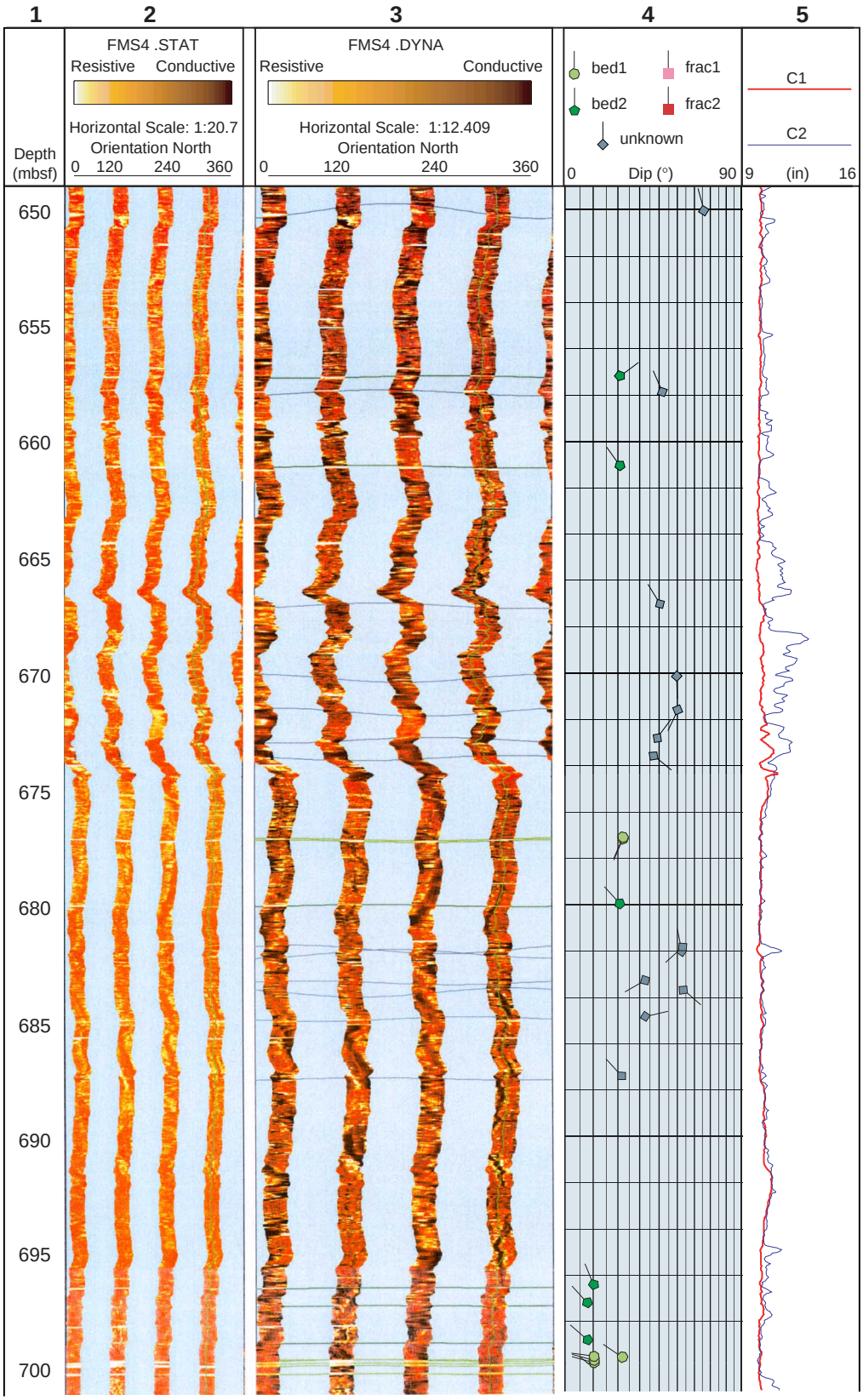

Figure AF3 (continued).

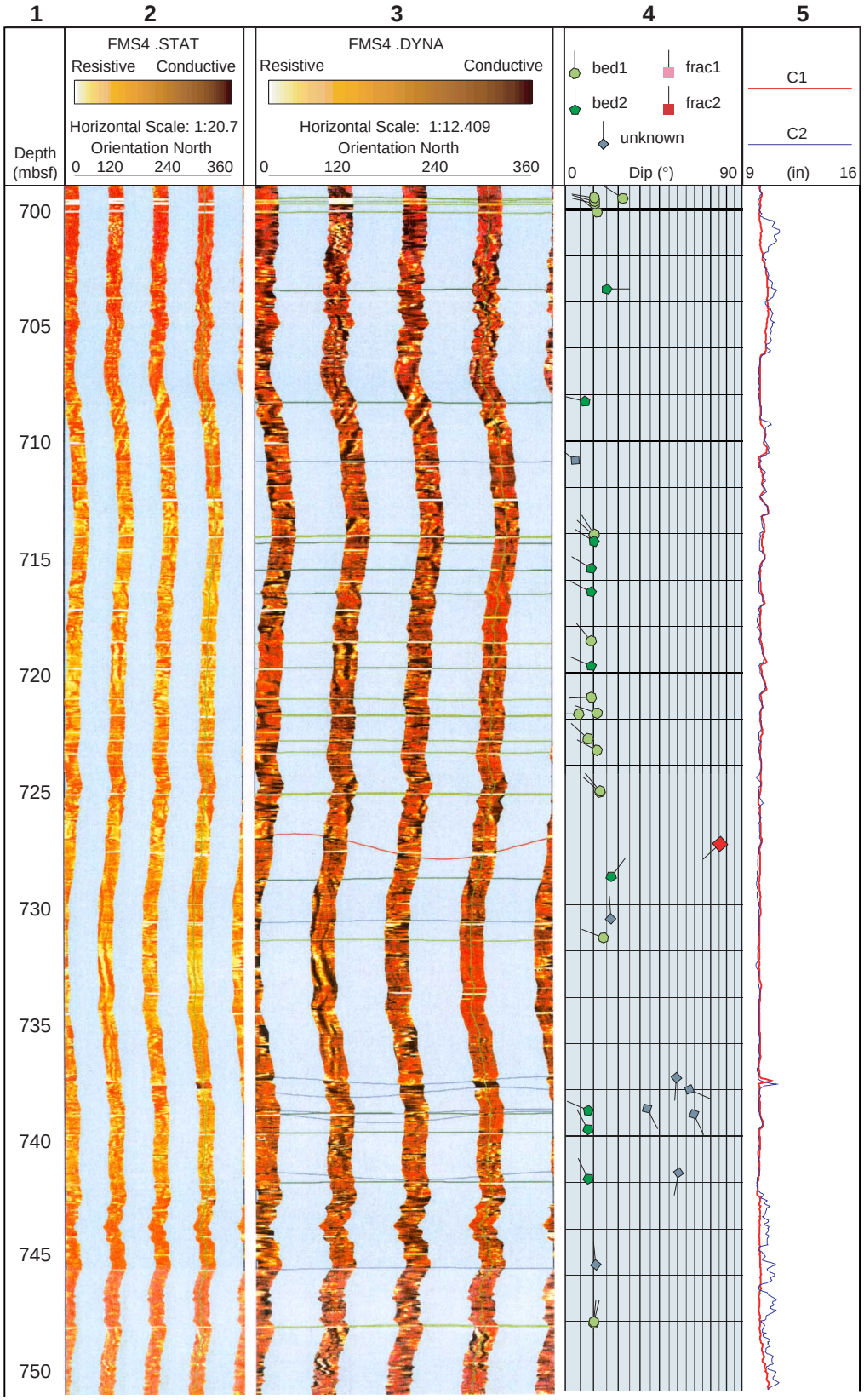

Figure AF3 (continued).